INVESTIGATION OF FRETTING FATIGUE IN TURBINE FIR TREE BLADE TO DISC JOINTS AT HIGH TEMPERATURE

Thesis submitted to the Department of Engineering Science of the University of Oxford in partial fulfilment of the requirements for the degree of Doctor of Philosophy

by

RODOLFO MIGUEL NOGUEIRA FLEURY

ST EDMUND HALL

OXFORD

MICHAELMAS TERM, 2015

for my family and friends

Abstract

Fretting fatigue is the phenomenon of combined contact and fatigue loads which may accelerate crack initiation and reduce the operational life of components. One of the most relevant problems of fretting fatigue occurs in the blade to disc assemblies, particularly those in the hot stages of gas turbines. The 'fir-tree' blade to disc assemblies in gas turbines operate at extreme conditions of loading and temperature, and the presence of multiple frictional contact points, often interacting with other stress concentrators, makes it an extremely challenging problems in solid mechanics. This thesis focus on two aspects of the problem found in 'fir-tree' assemblies: i) what is the impact of using single-crystal blades on the contact tractions and fretting fatigue behaviour; and ii) what is the effect of edge rounding on the contact tractions between the blade and disc?

In the first part of the thesis, the effect of single crystal orientation on the contact tractions is investigated. An analytical solution for the normal contact traction is used to evaluate the variation in contact peak pressure for different crystal orientation of single-crystal alloys. The full fretting stresses are also calculated using finite element analysis, and the results are compared with experimental data for fretting fatigue of nickel superalloys at high temperatures. An area averaging approach is also suggested to correlate fretting fatigue experimental results with plain fatigue data for the material and a good prediction was obtain when taken into account the stresses near the edge of contact.

A new approach for the solution of friction contact of elastic flat punches with rounded edges is introduced in the second part of this thesis. A three-quarter plane model is used as an asymptote to the region *very* close to the contact edge. Solutions for the contact law and peak pressure are obtained in terms of Williams' notch stress intensity factors. Then, edge asymptotes are used to solve the partial slip problem for relatively simple loading histories. An example problem for a finite punch with edge rounding is solved via finite element method and the semi-analytical solution presented. Contact tractions obtained via the asymptotic approach compare reasonably well with finite element output.

Acknowledgements

First, I would like to express my profound gratitude to my supervisors Prof. David Nowell and Prof. David Hills for their guidance throughout the course of this thesis. They have provided me helpful advice and suggestions, without which, the results obtained in this work would not have been possible. They have helped me overcome several unexpected problems faced during the course of this work. During these four years, they were always available when I needed their advice, with great willingness to help, and always demonstrating confidence in my work.

I also would like to thank Rolls-Royce plc and the Engineering and Physical Sciences Research Council (EPSRC) for their financial support throughout this thesis. I would also like to acknowledge the support of all the staff and technicians in the Solids Mechanics and Materials Engineering group at the University of Oxford.

I would like to express my special gratitude to Dr. Robert Paynter who has provided me with relevant technical input, as well as various advices. All of which made my time in Oxford easier. I also would like to thank the support and help from Robert Flicek, with whom I spent long hours discussing several technical and other issues. I also would like to thank all my friends in Oxford, in special, Firdaus, Diego and Julian, but also my friends in Brazil and elsewhere who helped me enjoy and relax during the last four years.

Finally, but definitely not least, I thank my mother, my father, my brothers and all my family in Brazil for their unconditional support and encouragement during the course of this thesis. I also thank my girlfriend Kathi for her companionship and for helping me during the difficult moments of the thesis.

Contents

Chapter 1

Introduction

The objective of this thesis is to investigate some aspects of contact mechanics and fretting fatigue that occur in blade to disc assemblies in turbines of aero-engines. The assembly of blades to disc at the high pressure stage of turbines is a very challenging structural problem which involves different aspects of solid mechanics. This thesis is dived in two parts and the following questions are investigated: i) how do single-crystal orthotropic blades affect the fretting fatigue life of a contacting isotropic component? and ii) how do the contact tractions and slip zone size behave near the edge of contact of an elastic flat punch with rounded edges (blade) and a flat body (disc)? The motivation and industrial context of this work are presented in this chapter. An introduction to contact mechanics and fretting fatigue are also given here, as well as some historical background of the field.

1.1 Motivation

The prediction of the service life of a component with the highest accuracy possible is increasingly one of the key aspects in today's design philosophy of mechanical parts. The understanding of the different failure mechanisms is very important in determining the safety and reliability of a product. Furthermore, the financial cost associated with maintenance and durability of the parts of a product during the course of its life is ever more important in the design of new mechanical components. Maintenance and replacement costs of parts represent a significant contribution to the total operational cost throughout different areas of mechanical engineering,

if taken into account over the total service life of components [Seemann, 2010]. The question of reliability and safety of a product requires a good understanding of its material properties and its behaviour under specific loading conditions. Any lack of knowledge on how and when a part will fail is normally compensated by overestimating the loads and/or part dimensions in the design. Needless to say, an overestimation of the dimensions of a mechanical component will incur greater cost, weight and, in the case of engines, higher fuel consumption. All of these factors also lead to higher environmental impact. In a time where efficiency is one of the main design considerations in most transport industries, a lower fuel consumption is often prioritised over power or speed. This search for greater efficiency is one of the main driving factors behind the push towards a better understanding of the service life of components, but also towards the development of new materials.

Among the different failure mechanisms that can be found in aero-engines, fatigue of components, and especially those where a contact with another component in the engine exists, is among the main causes for reduced operational life. This phenomenon of combined fatigue, contact between bodies, and small slip on the interface is referred to as *fretting fatigue*. Perhaps one of the most classical example of fretting fatigue is found in the blade to disc assembly of aero-engines. In order to facilitate maintenance and replacement of the blades in the engine, they are not welded to the disc, but simply assembled by sliding the blades into the disc. This results in small amplitude slip at the contact interface between the blade and disc during the operation of the engine (see §1.2.1), which accelerate crack initiation near the contact interface. Fretting fatigue has been the topic of research for many decades, particularly in the aerospace industry. Some of the early work on fretting was carried out by Waterhouse, who summarised the different aspects of fretting fatigue problems in Waterhouse [1981] and further details are given in §1.4.

The main goal of this thesis is to provide a better understanding of the stresses in partial slip contact and fretting fatigue problems. Also investigated are the factors that can lead to a greater degree of unpredictability in the service life of aero-engines. Understanding of the reduction of service life due to the combined phenomenon of contact and fatigue has been well developed for a series of materials commonly used in the rail, automotive and aeronautics

industries. However, the constant push towards greater efficiency of engines is often followed by the development of new materials and more extreme service conditions. This is the case, for example, of the significant increase in temperatures in the turbine stage of aero-engines. Therefore, new materials are constantly being developed to cope with such conditions. As will be shown in this thesis, some of those new materials being employed in the aerospace industry introduce new variables to the problem of fretting fatigue and life prediction for such materials needs to be better understood.

Controlled fatigue tests have been carried out by Rolls-Royce plc using a prototype specimen emulating the blade to disc contact. The disc is represented by the 'H-specimens' and a specimen with a 'fir-tree' type of blade root was used (Figure 1.1a). A cyclic load F was applied to the specimens, representing the centripetal force during the revolution of the disc. The characteristics of these tests are still very complex, with several contact points and stress concentrators. For example, since both the 'blade' and 'H-specimens' are under varying tension, cracks initiated and propagated on both specimens, and while some tests resulted in failure of the blade, others failed at the 'H-specimen' (Figure 1.1b). Note that the edge of the contact between the blade and disc is not the only point of stress concentration in the blade to root assembly, and some cracks originated from the notches on the 'H-specimen'. Due to the complexity of these experiments, the results have shown a large spread of fatigue lives. A few questions have been raised as a result of these tests: what is the impact of i) using of single-crystal blades with only partially controlled crystal orientation; ii) the manufacturing tolerance on the distribution of forces between the lobes; and iii) the high temperature environment, particularly oxidation on the interface, on the friction and contact stresses?

With the aim of answering some of the questions raised in the 'H-specimen' tests, simpler fretting fatigue experiments, under the MACE test programme, were conducted at the University of Oxford. The tests were carried out at the 'in-line' fretting fatigue rig, where a flat specimen of square cross section is submitted to fatigue loading and contacted by pads, on which normal and tangential loads are applied. The specimen and test geometries are briefly described in §3.2.2, but further details are found in the original work [Sarsfield, 2008]. These experiments were conducted with significantly simpler geometries and at room temperature, eliminating two

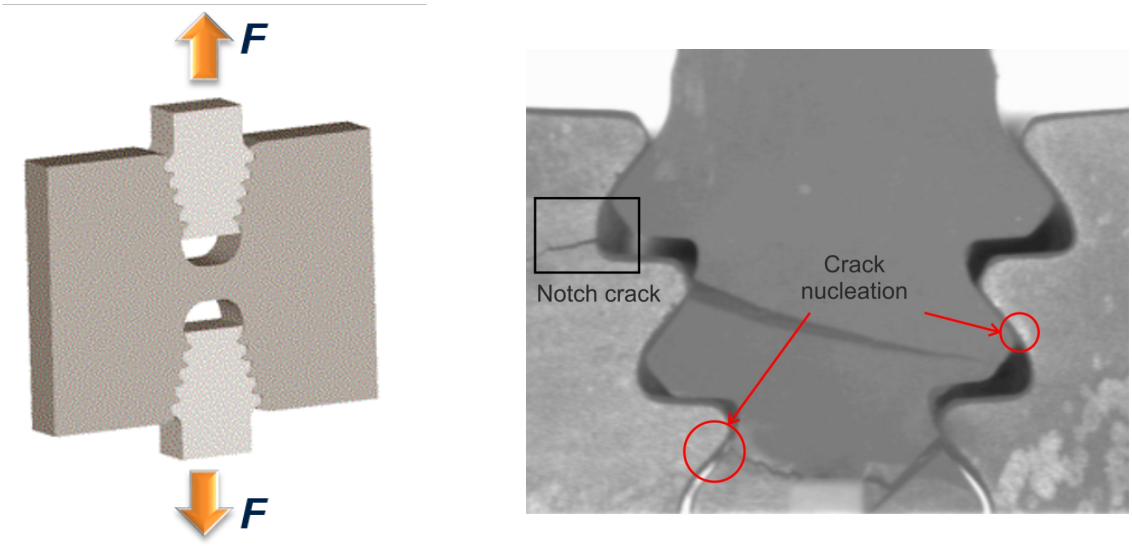

(a) (b)

Figure 1.1: (a) Schematic representation of the H-Specimen test; (b) Cracks on a fir-tree blade to disc assembly.

of the issues raised in the 'H-specimen' tests. However, a large scatter in fretting fatigue life was still observed for tests with similar load conditions (Figure 1.2). One important result from the MACE test programme is that some single-crystal test pads, used in the contact with isotropic specimens, were re-machined and the experiment repeated. The scatter was significantly reduced between tests with the same single-crystal pads. Hence, it was suggested that the uncontrolled orientation of the single-crystal pads was, perhaps, the main reason for the large variation in the fatigue life.

The results obtained in these two previous test programmes provided the motivation for the first part of this thesis. The main question that arose from these tests is the focus of investigation in this thesis, i.e. what is the effect of the single-crystal crystallographic orientation on the fretting fatigue life of a contacting isotropic body? The second part of this thesis focuses on the contact of a flat punch with rounded edges on a flat elastic body, which is found in the blade to disc assemblies. Note that the contact geometry in the 'H-specimen' tests, and of some of the pads used in the MACE tests, are in fact that of a flat punch with rounded edges. This type of contact has been investigated by several authors in the last decades, but most of the work assume that the contact tractions are uncoupled. An analytical solution for the partial slip problem of an elastic punch, and in the presence of friction, has not yet been developed.

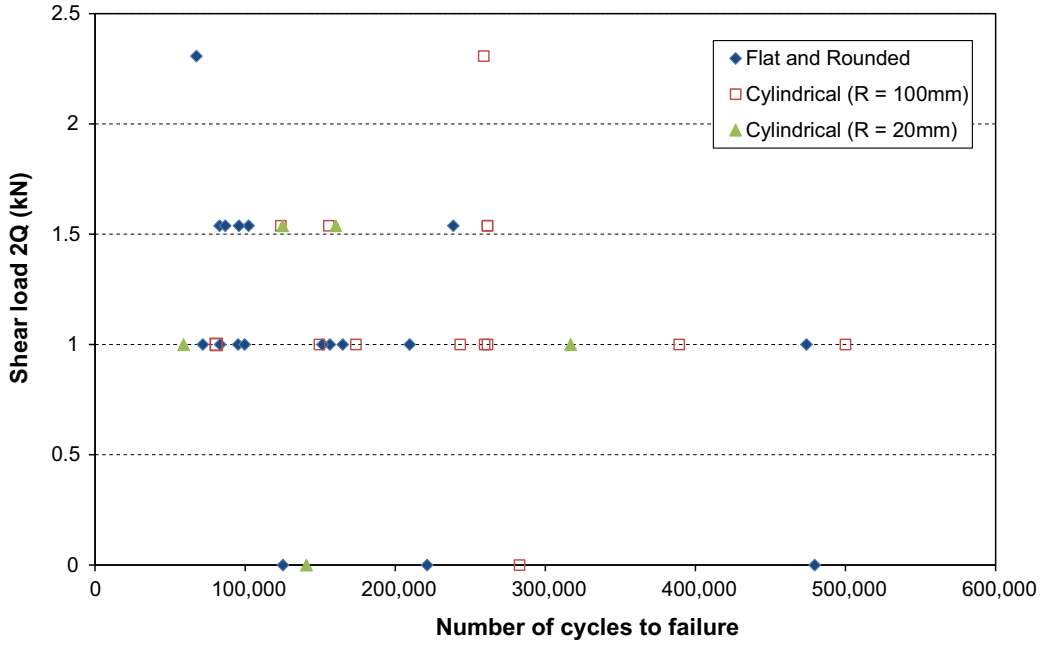

Figure 1.2: Number of cycles to failure in fretting fatigue. Results obtained in the MACE test programme with cylindrical and flat and rounded pads [Sarsfield, 2008].

1.2 Industrial context

1.2.1 Gas turbine engines

Aero-engines are normally comprised of three parts: fan, compressor and turbine stages. However, large engines may have multiple stages in the compressor and turbine, often referred by low pressure (LP) and high pressure (HP) stages (Figure 1.3). The fan draws part of the air into the LP compressor, which is then compressed further at the HP compressor. Then, the air, with a high pressure, enters the combustion chamber, where it is mixed with fuel and ignited elevating significantly the temperature of the gas. The hot gas exits the combustion chamber passes through a series of turbine stages, first the HP turbine and then the LP turbine, before being discharged through a nozzle. As the gas passes through the turbines, work done by the gas is transferred to the rotor of the turbine. The rotors of the turbine then rotate the fan and compressors through shafts in the central axis of the engine. Part of the energy captured by the turbine is used to accelerate air that bypasses the turbine. This type of engine is often referred to as 'turbofan' and is most common in civil aviation engines. The final thrust generated by the engine is a combination of the flow that passes through and flow that bypasses the turbine.

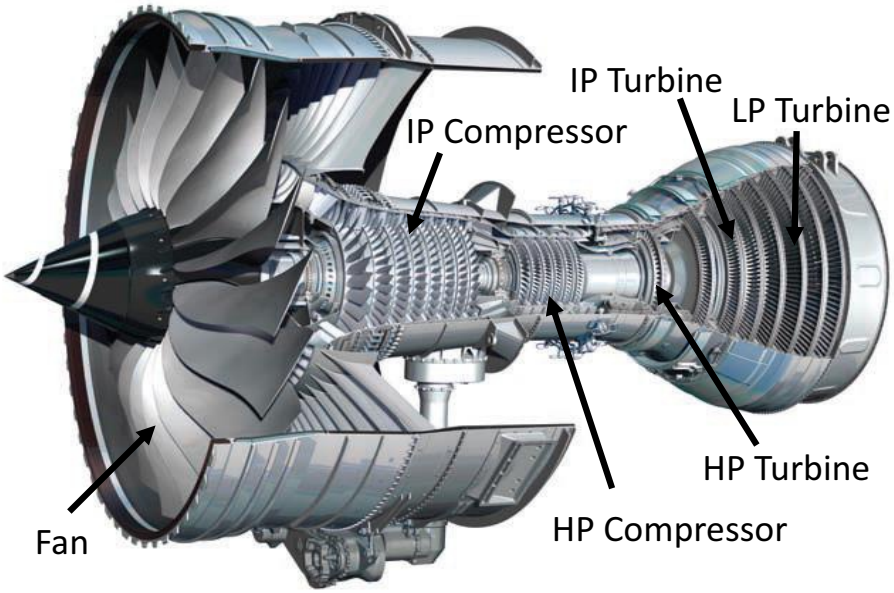

Figure 1.3: Trent 1000 turbo fan aero-engine.

Some larger modern engines may have additional intermediate (IP) stages between the LP and HP compressors and turbines, as well as a two shaft system, where the fan, for example, is driven by the LP turbine only. An example of turbofan aero-engine is presented in Figure 1.3.

In an engine as complex as a gas turbine, a large number of parts are in contact and also under oscillating loads during service. This will, often, lead to fretting fatigue and it is essential that the parts are properly maintained and replaced before a critical number of cycles is reached. Some parts, however, may be designed to be replaced more frequently than others. That is the case, for example, of blades in comparison with discs and shafts. Although some stages of the compressors are made of 'bliscs', i.e. rotor disc and blades made of a single part, in the most critical areas of the engine the blades are assembled to discs by simply sliding them into the discs. This allows an easy replacement of the blades once the critical number of cycles is reached or cracks are identified. However, the replacement of discs and shafts, for example, is not as simple as the replacement of blades and it is important that the design against fatigue of these 'critical' components be as accurate as possible. Hence, the tests carried out in this thesis focus on the fretting fatigue of polycrystalline alloys (disc), contacted by single-crystal pads (blade) and not the other way around.

Two types of blade to disc assemblies are commonly found in aero-engines. The 'dovetail'

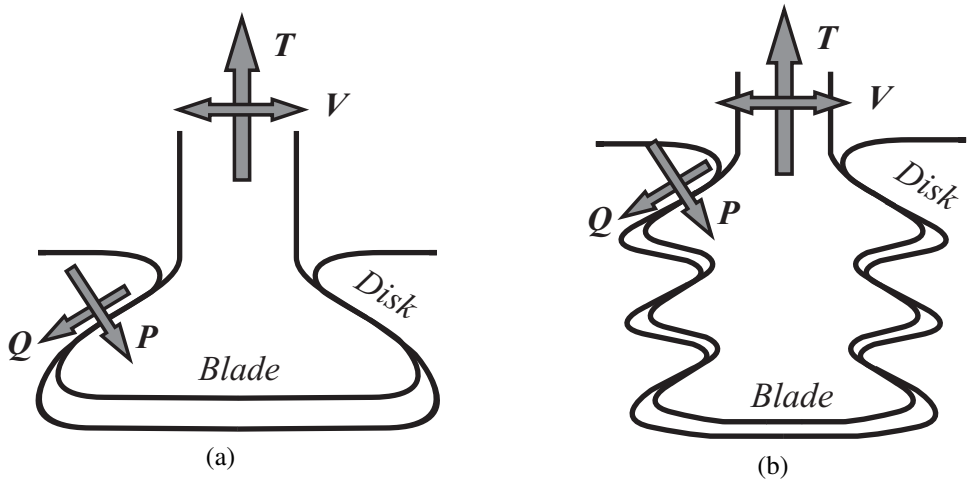

Figure 1.4: Scheme of (a) dovetail and (b) fir-tree blade to disk attachments. When tension T and vibration V are applied on the blades, normal and shear loads P and Q occur in the contact.

blade root type (Figure 1.4a) is normally found in the fan and colder stages of the engine. And the 'fir-tree' type blade root with multiple lobes is normally employed in the hot, and smaller, stages of the engine (Figure 1.4b). Although the analyses of fretting fatigue carried out in this thesis may be, in principle, applied to both types of blade root, the problem of single-crystal orientation is normally associated with the elevated temperature stages of the engine and, hence, with the fir-tree blade root. The work on the contact of the elastic flat punch with edge rounding, on the other hand, can be equally applied to 'dovetail' and 'fir-tree' blade root type assemblies.

1.2.2 Single-crystal nickel superalloys

The efficiency of current gas turbines is currently limited by the limits of the materials to withstand high temperatures. An increase in efficiency of gas turbines is generally achieved by higher temperatures in the engine. The search for materials that can sustain to their mechanical properties at high temperatures has led to the increase use of nickel alloys in high pressure turbine stages of aero-engines; polycrystalline and single-crystal alloys. Discs in the high pressure compressor and turbine are made of polycrystalline alloys, where, although much colder than the hot gas temperature ($\sim 1500°$C), the temperatures may reach 600-800°C. The turbine blades are extremely important for the generation of power by the engine and are also located in a critical area of the engine, where the temperatures may reach above the melting point of the material [Reed, 2006]. A complex cooling system is required in order to keep the blades be-

low their melting point. Turbine blades are regarded as one of the most demanding application for high temperature materials due to the high loads and temperatures involved [Sims, 1987]. Moreover, the tight gap between the blades and the outside chamber of the gas duct requires that a special attention be given to the creep resistance when selecting/developing alloys for high pressure turbine blade application. Excessive deformation of the blades may exceed the tolerance and result in failure of the component.

Single-crystal blades are used mainly due to their higher resistance to creep. The casting of a blade in a single grain improves overall creep resistance by eliminating grain boundary slip. This does not mean that single-crystal blades are not susceptible to creep. Other mechanisms, such as, slip planes dislocation creep and/or diffusion creep may occur. Nevertheless, single-crystal alloys are significantly more resistant to creep than polycrystalline alloys and a more suitable choice for high pressure turbine blades. The CMSX-4 nickel superalloy is among the most commonly employed single-crystal alloys for aero-engines blade manufacturing and it is the only one specifically studied here, although the general approach is valid for other alloys.

The characteristics of partial slip contacts (i.e., peak stress, contact width, slip zones, etc.) depend on the elastic properties and compliance of the bodies in contact. Furthermore, the properties of most metallic crystals are not isotropic and depend on their crystallographic structure and orientation. Nickel crystals, for example, have a face centred cubic (FCC) structure and orthotropic elastic properties (Figure 1.5). This means that some properties such as the elastic stiffness, are similar in three orthogonal principal directions (i.e. $\langle 100 \rangle$, $\langle 010 \rangle$ and $\langle 001 \rangle$), but vary in other crystal directions. During the casting of the blades, only one principal crystallographic direction (e.g. $\langle 100 \rangle$) is controlled to be along the long axis of the blade with a 20° tolerance.

Studies found in the literature suggest that mechanical behaviour of these alloys as, for example, fatigue strength and fracture toughness, depend on the direction of loading with respect to the crystal orientation. The impact of crystal orientation on the stress intensity factor of notches and crack growth in single-crystal has been investigated by Tinga [2006], where the necessity of using an anisotropic model to calculate the stress intensity factor has been highlighted. Karadge et al. [2008] have shown that the orientation of the crystal is also important for

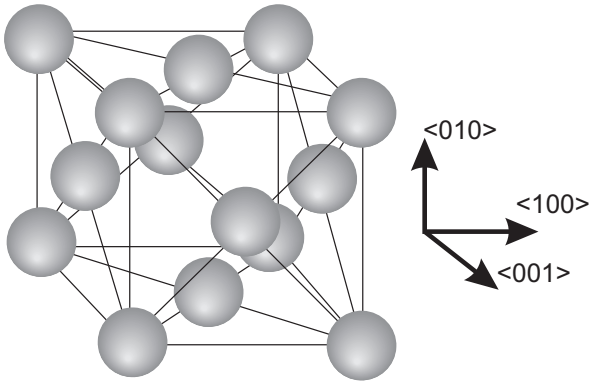

Figure 1.5: Face centred cubic (FCC) single-crystal structure and principal directions.

the "weldability" in linear friction welding. This is mainly due to directions of the primary slip systems in the crystal lattice during the linear welding process. The impact of crystal orientation on uniaxial plain fatigue life has been investigated by Arakere and Swanson [2002]. They found that distinct curves are obtained for different crystal orientations in strain controlled low cycle fatigue (LCF) tests, where stiffer crystal directions have showed lower fatigue resistance.

The use of single-crystals in components subjected to contact and fretting has also been the subject of previous investigations by other authors. Arakere and Swanson [2001] investigated contact subsurface stresses in single-crystal superalloy blades. By using a finite element model of the blade to disc attachment, they found that the maximum shear stress near the contact varied by a factor 2 when assuming the contact to be frictionless. It has been reported in [Matlik et al., 2009] and [Savage, 2012] that the material orientation can significantly change the stresses near the contact zone in the single-crystal blade. This effect can be expected since the elasticity tensor of an orthotropic material changes with respect to the orientation.

Very little work has been carried out on the impact of crystal orientation of a single-crystal body on the contact stresses of a contacting isotropic body. This is the main focus of the first part of this thesis, where the change in the normal contact pressure due to the crystal orientation of the CMSX-4 alloy is investigated in chapters 3 & 4. Particularly, the impact of the *secondary* principal directions on the contact stresses is investigated, i.e. when one of the crystal's principal directions is fixed normal to the contact, but the other two principal directions may be positioned in any direction on the plane of the contact interface, but always orthogonal to each other. The contact interface normal direction in the blade to disc assembly, however, has an angle

of about 45° deviation from the principal direction of crystal growth of single-crystal blades (see Figure 1.4). Although the specific case of the blade to disc contact interface inclination is not discussed here, the maximum change in contact pressure for all crystal orientations is investigated and it serves as a bound for the blade to disc contact problem.

1.3 Contact mechanics

Contact mechanics is the study of the interaction between two bodies pressed against each other. Interactions between bodies occur in many mechanical assemblies and crucial devices in engineering, such as gears, bearings, and bolted or riveted parts. In a typical contact problem one is generally interested in knowing the contact tractions, i.e. the distribution of normal and tangential forces along the interface; and the relative displacements that define the conditions of slip and stick inside the contact region. These unknowns depend on the applied load, the coefficient of friction at the interface, the geometry of the bodies in contact and their material properties. Contacts are a relevant stress concentrator in parts and assemblies, where failure and damage of the part is likely to originate from. The stress field around the contact zone, which, for instance, may be used to calculate the crack propagation life near the contact, can be obtained once the contact tractions are known. Hence, an understanding of the stresses around contact zones is important in the design of components. Furthermore, the size of slip zones and magnitude of slip are important in determining how the energy is dissipated in the contact and how this may accelerate surface damage such as fretting scars and wear, or crack initiation at the contact interface.

1.3.1 Historical background

Contact problems of the most various types have been investigated not only since the early development of machinery, but also since the construction of ancient monuments. The early studies of contact problems can be traced back to millennia [see Dowson, 1998]. In the 15^{th} century, Da Vinci had already attempted to measure the friction force and considered the influence of the surface area by measuring the force of blocks of different areas but same weight. He

found that the friction force is proportional to the weight of the block and independent of the surface area. These findings were formally formulated in the 17^{th} and 18^{th} century by Amontons [1699] and Coulomb [1785], based on their independent experiments. Despite the contribution of Da Vinci a few centuries earlier, the independence of the friction force on the area is often attributed to Amontons, while Coulomb gives his name to the famous friction force formula $Q = \mu P$, which states that the friction of sliding surfaces depends only on the normal force applied, P, and a coefficient, μ. This coefficient depends on the materials and surface finish of the contact pair and it is widely known as *the coefficient of friction*.

Despite the relevant work on contact mechanics centuries earlier, modern contact mechanics is widely regarded as having started with the work of Hertz [1881, 1885]. Hertz was attempting to understand how the optical properties of stacked lenses might change with the applied load when he derived the equation for the normal contact pressure between two elastic spheres. He considered both bodies as smooth half-spaces, i.e. semi-infinite spaces, with profiles described by second order polynomials. Hertz also assumed the contact to be frictionless and the material linear isotropic. However, work on the wheel on rail problem can be found prior to Hertz, particularly by Redtenbacher [1855], who tried to calculate dimension requirements for wheels, as described by Knothe [2008]. Redtenbacher used a reference undamaged wheel to calculate the relations of load, wheel radius and length of the contact. Nevertheless, it was the work of Hertz that really provided provided a breakthrough in the field of contact mechanics and it is still used today to study a wide range of problems.

Around the time Hertz derived the contact pressure equation for elastic spheres, major contributions to the field were also made by other authors. The French mathematician Boussinesq [1885] derived a solution for the stresses and displacements due to the application of a point load in a three-dimensional half-space using Green's functions. Boussinesq's solution was later modified by Flamant [1892] for a line load on a two-dimensional wedge loaded at its tip (if the internal wedge angle is π, the problem becomes that of a line load on a half-plane). Both these solutions are extremely powerful and, by the superposition principle, the integral of the point load solution (or line load if two-dimensional) allows for the derivation of the contact tractions for arbitrarily distributed loads on the surface of a half-plane, or punch problems with different

profiles.

In the beginning of the 20th century the solutions for several types of contact problems were developed. The first to solve the rolling contact problem, incorporating the shear tractions involved, is regarded as having been Carter [1922]. Carter was trying to prove the linear relationship between creep force and creep in rails and he idealised the problem by assuming both bodies were two-dimensional and regarded as half-planes. About twenty years later, two important work were undertaken on partial slip contacts. Cattaneo [1938] and Mindlin [1949] developed, independently, a solution for the problem of a Hertzian contact pressed by a normal force P and subsequently by an oscillating sinusoidal shear force $Q(t)$. Their solutions are the foundation for partial slip and fretting fatigue problems, and are still being used today to understand the contact tractions in fretting fatigue tests. One of the main books to summarize different aspects of the field of contact mechanics was written by Gladwell [1980]. A few years later, Johnson [1985], who was also the first to present a solution for a three-dimensional sliding problem [Johnson, 1958], wrote his book on contact mechanics providing a wide range of solutions to different contact problems.

The field of anisotropic contact mechanics had its main advances in the 1950s and 1960s, and among the early work found in the literature with solutions for anisotropic problems are those of Green and Zerna [1954] and Lekhnitskii [1963]. The latter summarized most of the Russian literature around that time, particularly the work of Galin [1953]. Sveklo [1964] and Willis [1967] extended the Boussinesq problem to anisotropic half-planes. Willis [1966] also presented work on the Hertzian contact problem in transversely isotropic bodies, using a Fourier transform method to reduce the Hertzian problem to one of evaluating contour integrals.

Some of the more recent developments in contact mechanics of anisotropic bodies, motivated mainly by the increase application of composite materials, are the work of Fan and Hwu. Fan and Keer [1994] solved the two-dimensional contact problem of a punch pressed onto an anisotropic elastic half-space, using the formalism for anisotropic elasticity of Stroh [1962]. Later, Fan and Hwu extended the original work to sliding punches [Hwu and Fan, 1998b] and the contact between two elastic anisotropic bodies [Hwu and Fan, 1998a], always using the Stroh formalism to incorporate the anisotropic elasticity into two-dimensional prob-

lems. A summary of two-dimensional contact problems of anisotropic bodies is presented in [Hwu, 2010]. Among some of the work carried out in the last decade is that of Swanson [2004], who have developed the full contact tractions on a three-dimensional Hertzian contact problem of orthotropic plates by combining the Willis' solution with that of Pagano [1970] to obtain detailed stress fields.

1.3.2 Types of contact problem

Contact problems may be characterised in different ways, and depending on the type of contact different techniques may be employed to solve the problem. The first classification of contact problems may be in terms of the change of the contact area. When the contact area increases with the applied load the contact is said to be *incomplete*. An example of incomplete contact is given in Figure 1.6a, where a cylindrical body is depicted and as the normal load is applied the contact area *advances*. When the contact area is defined only by the geometry of the bodies and independent of the applied load, the contact can be characterised as *complete*. Incomplete contact problems generally have a bounded normal contact pressure distribution at the edges; i.e. the contact pressure falls to zero as the point of observation moves toward the edge of the contact. One example of complete contact is the problem of a punch with atomically sharp corners in (Figure 1.6c). These two contact problems have completely different approaches to obtaining the normal pressure solution. For instance, the sharp punch problem may be solved by using a three-quarter plane problem as an asymptote to the contact problem [Hills et al., 2012]. Contrary to incomplete contacts, complete problems have a singular contact pressure near the edge of contact; i.e. if the contact is perfectly sharp the contact pressure goes to infinity at the edge of contact.

In practice, it is impossible to find an atomically sharp problem and most sharp punches will exhibit a small radius at the edge. The presence of radius at the edge will make the contact *locally* incomplete and the contact pressure bounded. Some contact problems may involve elements of both complete and incomplete contacts, as it is the case of *flat and rounded* punches; i.e. flat punches with rounded edges (Figure 1.6d). This class of contact problem may be regarded as incomplete since the area of the contact varies slightly near the rounded edges with

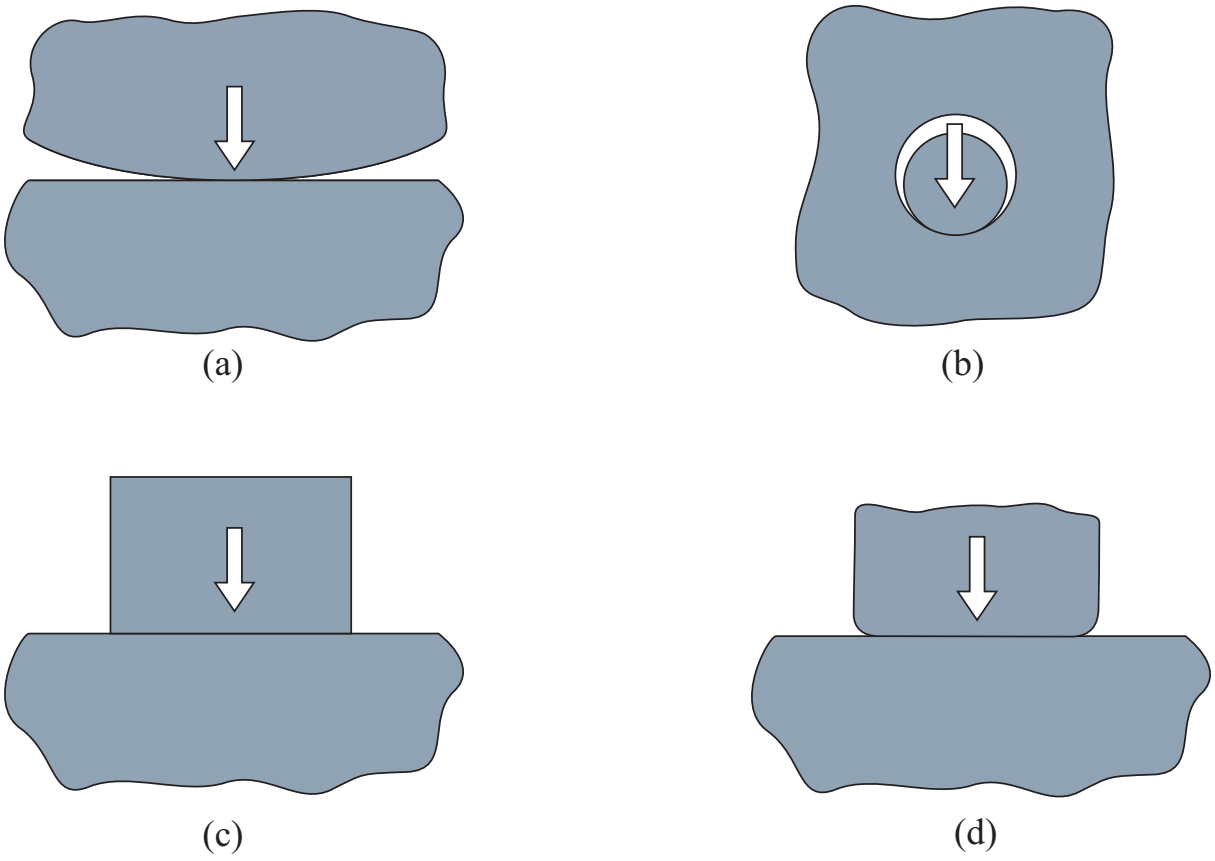

Figure 1.6: Types of contact: (a) Incomplete contact; (b) Conformal contact; (c) Complete contact; (d) Flat and rounded punch.

the normal load. However, since a large portion of the contact remains unchanged, a three-quarter plane asymptote to this problem may also be used, as in the sharp punch case. The use of three-quarter plane as an asymptote to the flat and rounded punch is shown in chapter 6.

A second class of characterisation of contact problems differentiates between *conformal* and *non-conformal* contacts. Non-conformal contact problems have a very small contact zone compared with the curvature of the body's surface, and if the area near the contact zone is magnified, the influence of the far boundaries can be neglected and the bodies can be idealised as half-spaces, or half-planes. This is an important classification of contact, since the possibility of idealising the bodies as semi-infinite is extremely useful when deriving analytical solutions. An example of non-conforming contact is the cylinder on a half-plane shown in Figure 1.6a. For most engineering materials the size of the contact area for a cylinder pressed on a plane will be very small compared to its curvature. The contact of a pin on a hole, on the other hand, may have a contact size of the same order of magnitude as the curvature of the bodies Fig-

ure 1.6b. This type of contact cannot be idealised as a half-plane, as the effect of the boundaries surrounding the contact zone cannot be neglected. This type of contact problem can be classified as *conformal* and is significantly more complex to solve. Conformal contact problems are outside the scope of this thesis.

Other types of contact exist. For instance, *receding* contacts show a reduction of the contact area as the applied normal load is increased. The separation of the contact introduces an extra complication to the contact problem. However, as the edges of the strip lifts off, it also reduces the remaining contact area to an incomplete contact, where the tractions fall to zero at the edges. The difference between a receding contact and a complete contact is not obvious, and it depends not only on the contact geometry but on the way the load is applied. Another challenging class of contact is the common-edged problem. Technique such as dislocation methods are currently being applied to this type of contact [Ramesh and Hills, 2015]. Despite the relevance of many of these different types of contact, the current investigation focuses mainly on incomplete contacts and, particularly, Hertzian contact problems and flat and rounded punch problems.

1.4 Fretting fatigue

Fretting is a small oscillatory displacement between two contacting solid bodies that may occur due to the vibration of the system or due to oscillating loads applied to one of the solids in contact. Many systems in mechanical engineering contain joints and assemblies of parts where fretting is likely to occur. Such systems (e.g. spline joints, riveted and bolted connections and dovetail joints between engine blades and discs) can be found in a wide range of industries. As a consequence of this relative movement between the surfaces of the bodies, surface damage and crack initiation are likely to occur. Furthermore, if fretting on the interface of the contact is combined with a cyclic mean stress on one of the bodies, the process of crack initiation and propagation may be accelerated, causing a significant reduction of the fatigue limit and, hence, the service life of the components in contact. This process is known as fretting fatigue and it can cause a life reduction of as much as ten times the standard fatigue life [Hills and Nowell, 1994]. Thus, the study and understanding of the processes involved in fretting fatigue and fretting wear problems are essential for the development of better models of life prediction for components

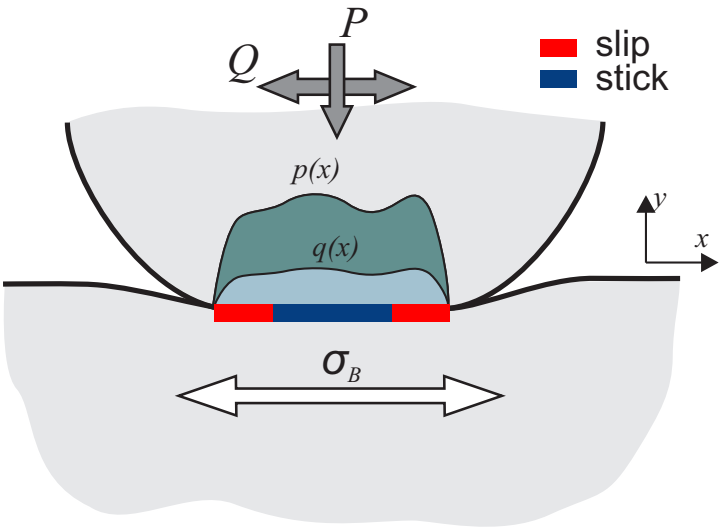

Figure 1.7: Schematic representation of partial slip contact and fretting fatigue.

under such conditions.

From the characteristics of relative displacement between bodies in contact, different types of surface damage may be expected. Vingsbo and Söderberg [1988] were the first highlight the importance of the different regimes of fretting. In a frictional contact between two bodies, there are three conditions of the tangential relative displacement between the bodies on the interface: adhesion, partial slip, and gross sliding. If the contact is adhered, there are no relative displacements between the bodies and surface damage is unlikely to occur. Under partial slip conditions, zones where tangential relative displacements occur, i.e. *slip* zones, may be found along the interface. If the interface is smooth and convex, e.g. Hertzian contact, the slip zones will occur at the edges with the presence of a central *stick* zone, where the contact is adhered (Figure 1.7). Small surface damage and wear occurs at the slip zones as a result of the relative displacements between the surfaces (see Figure 1.8). This is generally sufficient to accelerate crack initiation, and when combined with bulk cyclic tension may lead to fretting fatigue. If the applied tangential force on the body exceeds the sliding limit, then the problem becomes a gross sliding problem. Fouvry et al. [1996] have shown that under gross sliding the wear rate surpasses the crack propagation and, as a result, the fatigue life may increase. However, the surface wear may reach a point where failure may occur due to the reduced strength of the part. Fouvry et al. [1995] have defined a 'transition' regime, where the experiment starts in gross slip, but after a few cycles, and with the increase in coefficient of friction due to the surface wear, it

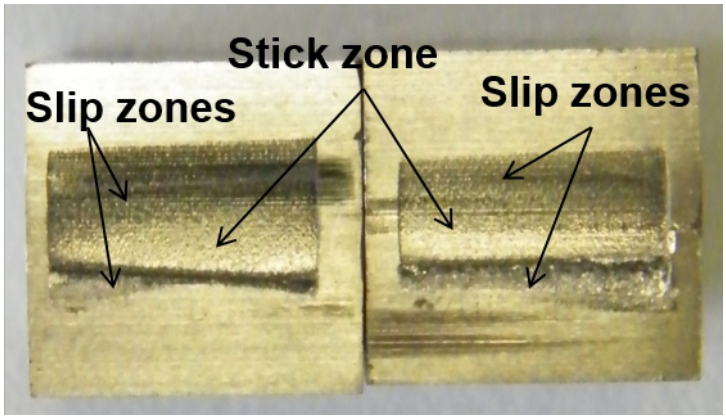

Figure 1.8: Example of fretting fatigue scar on the edges of the contact.

transitions to partial slip with the presence of a stick zone, as shown in Figure 1.9.

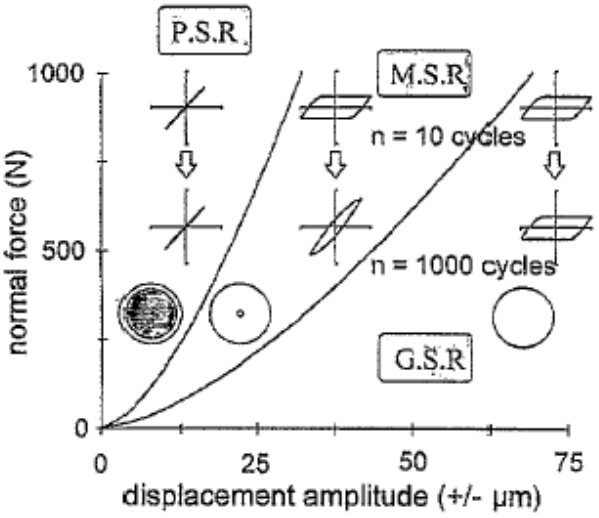

Figure 1.9: Map of the different fretting regimes: partial slip (P.S.R), mixed slip (M.S.R.) and gross sliding (G.S.R.) [Fouvry et al., 1996].

One of the most important early work in fretting fatigue is that of Waterhouse [1981], where mechanical and materials aspects of the subject are addressed. The Catanneo-Mindlin solution for partial slip Hertzian contact [Cattaneo, 1938; Mindlin, 1949] is perhaps the main analytical solution in the study of partial slip contact. An important analytical contribution to fretting fatigue problems was presented by Hills et al. [1988], where an extension to the Cattaneo-Mindlin problem for the existence of a bulk load in one of the bodies has been made. More recently, the work done by Ciavarella [1998] and Jäger [1997] have presented a more general formulation of the partial slip problem. The contribution made by them is used in chapter 7 in the partial slip investigation of contacts with elastic flat and rounded punches.

Fretting fatigue has been extensively studied for the past three decades and both analytical theories and experimental data are well established for simple geometries and isotropic materials. Much research has been carried out in fretting fatigue in the past two decades and a large amount of data is available for commonly used alloys, such as, titanium and aluminium alloys [Szolwinski and Farris, 1996; Lykins, 1999; Nowell, 1988; Araújo, 1998]. Fretting data for nickel based alloys are not as easily found and only recently has work with those alloys been carried out. Murthy et al. [2006] carried out fretting fatigue tests with the single-crystal IN100 nickel alloy. However, the fatigue specimens in their work were made of the single-crystal alloy itself with isotropic pads used to apply the contact tractions. Tests with single-crystal pads pressed onto an isotropic body are not easily found in the literature. The focus of this work is to investigate the impact of single-crystal pads on the fretting fatigue of isotropic bodies representing the discs of aero-engines.

Fretting is a strong stress concentrator and fatigue calculations based on the applied cyclic bulk load are not suitable for this kind of problem. Many techniques have been employed to take into account the high stresses near the contact concentration, many of them were originally developed for notch problems. Some of these techniques are based on the concept of a critical distance or volumes and an equivalence between these methods have been presented by Taylor [1999]. Fouvry et al. [2000] have shown that using the applied bulk fatigue load for correlating with fretting fatigue lives result in over-conservative predictions. They also suggested averaging the fatigue criterion, in this case Dang Van's fatigue criterion [Dang Van, 1972], over a 'critical' volume for better fatigue predictions. The critical volume approach has then been carried out by several authors in the past decade. Araújo and Nowell [2002] applied different fatigue criteria over a critical volume near the contact edge and found that the size of the critical volume is material dependent. Nowell and Dini [2003] explored different approaches for dealing with the high concentration in fretting fatigue problems. They also explored an analogy with notches to create equivalent stress gradients in fretting fatigue. One of these approaches is used in the analysis of the fretting fatigue results. In the finite element two-dimensional analysis carried out in chapter 4, a critical area method is used to obtain the averaged stress in the process zone for correlation with fretting fatigue life.

1.5 Summary

The work presented in this thesis focuses on issues of contact mechanics and fretting fatigue found in the blade to root assembly of aero-engines. Particularly, those at elevated temperature stages of turbines, where single-crystal nickel alloys are currently being used. This thesis is divided into two parts. The first part is aimed at investigating the impact of single-crystal bodies on the contact tractions and fretting fatigue. In the second part, a new semi-analytical approach for solving the partial slip contact problem of an elastic flat punch pressed onto an elastically similar half-plane is presented.

Different aspects of two-dimensional contact mechanics are presented in chapter 2. The formulation of plane strain contact problems for isotropic bodies is given, starting from the Flamant solution [Flamant, 1892] and integrating over the contact zone. The singular integral equations for the isotropic contact problem are obtained and the 'Hertzian' contact problem formulation is written down. Next, an anisotropic two-dimensional formulation is given using the Stroh formalism for anisotropic elasticity [Stroh, 1962]. The solution assumes that, in fact, the problem is in a state of *generalised* plane strain, where displacements may occur in the out-of-plane direction, but they depend only on the plane coordinates (e.g. $\mathbf{u}(x,y)$). The singular integral equations for the anisotropic case are presented and the closed form equation for the normal contact pressure are obtained. This solution is then used to solve a few example contact problems, where at least one of the bodies is anisotropic or orthotropic.

Different aspects of nickel single-crystal alloys are explored in chapter 3. The elastic properties of nickel crystal are discussed and, by using coordinate transformations, the elastic stiffness of single-crystal in different crystal directions are obtained. Nickel single-crystals have orthotropic elastic properties and the anisotropic contact solution of chapter 2 is used to investigate the effect of different crystal orientation on the contact tractions. Measurements of crystal orientation were also conducted on single-crystal pads used in the MACE tests to investigate the correlation between fretting fatigue lives and crystal orientation.

New fretting fatigue results are presented in chapter 4. These tests were conducted at high temperature and with a better control of the crystal orientation of single-crystal pads. Finite element analysis is used to obtain the stress for each test condition. The numerical results are

also used to investigate the impact of crystal orientation on the stresses near the contact edge. An area averaging approach for correlating the stresses near the edge of the contact with fretting fatigue lives is suggested. A comparison between using the applied bulk tension, the maximum stress at the surface of the contact, and the average stress on a 'process' zone near the edge of contact, and how each of them correlate with the fatigue life prediction of plain fatigue tests is also presented. Attempts to measure the coefficient of friction inside partial slip contact to compare the effect of crystal orientation on the coefficient of friction are described in chapter 5. This investigation aims to complement the analysis of fretting stresses of chapter 4 for a better correlation of the calculated fretting stresses and experimental fretting fatigue lives.

The flat punch with rounded edges problem is investigated in chapters 6 & 7. In chapter 6, formulations for the contact law, i.e. the variable size of the contact as a function of the applied load, and the peak contact pressure are presented. The solutions are derived from a dimensionless analysis of the independent variables of the problem and finite element analysis is used to calibrate the multiplier of the equations. The results are obtained by using a three-quarter plane asymptote to the contact problem, and loading the contact in terms of Williams' mode I and mode II notch intensity factors. Then, edge asymptotes for the normal and shear contact tractions are introduced in chapter 7. The contact law is then rewritten in terms of the edge asymptotes and the size of the slip zone is obtained from the Ciavarella-Jäger theorem for simple load trajectories. An example problem is used to compare the semi-analytical solution of the asymptotic approach with finite element solution of a finite punch problem.

Part I

Fretting fatigue and single-crystal alloys

Chapter 2

Contact mechanics

The formulation of the normal two-dimensional contact problem is presented in this chapter. The isotropic solution of plane contact problems is developed. The derivation starts from the Flamant solution for a line load on a half-plane and the displacements for an arbitrarily distributed load are obtained. The displacements of a distributed load on a half-plane are then used to obtain the contact singular integral equations in terms of the relative displacement gradients of the two bodies in contact. For some specific cases where the relative displacements of the bodies can be deduced *a priori*, the explicit equation of the contact normal pressure may be obtained. This is the case in Hertzian problems, where the contact surface relative displacements are parabolic. The formulation of the sliding contact between dissimilar isotropic bodies is also presented in this chapter as an introduction to coupled problems. From this solution, a parallel with the anisotropic contact problem can be drawn, where the normal and tangential contacts are also coupled.

A formulation of the anisotropic contact problem is also presented. First, a brief introduction to the Stroh formalism is given [Stroh, 1962]. Then, similarly to the isotropic case, the formulation starts from the Green's function for a line load on a half-plane and arrives at the singular integral equations for general anisotropic contact problems. The contact pressure solution for the case of two cylindrical bodies in contact is given explicitly by analogy with the dissimilar isotropic sliding cylinders solution. Some examples of the effect of anisotropy and the pressure distribution are given at the end of the chapter, where the effect of different aspects of anisotropy on the contact pressure is explored.

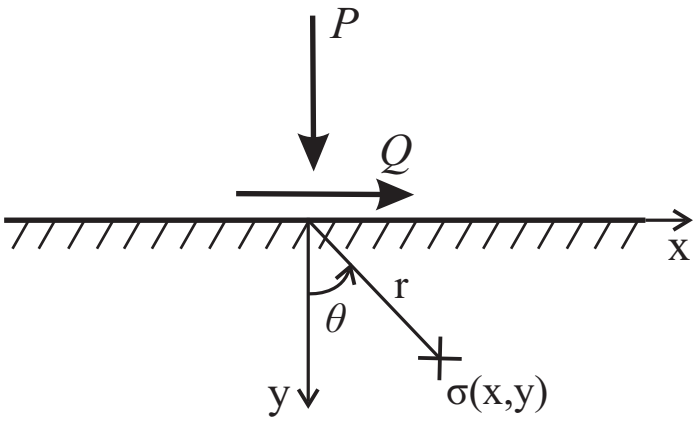

Figure 2.1: Concentrated normal and shear loads applied on a half-plane.

2.1 Plane contact of isotropic bodies

Provided that the deformation due to the contact of the bodies is small enough for the linear strain theory of elasticity to be applicable, and that the dimension of the area of the contact is small if compared to the radii of curvature of the bodies, the stresses can be calculated by considering the bodies as semi-infinite elastic solids bounded by a plane surface, i.e. as a half-plane. The half-plane approximation simplifies the boundary conditions of the problem by assuming zero stress and zero deformation as the body tends to infinity. A second assumption used here is that the length of the body in the out-of-plane direction is much greater if compared with the dimensions of the contact length. If this assumption is valid, the direct strain component in the out-of-plane direction is very small and can be neglected. Hence, plane strain equations are used henceforth in this chapter.

2.1.1 Line load on a half-plane - the Flamant solution

In order to find the surface traction distributions on the contact area the simpler problem of concentrated forces on the half-plane surface is presented (Figure 2.1). This problem was first solved by Flamant [1892] by modifying Boussinesq's three-dimensional solution for a point load on a half-plane [Boussinesq, 1885]. The problem of a concentrated shear force is analogous to the normal load problem. The Airy stress function for the problem of concentrated normal and shear forces is found in [Timoshenko and Goodier, 1963] and written in polar coordinates as

$$\phi(r,\theta) = -\frac{r\theta}{\pi}\left(P\sin\theta + Q\cos\theta\right), \tag{2.1}$$

where r is the radial distance to the point where the load is applied and θ is the angle measured from the y coordinate, which is normal to the half-space surface and positive inwards into the half-plane (Figure 2.1). By substituting the stress function into the biharmonic equation the stress components can be written as

$$\sigma_{rr} = -\frac{2}{\pi r}(P\cos\theta + Q\sin\theta), \tag{2.2a}$$

$$\sigma_{\theta\theta} = \tau_{\theta\theta} = 0. \tag{2.2b}$$

The solution above implies that a compressive normal line load applied on a half-plane causes only a radial compression. Also, it can be noted that $\sigma_{rr} \to -\infty$ as $r \to 0$ since the forces are finite and applied over an infinitesimally small area. However, in a real problem the high stress concentration at the point of loading would most likely cause plastic deformation of the body, but outside the small zone of plastic deformation the stresses will be close to the values given in (2.2). The stresses may be written in rectangular coordinates as [see Johnson, 1985]

$$\sigma_{xx} = \sigma_{rr}\sin^2\theta = -\frac{2}{\pi}(Py+Qx)\frac{x^2}{(x^2+y^2)^2}, \tag{2.3a}$$

$$\sigma_{yy} = \sigma_{rr}\cos^2\theta = -\frac{2}{\pi}(Py+Qx)\frac{y^2}{(x^2+y^2)^2}, \tag{2.3b}$$

$$\tau_{xy} = \sigma_{rr}\sin\theta\cos\theta = -\frac{2}{\pi}(Py+Qx)\frac{xy}{(x^2+y^2)^2}. \tag{2.3c}$$

By substituting equations (2.3) into Hooke's law, the strains at the surface can be obtained. The integration of the strain components gives expressions for the normal, $u(x)$, and tangential, $u_y(x)$, displacements at the surface. The displacements at the surface of the half-plane may be written as [see Hills and Nowell, 1994]

$$u_x(x) = P\left(\frac{\kappa-1}{8G}\right)\mathrm{sign}(x) - Q\left(\frac{\kappa+1}{4\pi G}\right)\ln|x| + \frac{C_1}{2G}, \tag{2.4a}$$

$$u_y(x) = -P\left(\frac{\kappa+1}{4\pi G}\right)\ln|x| - Q\left(\frac{\kappa-1}{8G}\right)\mathrm{sign}(x) + \frac{C_2}{2G}, \tag{2.4b}$$

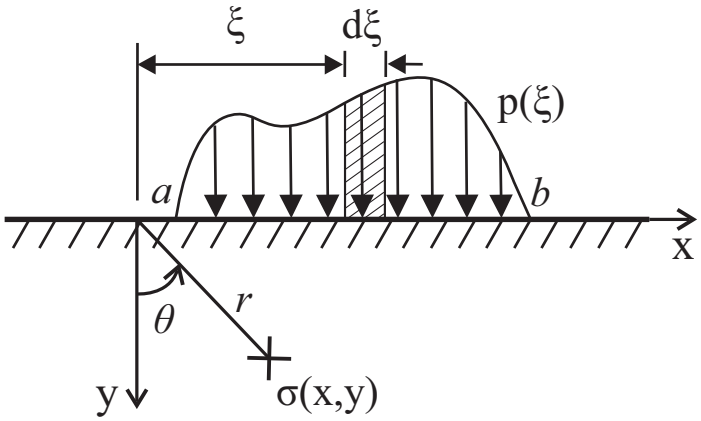

Figure 2.2: Arbitrarily distributed load on a half-plane.

where κ is the Kolosov's constant, defined as $\kappa = 3 - 4\nu$ for plane strain, and G is the shear modulus of elasticity. In equations (2.4), C_1 and C_2 are arbitrary constants which may be found by specifying the displacements relative to some remote datum. These constants are often an inconvenience when solving contact problems and a way to avoid dealing with them is to work in terms of the gradient of displacements along the surface of the half-space.

2.1.2 Contact between two-dimensional bodies of arbitrary shape

Now, instead of concentrated forces, it is considered that the load is applied over the area[1] $b < x < a$ along the half-plane surface with an arbitrary distribution in the form of normal pressure, $p(x)$, as illustrated in Figure 2.2. Similarly, a shear traction, $q(x)$, of arbitrary distribution over the same area may also be considered. In this case, the stresses due to distributed normal and tangential loads on a small element $d\xi$ at a location ξ along the surface can be written as

$$\sigma_{xx} = -\frac{2}{\pi}\left(\int_a^b \frac{p(\xi)(x-\xi)^2 d\xi}{[(x-\xi)^2+y^2]^2} y + \int_a^b \frac{q(\xi)(x-\xi)^3 d\xi}{[(x-\xi)^2+y^2]^2}\right), \tag{2.5a}$$

$$\sigma_{yy} = -\frac{2}{\pi}\left(\int_a^b \frac{p(\xi) d\xi}{[(x-\xi)^2+y^2]^2} y^3 + \int_a^b \frac{q(\xi)(x-\xi) d\xi}{[(x-\xi)^2+y^2]^2} y^2\right), \tag{2.5b}$$

$$\tau_{xy} = -\frac{2}{\pi}\left(\int_a^b \frac{p(\xi)(x-\xi) d\xi}{[(x-\xi)^2+y^2]^2} y^2 + \int_a^b \frac{q(\xi)(x-\xi)^2 d\xi}{[(x-\xi)^2+y^2]^2} y\right). \tag{2.5c}$$

[1] In a two-dimensional plane problem the unit of length regarding the out-of-plane depth is implied and a strip along the surface, e.g. $a < x < b$, has units of area. Similarly, the load applied has units of force per unit of out-of-plane length.

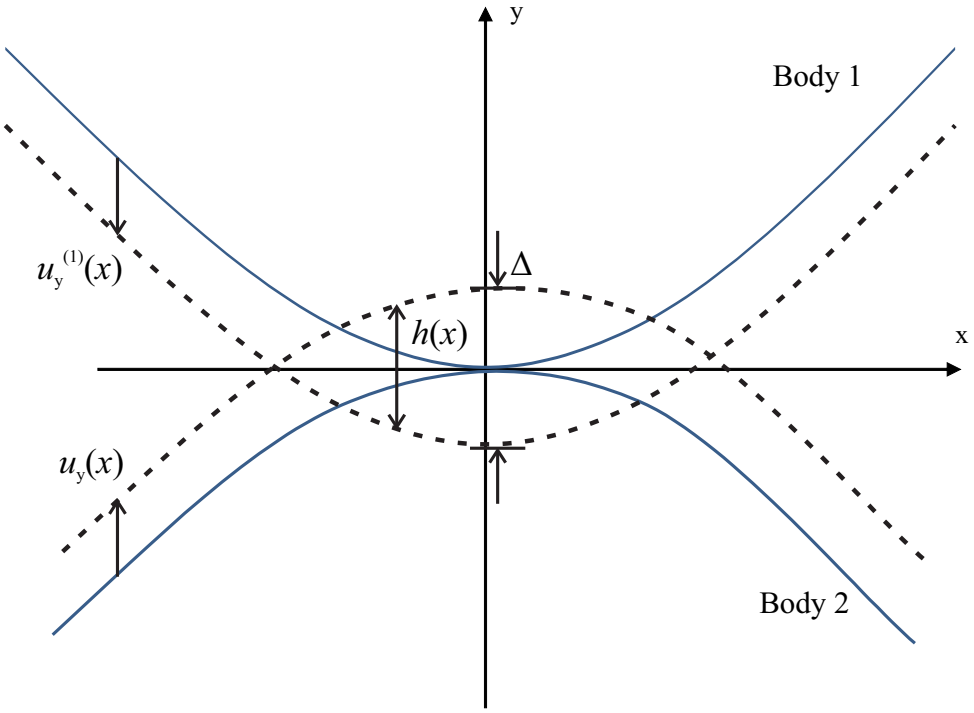

Figure 2.3: Contact surfaces of two anisotropic bodies.

Note that the convention that $\sigma_{yy}(x,0) \equiv -p(x)$ is used here and the contact pressure will always be positive on the loaded surface, while the direct stress normal to the surface is compressive.

As mentioned above, it is convenient is to solve the contact problem using the displacement gradients. If two bodies are in contact with each other, each will have the following gradient due to the presence of distributed normal and shear loads $p(x)$ and $q(x)$,

$$\frac{\partial u_x^{(i)}}{\partial x} = \frac{\kappa_i - 1}{4G_i} p(x) - \frac{\kappa_i + 1}{4\pi G_i} \int_a^b \frac{q(\xi)d\xi}{x-\xi}, \tag{2.6a}$$

$$\frac{\partial u_y^{(i)}}{\partial x} = -\frac{\kappa_i - 1}{4G_i} q(x) - \frac{\kappa_i + 1}{4\pi G_i} \int_a^b \frac{p(\xi)d\xi}{x-\xi}, \tag{2.6b}$$

where the subscript $i = 1,2$ refer to bodies 1 and 2 in contact. It is also useful to introduce a normal and tangential relative displacement of the surfaces in contact. The amount of overlap that would occur if the bodies could interpenetrate each other is given by $h(x) = \Delta - (u_y^{(1)}(x) - u_y^{(2)}(x))$ (Figure 2.3). Furthermore, the relative displacement in the tangential direction is given by $g(x)$, where $g(x) = u_x^{(1)}(x) - u_x^{(2)}(x)$. By using equations (2.6a) and (2.6b) the contact surface relative displacements are given by

$$\frac{1}{A}\frac{\partial h(x)}{\partial x} = \frac{1}{\pi}\int_a^b \frac{p(\xi)d\xi}{x-\xi} - \beta q(x), \tag{2.7a}$$

$$\frac{1}{A}\frac{\partial g(x)}{\partial x} = \frac{1}{\pi}\int_a^b \frac{q(\xi)d\xi}{x-\xi} - \beta p(x). \tag{2.7b}$$

The equations (2.7) show that the contact problem is, in its general form, a coupled problem. What this means is that when a normal load is applied, both a normal and a tangential relative displacement of the bodies is expected, and vice versa. The constants A and β in equations (2.7) depend on the elastic properties of the materials in contact and represent the effective compliance of the bodies and the influence of their elastic mismatch, respectively. They are defined as

$$A = \frac{\kappa_1 + 1}{4G_1} + \frac{\kappa_2 + 1}{4G_2}, \tag{2.8}$$

$$\beta = \frac{G_2(\kappa_1 - 1) - G_1(\kappa_2 - 1)}{G_2(\kappa_1 + 1) + G_2(\kappa_2 + 1)}. \tag{2.9}$$

Note that if the two bodies are elastically similar, Dundur's constant β is zero and equations (2.7) uncouple; i.e. the normal load causes only relative normal displacements and tangential loads tangential relative displacements. This is because the normal contact pressure results in identical tangential displacements in both bodies and no shear tractions arise under purely normal loading.

Equations (2.7a) and (2.7b) can be used to solve a wide range of contact problems. The solutions, or inversions, of those equations will be shown next for some specific contact problems. For the case of a frictionless contact or elastically similar bodies in contact, the problem is uncoupled and the solution of equation (2.7a) is given by [see Hills et al., 1993]

$$p(x) = -\frac{w(x)}{A\pi}\int_a^b \frac{h'(\xi)d\xi}{w(\xi)(\xi - x)} + Cw(x). \tag{2.10}$$

All problems studied in this work are incomplete and the pressure is bounded, falling to zero at the edge of contact. If the contact is smooth with bounded pressure distribution, $w(x) = \sqrt{a^2 - x^2}$ and $C = 0$ in equation (2.10). For other types of contact, such as, when the edge of one of the bodies is sharp and the pressure singular, the function $w(x)$ and constant C in (2.10) will assume different values, which may be found in [Hills et al., 1993].

2.1.3 Hertzian contact of cylindrical bodies

The most famous contact problem is probably that proposed by Hertz of two spheres pressed against each other [Hertz, 1881]. In two-dimensions Hertz's problem can be thought of as two infinitely long cylinders pressed onto each other [see Johnson, 1985]. Note that the problem of a cylinder pressed onto a half-plane can be solved by considering the radius of one of the cylinders to be infinite. The problem also assumes that the cylinders (or spheres if three-dimensional) are elastically similar. This is important to uncouple the equations of contact displacements in (2.7) by making Dundur's constant of elastic mismatch $\beta = 0$. The reason the Hertz problem is so widely used is that, when the contact area is small if compared with the radii of curvature of the cylinders, both bodies may be regarded as half-planes and also that the profile of the curved surface may be approximately described by second order polynomials. Both these assumptions allow for a closed form solution of the contact which is described next.

Consider the problem illustrated in Figure 2.3, where two bodies with cylindrical surfaces of radii R_i, with the index $i = 1,2$ representing bodies 1 and 2, respectively, come into contact. Each of the surfaces is described by a function $h_i(x)$. If the contact is small when compared with the size of the region in contact (i.e. $[a,b] \ll R_i$) the surfaces of the cylindrical bodies may be approximated by parabolic functions and written as $h_1(x) = x^2/2R_1$ and $h_2(x) = -x^2/2R_2$. The amount of overlap between the two undeformed surfaces that would otherwise occur if the condition of non-penetration was not satisfied can be written as

$$h(x) = \Delta - (h_1(x) - h_2(x)) = \Delta - \frac{1}{2}kx^2 \,, \tag{2.11}$$

where

$$k = \frac{1}{R_1} + \frac{1}{R_2} \,. \tag{2.12}$$

The slope of the relative normal displacement in (2.11) is $\partial h(x)/\partial x = -kx$. Equation (2.7a) may be rewritten by substituting (2.11). Note that the shear traction term will disappear for elastically similar materials ($\beta = 0$). Furthermore, if the equation is uncoupled, the area of the contact is symmetric and the contact area is $-a \leq x \leq a$, where a is the contact semi-width of

the contact. Then, equation (2.11) may be rewritten as

$$\frac{1}{\pi}\int_{-a}^{a}\frac{p(\xi)d\xi}{x-\xi}=-\frac{kx}{A}, \tag{2.13}$$

which is a Cauchy singular integral of the first kind whose solution may be found in [Hills et al., 1993]. The solution of the singular integral equation was given in (2.10), with $w(x)=\sqrt{a^2-x^2}$ and $C=0$, and the following equation for $p(x)$ is obtained,

$$p(x) = \frac{k\sqrt{a^2-x^2}}{A\pi}\int_{-a}^{a}\frac{\xi d\xi}{\sqrt{a^2-\xi^2}(\xi-x)} \tag{2.14a}$$

$$= \frac{k}{A}\sqrt{a^2-x^2}\,. \tag{2.14b}$$

It is observed that the pressure distribution in (2.14b) is elliptical. However, the solution of the equation in this form is not complete, since the semi-width of the contact is still unknown. The size of the contact may be obtained by invoking equilibrium and taking that the total normal force applied on the system needs to equal the pressure distribution on the contact, such that,

$$P=\int_{-a}^{a}p(\xi)d\xi=\frac{k\pi a^2}{2A} \tag{2.15}$$

with $-a\leq x\leq a$ being the contact area when the pressure distribution is symmetric. From equation (2.15), the contact size is defined as

$$a^2=\frac{2AP}{\pi k}\,, \tag{2.16}$$

where P is positive when causing compression in the convention used here. The contact pressure distribution in (2.14b) can be rewritten in terms of the independent variables of the problem as

$$p(x)=\frac{2P}{\pi a}\sqrt{1-\left(\frac{x}{a}\right)^2}=p_0\sqrt{1-\left(\frac{x}{a}\right)^2},\quad \text{with}\quad p_0=\frac{2P}{\pi a}\,. \tag{2.17}$$

The maximum contact peak pressure, p_0, is obtained fully in terms of the applied normal load, P, and the contact length, a. For isotropic elastically similar cylinders in contact the maximum pressure occurs at the centre of the contact. This is not necessarily true for elastically

dissimilar or anisotropic cylinders in contact, where there might be an offset of the peak contact pressure to the centre of contact. Equation (2.17) will be used in the example section §2.3 and throughout this work when the solution of two isotropic cylinders in contact is used for comparison purposes.

2.1.4 Sliding of two elastically dissimilar cylinders

In §2.1.3, either contacting cylinders considered as isotropic and elastically similar, or the surface is perfectly lubricated (i.e. frictionless interface). These assumptions result in a simplification of the contact equations by making $\beta = 0$ in equations (2.7a) and (2.7b) and, hence, the normal and tangential problems uncouple. If the bodies are not elastic similar, and nor is the interface frictionless, the problem remains coupled and both equations (2.7a) and (2.7b) need to be solved simultaneously. Solutions for the coupled problem of sliding isotropic elastically dissimilar cylinders can be found in [Johnson, 1985] and [Hills et al., 1993]. This problem can be used as an introduction to the anisotropic contact problem. In both cases the contact equations are coupled and a parallel can be drawn between the offset and distortion of the contact pressure caused by the elastic mismatch and anisotropy.

If the contact interface is frictional and the bodies are elastically similar, the problem is uncoupled. In this case, a shear traction will also act on the interface if there is a driving tangential force causing sliding between the two bodies. Furthermore, if Coulomb's law of friction is assumed to be governing the tangential contact problem, the limiting shear traction may be written as

$$q(x) = -\mu\, p(x)\text{sign}(\dot{x}) \tag{2.18}$$

when sliding occurs. Note that the shear traction opposes the direction of the sliding. The shear traction between elastically similar bodies will have the same elliptical distribution of the contact pressure, but scaled by the coefficient of friction μ. Hence the traction will also be symmetric and the centre of the maximum peak shear traction will also occur at the centre of the contact, if the bodies are cylindrical (Hertzian).

However, when there is an elastic mismatch between the bodies, the pressure distribution is no longer expected to be symmetric. An offset term must be added to the equation in (2.11) to

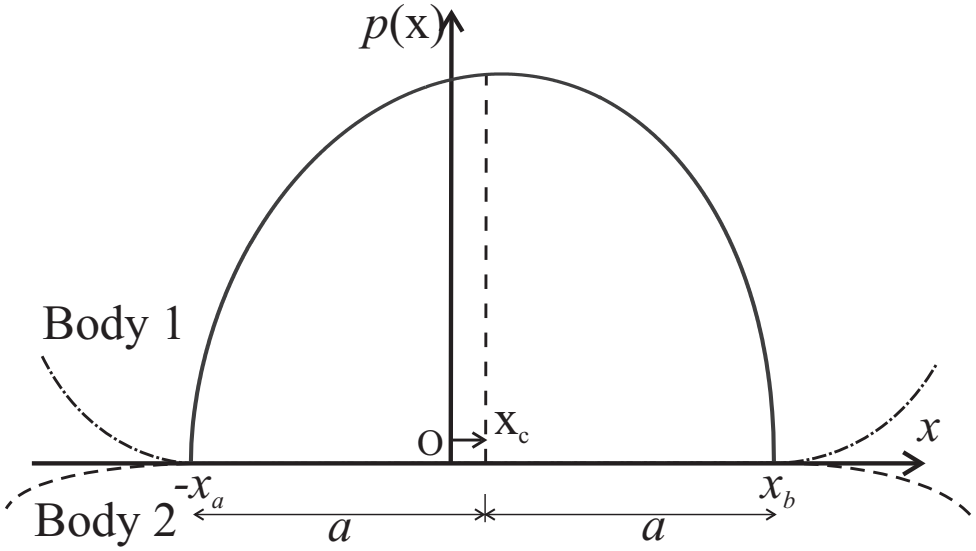

Figure 2.4: Non-symmetric pressure distribution due to the contact of two anisotropic cylinders loaded by a normal and shear loads.

account for the fact that the centre of the contact is no longer at the lowest point of the parabola. Equation (2.7a) is rewritten as

$$\frac{1}{\pi}\int_{-a}^{a}\frac{p(\xi)d\xi}{x-\xi}+\beta\mu p(x)=\frac{-k(x-x_c)}{A}\ , \tag{2.19}$$

where x_c is the offset of the centre of the pressure distribution normalized by the contact width. An illustration of the contact pressure of elastically dissimilar bodies is shown in Figure 2.4. Equation (2.19) is a Cauchy singular integral equation of the second kind and has an analytical solution [Hills et al., 1993]. Using appropriate normalization, the inversion of equation (2.19) results in the following expression for the contact pressure,

$$p(x)=p_0\left(1-\frac{x}{a}\right)^{m}\left(1+\frac{x}{a}\right)^{1-m}\ , \tag{2.20}$$

where

$$m=\frac{1}{\pi}\tan^{-1}\frac{1}{\beta\mu}\qquad 0<m<1\ . \tag{2.21}$$

Using the consistency condition, the tangential offset of the contact zone is found as $x_c=2m-1$ [Hills et al., 1993]. For elastically similar materials, where $\beta=0$, m becomes 1/2 and the offset is zero. The contact semi-width, a, and the peak pressure, p_0, for sliding problem of two

dissimilar elastic bodies are written as

$$p_0 = \frac{P \sin m\pi}{2\pi am(1-m)}, \tag{2.22}$$

$$a^2 = \frac{PA}{2\pi m(1-m)k}. \tag{2.23}$$

For most engineering problems, the constant of elastic mismatch, β, will not exceed 0.4 [Nowell et al., 1988]. In fact, one struggles to get even this, although the absolute limit of β is 0.5. For a typical high coefficient of friction of about 0.6, the value of m will be in the range 0.46 to 0.54 [Hills et al., 1993]. Hence, the distortion and offset of the contact pressure will often be very small when compared with the isotropic solution. Furthermore, the shear traction is normally smaller than the contact pressure. This often allows for satisfactory results using the Goodman approximation [Goodman, 1962], where the influence of the tangential traction on the contact pressure is neglected, but the effect of the normal pressure on the tangential traction is considered. In the next section, the influence of anisotropy on the contact pressure will be presented. The distortion and offset of the pressure distribution for anisotropic elastic cylinders will be presented and compared with the solution obtained for elastic dissimilar isotropic cylinders.

2.2 Plane contact of anisotropic bodies

In order to solve the two-dimensional plane contact problem of anisotropic bodies, the standard equations of elasticity must be first modified to incorporate anisotropy. Two main formalisms have been developed to study two-dimensional anisotropic elasticity; the Lekhnitskii formalism [Lekhnitskii, 1963] and the Stroh formalism [Stroh, 1962]. The first is a generalisation of the Muskhelishvili approach for solving two-dimensional deformations of isotropic elastic solids. Lekhnitskii's formalism assumes that the stresses depend on two coordinates only, i.e. $\sigma_{ij}(x,y)$, while Stroh's formalism assumes that the displacements depend only on those two coordinates, $u_i(x,y)$. The Stroh formalism has been well known in the material science community for many years, but only in the past two decades has it been increasingly widespread in engineering [Ting, 2000]. The Stroh formalism is mathematically elegant and technically powerful in solving two-

dimensional anisotropic elasticity problems and a complete description of the formalism can be found in [Ting, 1996; Bower, 2012].

In this section, an analytical solution of the contact problem between two anisotropic elastic bodies is discussed. The analytical solution presented here was first formulated by Hwu and Fan [1998b]. However, in their original work the contact problem was solved by using the 'Method of Analytical Continuation' to manipulate the complex variables from the Stroh formalism and, here, it is formulated by solving the contact singular integral equations. The solution can be applied to two-dimensional *generalised plane strain* problems and it uses the Stroh formalism to incorporate the elastic anisotropy of the bodies into the two-dimensional contact problem. A brief explanation of the Stroh formalism is presented first and the anisotropic contact problem is formulated subsequently. Next, the contact pressure distribution is obtained for the case of cylindrical bodies coming into contact, where, as in the Hertz case, the surfaces profiles can be approximated by parabolas. Some example problems of contact between anisotropic bodies solved by using the methodology presented are shown in §2.3, where the influence of anisotropy on the contact pressure is explored.

2.2.1 The Stroh formalism

In a two-dimensional plane strain problem, the displacement and strains in the out-of-plane direction are zero. For anisotropic bodies, strict plane strain deformation only occurs if the components of the elasticity tensor coupling in-plane direct stresses and out-of-plane shear strains, and *vice versa*, are zero [see Bower, 2012]. For orthotropic materials with cubic symmetry, which are presented in chapter 3, some orientations of the crystal satisfy this condition. The Stroh formalism assumes that the solid is in a state of *generalised plane strain*, i.e. the deformation in the out-of-plane direction is not necessarily zero, but that they do not vary with the out-of-plane length of the body. For example, if z is the out-of-plane coordinate, the deformation of the solid is a function of the coordinates x and y only, $u_i(x,y)$, with $i = x,y,z$. Note that the out-of-plane direct strain component is still zero, $\varepsilon_{zz} = 0$, since the displacement $u_z(x,y)$ does not vary in z. However, in contrast to the strict plane strain case, the shear strains in the out-of-plane direction, ε_{xz} and ε_{yz}, may be non-zero.

In a fixed rectangular three-dimensional coordinate system with coordinates x, y, z, the displacements are given by u_i, with $i = x, y, z$. σ_{ij} and ε_{ij} are the stress and strain components, respectively. The problem is assumed to be quasi-static and body forces are neglected. The three fundamental sets of equations of an anisotropic elastic problem are: the strain-displacement equations, the stress-strain law and the equilibrium equations. This set of equations is given, respectively, by

$$\varepsilon_{ij} = \frac{1}{2}\left(u_{i,j} + u_{j,i}\right) \tag{2.24a}$$

$$\sigma_{ij} = C_{ijks}\varepsilon_{ks} \tag{2.24b}$$

$$C_{ijks}u_{k,sj} = 0 \tag{2.24c}$$

where Newton's notation is used and comma stands for differentiation. The constants C_{ijks} are the components of the fourth order elastic stiffness tensor, with $i, j, k, s = 1, 2, 3$ [2]. In a two-dimensional problem, the second order differential equations (2.24c) are written in terms of two independent variables only, x and y, and the solution depend on a composite variable that is a linear combination of these two coordinates. The coefficient of x in the composite variable can be chosen to be unity and the general solution of the vector $\mathbf{u} = [u_x, u_y, u_z]^T$ may be written as

$$\mathbf{u} = \mathbf{a}f(z), \qquad z = x + py \tag{2.25}$$

where f is an arbitrary function of z. Substituting the general solution (2.25) into (2.24c), the following eigenrelation is obtained [Ting, 1996],

$$\{\mathbf{Q} + p(\mathbf{R} + \mathbf{R}^{\mathbf{T}}) + p^2\mathbf{T}\}\mathbf{a} = \mathbf{0}, \tag{2.26}$$

where p and $\mathbf{a}$ are the eigenvalue and eigenvector, respectively, and $\mathbf{Q}$, $\mathbf{R}$ and $\mathbf{T}$ are 3×3 matrices defined fully from the elasticity tensor as

$$Q_{ik} = C_{i1k1}, \quad R_{ik} = C_{i1k2}, \quad T_{ik} = C_{i2k2}. \tag{2.27}$$

[2] For convenience, the index notation of the stress, strain and elastic tensors in equations (2.24a-2.24c) is given in terms of 1, 2 and 3, which should be understood to correspond to coordinates x, y and z, respectively.

The matrices **Q**, **R** and **T** can also be written explicitly as

$$\mathbf{Q} = \begin{bmatrix} C_{11} & C_{16} & C_{15} \\ C_{16} & C_{66} & C_{56} \\ C_{15} & C_{56} & C_{55} \end{bmatrix}, \quad \mathbf{R} = \begin{bmatrix} C_{16} & C_{12} & C_{14} \\ C_{66} & C_{26} & C_{46} \\ C_{56} & C_{25} & C_{45} \end{bmatrix}, \quad \mathbf{T} = \begin{bmatrix} C_{66} & C_{26} & C_{46} \\ C_{26} & C_{22} & C_{24} \\ C_{46} & C_{24} & C_{44} \end{bmatrix}. \tag{2.28}$$

Note that the components of the elastic tensor C_{ij} in (2.28) are the components of the contracted matrix representation of the elasticity tensor, and the column and row corresponding to the direction z are suppressed in the plane analysis. For a non-trivial solution of **a**, one must have

$$\left| \mathbf{Q} + p\left(\mathbf{R} + \mathbf{R}^{\mathbf{T}}\right) + p^2\mathbf{T} \right| = 0. \tag{2.29}$$

The solution of (2.29) and (2.26) gives six pairs of eigenvalues p_k and eigenvectors $\mathbf{a_k}$, with $k = 1, 2, ..., 6$. The displacements of the problem given in (2.25) are obtained by a superposition of these solutions,

$$\mathbf{u} = \sum_{\alpha=1}^{6} \mathbf{a}_\alpha f_\alpha(z_\alpha), \qquad z_\alpha = x + p_\alpha y \tag{2.30}$$

and the stresses σ_{ij} are obtained by the following expression,

$$\begin{aligned} \sigma_{i1} &= (Q_{ik} + pR_{ik})a_k f'(z), \\ \sigma_{i2} &= (R_{ki} + pT_{ik})a_k f'(z)., \end{aligned} \tag{2.31}$$

where $f'(z)$ is the derivative of $f(z)$ in (2.25) with respect to the conjugate z [Ting, 1996].

One important characteristic of the Stroh formalism is that the stresses in (2.31) may be written in terms of a new vector **b**, which is defined as

$$\mathbf{b} = (\mathbf{R}^T + p\mathbf{T})\mathbf{a} = -\frac{1}{p}(\mathbf{Q} + p\mathbf{R})\mathbf{a}, \tag{2.32}$$

and the stresses can now be written as

$$\sigma_{i1} = -pb_i f'(z), \qquad \sigma_{i2} = b_i f'(z). \tag{2.33}$$

Furthermore, the stresses may also be written in terms of the stress function ϕ. Since the coefficients of the sextic equation for p given in equation (2.26) are all real, the solutions of p are three pairs of complex conjugates. Hence, the general solution of the displacements and stress function of an anisotropic elastic problem are obtained by superposition of these solutions,

$$\begin{aligned} \mathbf{u} &= \sum_{\alpha=1}^{3} \left\{ \mathbf{a}_\alpha f_\alpha(z_\alpha) + \bar{\mathbf{a}}_\alpha f_{\alpha+3}(\bar{z}_\alpha) \right\}, \\ \phi &= \sum_{\alpha=1}^{3} \left\{ \mathbf{b}_\alpha f_\alpha(z_\alpha) + \bar{\mathbf{b}}_\alpha f_{\alpha+3}(\bar{z}_\alpha) \right\}, \end{aligned} \tag{2.34}$$

where the overbar denotes the complex conjugate and $p_{\alpha+3} = \bar{p}_\alpha$, $\mathbf{a}_{\alpha+3} = \bar{\mathbf{a}}_\alpha$ and $\mathbf{b}_{\alpha+3} = \bar{\mathbf{b}}_\alpha$, with $\alpha = 1,2,3$. It is also observed that for most problems the arbitrary functions f_α have the same form and hence the solutions of displacements and stress functions become real,

$$\mathbf{u} = 2\mathrm{Re}\left\{\mathbf{A}\mathbf{f}(z)\right\}, \qquad \phi = 2\mathrm{Re}\left\{\mathbf{B}\mathbf{f}(z)\right\} \tag{2.35}$$

with $\mathbf{A}, \mathbf{B}$ and $\mathbf{f}$ being the vectors containing the three solutions of $\mathbf{a}_\alpha$, $\mathbf{b}_\alpha$ and $f_\alpha(z)$ respectively. Ting [1996] presents a summary of the formalism and shows that for a given problem all one has to do is to determine the unknown function $f(z)$ and obtain the respective eigenvectors. This function should be determined through the satisfaction of the boundary conditions of each problem. Another important feature of the Stroh formalism is that the vectors $\mathbf{a}$ and $\mathbf{b}$ are related by equation (2.32).

Using the orthogonality and closure relations of the formalism, Barnett and Lothe [1973] introduced three real tensors written as

$$\mathbf{S} = i(2\mathbf{A}\mathbf{B}^T - \mathbf{I}), \quad \mathbf{H} = 2i\mathbf{A}\mathbf{A}^T, \quad \mathbf{L} = -2i\mathbf{B}\mathbf{B}^T. \tag{2.36}$$

These tensors are obtained from the relations between the eigenvectors $\mathbf{a}$ and $\mathbf{b}$ of the Stroh formalism given in appendix A.

The Barnett-Lothe tensors are very useful in the analytical solution for anisotropic contact adopted. The standard approach to obtain these tensors is to calculate the eigenvalue and eigenvectors from (2.26) and substitute into (2.36). Explicit expressions of the Barnett-Lothe tensors for orthotropic materials can be found in [Dongye and Ting, 1989] and [Hwu, 1993]. However,

this solution assumes that the eigenvalues, p, and eigenvectors, $\mathbf{a}$, are all distinct. Special types of materials, such as mathematically degenerate materials, do not have three independent eigenvectors and cannot be solved by this method. These include isotropic and transversally isotropic materials. Alternative solutions have been developed for some special types of degenerate materials and the expressions for some of those classes of materials can be found in [Ting, 1997; Liou and Sung, 2008; Nakamura and Tanuma, 1997].

Barnett and Lothe [1973] derived an alternative method that allows one to obtain the tensors $\mathbf{S}$, $\mathbf{H}$ and $\mathbf{L}$ directly from the components of the fourth order elastic stiffness tensor $\mathbf{C}$ and the *fundamental elasticity matrix* $\mathbf{N}$ (see appendix A). They showed that the three tensors may also be obtained by integrating the components of the fundamental elasticity matrix in a rotated coordinate system, using appropriate orthogonal transformations. The tensors are obtained by the following integral expression

$$\mathbf{S} = \frac{1}{\pi}\int_0^{\pi} \mathbf{N}_1(\theta)\, d\theta, \qquad \mathbf{H} = \frac{1}{\pi}\int_0^{\pi} \mathbf{N}_2(\theta)\, d\theta, \qquad \mathbf{L} = -\frac{1}{\pi}\int_0^{\pi} \mathbf{N}_3(\theta)\, d\theta \tag{2.37}$$

Equation (2.37) is sufficient to obtain the elasticity tensors $\mathbf{S}$, $\mathbf{H}$ and $\mathbf{L}$ directly from the components C_{ijks} of the elastic stiffness matrix. By using this approach, there is no need to obtain the eigenvalue and eigenvectors p, $\mathbf{a}$ and $\mathbf{b}$, and the problems associated with degenerate materials are circumvented. However, the integrals (2.37) can be extremely lengthy to obtain analytically and numerical integration is often necessary. A numerical approach to solve equation (2.37) is presented in appendix A.

2.2.2 General anisotropic contact formulation

The problem of two contacting bodies illustrated in Figure 2.3 is considered again, but now the bodies are elastically anisotropic. The displacements of body i ($i = 1,2$) in the x, y and z directions are given by $u_x^{(i)}$, $u_y^{(i)}$ and $u_z^{(i)}$. Note that the displacement in the z directions needs to be taken into account because the anisotropy can induce shear in the out-of-plane direction for certain pairs of materials. Furthermore, the relative tangential displacement in the x and z directions of any pair of surface points is given by $g_1(x)$ and $g_3(x)$, respectively, and the amount

of normal overlap is given by the function $h(x)$. The derivative of the contact displacements is written as

$$\frac{\partial \mathbf{h}(x)}{\partial x} = \frac{\partial \mathbf{u}^{(1)}}{\partial x} - \frac{\partial \mathbf{u}^{(2)}}{\partial x} \tag{2.38}$$

with $\mathbf{h}(x) = [g_1(x), h(x), g_3(x)]^T$ and $\mathbf{u} = [u_x, u_y, u_z]^T$.

Using the Stroh formalism, the surface Green's function for a line load on a half-space at the surface $y = 0$ is given by [see Ting, 1996]

$$\mathbf{u} = \frac{1}{\pi} \mathrm{Im}\left\{\mathbf{A}\mathbf{q}\ln(x)\right\} \tag{2.39}$$

with $\mathbf{q} = \mathbf{B}^{-1}\boldsymbol{\zeta}$. $\mathbf{A}$ and $\mathbf{B}$ are the tensors containing the Stroh formalism eigenvectors defined in §2.2.1 and $\boldsymbol{\zeta}$ is the line force vector. Let $\mathbf{t}(x) = [q_1(x), p(x), q_3(x)]^T$ be the tensor of the distributed loads on the surface, where $p(x)$ is the normal contact pressure distribution and $q_1(x)$ and $q_3(x)$ are the shear tractions in the x and z directions, respectively. For a distributed in plane load, the derivative of the displacements of body i can be written as [see Rajeev and Farris, 2002]

$$\frac{\partial \mathbf{u}^{(i)}}{\partial x} = \mathrm{Re}(\mathbf{A}\mathbf{B}^{-1})\mathbf{t}(x) + \mathrm{Im}(\mathbf{A}\mathbf{B}^{-1})\frac{1}{\pi}\int_{x_a}^{x_b} \frac{\mathbf{t}(\xi)}{x-\xi} d\xi \tag{2.40}$$

Combining equations (2.38) and (2.40) and with appropriate change of signs, the governing singular integral equations for two contacting anisotropic bodies are

$$\frac{\partial \mathbf{h}}{\partial x} = \mathrm{Re}(\mathbf{M}^*)\frac{1}{\pi}\int_{x_a}^{x_b} \frac{\mathbf{t}(\xi)}{x-\xi} d\xi + \mathrm{Im}(\mathbf{M}^*)\mathbf{t}(x) \tag{2.41}$$

with $\mathbf{M}^* = \mathbf{M}_1^{-1} + \bar{\mathbf{M}}_2^{-1}$ and $\mathbf{M}_k = -i\mathbf{B}_k\mathbf{A}_k^{-1}$. The impedance tensors $\mathbf{M}_k$ can also be written as

$$\mathbf{M}_k^{-1} = \mathbf{L}_k^{-1}(\mathbf{I} + i\mathbf{S}_k^T) = (\mathbf{I} - i\mathbf{S}_k)\mathbf{L}_k^{-1}, \quad k = 1, 2. \tag{2.42}$$

$\mathbf{S}_k$ and $\mathbf{L}_k$ are the Barnett-Lothe tensors defined in equations (2.36) and (2.37).

Equation (2.41) is the singular integral equation for a general contact problem of anisotropic bodies. The coupling in the anisotropic contact depends on the imaginary part of the bimaterial tensor $\mathbf{M}^*$. Note that the coupling due to the elastic dissimilarity of the bodies is also included

in $\mathbf{M}^*$, which takes into account the elasticity tensor of both bodies in contact. Other types of coupling, such as, geometrical coupling, are not included in the singular integral equation (2.41) and this formulation assumes that the normal and tangential contact are coupled solely due to the elastic dissimilarity and/or anisotropy of the bodies. The existence of an analytical solution of a particular problem will depend, again, on the knowledge of the gradient of relative deformation on the contact interface, and for cylindrical bodies in contact, the contact pressure distribution is shown next in §2.2.3.

2.2.3 Anisotropic contact of cylinders

Assuming that the bodies in contact are non-conforming cylinders and that their radii of curvature are large enough when compared to the contact area, as in §2.1.3, the half-plane assumption may be employed. Moreover, the profile $h(x)$ of the boundaries in contact may be approximated by a parabola and is also defined by equation (2.11). Coulomb's law of friction is assumed and if the contact slides in the x or z direction, the shear tractions are given by $q_1(x) = \mu_1 p(x)$ or $q_3(x) = \mu_3 p(x)$, respectively, where μ_1 and μ_3 are the coefficients of friction in the x and z directions. Note that the formulation allows for the coefficient of friction in the contact interface being different depending on the direction of slip. Equation (2.41) for the normal contact displacement may be rewritten as

$$\frac{\partial h(x)}{\partial x} = \mathrm{Re}(\gamma)\frac{1}{\pi}\int_{x_a}^{x_b}\frac{p(\xi)}{x-\xi}d\xi + \mathrm{Im}(\gamma)p(x)\ , \tag{2.43}$$

with

$$\gamma = m^*_{22} + \eta_1 m^*_{21} + \eta_3 m^*_{23}\ , \tag{2.44}$$

where η_1 and η_3 are the load ratios between the normal and tangential loads in the x and z directions, respectively, and m^*_{ij} $(i,j = 1,2,3)$ are the components of the bimaterial matrix $\mathbf{M}^*$. Note that if the bodies are sliding, the load ratio will be limited by the coefficient of friction in the direction of sliding if Coulomb law of friction is assumed. Reorganising (2.43) and using

equation (2.11), one obtains

$$\frac{1}{\pi}\int_{x_a}^{x_b}\frac{p(\xi)}{x-\xi}d\xi+\frac{\mathrm{Im}(\gamma)}{\mathrm{Re}(\gamma)}p(x)=-\frac{kx}{\mathrm{Re}(\gamma)}\ . \tag{2.45}$$

The singular integral equation (2.45) is very similar to the equation of two dissimilar sliding elastic bodies given in [Hills et al., 1993] and, by analogy, the solution for the pressure distribution is written as

$$p(x)=-\frac{\sin\pi m}{\mathrm{Re}(\gamma)}k(x-x_a)^{1-m}(x_b-x)^m,\quad x_a<x<x_b \tag{2.46}$$

where x_a and x_b are the limits of the contact region (Figure 2.4) and m is defined as

$$m=\frac{1}{\pi}\tan^{-1}\left(\frac{\mathrm{Re}(\gamma)}{\mathrm{Im}(\gamma)}\right),\quad 0\leq m<1. \tag{2.47}$$

The variables γ and m depend solely on the elastic stiffness of the bodies and the coefficient of friction at the interface. The expressions for the limits of the contact area x_a and x_b can be found in [Hwu and Fan, 1998a], where a similar solution was obtained by using the 'Method of Analytical Continuation'. The contact limits are given by

$$x_a^2 = \frac{m(\gamma+\bar{\gamma})P}{\pi(1-m)k}, \tag{2.48a}$$

$$x_b^2 = \frac{(1-m)(\gamma+\bar{\gamma})P}{\pi mk}, \tag{2.48b}$$

where $\bar{\gamma}$ is the complex conjugate of γ and P is the applied normal load. From these expressions, the contact semi-width a can be shown to be

$$a^2=\frac{P\mathrm{Re}(\gamma)}{2\pi km(1-m)} \tag{2.49}$$

with an offset of the centre of pressure given by $x_c=(2m-1)a$ (Figure 2.4).

These results show an equivalence between the anisotropic and the isotropic solutions for sliding contact of cylinders presented in §2.2.3. Thus, by comparing (2.49) with the isotropic

formulation, it can be deduced that $\mathrm{Re}(\gamma)$ gives the combined elastic compliance of the bodies in contact and m measures the degree of elastic mismatch and anisotropy. Note that coupling due to the elastic dissimilarity only occurs if the contact is frictional in the isotropic solution of dissimilar elastic cylinders. The same is true for anisotropic contacts, since the term m^*_{22} in (2.44) is always real and, hence, the problem is uncoupled, $m = 0.5$, if the problem is frictionless ($\mu_1 = \mu_2 = 0$). This is due to the fact that the impedance tensors are Hermitian (i.e. $\mathbf{M}_k = \overline{\mathbf{M}}_k^{\,T}$), as proven by Ting [1996]. Equations (2.46), (2.48a) and (2.48b), together, define the normal contact problem for anisotropic cylinders in contact. For sliding cylinders, the shear traction can also directly obtained by scaling the normal contact pressure distribution (2.46) using the coefficient of friction in the direction of slip.

2.3 Example problems of anisotropic contact

A few example problems of contact of anisotropic bodies are solved in this section. First, the anisotropic contact solution is used to solve the frictional contact of two anisotropic cylinders. This problem was solved by Hwu and Fan [1998a] and the size of the contact and parameters of the contact formulation are compared with their results. The influence of the coefficient of friction is investigated for the same problem of two anisotropic cylinders. The last example analysed is used to investigate the effect of the elastic modulus normal to the contact on the pressure distribution and maximum peak stress. A similar example problem was solved by Bagault et al. [2012a], but for the three-dimensional contact of a rigid sphere pressed onto an elastic half-plane. These problems are used to validate the formulation presented in this chapter by comparing the solution with results found in the literature.

2.3.1 Two anisotropic cylinders

The first example considered is that of two anisotropic cylinders pressed against each other presented in [Hwu and Fan, 1998a]. Hwu and Fan used an explicit solution of the Barnett-Lothe tensors $\mathbf{S}$ and $\mathbf{L}$ for orthotropic materials obtained in [Ting and Hwu, 1988]. A code was written in Matlab implementing the general anisotropic solution described in §2.2.3 and

the Barnett-Lothe integral formalism is used. A numerical integration of equations (2.37) was implemented, as described in appendix A.3, to obtain the impedance tensors of (2.42). Although technically this solution is no longer fully analytical, the numerical approach for obtaining the Barnett-Lothe tensors can be justified for being more general than the analytical solutions available. Contrary to the analytical solutions for the tensors found in [Dongye and Ting, 1989] and [Hwu, 1993], the numerical approach does not have a problem with degenerate materials and, therefore, it is valid for any material, including isotropic materials.

In the example problem used by Hwu and Fan [1998a] the two cylinders in contact have the following material properties:

$$E_1^{(1)} = 114.8\text{GPa}, \;\; E_2^{(1)} = 48.0\text{GPa}, \;\; G_{12}^{(1)} = 24.0\text{GPa}, \;\; \nu_{12}^{(1)} = 0.21,$$
$$E_1^{(2)} = 60.7\text{GPa}, \;\; E_2^{(2)} = 24.8\text{GPa}, \;\; G_{12}^{(2)} = 12.0\text{GPa}, \;\; \nu_{12}^{(2)} = 0.23.$$

The radius of the cylinders are $R_1 = 100$ m and $R_2 = 200$ m and the coefficient of friction in the contact interface is $\mu_1 = \mu_2 = 0.5$. The problem is two-dimensional and generalised plane strain assumption is used. A normal load $P = 1$ kN/m and a tangential load Q, where $Q/P = 0.4$, are applied in the directions y and x, respectively, and hence the load ratio in the x direction is $\eta_1 = 0.4$. It is also assumed that the load ratio is zero in the out-of-plane direction, $\eta_3 = 0$. For the materials used, the elasticity tensor terms that couple the direct and shear stresses and strains in the normal and out-of-plane directions are zero and, hence, the shear load ratio η_3 does not affect the contact pressure. However, this is not necessarily the case with many anisotropic and orthotropic materials. In their paper, Hwu and Fan assumed that a tangential force lower than the sliding limit is applied and that the shear traction has a profile of the distribution similar to the normal pressure but scaled by the ratio Q/P. However, this is only true if both normal and tangential loads are applied simultaneously, otherwise partial slip will occur in the interface and the shear traction distribution will *not* be equal to the contact pressure scaled by the ratio between the applied shear and normal loads. Note that the contact tractions in this problem, where the loads are applied simultaneously and $Q/P = 0.4$, are identical to those of two cylinders sliding where the coefficient of friction is $\mu_1 = 0.4$.

The parameters of the contact solution obtained here are the same as the ones listed by

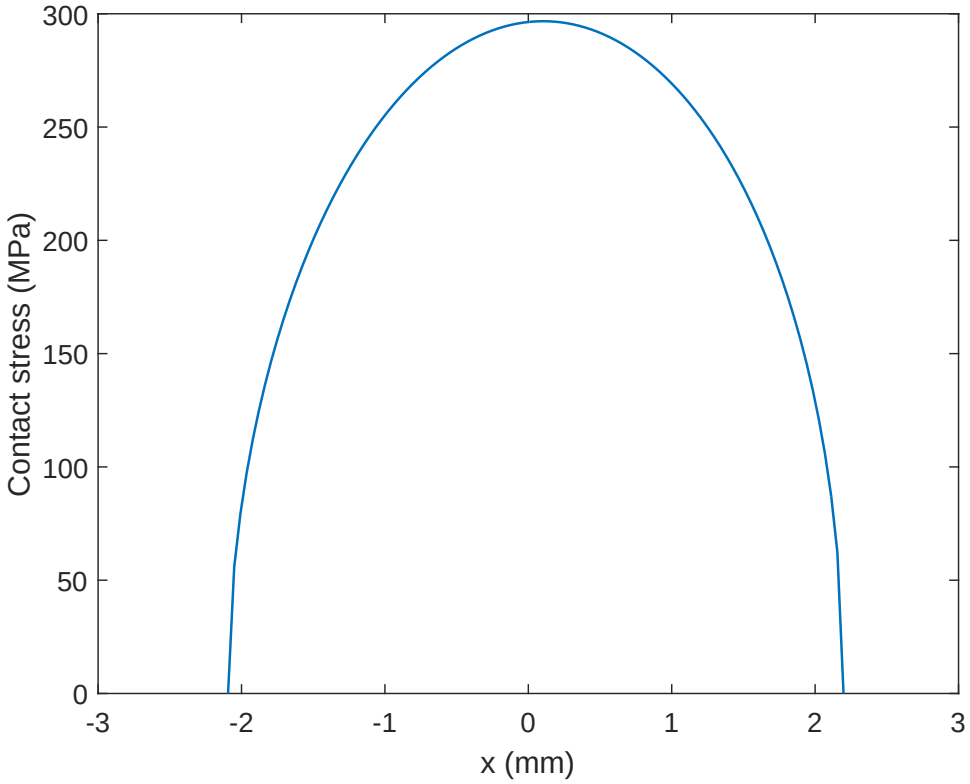

Figure 2.5: Contact pressure distribution of the example problem given in [Hwu and Fan, 1998a].

Hwu and Fan [1998a]. The coefficients γ and m given in equations (2.44) and (2.47) are $\gamma = (10.843 + 0.414i) \times 10^{-8}$ mm^2/N and $m = 0.4879$, respectively. The contact limits are given by $x_a = 2.094$ mm and $x_b = 2.198$ mm, where the semi-width $a = 2.146$ mm and the offset $x_c = 0.052$ mm. The normal contact pressure is presented in Figure 2.5. Although it is not very noticeable, the pressure distribution is not symmetric and there is a small offset of the centre of pressure. In fact, for most orthotropic engineering materials, e.g. carbon fibre composites and single-crystal parts, the asymmetry of the pressure distribution and offset will be relatively small. Nevertheless, the use of the anisotropic contact solution is still necessary, since the contact compliance of orthotropic materials will still be, for most cases, significantly different from that of isotropic bodies in contact.

2.3.2 The effect of the coefficient of friction on the contact pressure

The influence of the coefficient of friction on the contact pressure is now investigated for the same problem of two anisotropic cylinders presented previously. However, the cylinders are

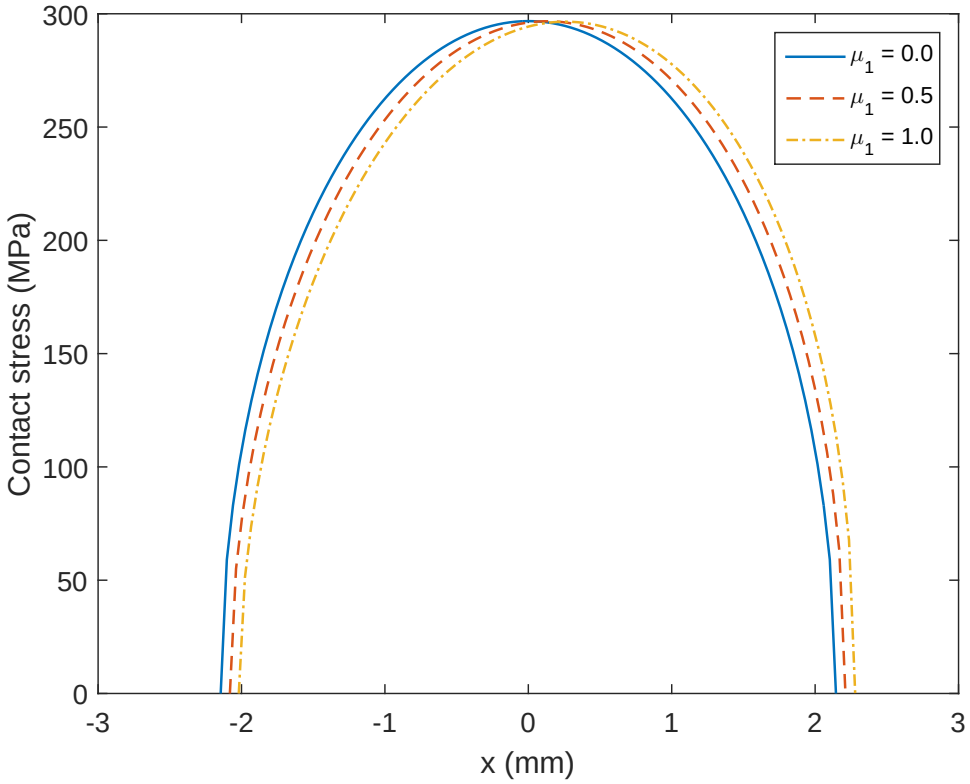

Figure 2.6: Contact pressure distribution for different values of friction coefficient.

considered to be sliding here. Different values of coefficient of friction μ_1 are assumed for the contact interface. By changing the value of the coefficient of friction, the offset of the contact centre of pressure, x_c, increases (Figure 2.6). The pressure profile also becomes more asymmetric the higher the coefficient of friction. This effect is more evident when the contact tractions are plotted as a function of the normalised contact size (Figure 2.7). For the material properties used in this example problem, the effect of the out-of-plane load ratio does not change the contact pressure. This is because there is no coupling between stresses and strains in the normal and out-of-plane directions for the materials of §2.3.1. This is not necessarily true for all cases, and for a fully anisotropic material the load ratio in the out-of-plane directions needs to be taken into account. However, fully anisotropic materials are not commonly found in engineering components and this work will focus mainly on orthotropic materials, where for some orientations the out-of-plane tractions will not change the contact traction; those are the orientations of symmetry which are discussed in chapter 3.

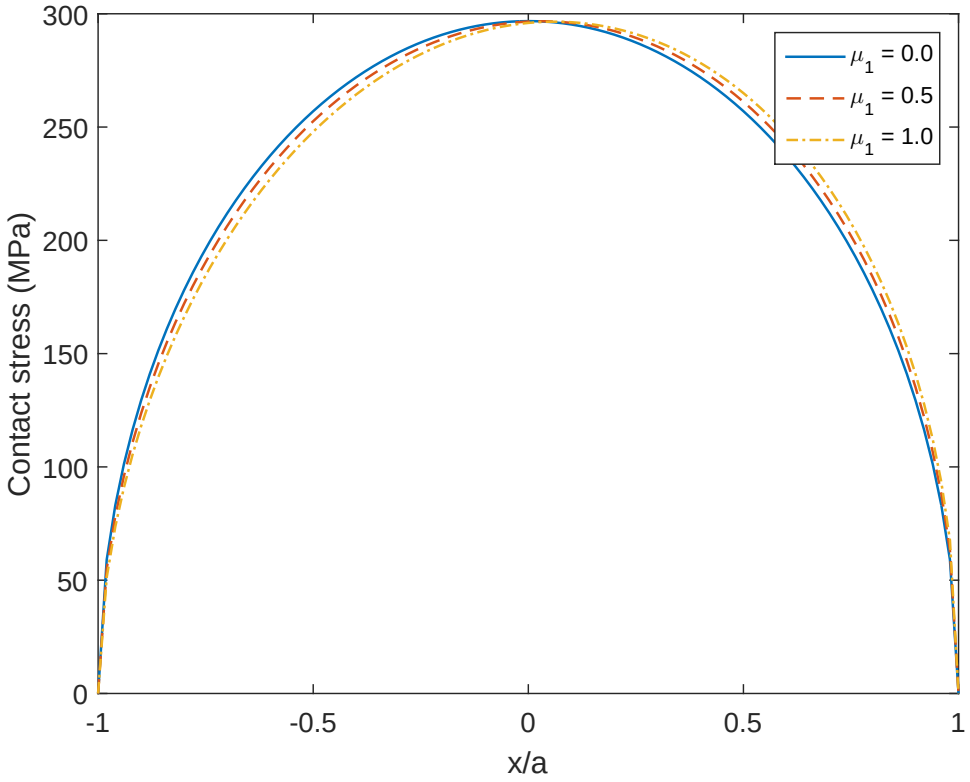

Figure 2.7: Normalised contact pressure distribution with respect to the contact width for different values of friction coefficient.

2.3.3 Effect of the normal elastic stiffness on the contact pressure

A recent work on anisotropic contact problem was presented by Bagault et al. [2012a], who explored the effect of the variation of the elastic constants and material orientation of the anisotropic body on the contact pressure. Their work was carried out on a three dimensional contact of a rigid sphere indenting an anisotropic half-space. Here, the problem analysed is one of an infinitely long rigid cylinder of radius R pressed onto an anisotropic elastic half-plane. The fact that the problem in [Bagault et al., 2012a] is three-dimensional and *not* a plane contact problem means that, strictly speaking, the results are not comparable. Nevertheless, the general trend of the variation of the contact pressure is analysed.

The properties of the elastic half-space are initially given as isotropic, with the shear modulus defined as $G = E/2(1+\nu)$. Then, the elastic stiffness in the direction normal to the contact is multiplied by an arbitrary factor. Here, only the effect of the stiffness in the direction normal to the contact problem is investigated, which is the one that causes the biggest variation in the contact pressure. The variation of the pressure due to changes in the tangential elastic stiffness

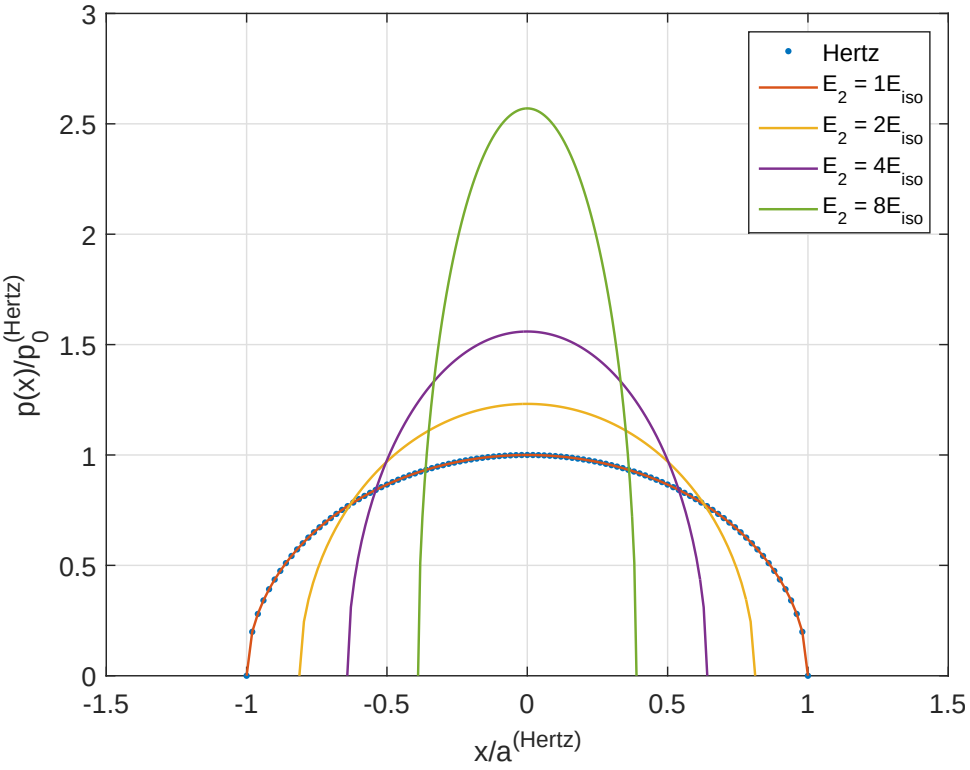

Figure 2.8: Contact pressure distribution for different values of friction coefficient.

may be found in [Bagault et al., 2012a] and [Bagault et al., 2012b]. The elastic stiffness E_2, in the direction normal to the contact interface, was changed by a factor 1, 2, 4 and 8 times the isotropic stiffness E_{iso}. The results are presented in Figure 2.8, where the pressure and contact semi-width are normalised by the Hertzian solution of two isotropic bodies. Note that the solution of the anisotropic formulation for when the elastic stiffness $E_2 = E_{iso}$ is identical to the solution for an isotropic cylinder in §2.1.3, which demonstrates that the anisotropic formulation given in this section is valid for any material, including isotropic ones.

Perhaps a more interesting problem is that of the same anisotropic body, where a material rotation θ is applied instead of varying the elastic stiffness in one direction only. The material rotation about the x axis is considered here and at $\theta = 0^\circ$ the elastic stiffness normal to the contact is three times the isotropic stiffness, $E_2 = 3E_{iso}$ (Figure 2.9). The material rotation is carried out by a rotation of the elasticity tensor. Details about material rotations are presented in chapter 3. The results for the pressure distribution is shown in Figure 2.10. The maximum peak pressure occurs when the direction of E_2, the stiffest material direction, is normal to the contact, with an increase of about 40% in the peak pressure when compared with the fully

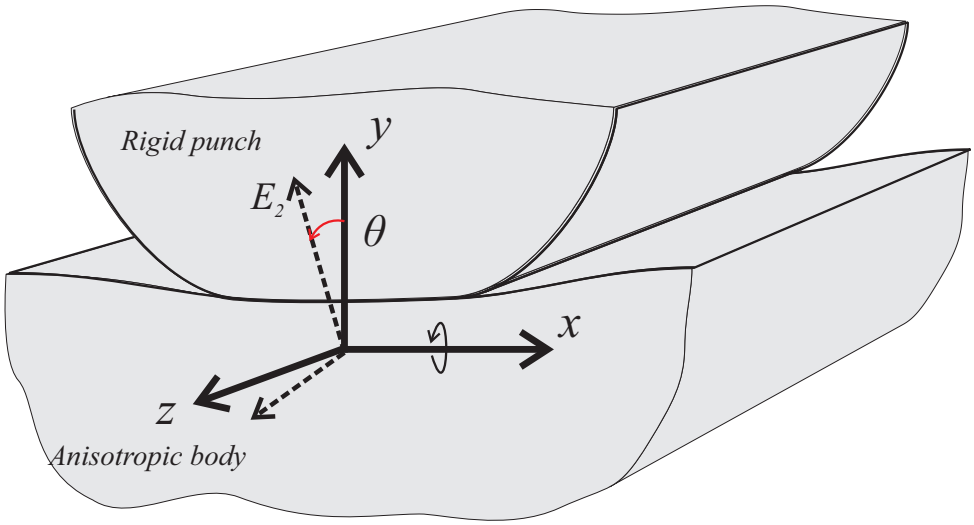

Figure 2.9: Material rotation about the x axis in the example problem of a rigid punch pressed onto an anisotropic half-plane.

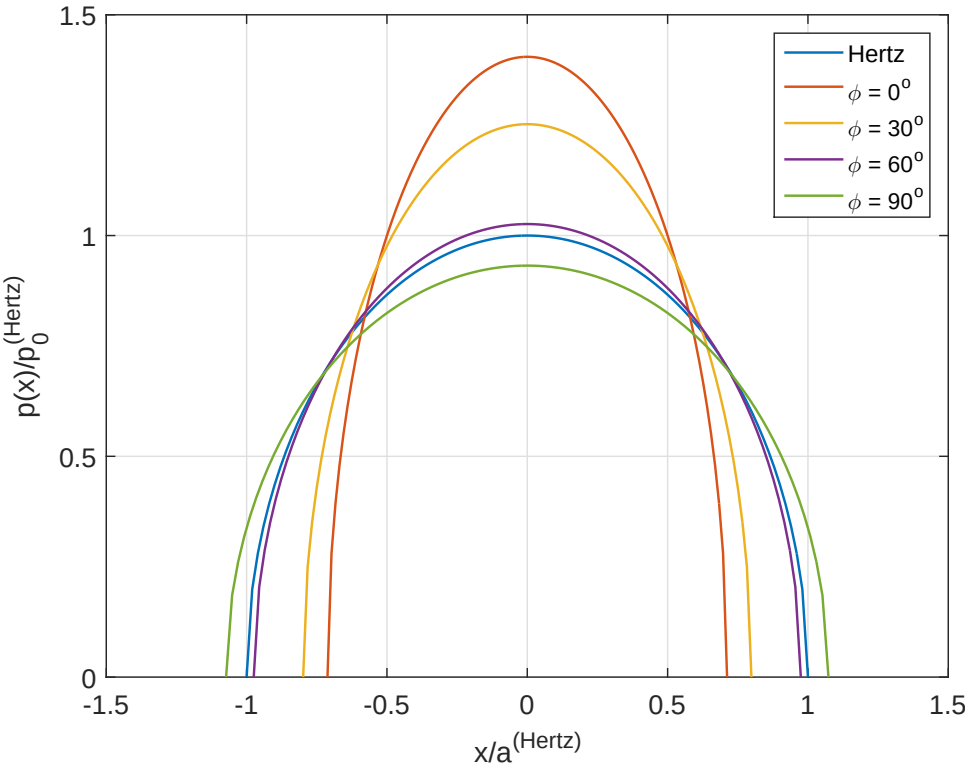

Figure 2.10: Normalised contact pressure distribution with respect to the contact width for different values of friction coefficient.

isotropic solution. The minimum occurs at $\theta = 90°$, with a peak pressure smaller than the isotropic solution.

The examples presented in this section have shown that the formulation presented in §2.2.2 may be used to study a wide range of problems involving the contact of anisotropic bodies.

Note that for most engineering materials, the presence of friction and tangential loads will not change the maximum contact pressure significantly, and if one is interested only in knowing the maximum direct stress normal to the contact, equation (2.46) may be employed directly. Next, the problem of nickel single-crystal materials will be investigated. Despite the fact that a large variation of the pressure was observed in the last example problem, e.g. 250% increase for $E_2 = 8E_{iso}$, smaller variations of peak pressure are anticipated for nickel single-crystals. This is because the increase in elastic stiffness in single-crystal problems occurs only due to material rotation, and the elastic stiffness ratio between the stiffest and most compliant directions in a nickel single-crystal is less than 3. Furthermore, it can also be anticipated that the variation due to material rotation will not be as high as the one presented in Figure 2.10, since the variation of stiffness in the different material direction of an orthotropic single-crystal is more complex, with some directions being stiffer, but others more compliant. Nevertheless, the problems presented here give a useful insight on the variations in contact tractions that one might expect when solving anisotropic contact problems.

Chapter 3

Anisotropy of Single-crystal Ni alloys and the contact pressure

The characteristics of the CMSX-4 elastic properties are presented and the rotation of the elastic tensor for different crystal directions is discussed in this chapter. An indentation technique for measuring crystal orientation is presented and it is applied to analyse previous fretting tests. These results are an important motivation to this work since they suggest that fatigue lives may depend on the orientation of the crystal. Then, the influence of the crystal orientation on the contact pressure is investigated. The effect of the crystal secondary principal directions on the fretting stresses are discussed in chapter 4, where numerical and experimental results are presented. Some of the findings obtained in this work regarding the influence of crystal orientation on the stresses and fatigue of a contacting polycrystalline alloy are reported in [Fleury et al., 2014].

3.1 Characteristics of single-crystal Ni alloys elasticity

A discussion on the variation of elastic stiffness in all directions of a nickel single crystal is presented in this section. First, the general characteristics of the elastic tensor of cubic crystals are briefly introduced. The elastic properties of the CMSX-4 alloy are given here, as well as the properties of the polycrystalline nickel alloy RR1000, which is used as the other body in contact. The CMSX-4 properties are used as a practical example of the range of variation between the

stiffest and most compliant directions of nickel crystals. Some aspects of the algebra of tensor rotations are also presented in this section. The tensor rotation algebra is used henceforth in the calculation of the elastic tensor for different crystallographic orientations. The material properties of nickel superalloys and the tensor rotation algebra presented here will be used in the following sections to study the impact of single-crystal orientation on the contact tractions.

3.1.1 Elastic properties of the CMSX-4 alloy

Single-crystal nickel superalloys have face centred cubic (FCC) structure and orthotropic elastic properties. The elastic tensor of general orthotropic materials can be completely characterised by nine independent material constants [Bower, 2012]. However, crystals with cubic symmetry (e.g. FCC and BCC crystals) are a special class of orthotropic material and the number of independent material constants necessary to describe the elasticity tensor may be reduced. The components C_{ij} of the elasticity tensor of FCC crystals, which are here presented in its two-dimensional matrix representation, can be completely characterised by three material constants: the Young's modulus, E, the Poisson's ratio, ν, and shear modulus, G, as long as the crystallographic orientation is also known [Nye, 1985]. The stress-strain[1] relations of an orthotropic material with cubic symmetry, and with the principal directions aligned with the reference orthogonal coordinate system, may be written as

$$\begin{Bmatrix} \sigma_{11} \\ \sigma_{22} \\ \sigma_{33} \\ \sigma_{12} \\ \sigma_{13} \\ \sigma_{23} \end{Bmatrix} = \begin{bmatrix} C_{11} & C_{12} & C_{12} & 0 & 0 & 0 \\ C_{12} & C_{11} & C_{12} & 0 & 0 & 0 \\ C_{12} & C_{12} & C_{11} & 0 & 0 & 0 \\ 0 & 0 & 0 & C_{44} & 0 & 0 \\ 0 & 0 & 0 & 0 & C_{44} & 0 \\ 0 & 0 & 0 & 0 & 0 & C_{44} \end{bmatrix} \begin{Bmatrix} \varepsilon_{11} \\ \varepsilon_{22} \\ \varepsilon_{33} \\ 2\varepsilon_{12} \\ 2\varepsilon_{13} \\ 2\varepsilon_{23} \end{Bmatrix}, \tag{3.1}$$

where

$$C_{11} = \frac{E(1-\nu)}{1-\nu-2\nu^2}, \quad C_{12} = \frac{E\nu}{1-\nu-\nu^2}, \quad C_{44} = G. \tag{3.2}$$

[1] Although the engineering stress-strain relations are used here, the shear strain components ε_{ij} are tensor strains and they relate to the engineering shear strains by $\gamma_{ij} = 2\varepsilon_{ij}$ $(i \neq j)$. More details about tensor and engineering definitions of strain are discussed in [Bower, 2012].

The anisotropy of crystals is often characterised by Zener's factor, which is given by the relation between E, ν and G, and may be introduced as

$$D = \frac{2G(1+\nu)}{E} = \frac{2C_{44}}{C_{11}-C_{12}}, \tag{3.3}$$

where, for isotropic materials, $D = 1$, and the relation $G = E/2(1+\nu)$ holds[2]. Physically, Zener's factor represents the ratio between the resistance to shear on the plane $\{100\}$ in the $\langle 010 \rangle$ direction, C_{44}, and the resistance to shear deformation on the $\{110\}$ plane in the $\langle -110 \rangle$ direction, $(C_{11}-C_{12})/2$. When the orthogonal reference coordinate system coincides with the principal directions, the elasticity matrix of FCC crystals differs from isotropic materials only by the fact that D is not equal to 1. In fact, this constant can be thought of as a measure of the anisotropy of the material and for the CMSX-4 alloy studied here, $D \simeq 2.8$. This value is obtained with the material properties given in Table 3.1. This anisotropic constant is correlated with the variation of the elastic stiffness in the different crystallographic directions, where the higher the anisotropy of the crystal, i.e. the higher A, the higher the difference between the most stiff and most compliant directions.

The CMSX-4 alloy was designed to withstand its strength at high temperatures. Its yield stress, for example, increases with increasing temperatures up to a peak at approximately 800°C [Reed, 2006], above which the mechanical strength of the alloy falls significantly. The yield stress can vary from approximately 1000 MPa at room temperature up to 1200 MPa at about 800°C. Nevertheless, the alloy becomes more and more compliant as the temperature increases. This variation in the elastic stiffness will have a direct impact on the contact stresses. The material elastic constants at room temperature (20°C) and at 680°C are presented in Table 3.1[3]. The elastic properties of the RR1000 polycrystalline nickel alloy at room temperature and at 680°C are also presented. Note that for the RR1000, the shear modulus, G, is $G = E/2(1+\nu)$. This is an isotropic alloy that will be later used in the analysis of contact pressure. It is also useful to notice how the properties of the single-crystal alloy in the principal directions compare

[2] Zener's anisotropic factor is generally represented by the letter A. However, to avoid confusion with the contact effective compliance A used in chapter 2, the letter D will be used henceforth in this thesis to represent the anisotropy factor.

[3] These values were given by Rolls-Royce plc for modelling purposes and no reference to the original experimental data were provided.

Material property	CMSX-4 (20°C)	CMSX-4 (680°C)	RR1000 (20°C)	RR1000 (680°C)
Young's modulus E (GPa)	127.9	104.9	226.0	187.2
Poisson's ratio ν	0.377	0.389	0.27	0.309
Shear Modulus G (GPa)	130.9	108.7	88.9	69.6

Table 3.1: Elastic properties at room temperature and 680°C of the CMSX-4 single-crystal alloy, along the crystal's principal directions, and the RR1000 polycrystalline alloy.

with the bulk elastic properties of a polycrystalline nickel alloy. With the material constants given, one may now construct the elastic tensor of the CMSX-4 when the reference coordinate system is aligned with the crystal principal directions from equations (3.2) and (3.1). By a basis transformation of the tensor, which is presented next, it is also possible to determine the elastic modulus in each crystal direction.

3.1.2 Coordinate transformation of the elasticity tensor

The stress and strain state of any point may be expressed in any coordinate system. For isotropic materials it is convenient to work in the geometry and loading coordinate system of the part in question, since the properties of the material are the same in any direction. For orthotropic materials, a material coordinate system is also relevant for determining the state of stress of an arbitrary point in the solid. However, the choice of working in terms of the coordinate system of the boundary conditions is often the preferred one. In order to determine the stress-strain relation of an anisotropic, or orthotropic, material in any point of the solid, it is important to map the orientation of the material coordinate system to the coordinate system of the applied loads and boundary conditions. One way of achieving that is to use basis rotations of the material properties to the geometry and loading reference system. In order words, one must use tensor rotation of the elasticity tensor, for example, to translate it from the material coordinate system to the coordinate system in which the loads and stresses are described.

Basis change may be achieved by applying an Euler rotation to the material coordinate system. The Euler rotation theorem states that any rigid body rotation may be described by three angles, known as the Euler angles. Euler angles are the angles of rotation about one of the coordinate system own axis. Typically, three intrinsic rotations can be used to rotate the

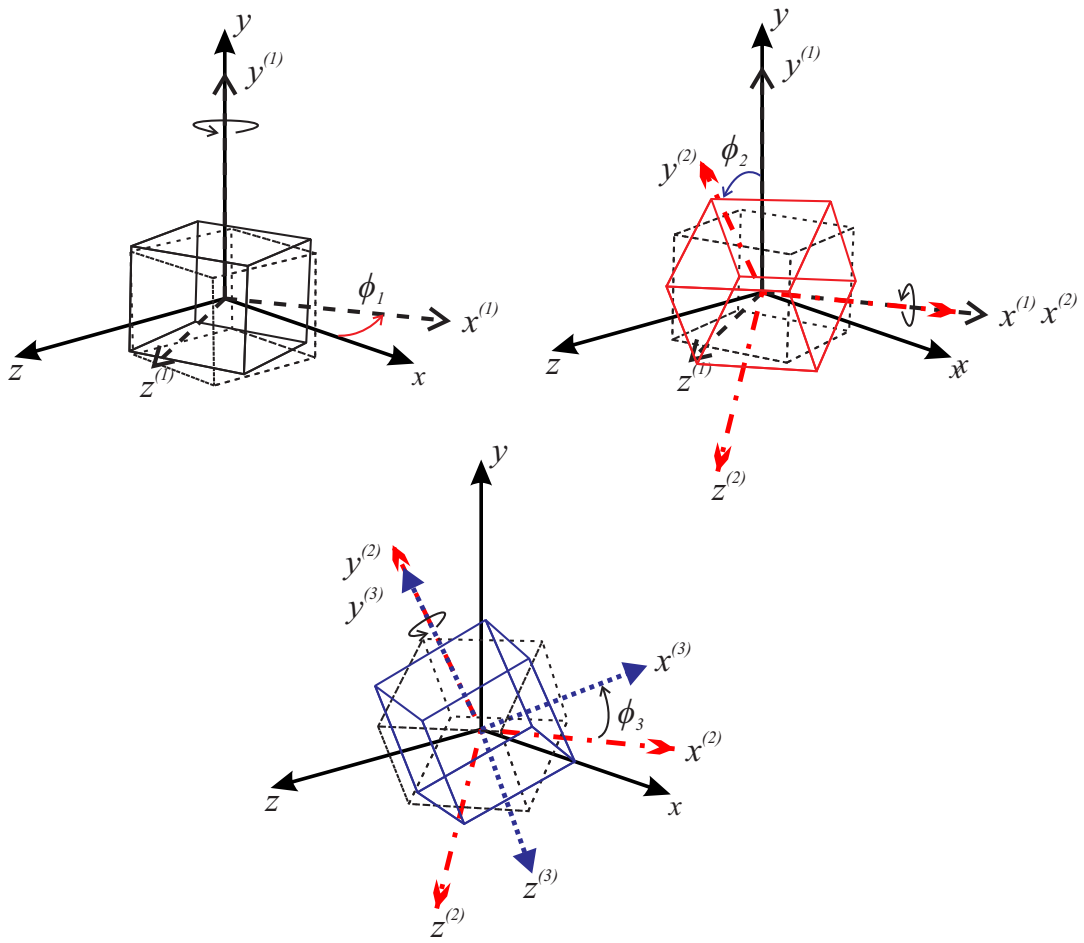

Figure 3.1: Euler rotation Y-X'-Y'' (ϕ_1, ϕ_2, ϕ_3, respectively) of a cubic crystal in a 3D Cartesian system.

coordinate system, such that, the first and third rotations are performed about the same, but rotated, axis. For example, here, the crystals will be rotated by applying the Y-X'-Y'' rotation. This is done by, first, applying a rotation about the y axis of the material Cartesian coordinate system by an angle ϕ_1, followed by a rotation ϕ_2 about the *new* rotated axis $x^{(1)}$ and, finally, a rotation ϕ_3 is performed about the *new* twice rotated axis $y^{(2)}$. The three Euler rotations of the type Y-X'-Y'' of a cubic crystal in a Cartesian coordinate system are shown in Figure 3.1.

Each of the three individual rotations are described by the following rotation matrices,

$$\Omega_y = \begin{bmatrix} \cos\phi_1 & 0 & \sin\phi_1 \\ 0 & 1 & 0 \\ -\sin\phi_1 & 0 & \cos\phi_1 \end{bmatrix}, \quad \Omega_{x'} = \begin{bmatrix} 1 & 0 & 0 \\ 0 & \cos\phi_2 & -\sin\phi_2 \\ 0 & \sin\phi_2 & \cos\phi_2 \end{bmatrix}, \quad \Omega_{y''} = \begin{bmatrix} \cos\phi_3 & 0 & \sin\phi_3 \\ 0 & 1 & 0 \\ -\sin\phi_3 & 0 & \cos\phi_3 \end{bmatrix}, \tag{3.4}$$

and the final rotation matrix is obtained by the combination of all three rotations as

$$\boldsymbol{\Omega} = \Omega_y \Omega_{x'} \Omega_{y''} = \begin{bmatrix} c_1c_3 - c_2s_1s_3 & s_1s_2 & c_1s_3 + c_2c_3s_1 \\ s_2s_3 & c_2 & -c_3s_2 \\ -c_3s_1 - c_1c_2s_3 & c_1s_2 & c_1c_2c_3 - s_1s_3 \end{bmatrix}, \tag{3.5}$$

where c_i and s_i (with $i = 1,2,3$) are abbreviations for $\cos\phi_i$ and $\sin\phi_i$, respectively. Rigorously, the elasticity tensor is a fourth order tensor and the elements of the rotated fourth order tensor, C^*_{ijks}, are given by $C^*_{ijks} = \Omega_{ip}\Omega_{jq}\Omega_{kr}\Omega_{st}C_{pqrt}$. However, if the contracted matrix representation of the elasticity tensor is used, the rotation of the elasticity matrix is given by

$$\mathbf{C}^* = \mathbf{K}\mathbf{C}\mathbf{K}^T, \tag{3.6}$$

where

$$\mathbf{K} = \begin{bmatrix} \mathbf{K_1} & \mathbf{K_2} \\ \mathbf{K_3} & \mathbf{K_4} \end{bmatrix}. \tag{3.7}$$

The elements of the matrices $\mathbf{K_1}$, $\mathbf{K_2}$, $\mathbf{K_3}$ and $\mathbf{K_4}$ are given by [see Ting, 1996; Bower, 2012]

$$K_{1ij} = \Omega_{ij}{}^2; \tag{3.8a}$$

$$K_{2ij} = \Omega_{i\,\mathrm{mod}(j+1,3)}\Omega_{i\,\mathrm{mod}(j+2,3)}; \tag{3.8b}$$

$$K_{3ij} = \Omega_{\mathrm{mod}(i+1,3)\,j}\Omega_{\mathrm{mod}(i+2,3)\,j}; \tag{3.8c}$$

$$K_{4ij} = \Omega_{\mathrm{mod}(i+1,3)\,\mathrm{mod}(j+1,3)}\Omega_{\mathrm{mod}(i+2,3)\,\mathrm{mod}(j+2,3)} \tag{3.8d}$$

$$+\Omega_{\mathrm{mod}(i+1,3)\,\mathrm{mod}(j+2,3)}\Omega_{\mathrm{mod}(i+2,3)\,\mathrm{mod}(j+1,3)}. \tag{3.8e}$$

The function $\mathrm{mod}(i,3)$ in equation (3.8a) is the modulo function and it is defined as

$$\mathrm{mod}(i,3) = \begin{cases} i & i \leq 3 \\ i-3 & i > 3 \end{cases}.$$

The implementation of these tensor transformations are straightforward. A code was written in Matlab and used to rotate the elastic tensor to any orientation desired. This procedure for the

rotation of the elastic tensor was used in the example problem presented in §2.3.3 and is also used for all the analysis of crystal orientation presented next. Note that the choice of using an intrinsic rotation of the type Y-X'-Y'' is completely arbitrary and any other rotation systems could have been used in the tensor transformation. However, it is convenient to use the rotation about the y axis as the first Euler rotation, since one of the questions that are investigated here is the impact of the orientation of the secondary principal directions of the crystal on the contact tractions, which is the rotation of the crystal about the axis normal to the contact. Hence, the use of the Y-X'-Y'' rotation simplifies the calculation of the rotated tensor, since, for this specific case, only the first rotation is necessary. Next, the calculation of the elastic stiffness for the different directions of the CMSX-4 crystal is presented.

3.1.3 Elastic stiffness of nickel crystals in different directions

The elastic stiffness of the CMSX-4 nickel alloy crystals varies with the crystal direction. The axes of the material coordinate system, x, y and z, are assumed to be originally aligned with the material's principal directions $\langle 100 \rangle$, $\langle 010 \rangle$ and $\langle 001 \rangle$, respectively. If the reference material coordinate system is rotated by an angle ϕ_1 ($0 < \phi_1 < 360^\circ$) about the y axis, parallel to the $\langle 010 \rangle$ principal axis, and by an angle ϕ_2 ($0 < \phi_2 < 180^\circ$) about the *new* rotated $x^{(1)}$ direction, the rotated $y^{(2)}$ axis sweeps all directions of the crystal (see Figure 3.1). Therefore, it is possible to use these first two rotations to determine the value of the elastic stiffness in all directions within the 3D Cartesian space, by calculating the stiffness along the direction of the $y^{(2)}$ axis as it is rotated. Note that, here, only two rotations are sufficient to cover all directions of the crystal. The third Euler rotation shown in Figure 3.1 is necessary for a full rotation of the crystal, but it is not needed to calculate the elastic stiffness in all crystal directions. In the last rotation of Figure 3.1, the axes $y^{(3)}$ and $y^{(2)}$ remain in the same direction and, hence, the third Euler rotation does not change the stiffness in the direction of the rotated $y^{(2)}$ axis.

For the calculation of the elastic stiffness in the different crystal directions, it is convenient to work in terms of the compliance tensor. This is because the elastic stiffness in the direction of the three Cartesian coordinate system axes may be obtained directly from the *rotated* elasticity tensor diagonal components without the need to evaluate the Poisson's ratio in the new orienta-

tion. Note that, the diagonal terms of the elasticity tensor in (3.2) depend on the Poisson's ratio and the elastic stiffness, and as the elasticity tensor is rotated, both the Poisson's ratio and the stiffness modulus change. Hence, it is not straightforward to obtain the value of $E_{\langle ijk \rangle}$ in the material direction $\langle ijk \rangle$ from the rotated elasticity tensor component C^*_{22}, equation (3.6), since $\nu_{\langle ijk \rangle}$ also varies. The calculation of the stiffness becomes significantly simpler when using the compliance tensor instead. The strain-stress relation and the compliance tensor for material with cubic symmetry and when the crystal principal directions are aligned with the coordinate system axes are

$$\begin{Bmatrix} \varepsilon_{11} \\ \varepsilon_{22} \\ \varepsilon_{33} \\ 2\varepsilon_{12} \\ 2\varepsilon_{13} \\ 2\varepsilon_{23} \end{Bmatrix} = \begin{bmatrix} S_{11} & S_{12} & S_{12} & 0 & 0 & 0 \\ S_{12} & S_{11} & S_{12} & 0 & 0 & 0 \\ S_{12} & S_{12} & S_{11} & 0 & 0 & 0 \\ 0 & 0 & 0 & S_{44} & 0 & 0 \\ 0 & 0 & 0 & 0 & S_{44} & 0 \\ 0 & 0 & 0 & 0 & 0 & S_{44} \end{bmatrix} \begin{Bmatrix} \sigma_{11} \\ \sigma_{22} \\ \sigma_{33} \\ \sigma_{12} \\ \sigma_{13} \\ \sigma_{23} \end{Bmatrix}, \tag{3.9}$$

where

$$S_{11} = \frac{1}{E}, \quad S_{12} = -\frac{\nu}{E}, \quad S_{44} = \frac{1}{G}. \tag{3.10}$$

Hence, the elastic stiffness in an arbitrary direction of the crystal $\langle ijk \rangle$ may be obtained by calculating the inverse of the rotated S^*_{22} component, i.e. the component that correlates ε_{22} and σ_{22}, for a rotation that align the y axis of the material coordinate system with the respective $\langle ijk \rangle$ direction of the crystal ($E_{\langle ijk \rangle} = 1/S^*_{22}$). Note that in equation (3.9) $S_{22} = S_{11}$, but once the compliance matrix is rotated this may no longer be true.

An illustrative representation of the changes of the elastic stiffness in a CMSX-4 crystal can be obtained by plotting the magnitude of the elastic stiffness, E, as the radius of a three-dimensional solid (Figure 3.2a). The Young's modulus has its smallest value in the crystal's principal directions, $\langle 100 \rangle$, $\langle 010 \rangle$ and $\langle 001 \rangle$. The stiffness increases by a factor of approximately 2 in the directions along the diagonal of the cube faces ($\langle 110 \rangle$, $\langle 101 \rangle$, $\langle 011 \rangle$) and the stiffest directions are the ones connecting the farthest points in the cube, $\langle 111 \rangle$, which is approximately 2.3 times the stiffness in the $\langle 100 \rangle$ direction. The values of the elastic stiffness in

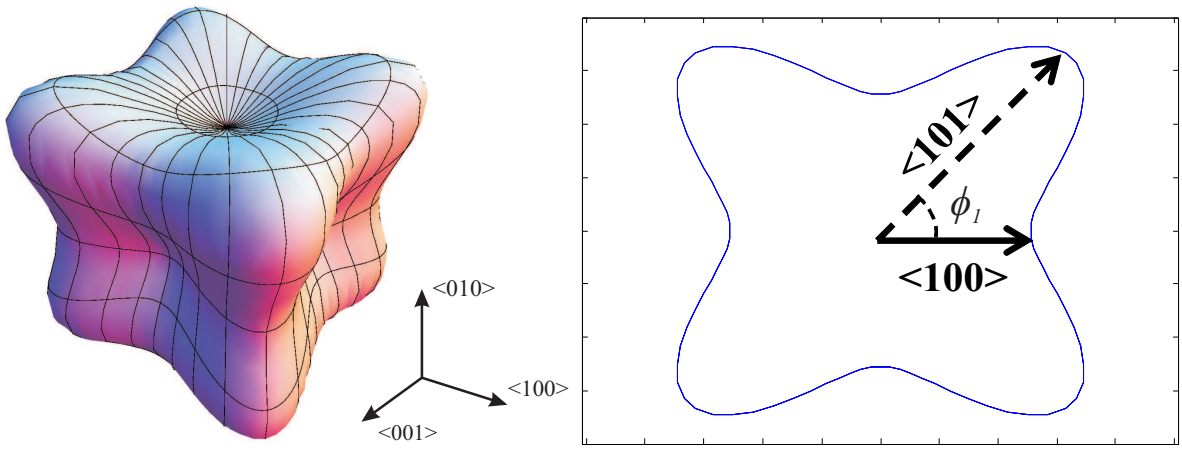

(a) (b)

Figure 3.2: (a) Variation of the elastic stiffness as a function of crystallographic directions, with the radius being the magnitude of the elastic modulus; (b) Magnitude of the elastic stiffness in the $\langle 100 \rangle$-$\langle 001 \rangle$ plane.

some of the crystal directions at room temperature and 680°C are presented in Table 3.2.

Crystal direction	**Young's modulus E at 20°C (GPa)**	**Young's modulus E at 680°C (GPa)**
$\langle 100 \rangle$	127.9	104.9
$\langle 110 \rangle$	230.1	191.9
$\langle 111 \rangle$	287.6	242.2

Table 3.2: CMSX-4 elastic properties in the direction of different crystal directions at room temperature and 680°C.

In the plane defined by the crystal directions $\langle 100 \rangle$ and $\langle 001 \rangle$ the elastic stiffness varies as in Figure 3.2b. This is the plane of the secondary crystal direction in the contact problem, since it is assumed that the crystal direction $\langle 010 \rangle$ is normal to the contact, with the specified tolerance of 20° deviation. There are two directions of symmetry of the elastic stiffness in the $\langle 100 \rangle$-$\langle 001 \rangle$ plane of Figure 3.2b; one at $\phi_1 = 45°$ and another at $\phi_1 = 90°$ ($\phi_2 = \phi_3 = 0$). The symmetry will be exploited in the calculation of the contact normal pressure, where a rotation of $0 \leq \phi_1 \leq 45°$ is enough to obtain the maximum variation of contact stresses due to the *secondary* principal directions of the crystal.

3.2 Previous experimental results and the crystal orientation

The first analysis of the impact of the anisotropy of single-crystals on the contact tractions is to measure the orientation of CMSX-4 pads used in previous fretting fatigue experiments carried out at the University of Oxford under the MACE experimental programme. The correlation between fretting fatigue life and crystal orientation of the pads is investigated. The original fretting fatigue results are presented in detail in [Sarsfield, 2008]. These tests have shown a large scatter in fretting fatigue life when single-crystal pads were used. The orientation of one principal direction of the single-crystal pads was known to be aligned with the long dimension of the pad, within a given tolerance, and the other two principal directions are uncontrolled (Figure 3.4b). A brief explanation of the fretting fatigue experimental procedure is given here, but further details are found in the original work [Sarsfield, 2008]. Other aspects of fretting fatigue experiments are discussed in chapter 4. A technique for measuring the secondary crystal orientation by indentation of the single-crystal is used. This technique is employed on the pads used in the fretting fatigue tests of [Sarsfield, 2008] and the correlation between crystal orientation of the single-crystal pad and fretting fatigue life is analysed.

3.2.1 Measurement of crystallographic orientations by indentation

An indentation technique for measuring the orientation of the principal crystallographic directions on the plane normal to the contact was applied to the single-crystal pads. The technique was introduced by [Huang et al., 2009] and it consists of indenting the plane normal to one of the principal directions with an axisymmetric indenter to find the remaining two principal directions. It is known from the manufacturing specifications of the fretting fatigue pads that the principal direction $\langle 010 \rangle$ is parallel to their longest axis, with a tolerance of 20° in any direction (Figure 3.4b). Hence, an indentation on the face opposite to the cylindrical face can provide, at least approximately, the other two principal directions. Because of the difference in elastic stiffness and yield limit of single-crystal alloys in different crystallographic directions, the resulting mark on the surface of the material by an axi-symmetric indenter (e.g. Rockwell C hardness tester) is an almost square shaped profile. From the residual deformation after the indentation, it is possible to determine the principal directions of the crystal.

The difference between indenting an isotropic and an orthotropic body is exemplified in Figure 3.3. An indentation by a conical indenter on an isotropic body will result in a circular residual hole on the surface as shown in Figure 3.3a. Since the properties of the material are the same in all directions, the residual deformation of the isotropic body will have the same shape as the indenter. However, nickel single-crystal alloys' elasto-plastic properties vary with the crystal direction. The residual deformation on the face of a single-crystal pad penetrated by a conical indenter, and whose normal is parallel to one of the crystal's principal direction, is shown in Figure 3.3b. The elastic stiffness of the CMSX-4 pad on the face normal to the $\langle 010 \rangle$ direction, for example, is displayed in Figure 3.2b. Due to higher elastic stiffness and lower yield limit in the diagonal directions, e.g. $\langle 101 \rangle$, and given that the applied strain is uniform, those directions suffer larger plastic deformation and are represented by the corners in the indentation residual mark in Figure 3.3b. The principal directions are the least stiff ones and, hence, the sides of the square shaped mark, 45° from the corners of the mark.

This technique was used to measure the orientation of the other two principal directions of single-crystal pads used in fretting fatigue tests, assuming that one of the principal directions is aligned with the pad's long axis. The angle ϕ_1 between the crystallographic direction $\langle 100 \rangle$ and the x axis is used in §3.2.2 to characterise the crystal orientation of each single-crystal pad. Although it is not strictly a non-destructive technique, since it causes permanent damage by deforming plastically the face of the single-crystal pad, the indentation technique does not affect the zone near the cylindrical face in contact and the pads can still be used later without compromising the results. Furthermore, other traditional methods of measuring crystallographic orientation, such as, EBSD and X-Ray diffraction, often requires sample preparation and sectioning of the specimens, which are not very practical when a measurement of the pad before the test is required.

3.2.2 Crystal orientation and the MACE tests

The MACE tests carried out a few years ago at the University of Oxford provided one of the main motivations to pursue this investigation of the impact of crystal orientations on contact tractions. The scatter observed when single-crystal pads were used, was significantly higher

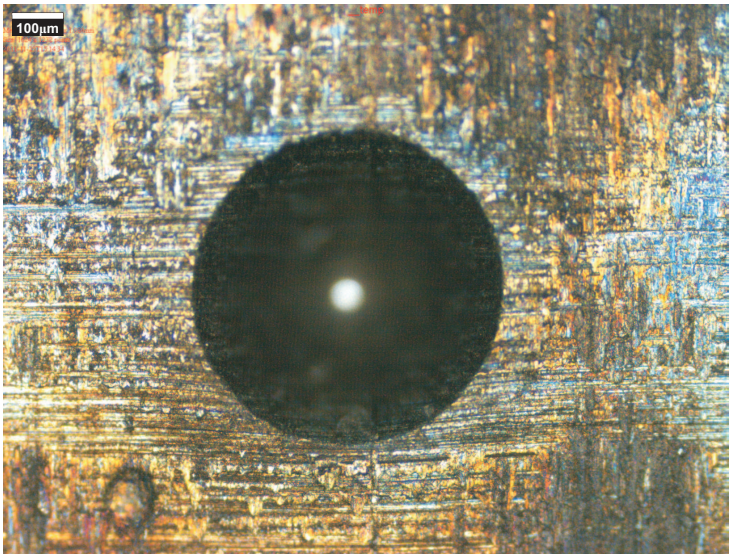

(a)

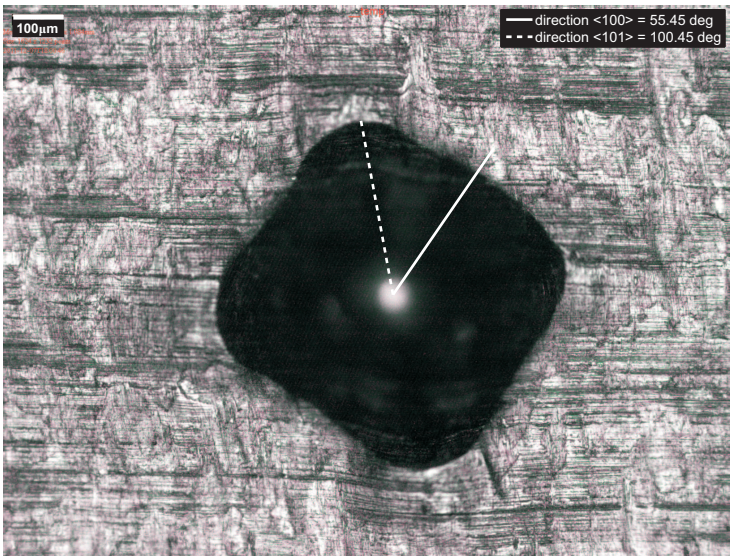

(b)

Figure 3.3: Indent mark on the surface of (a) a polycrystalline nickel alloy and (b) a single-crystal nickel alloy.

than tests with isotropic alloy pads [Sarsfield, 2008]. Although one of the crystal directions was controlled to be normal to the contact in those tests, not much attention was given to the orientation of the other two principal directions. Using the technique described in §3.2.1, the other principal two directions of the single-crystals, namely the $\langle 100 \rangle$ and $\langle 001 \rangle$ directions, are measured. Then, the fretting fatigue life of the tests are correlated with the crystallographic directions of the pads measured for each test.

The MACE programme involved a large number of tests, which included different pad geometries and different applied shear loads. Here, only tests with cylindrical face pads are con-

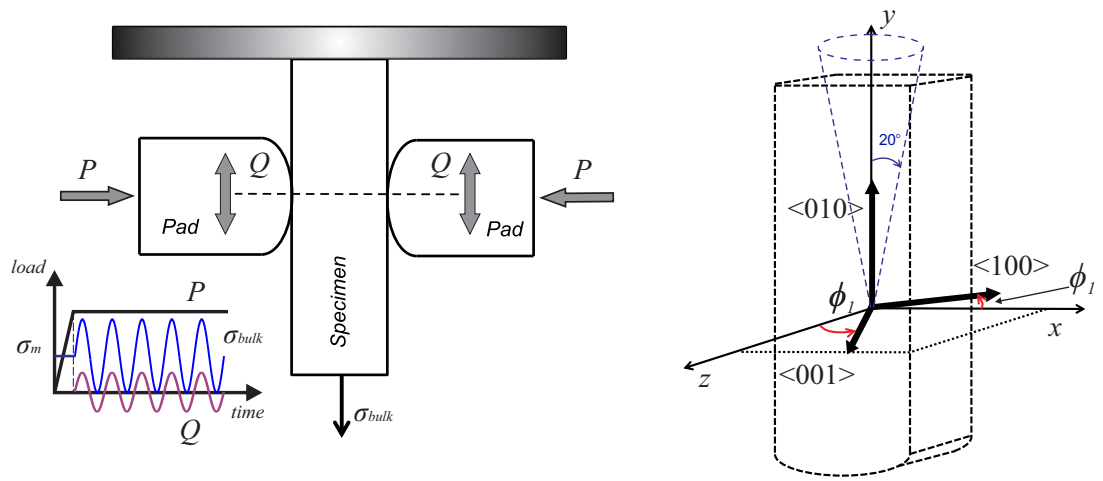

Figure 3.4: Schematic representation of (a) the fretting fatigue "in-line" rig; and (b) the single-crystal pads' crystallographic orientation.

sidered, since contact problems with cylindrical bodies are significantly simpler to solve. The contact solution for problems with flat and rounded pads, on the other hand, is more complex, particularly when both bodies are elastic. This problem is addressed in in chapters 6 & 7, where a semi-analytical solution for elastic flat and rounded punches on elastic half-planes is presented.

The specimens were made of the polycrystalline nickel superalloy Udimet 720Li. They were tested with both single-crystal (CMSX-4) and polycrystalline (Udimet 720Li) pad pairs pressed onto it. The tests were carried out on the "in-line" fretting fatigue rig, where two in-line actuators control the shear load, Q, and the bulk load, σ_{bulk}. Both the shear and bulk stress loads are oscillatory and in-phase, such that, the shear force was pulling the specimen up as the specimen bulk load was maximum (60 kN). A normal load, P, was applied by a manual hydraulic actuator and held constant throughout the test. A schematic representation of the test rig and the loads applied are shown in Figure 3.4a. It is also important to keep in mind that these tests were conducted at room temperature while the ones presented in chapter 4 are tested at high temperature. Furthermore, greater attention is given to the crystal orientation of single-crystal pads in the new test programme of chapter 4.

In the crystal orientation analysis, only the results of cylindrical pads with radius $R = 100$ mm

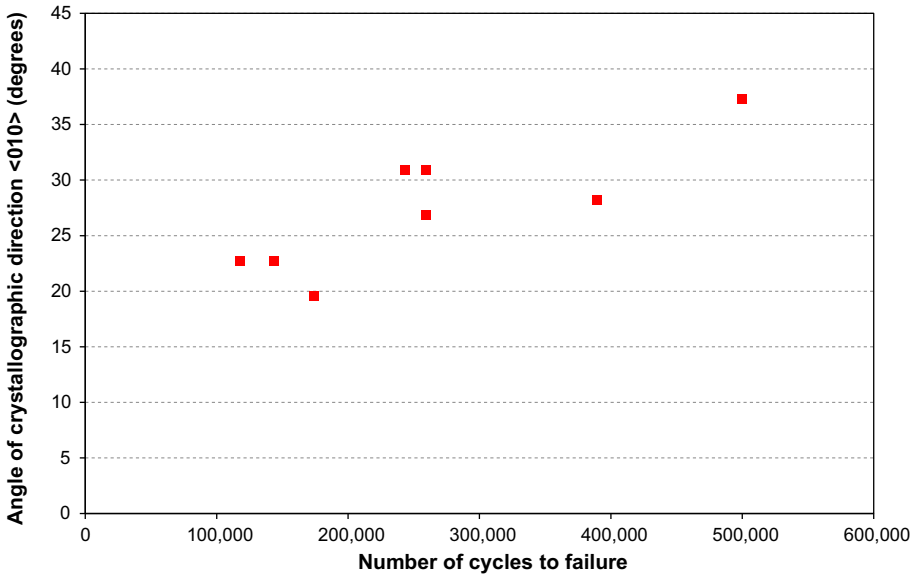

Figure 3.5: Correlation between average deviation of crystal direction $\langle 100 \rangle$ to the x axis and fatigue life of the tests. The fatigue data was originally obtained from [Sarsfield, 2008].

and applied maximum shear load of $2Q = 13$ kN are used. All these tests, except 2, had a constant normal pressure applied $P = 38$ kN throughout the test. Test numbers 33 and 35 (Table 3.3) had an applied normal load of $P = 19$ kN. Furthermore, tests with the same applied maximum shear load ($2Q = 13$ kN) and single-crystal pads had a scatter of the specimen life varying from $117,563$ cycles to failure to unbroken after $500,000$ cycles, i.e. "run-out" test. The crystal orientation of both pads in each test are measured by indentation. The deviation from the $\langle 100 \rangle$ direction to the x axis (see Figure 3.4b) are averaged between both pads and then plotted against the fatigue life. The symmetry of the crystal elastic properties about the angle $\phi_1 = 45^\circ$ is exploited here. Note that misorientations of $\phi_1 = 30^\circ$ and $\phi_1 = 60^\circ$ between $\langle 100 \rangle$ and the x axis have a similar effect on the contact tractions but with opposite out-of-plane stresses, when the direction $\langle 010 \rangle$ is fixed and parallel to the y axis. The results are plotted in Figure 3.5 and the list of tests and crystal orientation of each pad is given in Table 3.3.

The results shown in Figure 3.5 suggest a correlation between crystal orientation of the single-crystal pads and fretting fatigue life. However, the absence or small number of data at angles close to 0° and 45° makes it difficult to precise the exact trend of these results. Also, it is important to remember that some tests had pads with different orientations. That could cause the contact tractions to be different on each side of the specimen and, if the crack originating from

Test number	**Cycles to failure**	**Pad 1 ϕ_1 (degrees)**	**Pad 2 ϕ_1 (degrees)**	**Average exploiting 45° symmetry (degrees)**
11	258,990	27.2	26.3	26.8
22	389,159	26.3	30.0	28.2
33	500,000	52.7	52.7	37.3
35	173,834	7.2	31.8	19.5
38	243,272	31.8	30.0	30.9
39	259,541	31.8	30.0	30.9
42	117,563	79.1	55.4	22.7
43	143,564	79.1	55.4	22.7

Table 3.3: Test number, number of cycles to failure and measured orientation of pads used in the MACE test programme.

one specific side is dominant over the other, the average of the orientation of both pads used here becomes inappropriate. This has resulted in the suggestion that the next test programme be made with matching pads on both sides, as it is the case of the results presented in chapter 4. The scatter for tests with similar crystal orientation in Figure 3.5 is much smaller than the overall scatter observed. This is an indication of the correlation with the crystal orientation and has been an important factor in the motivation to carry out this analysis.

3.3 Analytical investigation of single-crystal contact pressure

The analytical anisotropic contact solution presented in §2.2 is used here to calculate the impact of the single-crystal orientation on the contact pressure. The two-dimensional Hertzian contact problem of a cylinder pressed onto a half-plane is used in this analysis. First, it is presented the variation in contact pressure of isotropic bodies in contact, when the stiffness of one of the bodies is increased by a factor 2. Note that this is approximately the same variation in elastic stiffness found in the CMSX-4 single-crystal when rotating the crystal about one of its principal directions, whilst keeping this principal directions fixed and parallel to one of the geometry coordinate axes. The impact the crystal orientation with respect to the pad geometry about each of the principal directions is shown. The maximum possible increase in peak stress is also investigated by orientating the crystal in all possible directions. This is all done for the case of a CMSX-4 material pressed on an isotropic RR1000 nickel superalloy. With the tests at

high temperature in mind and the real application of blade to disc assemblies in the engine, the properties of the materials at high temperature are used in this section.

3.3.1 Effect of elastic stiffness in an isotropic contact problem

To study the influence of the elastic stiffness on the contact peak pressure and pressure distribution, two cases were considered. In the first, both bodies 1 and 2 have Young's modulus $E_1 = E_2 = E$ and Poisson's ratio $\nu_1 = \nu_2 = \nu$. In the second case, the elastic stiffness of one of the bodies is increased by a factor of 2, $E_2 = 2E$, and the Poisson's ratio remains the same. The contact is assumed to be frictionless and hence the coupling due to the elastic dissimilarity is neglected. The contact stress distribution, $p(x)$, peak pressure, p_0, and contact semi-width, a, are calculated by using the Hertzian theory for contacting solid cylinders given in [Johnson, 1985] and presented in §2.1.3.

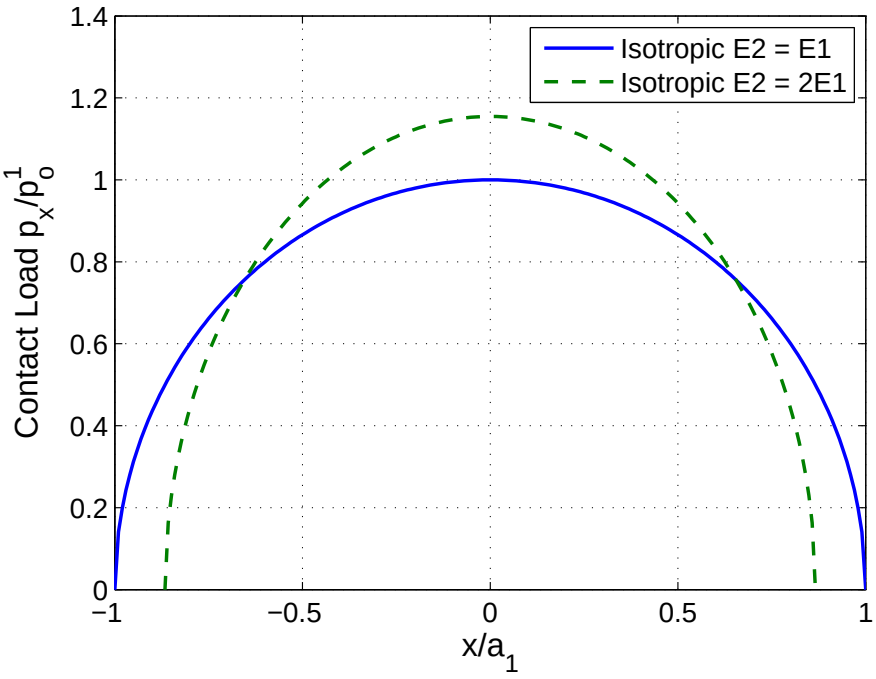

Figure 3.6: Effect of elastic stiffness on the contact peak stress of isotropic Hertzian contact.

The change in the Young's modulus of one of the bodies causes a variation in the contact stiffness, defined by the constant $E^* = 2/A$, where A is the contact compliance given in (2.8). Increasing the elastic stiffness by a factor of 2, the constant E^* is increased by 33.3%. The contact semi-width depends on $\sqrt{1/E^*}$ and the peak stress depends on the $\sqrt{E^*}$. Hence, the

second case has a reduction by 13.4% in the size of a and an increase of 15.47% in peak stress. The pressure distributions for both studied cases of isotropic elastic contact are shown in Figure 3.6, normalised by the peak pressure and contact width of case 1, p_0^1 and a_1. Note that the variation in elastic stiffness considered here is of the same magnitude as the variation that occurs in different directions of the single-crystal alloy in the plane of any two principal directions. It can be expected that the variations in peak stress due to crystallographic orientation of single-crystals will be of the same order of magnitude, but smaller than the variation in the analysis with two isotropic materials. That is because the variation in elastic stiffness in the orthotropic case is not uniform and not all the directions have a variation of elastic stiffness as great as 2 (Figure 3.2b). Hence, the isotropic problem provides a useful bound to the orthotropic one.

3.3.2 Contact pressure between single-crystal and polycrystal Ni alloys

Using the contact solution of elastically dissimilar anisotropic bodies presented in §2.2.2, the pressure distribution and contact width are obtained and compared between different crystallographic orientations. The problem of a contact between a flat specimen made of polycrystalline RR1000 alloy and a cylindrical pad made of single-crystal CMSX-4 alloy, with radius $R = 100$ mm, is solved. The solution uses the approximation of both bodies to half-planes, as discussed in §2.2.2. According to the convention used in this work, the reference material orientation is that with the three principal directions parallel to the three Cartesian system axes of the geometry of the bodies. The contact pressure is analysed without taking into account friction in the interface. The symmetries in the elastic stiffness variation of the crystal are exploited. If the crystal is rotated about direction $\langle 010 \rangle$, parallel to the y axis of the body, it is expected that any rotation greater than 45° be a mirrored solution (i.e. orientation ϕ_1 of 60° is equivalent to 30° but with opposite sign in the out-of-plane shear). The variation of the contact pressure is analysed for crystal rotations about each of the principal directions (Figure 3.7). Note that these are not physical rotations of the indenter, but rotations of the crystal with respect to the punch's geometry.

The change in contact pressure is directly correlated with the variation of the elastic stiffness. Furthermore, the highest variation in elastic stiffness during the rotation about one of the

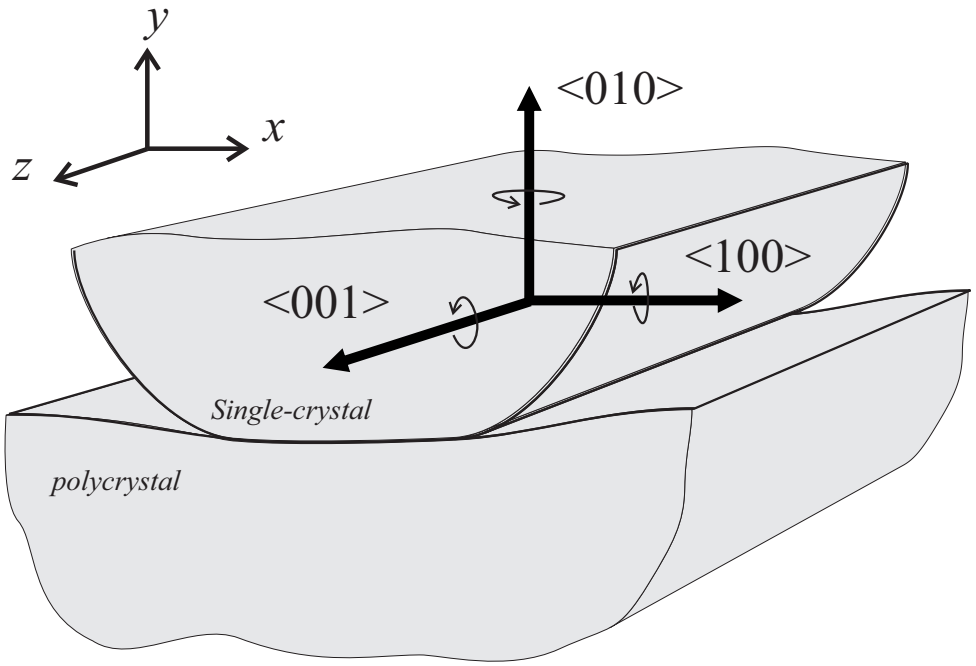

Figure 3.7: Schematic representation of the crystal rotation about each principal direction in the two dimensional Hertzian contact problem

principal directions occurs between the principal direction itself and the diagonal directions, positioned 45° away from the principal directions (e.g. between $\langle 100 \rangle$ and $\langle 101 \rangle$ directions). Hence, in order to obtain the maximum variation in contact pressure for a rotation about one of the principal directions, it is sufficient to rotate them by an angle of 45°. The contact pressure for a crystal orientation 45° rotated about each of the three Cartesian axes are shown in Figure 3.8. The results are normalised by the peak stress solution of the reference crystal orientation, p_0^{00deg}. The relative differences in peak stress are given in Table 3.4. Because the contact is assumed to be frictionless, the coupling of the problem disappears and no offset of the centre of the contact occurs. The highest increase in peak stress, 6.30%, occurs when the crystal is rotated about the x axis, that is, rotating the crystallographic direction $\langle 010 \rangle$ on the plane perpendicular to the plane of analysis (see Figure 3.7). The maximum variation in peak stress of 2.58% with respect to the reference orientation is found for rotations about $\langle 010 \rangle$. Those represent the misorientations of the secondary principal directions, when the principal direction $\langle 010 \rangle$ is kept normal to the contact, which is the primary focus of this work.

Another important aspect of the solution is that a rotation about the out-of-plane z axis, i.e. aligning the stiffer crystal direction $\langle 110 \rangle$ with the normal and tangential contact directions,

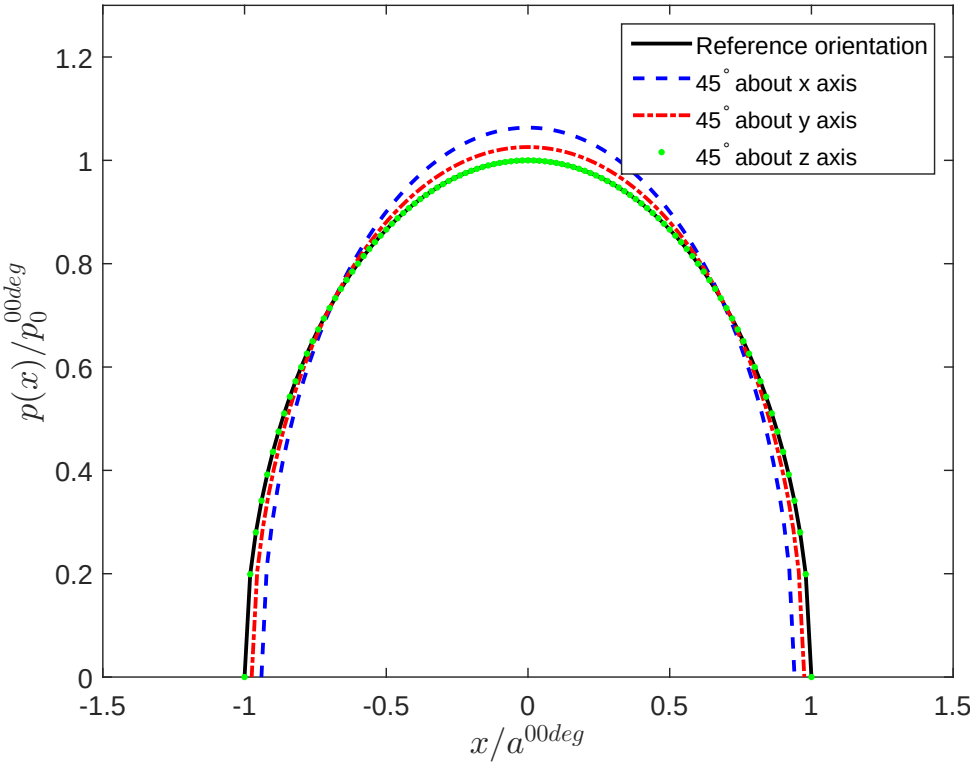

Figure 3.8: Normal contact tractions for a contact between a polycrystalline flat specimen and a single-crystal cylindrical pad with different crystallographic orientations.

Rotation angle	**Contact semi-width a/a^{00deg}**	**Peak stress p_0/p_0^{00deg}**
45deg about x-axis	0.940	1.063
45deg about y-axis	0.976	1.026
45deg about z-axis	1.000	1.000

Table 3.4: Relative difference in contact properties due to crystallographic orientation.

does not affect the tractions in a frictionless contact problem. This observation can be explained by looking at the analytical anisotropic contact solution and the integral formulation of the Barnett-Lothe tensors in equation (2.37). Even if a stiffer direction of the crystal is along the contact normal, which intuitively might lead one to believe that higher contact tractions will be obtained, the compliance term does not change in value. That happens because the integrals in equation (2.37) sum the elastic stiffness in all directions on the plane of analysis and the sum remains constant, even though the stiffer principal directions are now aligned with the normal and tangential directions. That is also the reason why the change in peak stress was not as great as the one seen in the isotropic problem of §3.3.1.

3.3.3 Contact peak pressure as a function of crystal orientation

Using the Euler rotation described in §3.1.2, a complete rotation of the material coordinate system is employed. All possible orientations of the crystal are investigated and the maximum possible variation of the contact pressure is found. Exploiting again the crystal symmetries, the three Euler angles, ϕ_1, ϕ_2 and ϕ_3, are varied from 0° to 90°. For each combination of angles the contact pressure distribution and maximum contact peak stress are calculated by the analytical anisotropic solution. A surface plot of the variation of contact pressure normalised by the reference orientation peak pressure, p_0^{00deg}, is presented in Figure 3.9. The contact peak stress has a maximum increase of $1.063p_0^{00deg}$ (6.30% higher) at orientations similar to the 45° rotation about the x axis of the previous section (e.g. $\phi_1 = 0^\circ$, $\phi_2 = 45^\circ$ and $\phi_3 = 0^\circ$). Note that, other combinations of Euler angles may have equivalent orientations of the crystal because of the planes of symmetries in FCC crystals. The orientations with higher contact peak pressure are also the ones with smaller contact area. These orientations of maximum peak pressure do not have the stiffest crystal direction, $\langle 111 \rangle$, normal to the contact. However, they have two stiffest directions, i.e. two diagonals of the cube, in the plane of analysis and the integrals of the fundamental elasticity tensors in equation (2.37) have their highest values.

Due to the manufacturing tolerances of the pads used in the fretting fatigue tests, the maximum deviation between $\langle 010 \rangle$ and the y axis is 20° in any direction, as it is illustrated in Figure 3.4b. This is also true for the blades in engines, although the contact interface between blades and discs is not normal to the principal direction of the crystal growth. The blade to disc contact pressure for the different crystal orientations is not covered here, but the maximum contact pressure variation in the assembly is bounded by the results shown in Figure 3.9, where all possible crystal orientations with respect to the contact interface were analysed.

Here, the same procedure of crystal rotation is applied, but with the ϕ_2 Euler angle varying only from 0° to 20°. The Euler angles ϕ_1 and ϕ_2 are rotated from 0° to 90° as before. The variation of contact peak contact pressure as a function of the Euler rotations, and normalised by p_0^{00deg}, is presented by the surface plots of Figure 3.10. The maximum increase in peak stress in the case of a maximum deviation of 20° about the contact normal is $1.035p_0^{00deg}$ (3.50% higher) when $\phi_1 = 0$, $\phi_2 = 20^\circ$ and $\phi_3 = 45^\circ$. This represents the maximum change in contact

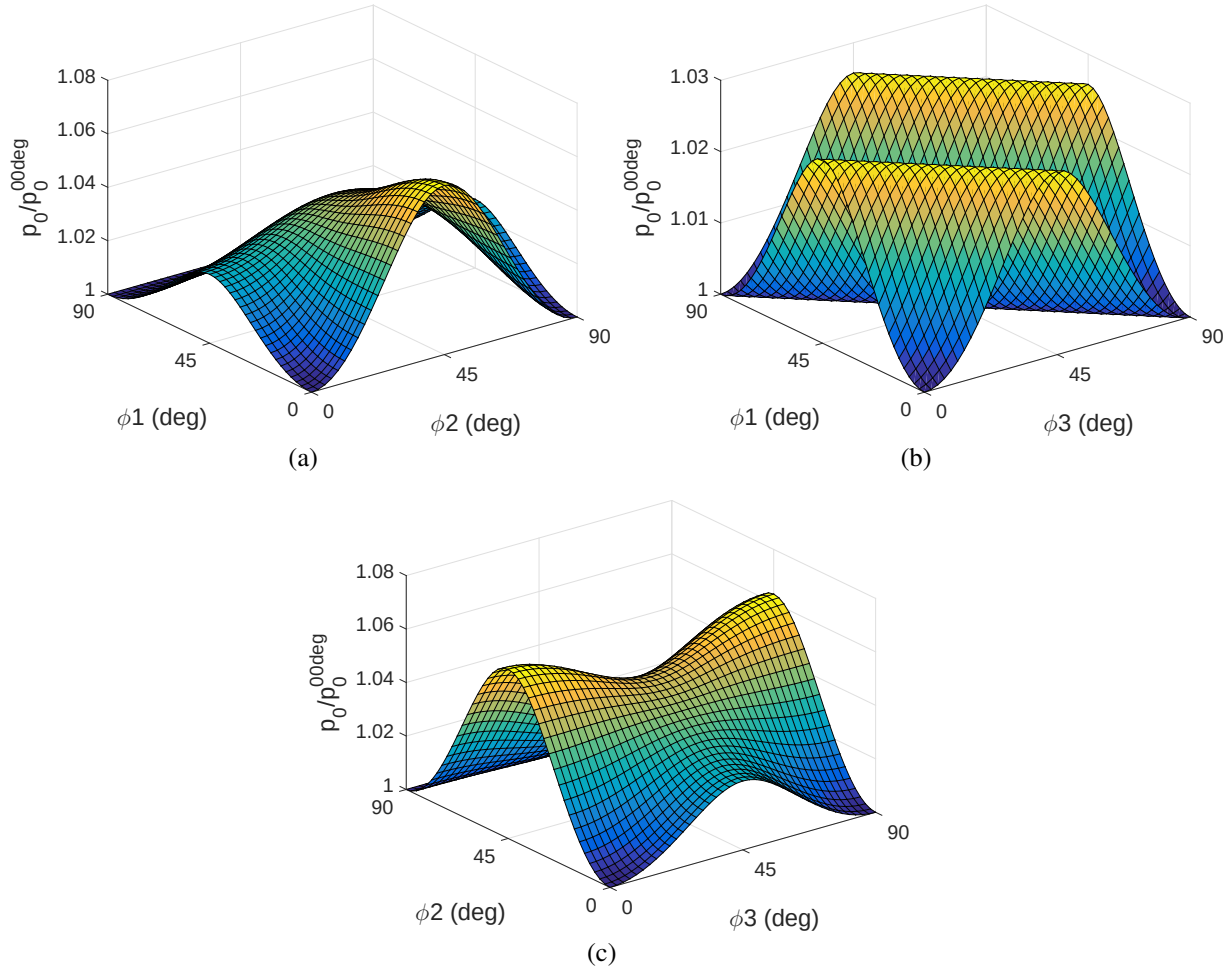

Figure 3.9: Contact peak stress variation for all possible crystal orientations and normalised by the peak stress of the reference orientation, p_0^{00deg}. The Euler angles ϕ_1, ϕ_2 and ϕ_3 represent the Euler rotation of the type Y-X'-Y''.

pressure that one might expect in the fretting fatigue tests, where the manufacturing tolerance of the single-crystal pads assures that one of the crystal's principal directions is parallel to vertical axis of the pad within a 20° tolerance.

3.4 Discussion

Different aspects of single-crystal nickel alloys and the impact of their elastic properties on the contact pressure have been presented in this chapter. Previous studies on single-crystal alloys have focused on the stresses on the single-crystal body and their variation with the crystal orientation. The impact of crystal orientation on the fretting fatigue life of a contacting isotropic body is the main focus of investigation in this chapter. The results of the MACE tests carried

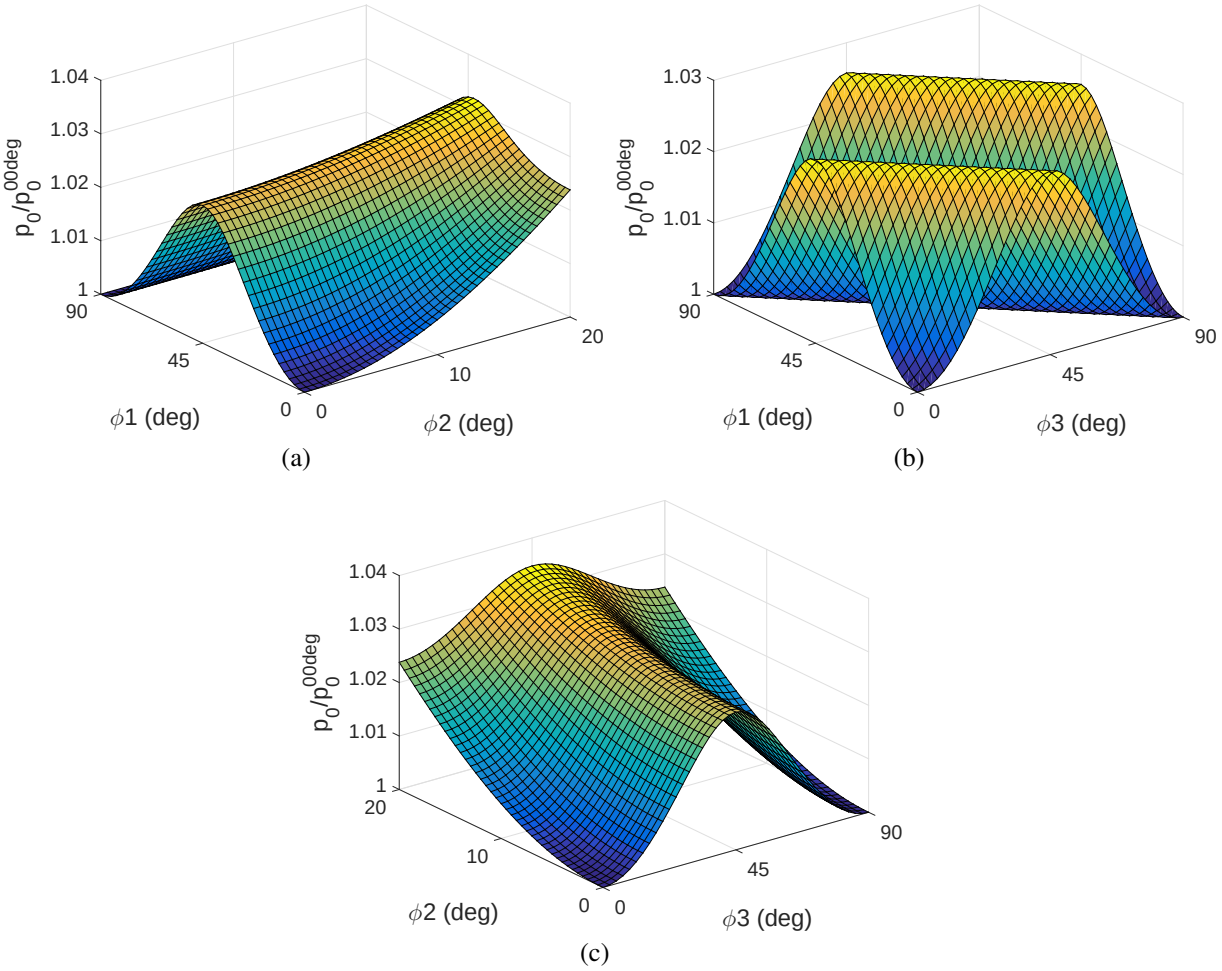

Figure 3.10: Contact peak stress variation for all possible crystal orientations given the 20° manufacturing tolerance of the crystal orientation. The Euler angles ϕ_1, ϕ_2 and ϕ_3 represent the Euler rotation of the type Y-X'-Y''.

out previously at the University of Oxford show some indications of correlation between single-crystal orientation and the number of cycles to failure, where the scatter between tests with pads at similar orientations is significantly smaller than the overall test scatter. The implication of this apparent correlation is that the orthotropic properties of the single-crystal body change the contact tractions at the interface with its crystal orientation. Note that, the variation of fretting fatigue life here occurs on the isotropic body and, hence, any effect of the single-crystal orientation on the isotropic body is 'transmitted' through the contact interface. In order words, any change in the fretting fatigue life of the isotropic alloy must be due to changes in the contact tractions. Two are the possible changes in contact tractions that may occur due to crystal orientation: i) the contact pressure changes with the variation in elastic stiffness for different crystal orientations; and/or ii) the coefficient of friction at the contact interface depends

on the orientation of the single-crystal. The first effect also has implications on the contact shear tractions, since the shear traction distribution in the slip zones at the edge of contact, for example, are given by the contact pressure scaled by the coefficient of friction. The second possibility builds upon the assumption that the coefficient of friction results from the elasto-plastic properties of both bodies' asperities at the micro scale [Mulvihill et al., 2011], and if the elastic stiffness in the crystal direction tangent to the contact changes, the coefficient of friction could also change. The influence of the crystal orientation on the friction is investigated in chapter 5.

The variation of contact pressure was also investigated in this chapter. For single-crystal CMSX-4 cylinders of different crystal orientations pressed onto RR1000 specimens, the variation in contact pressure is not greater than 6.3% with respect to the reference orientation. This is much lower than the variation observed in the example problem of §2.3.3. There, the stiffness in one Cartesian axis is three times higher than in the other two axes, and the contact pressure varies by up to 40% with respect to the reference orientation by changing the material orientation of the anisotropic body. These two problems have clear differences in the material properties; one is an orthotropic material with cubic symmetry and the other is an arbitrary anisotropic material. However, it is also important to highlight that in the example problem of §2.3.3, the other body in contact is rigid and all the deformation is accommodated in the anisotropic body. In the CMSX-4/RR1000 problem, the two bodies have elastic stiffness of the same order of magnitude and some deformation is accommodated in the isotropic body as well.

In order to compare these two problems, it is important to investigate the effect on the contact pressure of the elastic stiffness of an isotropic body pressed against the CMSX-4 alloy. The impact of increasing the elastic stiffness of the isotropic body on the contact pressure in the problem of a cylindrical CMSX-4 pad pressed onto an isotropic flat body of §3.3.2 is displayed in Figure 3.11. The contact pressure for the rotation about the x axis normalised by the reference orientation for the respective stiffness of the isotropic punch are presented. The stiffness of the isotropic body is initially that of the RR1000 at 680°C and a stiffness multiplier n is used to increase the stiffness of the isotropic body. The results show an increase in the contact pressure variation as the isotropic body becomes stiffer. In the case of the CMSX-4 alloy,

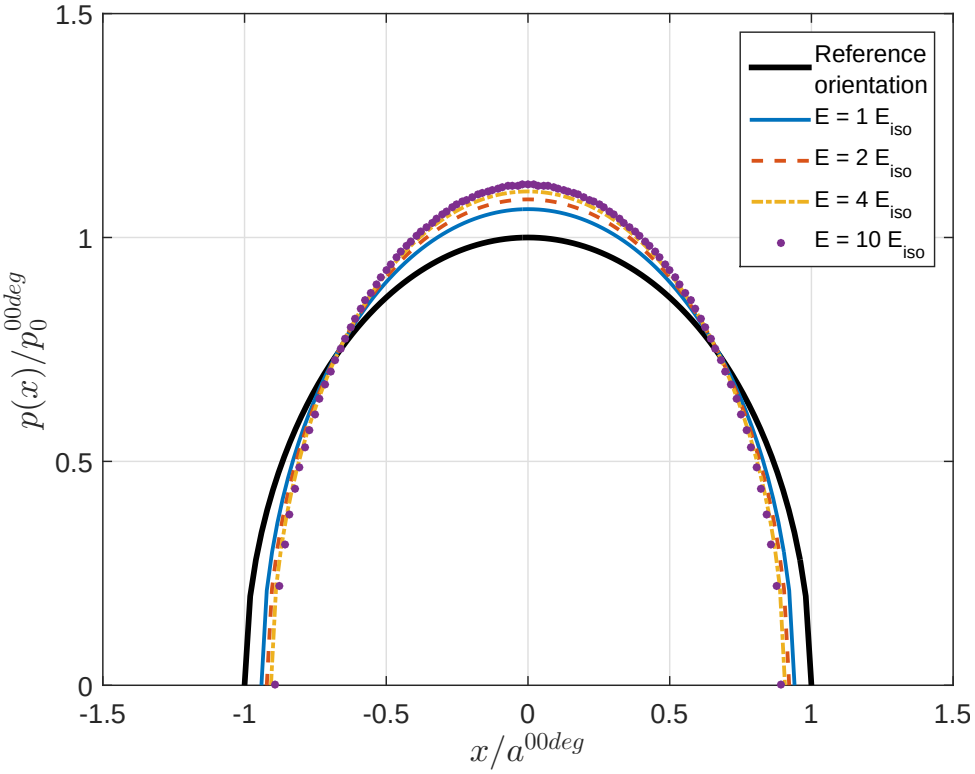

Figure 3.11: Contact pressure for the orientation 45° rotated about the x axis ($\phi_1 = 0°$, $\phi_2 = 45°$ and $\phi_3 = 0°$) for different stiffness of the isotropic body pressed onto the CMSX-4 cylinder.

the maximum variation in contact peak pressure increases by 13% (at the orientation $\phi_1 = 0°$, $\phi_2 = 45°$, $\phi_3 = 0°$) with respect to the reference orientation when the isotropic body is rigid. The variation in contact peak pressure with the elastic stiffness multiplier, n, of the isotropic body is shown in Figure 3.12. The variation in contact pressure for a CMSX-4 pad pressed onto a rigid flat body is still smaller than the variation of 40% in §2.3.3, but this difference is now only due to the different properties of the materials used in the two problems.

The variations in contact peak pressure due to crystal orientation for the contact between CMSX-4 cylindrical pads and RR1000 flat specimens are significantly smaller than it was expected based on the variation of fretting fatigue lives in the MACE tests. When taking into account the 20° tolerance of the principal direction $\langle 010 \rangle$ in the manufacturing of the pads, the variation in peak contact pressure is less than 3.5%. Analytical calculations of contact peak pressure were carried out with the high temperature material properties, while the fretting fatigue tests presented in this chapter were carried out at room temperature. However, the difference in the elastic stiffness at room temperature and 680°C is not the reason why these results do not correlate. Although the isotropic material becomes more compliant at high temperatures

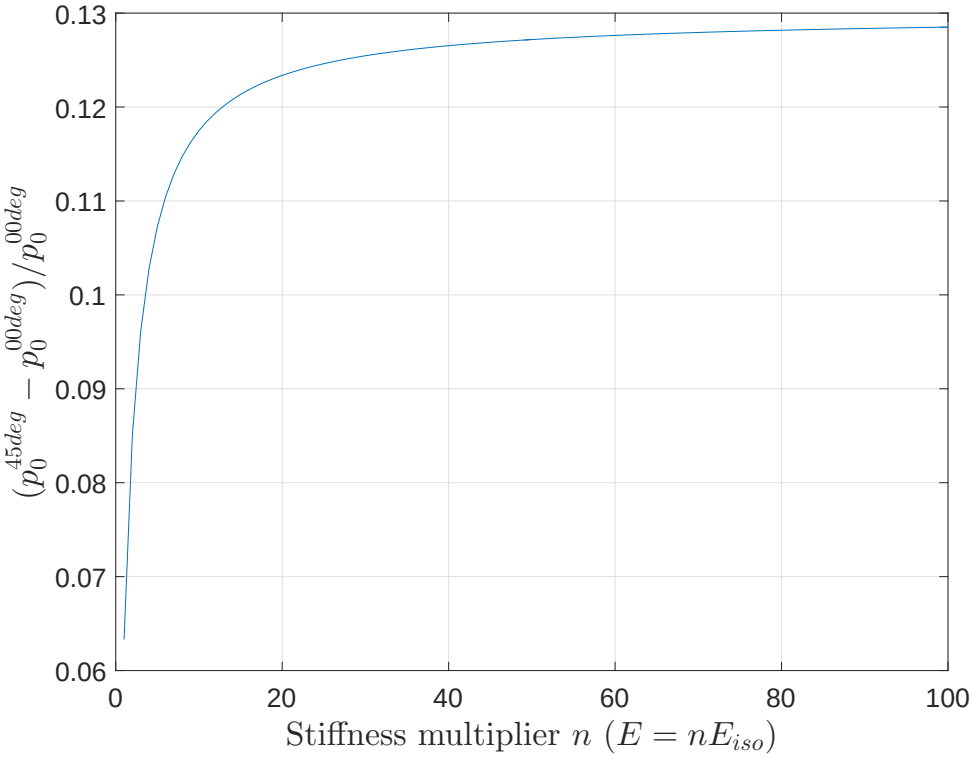

Figure 3.12: Contact pressure for the orientation 45° rotated about the x axis ($\phi_1 = 0°$, $\phi_2 = 45°$ and $\phi_3 = 0°$) for different stiffness of the isotropic body pressed onto the CMSX-4 cylinder.

and, as shown in Figure 3.12, this will have some effect on the maximum variation of contact peak pressure, the single-crystal also become more compliant and the variation in peak stress is expected to be approximately the same. In fact, the maximum peak stress at room temperature varies by up to 3.4%, when taking into account the 20° tolerance.

The results obtained in this chapter indicate that only a small variation in the contact pressure occurs in a Hertzian contact between polycrystalline and single-crystal nickel alloys of different crystal orientations. The normal contact pressure does not provide the full picture of the impact of crystal orientation on the fretting fatigue life of a contacting isotropic body. It is important to note that the shear tractions play an important role in the state of stress near the contact edge and, hence, in the crack initiation and small crack propagation. The stresses near the contact edge are investigated via finite element method in chapter 4. The shear stresses will be directly dependent on the coefficient of friction at the contact interface, and an attempt to investigate the change in friction due to crystal orientation is presented in chapter 5. Although the effect of the crystal orientation on the contact stresses is expected to be of the same order of magnitude as the variations in contact pressure presented in this chapter, the analysis of the fretting stresses is

important for a comparison with the experimental results. Even if the change in stress is not as high as expected, variation in crystal orientation might explain a larger scatter in experiments with single-crystal pads than with polycrystalline pads. The MACE tests data used in this chapter is limited and new experimental results are also presented in the next chapter. The new results will then be compared with the variation in the stresses near the contact edge for different orientations.

Chapter 4

Fretting fatigue of nickel superalloys at high temperature

Fretting fatigue experiments at high temperature were conducted and the results are presented in this chapter. All tests presented have a 'Hertzian' contact and the impact of crystallographic orientation of single-crystal pads is investigated. An investigation on the impact of different test frequencies is also carried out for tests with similar isotropic pads. The experimental procedure and set-up are described in §4.1. The analysis of the contact tractions as a function of crystal orientation presented in chapter 3 is extended to the frictional case. The partial slip problem for single-crystals is analysed using finite element analysis. The results of the contact stress analysis are also compared with the fretting fatigue experimental lives using an area averaging approach to take into account the high stress concentrations. Finally, some preliminary three-dimensional analysis of the partial slip problem is carried out to investigate the out-of-plane shear tractions for certain orientations of the single-crystal pads.

4.1 Fretting fatigue tests

The methods and procedure of used in the fretting fatigue tests at high temperature are described in this section. The fretting fatigue results are presented and an initial analysis is carried out, but further analyses are presented in the following sections. The tests presented here are part of a larger SILOET II test programme in collaboration with Rolls-Royce plc and they were carried

out with different materials and pad geometries. Only the pads with cylindrical face, 'Hertzian' contact, are presented here. They are used to investigate the impact of crystal orientation on the fretting fatigue life. The reason the focus of this work is on the cylindrical pads is that the smooth convex surface in contact results in well-known contact pressure and stress profiles. From the experimental point of view, Hertzian contacts are also less sensitive to misalignments between the pad and specimens. The experimental tests were carried out by Dr. Paynter at the University of Oxford, but the analyses of the results were part of the scope of this thesis, particularly that of single-crystal and Hertzian pads. The results of the test programme are described in detail in [Paynter and Fleury, 2013].

4.1.1 Experimental method

High temperature fretting rigs have been developed in the past two decades to reproduce the fretting conditions in the blade to disc assembly of gas turbines. Although not as high as the combustion temperatures, the temperature at the root of the blades, where multiple contact points between blades and the disc occur, are still very high for metallic alloys. Their properties show significant change compared to room temperature and hence it is important to conduct tests at similar temperatures. The experimental work was carried out on a rig at the University of Oxford custom built for high temperature fretting fatigue tests. A picture of the experimental is shown in Figure 4.1. The rig is equipped with three hydraulic actuators (each 100 kN in capacity): two that pull on each end of the fatigue specimen and a third that applies force to clamp the pads to the specimen. The furnace is of a compact design, has PID control and can be operated up to 900°C. The temperature feedback is via thermocouple embedded in the pad holder; this has been calibrated against measurements where thermocouples were embedded in a lightly loaded fatigue specimen and at the contact face of the pads.

A schematic representation of the rig and the loads applied during the test, as well as of the contact between the specimen and pads, are presented in Figure 4.2a. The pad geometry and its crystallographic orientation are illustrated in Figure 3.4b. The geometry and manufacturing tolerance of the crystal orientation are similar to the ones used in the MACE tests presented in chapter 3. The same 20° tolerance of deviation between the $\langle 010 \rangle$ crystal direction and the

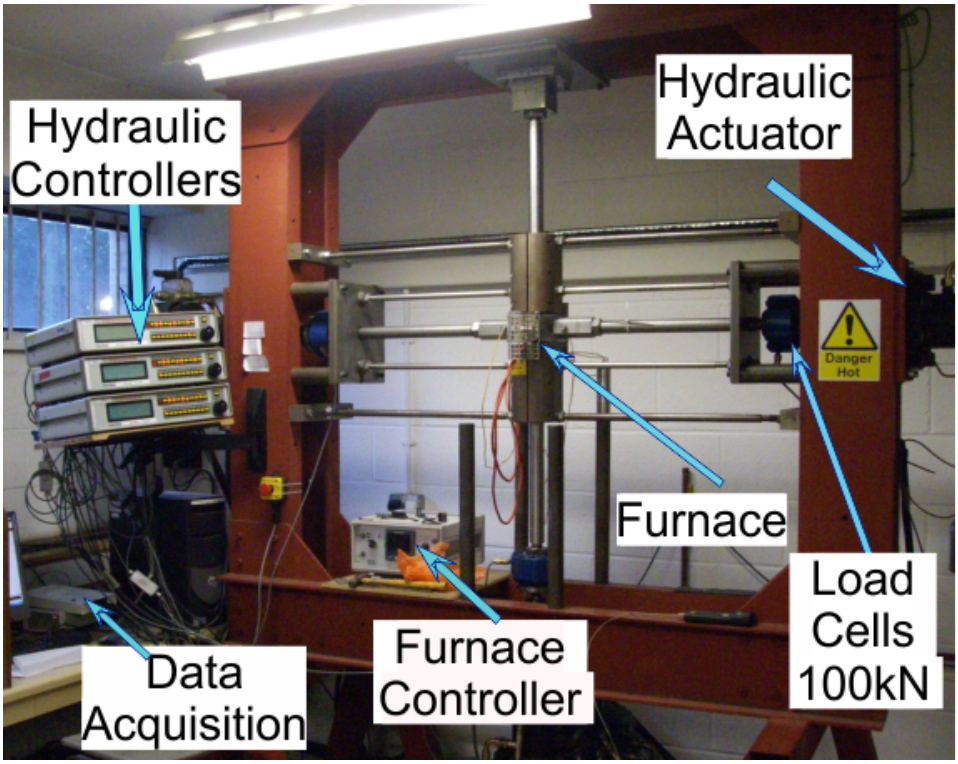

Figure 4.1: Picture of the fretting fatigue rig for high temperature tests.

axis of the longest dimension of the pad (y axis in Figure 3.4b) applies here. The orientation of the principal directions in the plane of contact were measured beforehand for each tests. It was assured that both pads in each test had similar secondary crystal principal orientations and, whenever possible, that they were manufactured from the same casting slab, so that the orientations were identical. A non-destructive[1] indentation technique was used in the measurements of crystallographic directions. Note that, the procedure employed here to measure the secondary crystal principal direction before each test is an attempt to eliminate the uncertainty caused by pads with different orientation on each side of the specimen in the MACE test programme. By using pads with similar orientation, it is assured that both sides of the specimen have similar contact tractions and the probability of cracks originating from each side is the same.

The fatigue specimens are made of the polycrystalline Ni-based alloy, RR1000, representing the hub of the turbine disc, and the pads are made of a single-crystal alloy, CMSX-4, representing the blade roots. Tests with pads made of RR1000 alloy, same material as the specimen, were also conducted for comparison with the single-crystal results. All tests were conducted at

[1]By non-destructive it is meant that the pads can still be used afterwards, since the indentation is made far from the contacting face. Indentation methods generally cause damage, but are not necessarily destructive.

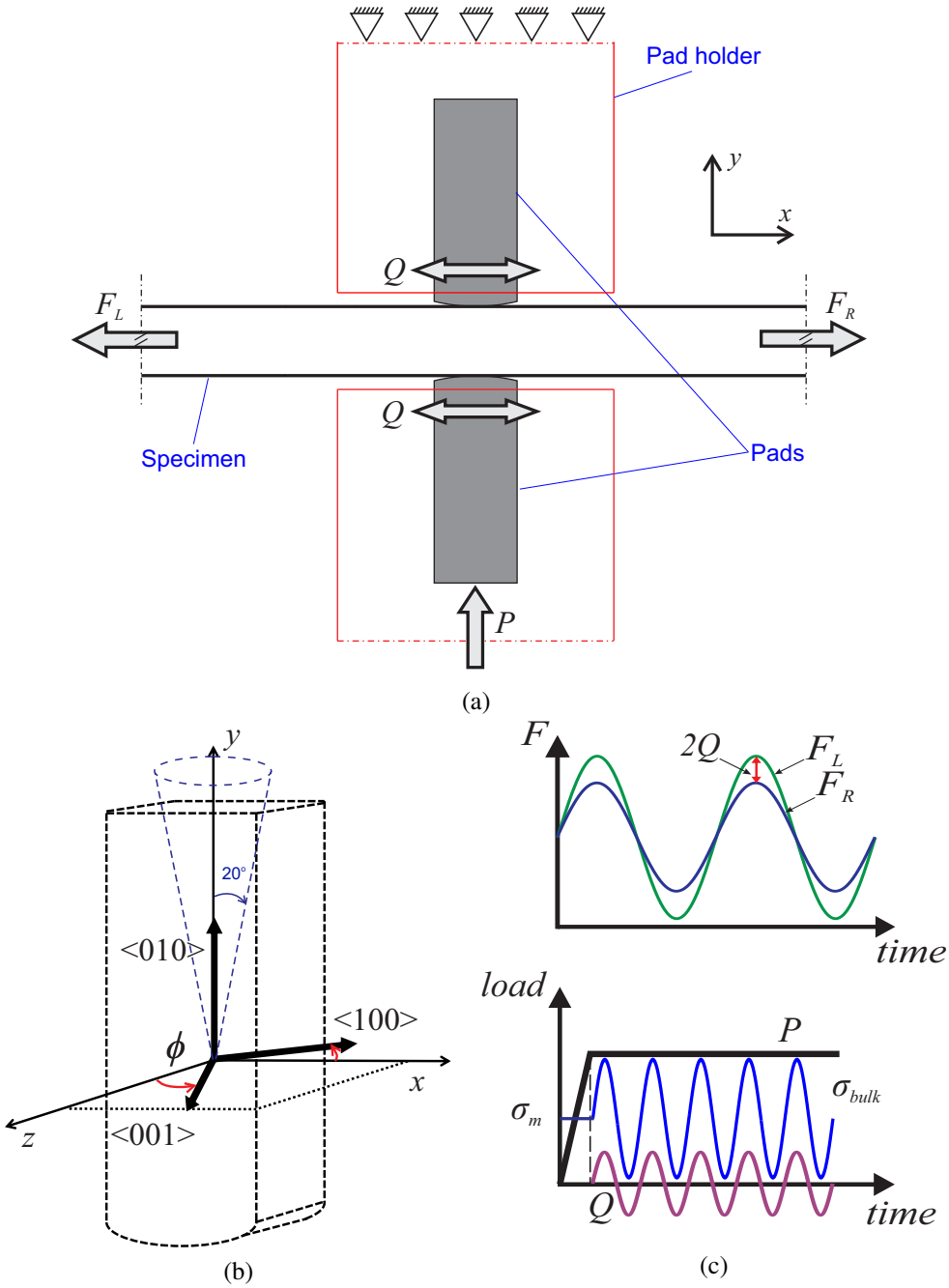

Figure 4.2: (a) Schematic representation of the fretting fatigue hot rig; (b) Schematic representation of the single-crystal pad's geometry and crystal orientation; (c) Fretting fatigue load history and definition of shear load by the difference of applied force amplitude.

an elevated temperature of 680°C. The polycrystalline specimen has 10×10 mm cross-section in the centre and it is long enough so that it can be attached to hydraulic actuator outside the furnace. The pads have a 12 mm width in the z direction and a radius $R = 100$ mm in the cylindrical face. The pad is wider than the specimen in the z axis to avoid alignment issues in that direction and significant edge effects on the specimen, which would happen if the edge of the

pad was contacting the surface of the specimen. The pad protrudes 2 mm out of the pad holder. The shear force is transmitted to the pad at the contact interface and this force times the distance of the protrusion will induce a moment load which will induce a small rotation of the pad at the contact. Hence, the protrusion was reduced as much as possible to avoid rotation of the pad.

The normal contact force, $P = 17.7$ kN, was applied by the bottom actuator and kept constant throughout the test and for all tests. Special care was taken to assure the specimen was not bent after applying the normal force. The fatigue load was obtained by in-phase tension applied to the two ends of the specimen by the left and right actuators. However, the amplitudes of the left and right loads are different, such that, the difference in amplitude induces shear tractions at the contact interface. All partial slip tests were conducted at a constant Q/P ratio of 0.246; this value was chosen to assure partial slip based on an initial estimate value of 0.35 for the coefficient of friction advised by Rolls-Royce plc. Fatigue cyclic loading in the specimen results from the mean of the left and right actuator loads and, hence, the resultant shear force is also in-phase with the fatigue loading. The fatigue load range, σ_{rng}, at the centre of the specimen is given by the average of the tension applied at each end of the specimen. The load ratio during the tests, i.e. the ratio between the minimum and maximum applied tension in the load cycle, $R_\sigma = \sigma_{min}/\sigma_{max}$, is $R_\sigma = 0.2$. The history of the loading and the definition of the shear load, Q, by the difference of the applied load are shown in Figure 4.2c.

4.1.2 Fretting fatigue results

Initial tests were conducted with the RR1000 pads at a higher frequency, 3Hz. Full sliding tests at similar frequency were also conducted and they gave an experimental estimate of the coefficient of friction between 0.5 and 0.6. Nickel alloys form an oxide layer at high temperatures, which has a lower coefficient of friction than the base material. It is believed that the oxides did not have sufficient time to form and so the frequency of the tests was reduced to 0.25 Hz. At lower frequencies, an increase in fatigue lives was observed for tests subjected to the same load range. This may be because at a lower frequency there is more time for oxide growth, resulting in reduced friction and lower stress at the contact edge. In the laboratory tests, one complete load cycle represents an event that happens approximately once per flight in the actual engine,

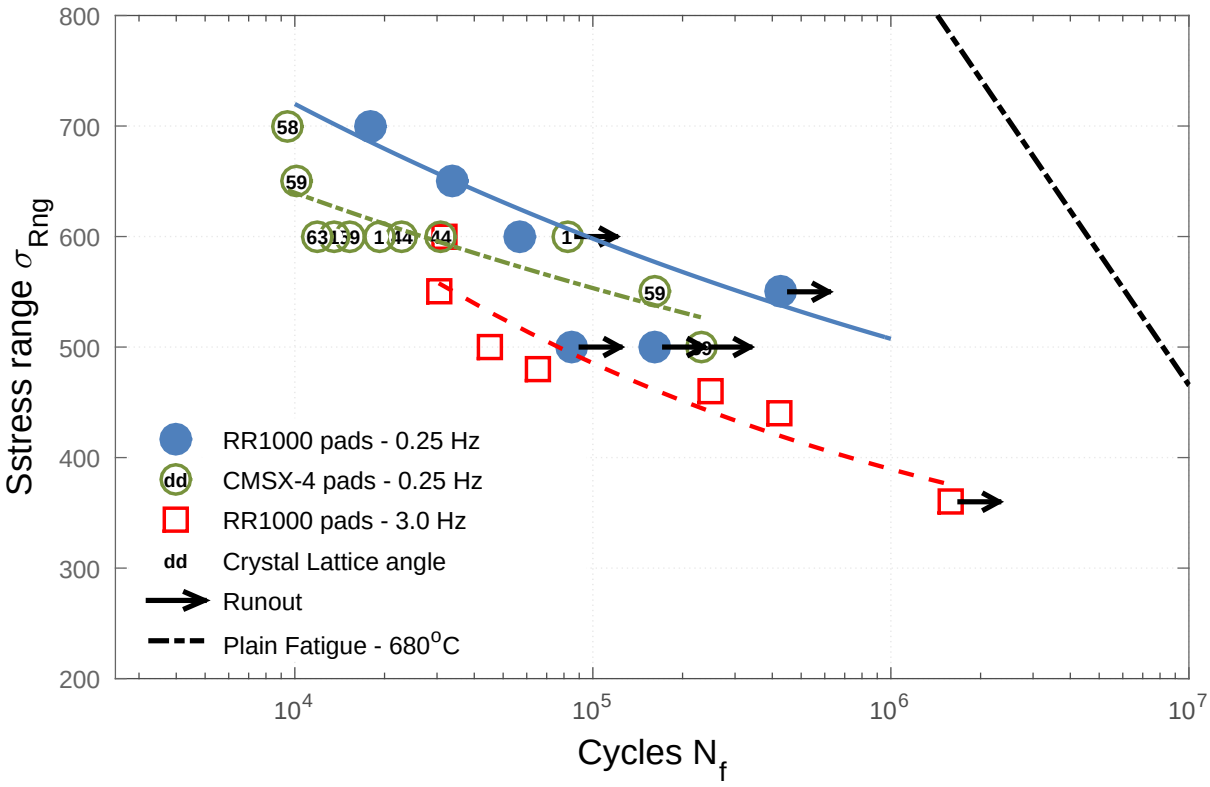

Figure 4.3: Experimental results for fretting fatigue of Ni-based superalloys at high temperature.

i.e. loading and unloading occurs during start-up/shut down of the engine, although changes in the flight regime may also affect the contact conditions. Thus, neither tests are entirely representative of true service conditions, where fretting occurs at a much lower frequency. It is desirable, however, to allow more time for oxide growth, and, in this sense, the lower frequency tests are more representative. The effect of test frequency on fretting energy wear rate, i.e. the wear rate as a function of the dissipated fretting energy, of titanium alloys in gross slip regime has been reported by Van Peteghem et al. [2011]. The longer oxidation time at lower frequencies has been associated with an increase of the oxide layer which is later more easily removed from the interface. However, the amount of wear in partial slip is very small and the only effect of this oxide layer on the tests is the lower coefficient of friction at the contact interface.

The experimental results are summarised in Figure 4.3. Tests with single-crystal pad pairs were carried out with matched crystallographic orientations, so that the contact stresses on both sides of the specimen would be the same. The numbers inside the green circles for tests with single-crystal pads give the orientation of secondary principal crystallographic direction $\langle 100 \rangle$ with respect to the x axis. Pads with a crystal orientation of approximately $\phi_1 = 60^\circ$

were used in a variety of stress ranges to be comparable with polycrystalline pad tests. The number of cycles to failure, N_f, is plotted against the bulk stress range, σ_{rng}, at the centre of the specimen. Overall, tests with CMSX-4 pads presented shorter lives when compared to tests with RR1000 pads under the same conditions of load and frequency. This is believed to be due to higher coefficient of friction of the RR1000/CMSX-4 pair when compared to the RR1000/RR1000 pair. Tests with different crystallographic orientation pads have been carried out at the same load range of 600 MPa to investigate the correlation of fretting fatigue life with crystal orientation. A small variation in the results with different crystal orientation was observed (see green circles at 600 MPa in Figure 4.3). Possible explanations for this variation in life due to crystal orientation are covered in following sections. The trend lines of the three sets of tests conducted are presented to illustrate the variation in life between them. This variation is believed to be largely due to different coefficients of friction. Note that all fretting fatigue results presented shorter lives when compared with the plain fatigue data at 680°C (dash-dotted black line). These results are correlated with plain fatigue data of the RR1000 alloy latter on in this chapter, when a better correlation between fretting fatigue and plain fatigue based on the stresses near the contact edge is proposed.

4.2 Two-dimensional analysis of fretting stresses

4.2.1 Finite element model

A two-dimensional finite element model is created in ABAQUS/CAE 6.10 to i) study how different stress ranges and crystal orientations of single-crystal pads affect the region of high stress concentration at the trailing edge of the contact; and ii) obtain a better correlation between fretting fatigue and plain fatigue data by using the averaged stress near the contact edge as a correlation parameter. The geometry of the finite element model is built according to the dimensions of the experiments described earlier and plane strain condition is assumed. For orientations with symmetry in the z axis ($\phi_1 = 0^\circ$ and $\phi_1 = 45^\circ$), the plane strain assumption for orthotropic pads is no different from isotropic pads. For other orientations, displacements in the z direction occur and the problem is in fact in a state of *generalised* plane strain. However, it

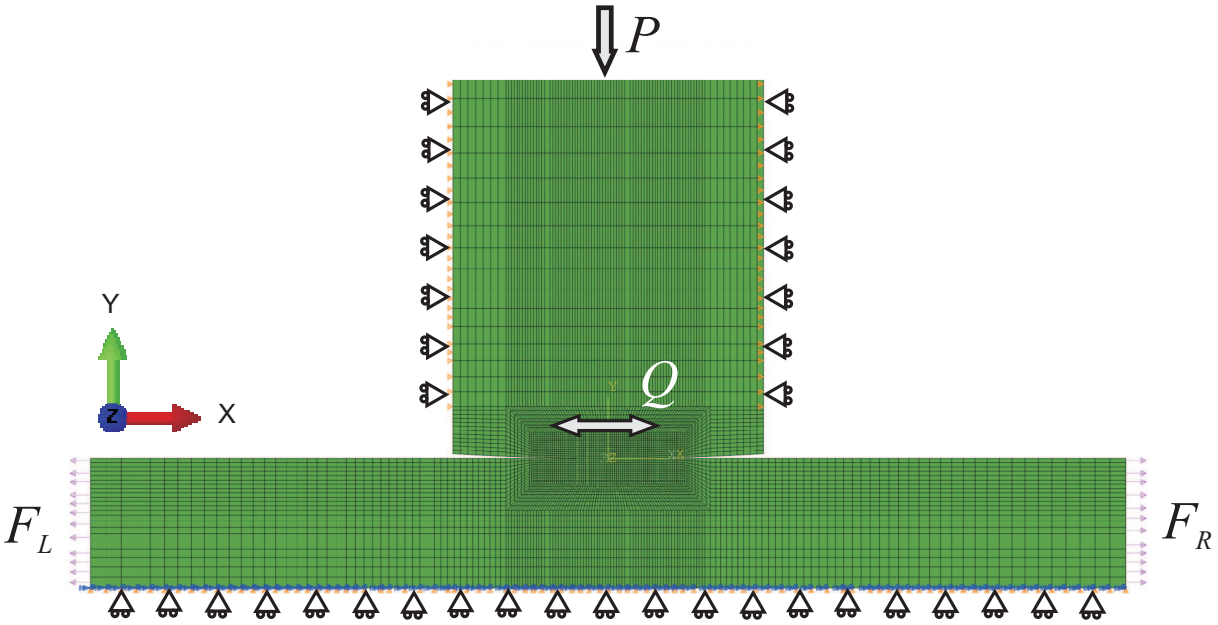

Figure 4.4: Mesh and boundary conditions used in the partial slip fretting stress analyses.

has been verified in three-dimensional analysis that the stress σ_{xx}, which is being used in our analysis, remains approximately constant along the z axis for those orientations and the strain component ε_{zz} is about one-tenth of the other strain components. Hence, whilst the solution is not, strictly speaking, plane strain, a two-dimensional approximation is still appropriate. The symmetry of the test is used to model only half of the polycrystalline specimen and the dimensions are set as 5×40 mm. The vertical dimension of the pad is chosen to be long enough so that the boundary conditions at the top of the pad do not affect the pressure distribution i.e., ten times the contact semi-width. The cylindrical single-crystal pad has radius $R = 100$ mm and width of 12 mm. The 2 mm protrusion of the pad with respect to its support is also taken into account when applying the constraint boundary conditions in the x direction. The properties of the single-crystal CMSX-4 alloy are input in the analysis via the 21 independent variables of the elastic stiffness matrix. Initially, the crystal's principal directions are aligned with the Cartesian coordinate system. Euler rotations, as described in §3.1.2, are applied to obtain the transformed elastic constants for different crystal orientations, including out-of-plane rotations, which cannot be made by using ABAQUS' material rotation tool.

The geometry and mesh used are illustrated in Figure 4.4. The loading of the finite element model follows the same procedure as the experimental tests. First, a mean load was applied to the specimen and only then the two parts are put into contact with displacement control. The

normal load, P, is applied subsequently. Once the contact is established, the sinusoidal fatigue loads, F_L and F_R, are introduced with different amplitudes, such that the difference between them induces the shear load, Q, at the contact interface. As long as Q is smaller than μP, with μ being the average coefficient of friction, the contact remains in partial slip and no rigid body sliding occurs. Two complete cycles were used in the analysis which has been shown to be sufficient to simulate the steady state behaviour of the solution.

A two-dimensional plane strain linear element CPE4R of size $h_e = 20$ μm, two times larger than the nominal grain size of the RR1000 alloy, is used near the contact region. A convergence study with a large model, approximating to a half-plane condition, has shown that at this level of mesh refinement near the contact an error of approximately 3% is achieved when compared to the analytical solution in terms of maximum stress σ_{xx} at the edge of the contact. An error of less than 2% is found in the convergence of the numerical solution itself. Due to the large number of simulations involved in the analysis, this level of accuracy seems sufficient. In addition, the convergence analysis used a single point parameter, the peak stress p_0, and the discretisation near the contact was the main source of error. Since it is used an area averaging approach in the analysis presented next, it is expected that the level of accuracy in the numerical model was in effect higher.

4.2.2 Area averaging method

Stress based critical volume (or area) methods for fatigue thresholds have been widely used in the past to assess the life of notched components. Similarities between notch problems and fretting fatigue problems in terms of stress concentration and stress gradients can lead to the application of such methods also to fretting fatigue problems [Nowell and Dini, 2003]. Relevant work combining the method of critical distance and fretting has been carried out in recent years [Araújo et al., 2008; Ferré et al., 2013]. Moreover, Taylor has shown in his unified theoretical model that the point, line and area methods can be applied to notches without loss of accuracy [Taylor, 1999]. One of the most common approaches in industrial designs is the point method, due to its simplicity of taking the value of the stress at a single point near the notch. However, it is not simple to combine this method with finite element analysis, since the discrete nature of

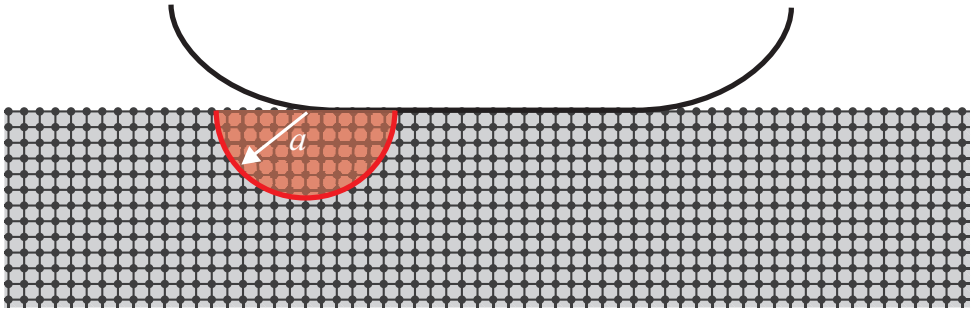

Figure 4.5: Area averaging method under the contact edge, using the finite element gauss points.

the finite element solution would probably require an interpolation of the stresses to the critical point, compromising the quality of the results. Following this line of thought, the area averaging method can easily be implemented by using the integration points inside the area of radius a_0 to get the averaged solution (Figure 4.5). The quality of the solution will depend, however, on the number of integration points in that area.

It is well known that the only non-zero stress component at the edge of the contact is σ_{xx}. For points deeper inside the body, other components of the stress tensor have a non-zero value as well. However, the magnitude of the remaining stresses is small when compared to the magnitude of σ_{xx} and they will, therefore, be neglected in the analysis that follows. Using this approach, it is assumed that cracks would not initiate if the averaged variation of stress $\Delta\sigma_{xx}$ is less than the plain fatigue limit. The variation $\Delta\sigma_{xx}$ is defined as the difference of stress σ_{xx} at the times for which $Q = Q_{max}$ and $Q = Q_{min}$. One way of defining the size of the process zone is by using the El Haddad's length parameter [El Haddad et al., 1978], equation (4.1), where ΔK_o is the long crack threshold stress intensity factor range and $\Delta\sigma_{fl}$ is the plain fatigue limit of an uncracked material.

$$a_0 = \frac{1}{\pi}\left(\frac{\Delta K_o}{\Delta\sigma_{fl}}\right)^2 \tag{4.1}$$

El Haddad's parameter can be thought of conceptually as a material property, since ΔK_o and $\Delta\sigma_{fl}$ are normally considered as such. Nickel based alloys do not have a clear fatigue limit and the fatigue limit was defined as that for a life of 10^7 cycles in a plain fatigue test at high temperature. The long crack threshold intensity factor range was defined as the intensity factor range for a crack growth of 5×10^{-8} m/cycle. Using the material properties provided by Rolls-Royce plc, the radius found for the material properties of the RR1000 alloy was $a_0 = 71.9\ \mu$m.

The characteristic length a_0 was used in the area averaging method, resulting in an averaging over 20 integration points for the given mesh parameters. Changes to the averaging method could be achieved by adding weight functions that take into account the stress concentration in the process zone. Alternatives to the El Haddad's parameter are often determined by the material's micro-structure, e.g. the grain size. One of these models has been introduced by Ritchie et al. [1973] and it assumes that the critical length is twice the grain size of the material. The nominal grain size of the RR1000 superalloy is approximately 10μm and, hence, the critical distance given by Ritchie's model would be 20μm. Note that the critical distance is half the length a_0 and, using the El Haddad's parameter, the critical distance is about 36μm.

4.2.3 Fretting stresses as a function of crystal orientation

Two sets of analysis are carried out with single-crystal pads. The first involves varying two parameters: the crystallographic orientation and the coefficient of friction at a constant bulk stress range. The second investigates the stresses for different bulk stress ranges applied. The latter analysis is carried out only for the orientation of $\phi_1 = 30^\circ$, since all tests conducted at a different stress range had a similar mirrored crystallographic orientation ($\phi_1 = 60^\circ$). Note that when $\phi_2 = \phi_3 = 0$ the principal direction $\langle 010 \rangle$ is parallel to the longest axis of the pad and in this case ϕ_1 gives the direction of the secondary principal directions in the x-z plane. The variation of the crystallographic orientation is achieved by transformation of the elastic stiffness matrix in a Matlab subroutine, as described in §3.1.2. The finite element input file (.inp) is then modified to include the 21 transformed components of the elastic stiffness matrix of an anisotropic elastic model.

The shear tractions in a complete fretting fatigue cycle obtained from finite element simulations are presented in Figure 4.6. In the idealised contact of two half-planes, the shear tractions are given by the Cattaneo-Mindlin solution. Here, the shear traction distribution differ from the analytical solution, although slightly, due to the finite dimensions of the specimen and the pad, and also due to the orthotropic properties of the single-crystal. The oscillation near the right hand edge of the contact is due to a small local rigid body rotation of the pad as a result of the loads applied and boundary conditions. The local rotation of the pad changes the contact

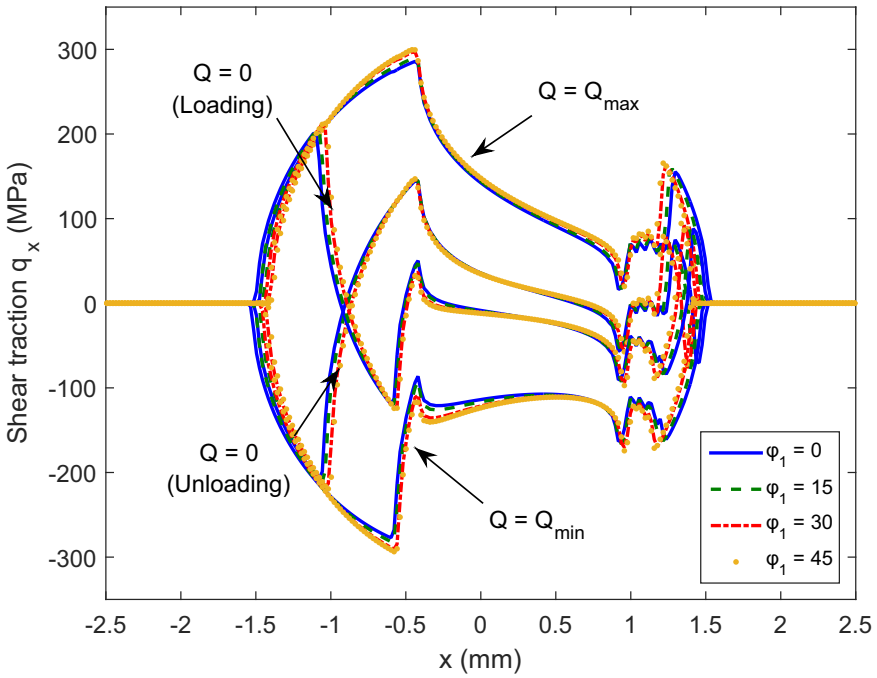

Figure 4.6: Shear tractions during one cycle of shear loading, Q, for different crystal orientations at a load range of 600 MPa and $\mu = 0.4$.

.

zone and induces some initial shear to 'lock-in' in the first cycle, which is then carried out in the steady state of the stresses. The rotation is due to a resultant moment acting on the pad as a result of the shear load in the contact interface and displacement constraints on the sides of the specimen. Note that, in the Cattaneo-Mindlin solution there is no resultant moment and no rotation in the contact zone. The shear traction falls to zero near the edge, as expected for smooth convex surfaces, and a small change in the shear traction occurs with the orientation of the crystal.

There is a small increase in the maximum shear traction with the crystal orientation, where it is minimum for $\phi_1 = 0^\circ$ and maximum for $\phi_1 = 45^\circ$ (see curves for $Q = Q_{max}$ in Figure 4.6). The contact size also changes with the orientation and the contact size is smallest for the crystal orientation $\phi_1 = 45^\circ$. However, although the shear tractions fall smoothly to zero at the contact edges, the stress component parallel to the fatigue load direction on the specimen, σ_{xx}, is maximum at that point. The variation of the direct stress $\Delta\sigma_{xx}$ is the main driver for the crack propagation and it is used here to investigate the impact of different crystal orientations on the fatigue life. Although there is a region under the contact edge that has, in fact, a multiaxial state

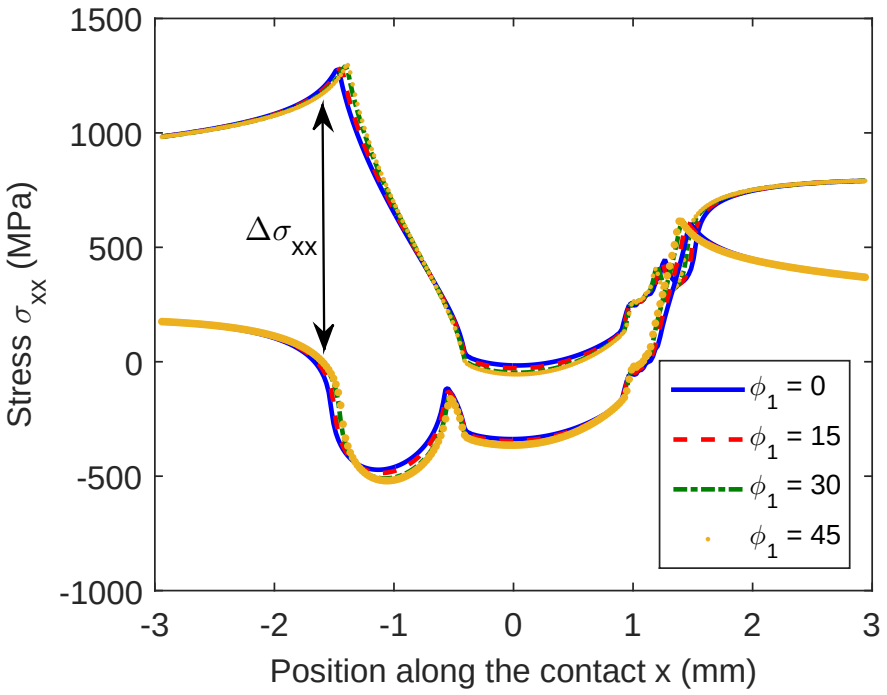

Figure 4.7: Stress σ_{xx} along the contact interface for different crystal orientations at maximum and minimum shear load instants, load range of 600 MPa and $\mu = 0.4$.

of stress, the component σ_{xx} is the highest component of stress and an approximation is used here by neglecting the other components near the edge of contact in the correlation of stresses and fretting fatigue life.

The stress σ_{xx} at the surface of the specimen at the load instants $Q = Q_{max}$ and $Q = Q_{min}$ are presented in Figure 4.7. Note that the maximum stress at the load instant $Q = Q_{max}$ is just above the material's yield limit, but only in a very small zone near the edge of the contact and at the surface of the specimen. A sharp drop in the stress occurs along the y direction inwards into the specimen and any plastic strain that may occur are restricted to zones very close to the surface of the specimen. The stress range, $\Delta\sigma_{xx}$, during a complete fretting cycle is given by the subtraction of the two curves. The curves showing the distribution of $\Delta\sigma_{xx}$ along the contact interface for four different values of ϕ_1 (i.e. a rotation about the contact's normal direction) are shown in Figure 4.8. Again, the stress seems to reach a maximum value at the orientation $\phi_1 = 45°$. It is also clear from these results that one must change the centre of the averaging area for each crystallographic orientation, since the location of the contact edge also changes slightly.

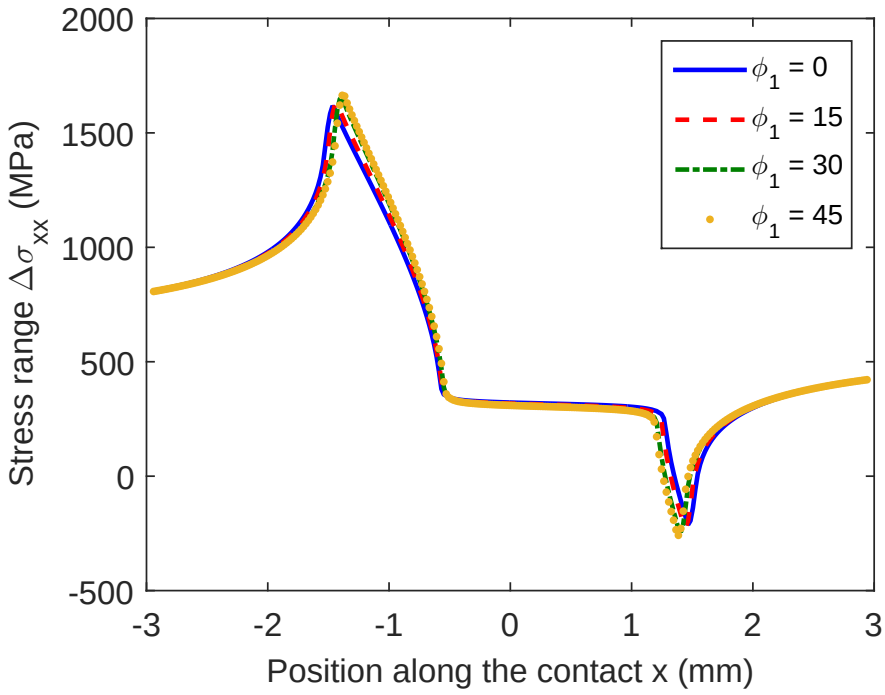

Figure 4.8: Stress variation $\Delta\sigma_{xx}$ along the contact interface for different crystal orientations, load range of 600 MPa and $\mu = 0.4$.

The relative change in stress with respect to the reference crystallographic orientation is shown in Figure 4.9. The maximum variation in stress due to a rotation of the crystal about the normal direction is about 1.5% at $\phi_1 = 45°$. This is of the same order of magnitude as the variation of the normal pressure found in the frictionless analysis of chapter 3. Furthermore, any change in coefficient of friction seems to affect equally the contact of pads with different crystallographic orientations (Figure 4.10). If the coefficient of friction varies with the crystallographic orientation, which is not yet clear, but has been reported by other authors under certain conditions [Huang et al., 2009], there is likely to be a greater influence of orientation on the overall change in stresses. An increase of 0.05 in the coefficient of friction can lead to a stress range $\Delta\sigma_{xx}$ 4% higher. If the coefficient of friction increase is combined with the crystal orientation variation, i.e. if the crystal orientation with highest stress variation, $\phi_1 = 45°$, also has an increase in the coefficient of friction of 0.05, then the maximum variation in the stress range, $\Delta\sigma_{xx}$, could go up to 7% with respect to the reference orientation.

Note that the stress (or strain) variation near the edge of contact will accelerate crack initiation and, consequently, reduce the fatigue life of the component. Therefore, if the coefficient of

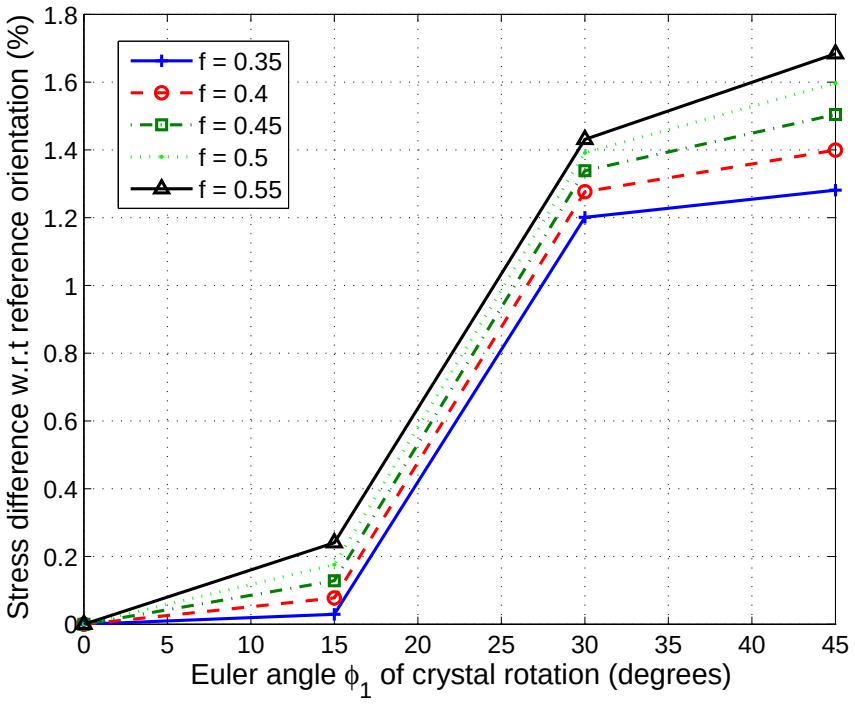

Figure 4.9: Relative difference in stress range $\Delta\sigma_{xx}$ as a function of crystallographic orientation.

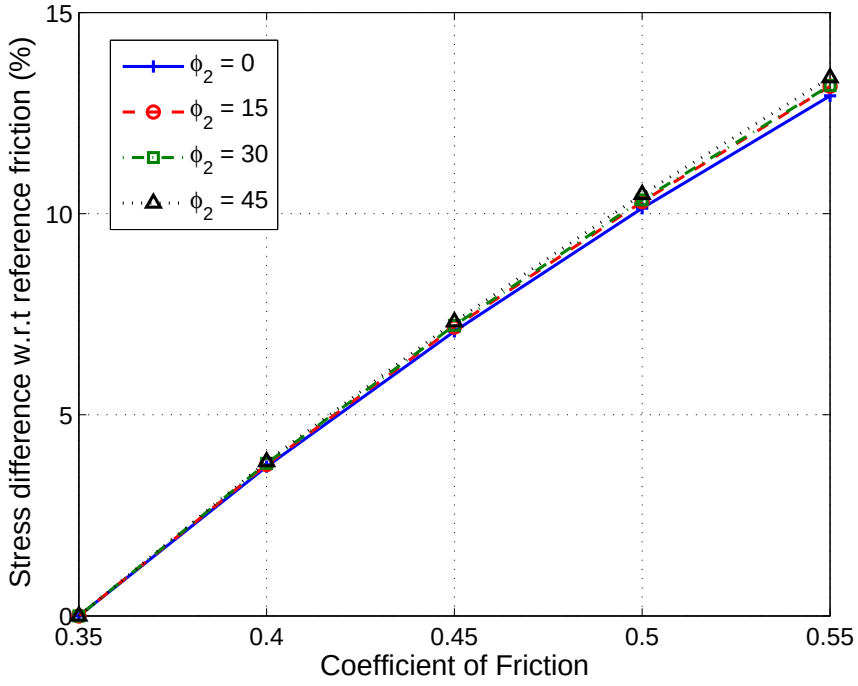

Figure 4.10: Relative difference in stress range $\Delta\sigma_{xx}$ as a function of the coefficient of friction.

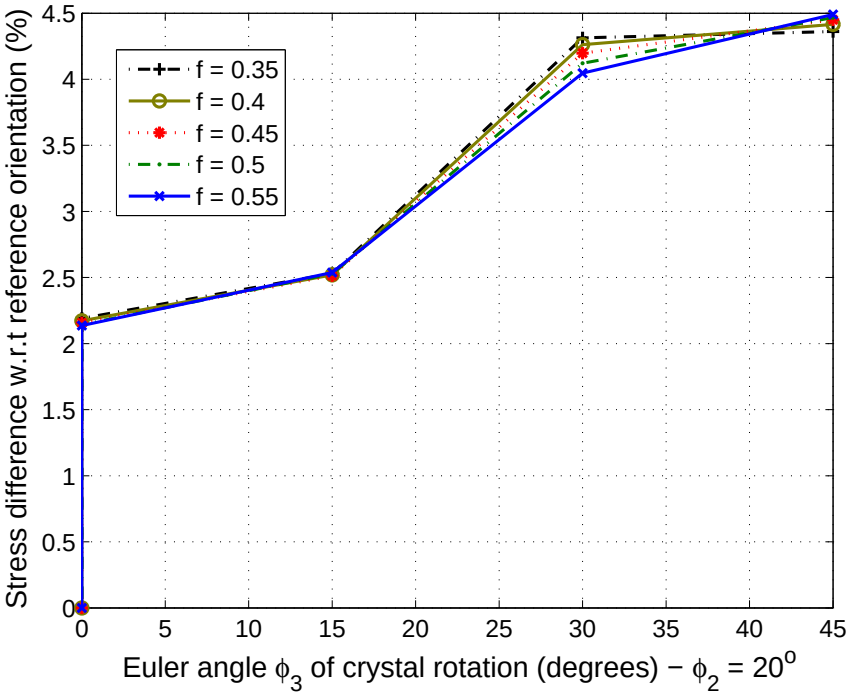

Figure 4.11: Relative difference in stress range $\Delta\sigma_{xx}$ as a function of crystallographic orientation. Varying ϕ_3 with constant $\phi_1 = 0°$, $\phi_2 = 20°$.

friction varies with the crystal orientation of the contacting single-crystal pad, the fatigue life of the polycrystalline specimen will vary as well. In fact, the fatigue life will not only depend on the variation but, in a multiaxial problem, it may also depend on the load path of the problem as well. In that case, multiaxial energy dissipation fatigue criterion may predict the fatigue life with good accuracy [Korsunsky et al., 2007]. Although the state of stress is multiaxial in this problem, at the edge of the contact the only non-zero component of stress is σ_{xx}. Furthermore, because the loading applied is periodic (sinusoidal), it is reasonable to work in terms of the variation $\Delta\sigma_{xx}$ only.

The most severe case in the analytical analysis of §3.3.2 is for a crystal orientation $\phi_1 = 0°$ and $\phi_2 = 45°$ (rotation about the x axis). However, it is known from the manufacturing specifications that the maximum deviation of the principal direction $\langle 010 \rangle$ with respect to the y axis is $20°$, as it was shown in §4.1.1. If the direction $\langle 010 \rangle$ is inclined $20°$ out of the plane of analysis ($\phi_1 = 0$ and $\phi_2 = 20°$) and only then the crystal is rotated about that direction, an increase in stress of up to 2.5% is seen for the orientations of $\phi_3 = 0°$ and $\phi_3 = 15°$ when compared to the case with completely vertical $\langle 010 \rangle$ crystal direction (Figure 4.11). Note that $\phi_2 = 20°$ is

the worst case of misalignment of the crystallographic direction $\langle 010 \rangle$ and if $\phi_1 = 0$, then ϕ_3 is the angle of the secondary principal crystal direction. At angles close to the 45°, the maximum variation in stress $\Delta\sigma_{xx}$ occurs of about 4.5% when compared with the reference orientation (Figure 4.11). Again, the stress variation is of the same order of magnitude found in the frictionless analysis of chapter 3. This can be expected since the partial slip problem can be thought of as a superposition of the sliding solution.

4.2.4 Fretting stresses as a function the applied stress range

The analysis carried out with RR1000 pads has two varying parameters, the coefficient of friction and the applied stress range σ_{rng}. The goal of this study is to obtain the averaged stress near the contact trailing edge for each one of the experimental test conditions. These results will be used later on in the correlation between life and stress. The maximum stress σ_{xx} occurs at the contact trailing edge of contact and at the load instant $Q = Q_{max}$. The variation of stress at that point is used as the fatigue correlation parameter. The variation of stress near the contact edge was obtained for several values of applied stress range and coefficient of friction, using the area averaging method. The results are summarized in Figure 4.12. The variation of the applied stress range, on the other hand, changes the stress almost linearly. The results correlating lives and the obtained stress are shown in §4.3.

The same procedure for the calculation of the averaged stress near the contact edge under different conditions of applied bulk stress and coefficient of friction is carried out for the tests with CMSX-4 pads. Since all tests with CMSX-4 pads under different bulk stress range had an orientation of approximately $\phi_1 = 60°$, only simulations at $\phi_1 = 30°$ (mirrored orientation) are carried out here. The averaged stress variation $\Delta\sigma_{xx}$ as a function of the bulk stress and the coefficient of frictions is presented in Figure 4.13. The range of coefficient of friction used in the numerical simulations is only from $\mu = 0.4$ to $\mu = 0.55$. Note that $\mu = 0.55$ is the stabilised coefficient of friction at gross sliding after a few cycles and $\mu = 0.4$ is the initial estimate of the coefficient of friction for the pair RR1000/CMSX-4. These results are used next in the correlation of the fretting fatigue lives with the averaged stress near the contact edge.

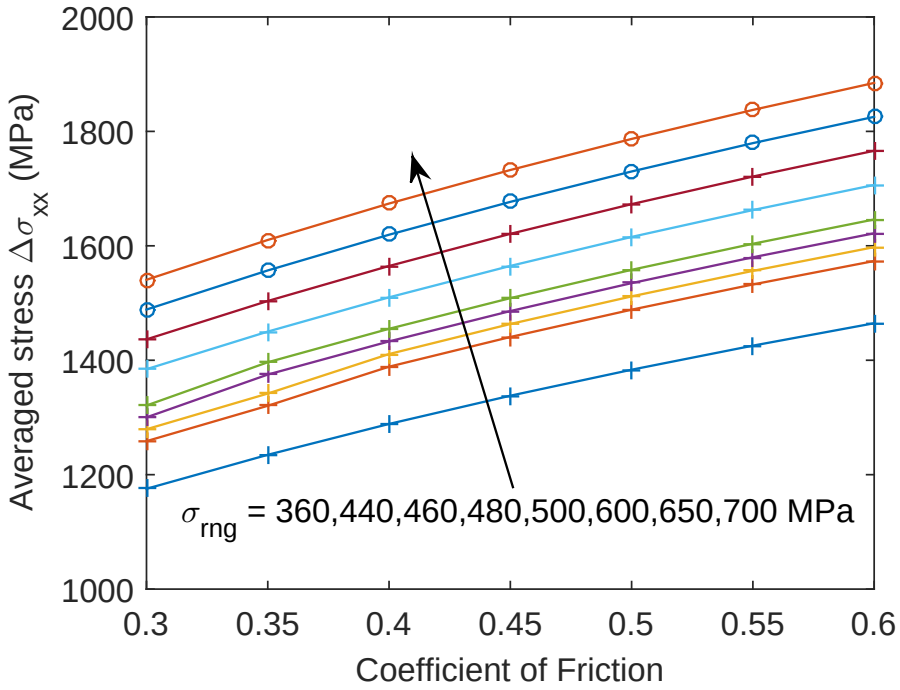

Figure 4.12: Variation of stress range at the edge of the contact as a function of the applied bulk stress range and the coefficient of friction - RR1000 pad

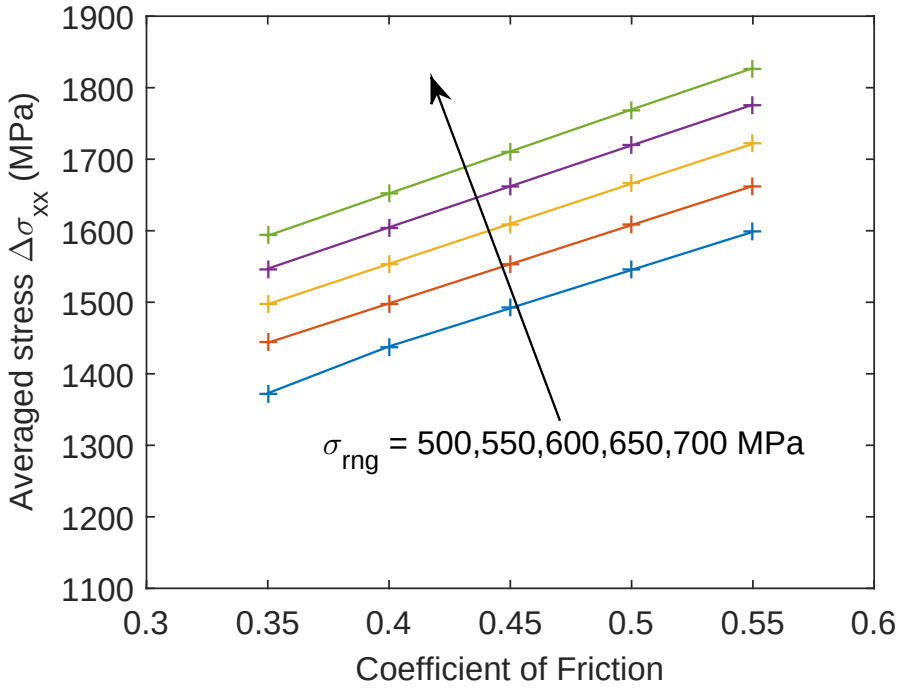

Figure 4.13: Variation of stress range at the edge of the contact as a function of the applied bulk stress range and the coefficient of friction - CMSX-4 pad at $\phi_1 = 30^\circ$

4.3 Correlation of fretting fatigue results

4.3.1 Averaged stress near the contact edge and fretting fatigue life

Using the methodology described and the numerical results presented in the previous sections, the stresses of the experimental partial slip tests are analysed. The plain fatigue data of the RR1000 alloy at the same high temperature (680°C) is used as the reference life of the specimen. Here, it is assumed that fretting fatigue and plain fatigue are somewhat comparable and that, by scaling the stresses correctly, it is possible to get a correlation between both experiments. The initial estimate of coefficient of friction, $\mu = 0.35$, is used to obtain the stresses near the contact trailing edge. The results are shown in Figure 4.14, where $\mu = 0.35$ gives best fit with respect to the plain fatigue data. Note that in partial slip, the coefficient of friction is not known a priori but it is considered that it is smaller in value than the ones obtained in gross sliding. This assumption is made based on the indications that the coefficient of friction for the analysed materials depends on the load ratio Q/P and, therefore, would be smaller in partial slip. Moreover, significant wear occurs in gross sliding tests and it is believed that, as the surfaces of the parts wear out, the coefficient of friction increases. Almost no wear, however, is seen in the specimen after a partial slip test.

The changes in contact stresses due to crystallographic orientation did not improve the correlation of results. The orientation with higher contact stress also had a longer life for similar applied stress range. However, the real value of the coefficient of friction still needs to be taken into account and, here, it is assumed to be constant for all crystallographic orientations. Furthermore, the influence of the 20° deviation on the stress may have a greater influence than it was thought at first and perhaps that would be needed to be taken into account in future analysis. Another aspect of the results in Figure 4.14 is the difference in slope between the fretting fatigue and plain fatigue curves. It is still not clear if this difference could be due to the different load ratio, R_σ, between the tests ($R_\sigma = 0$ for the plain fatigue test and $R_\sigma = 0.2$ for the fretting fatigue tests) or simply due to the different nature of the problems; i.e. fretting fatigue versus plain fatigue.

The difference between the results with RR1000 pads carried out at 0.25 Hz and 3.0 Hz is

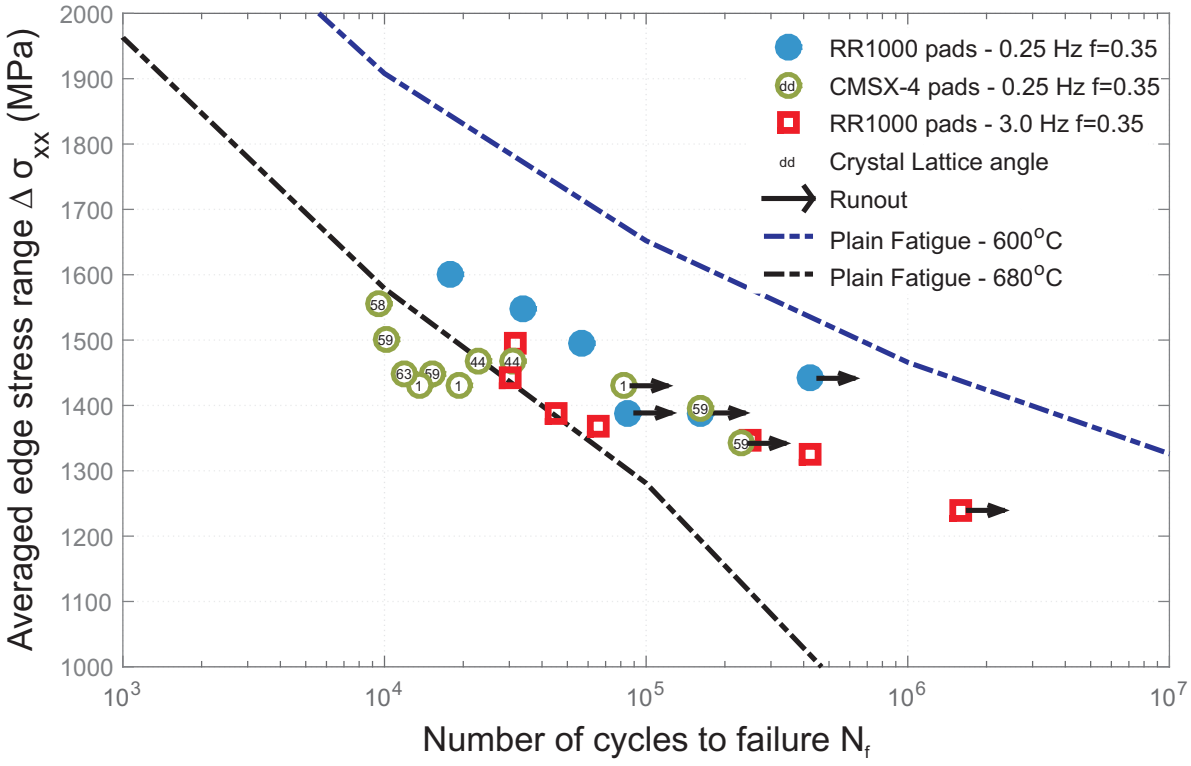

Figure 4.14: Correlation of stress under the trailing edge of the contact and fretting fatigue lives.

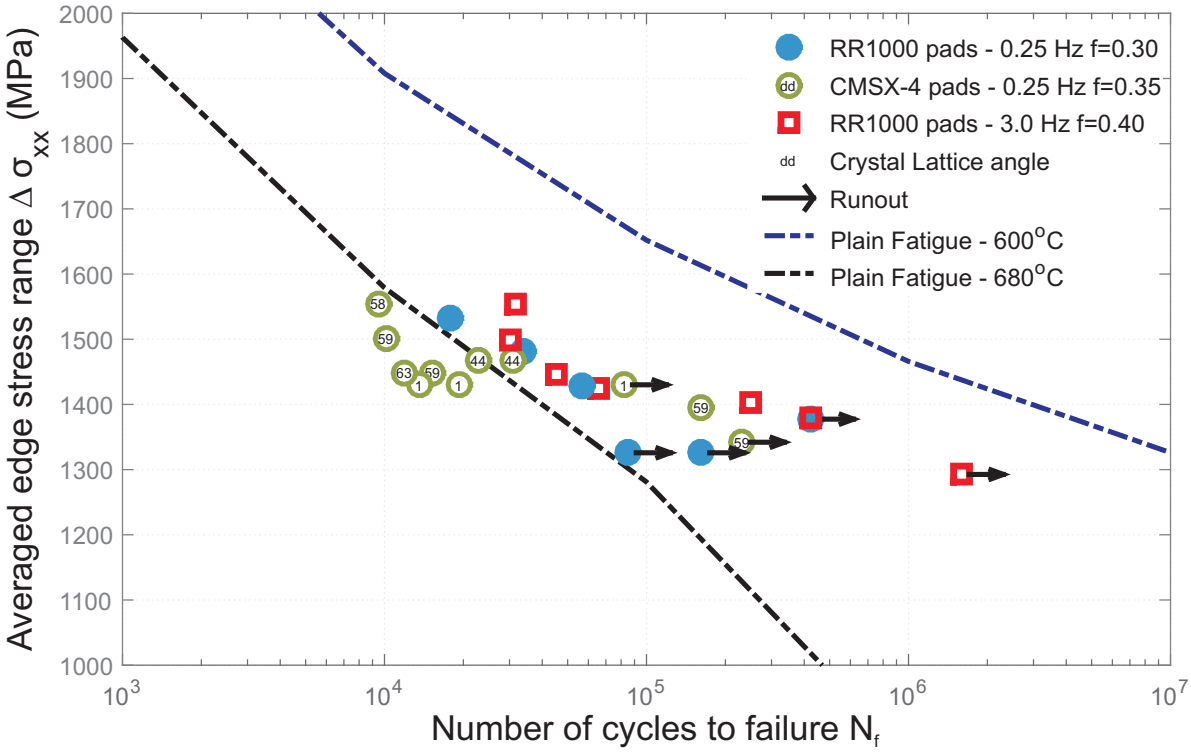

Figure 4.15: Correlation of stress under the trailing edge of the contact and fretting fatigue lives with a “corrected” coefficient of friction.

believed to be due to the time that the oxide glaze takes to form in the contact. The nickel oxide needs only a few seconds to form and, during the low frequency tests, which take four seconds to complete one cycle, the rate at which the oxide is being removed may be low enough to allow the regrowth of enough oxide during the load cycle. The nickel oxide is harder than the nickel superalloy and the coefficient of friction is lower. Hence, the oxide will also have an impact on the contact tractions. In fact, since the oxide is harder than the superalloy, the variation in contact tractions due to the crystal orientation might be higher than originally calculated, as shown Figure 3.12.

The presence of oxide in the contact would reduce the coefficient of friction and, hence, change the stresses near the contact edge. Therefore, the tests conducted at 0.25 Hz would have a lower value of μ when compared to the ones carried out at a load frequency of 3.0 Hz. Moreover, friction tests conducted with RR1000 and CMSX-4 pads on a RR1000 specimen have shown that the coefficient of friction for the CMSX-4/RR1000 pair is higher than RR1000/RR1000 (see chapter 5). Therefore, it is proposed that a correction of the coefficient of friction in the S-N chart be introduced to reduce the scatter of the results. It is assumed that the tests with RR1000 pads and 0.25 Hz frequency have a smaller value of friction $\mu = 0.30$ and that the tests carried out at 3.0 Hz have greater coefficient of friction, e.g. $\mu = 0.40$. The tests with CMSX-4 pads have a greater value of friction when compared with the RR1000 at similar frequency, e.g. $\mu = 0.35$. The modified results are shown in Figure 4.15 and it can be seen that the dispersion of the points in the chart reduces with the modified coefficient of friction. The value of the coefficient of friction presented here does not necessarily correspond to the true value, which cannot be easily measured in partial slip, but the idea that the coefficient is changed due to the glaze formation and that it is higher for the tests with CMSX-4 pads seems to be valid. No change in the coefficient of friction for CMSX-4 with respect to the crystallographic orientation was made and they were assumed to be constant. For a better correlation of the CMSX-4 pads, further analyses of the friction behaviour for different crystallographic orientations need to be carried out.

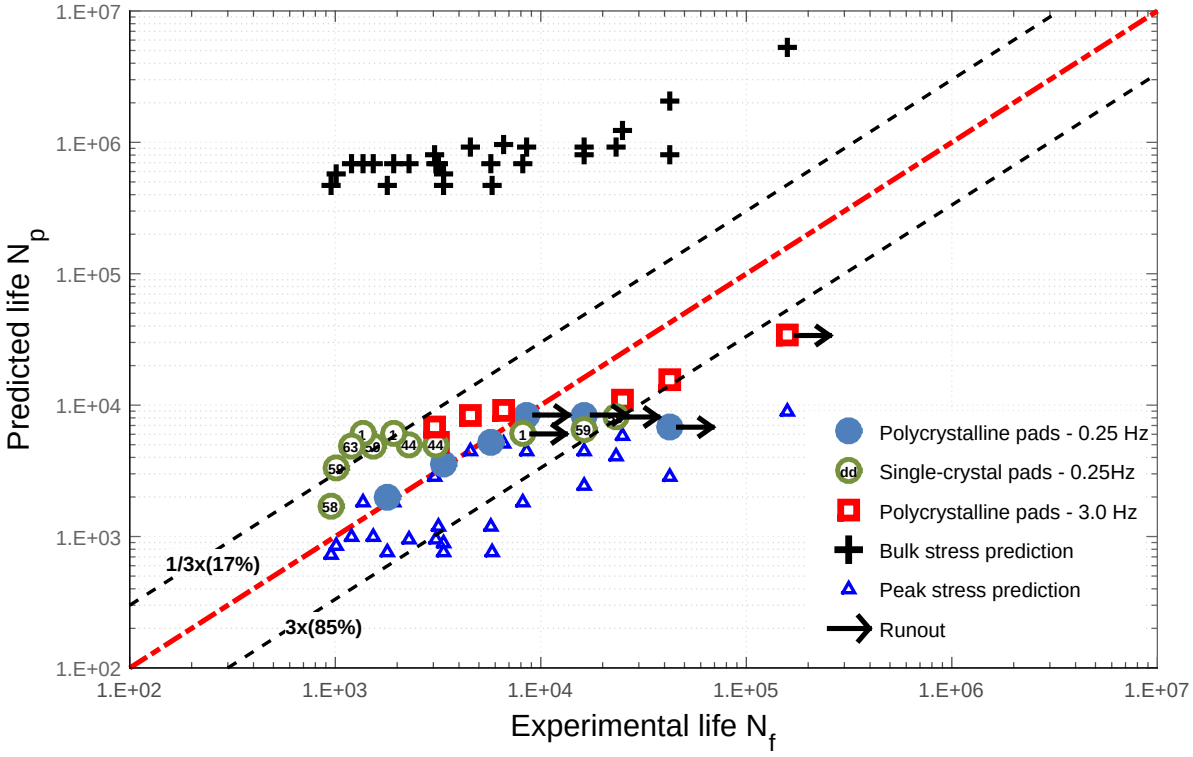

Figure 4.16: Experimental life versus predicted life based on the plain fatigue data and taking into account the stresses near the contact edge.

4.3.2 Experimental life versus predicted life

The results for predicted life versus experimental life of fretting fatigue test are shown in alternative form in Figure 4.16. The prediction is based on the plain fatigue curve of the RR1000 alloy at 680°C. The curves of $1/3$ and 3 times the predicted life, black dashed lines, are plotted together with the predicted life line in Figure 4.16. The 17% and 85% label on the graph represent the experiments' respective Weibull cumulative probability at those curves. The black cross points represent the fretting fatigue data based on the bulk load. It can be noted that, when considering the applied bulk load range for life correlation, the tests present significantly lower lives than expected. On the other hand, if the peak stress prediction at the interface is used, the results are slightly overestimated. A significant improvement in the correlation of plain fatigue and fretting fatigue datum was achieved by implementing the area averaging method and using the stresses near the contact edge as the main parameter for life correlation. After scaling the stresses, the majority of the points, 70%, lies within the factor 3 curves.

These results illustrate what has been known by the fretting fatigue community for a while

now: that the stresses near the contact play a more important role in the overall fretting fatigue life than the applied bulk stress. However, those stresses are often related and the fatigue stress range variation is sometimes what induces shear and vibration near the contact in the first place. The bulk fatigue stress on the body can be important in the crack propagation stage and without sufficiently high fatigue loads, crack may initiate but not propagate, causing no component failure. In the above fretting fatigue tests the crack spends most of its life in the region of influence by the contact stresses, whether in the initiation or propagation stage. This explains why the correlation of experimental and predicted lives are better when using the stresses near the contact edge as the stress parameter.

4.4 Out-of-plane shear in a three-dimensional contact

A stress σ_{xx} in the x direction applied to an isotropic body will excite the direct strain components ε_{xx}, ε_{yy} and ε_{zz}; the last two due to the Poisson's effect. One important aspect of anisotropic bodies is that the material response for a loading in the x direction might excite all strain components, including the shear strains ε_{xy}, ε_{xz} and ε_{yz}. In the case of orthotropic materials with cubic symmetry, the response of a loading in a given direction will depend on the material orientation with respect to the direction of loading. If, for example, the single-crystal orientation has its principal directions in the directions of the applied direct stress, the material response will be similar to that of an isotropic material, in the sense that only direct strains are excited. It was shown in §3.1.1 that the elastic tensor components that couple direct stresses with shear strains, and *vice versa*, are zero when the single-crystal's principal directions are parallel to the loading coordinate systems' axes. In fact, this is true for any orientation of symmetry, as, for example, when the crystal is oriented 45° about the y axis ($\phi_1 = 45°$, $\phi_2 = 0°$, $\phi_3 = 0°$). Any other crystal orientation between $\phi_1 = 0°$ and $\phi_1 = 45°$ will have non-zero components coupling direct and shear stresses and strains. If that is the case, one might expect that a normal force applied to the contact between a CMSX-4 pad and a RR1000 specimen will cause out-of-plane displacements and shear stresses, as will the shear traction applied in the x direction. The shear tractions at the interface play an important role in the initiation of cracks and, hence, in fatigue lives. Therefore, the existence of an out-of-plane shear stress (i.e. shear

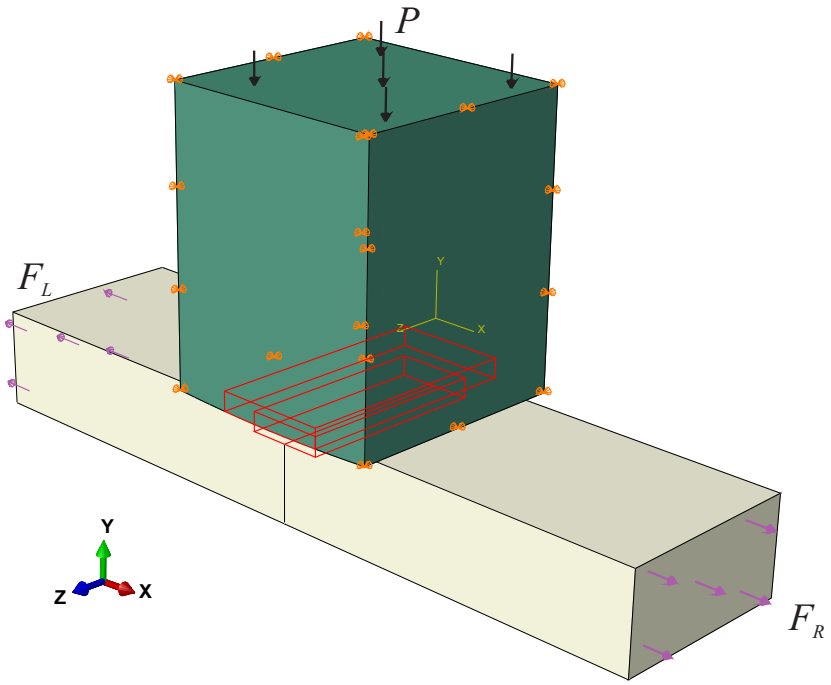

Figure 4.17: Finite element 3D model of a CMSX-4 pad pressed onto an RR1000 specimen.

in the z direction in the example of §4.2) for some orientations may reduce the fretting fatigue life. Although the contribution of out-of-plane shear traction due to the normal load does not have a cyclic component, the contribution due to the applied shear traction does vary cyclically and may contribute to an acceleration of the crack initiation. A brief analysis of the out-of-plane shear is presented in this section using a finite element three-dimensional (3D) model.

4.4.1 3D Finite Element model for out-of-plane shear traction analysis

A three-dimensional finite element model was designed in ABAQUS based on the fretting fatigue specimen and pad geometries. The geometry of the model are based on the experimental set-up given in §4.1.1 and an illustration of the finite element model is presented in Figure 4.17. The radius of the cylindrical face of the pad is $R = 100$ mm. The pad section dimension is 12×12 mm and the longer length in the y direction was chosen to be 'long enough', such that, the stress concentration due to the load applied at the top does not affect the contact tractions. The symmetry of the problem in the y direction is exploited and the specimen dimensions are $50 \times 5 \times 10$ mm. A normal load $P = 17.7$ kN is applied at the top of the pad. The faces of the pad normal to the x axis are constrained in the x and z directions. A symmetry boundary condi-

tion in the y direction is applied under the specimen. The fatigue loads F_R and F_L are sinusoidal and applied in the faces of the specimen normal to the x axis, as shown in Figure 4.17. An oscillating shear load is also applied to the interface by controlling the difference in amplitude between the fatigue loads F_R and F_L.

A sub-modelling technique is used to obtain the contact tractions in greater detail. A smaller region near the contact zone is selected and the loads and displacements of the global model are applied to the boundaries of the sub-model (region highlighted in red in Figure 4.17). Hexagonal reduced integration elements, C3D8R, are used and the contact interface is discretised by 80×65 elements. The contact is resolved by the penalty method with a stiffness ten times greater than the default ABAQUS stiffness (calculated by the size and material stiffness of the elements). The CMSX-4 properties were assigned to the pad and different orientations of the crystal were tests, but always keeping the material direction $\langle 010 \rangle$ normal to the contact interface. The RR1000 alloy properties at 680°C were assigned flat specimen. The normal and tangential traction distributions were obtained and an investigation of the out-of-plane shear traction is presented next.

4.4.2 Out-of-plane contact tractions

Using the model described in §4.4.1, the out-of-plane shear traction component (in the z direction in Figure 4.17) in the centre of the contact, $z = 0$, is obtained. The contact pressure remains constant throughout the test. An example of the contact normal pressure for the reference orientation of the single-crystal ($\phi_1 = \phi_2 = \phi_3 = 0°$) is shown Figure 4.18. The high concentration of stress at the edges of the contact in the z direction is due to the fact that the edges are not matching. This 'end effect' on contact tractions is explained in [Johnson, 1985]. Note that the edges of the specimen in the experimental specimens are slightly rounded. The presence of edge rounding reduces the peak stress at the extremities, which is not taken into account in the numerical model. However, the focus here is on the centre of the contact, $z = 0$, and the edge effect is neglected in this analysis. Note that despite the high stresses at the edge of the specimen, cracks are observed throughout the surface of the specimen and fracture originates almost as frequently from the contact edge as from the centre of the specimen. In a sinusoidal fretting

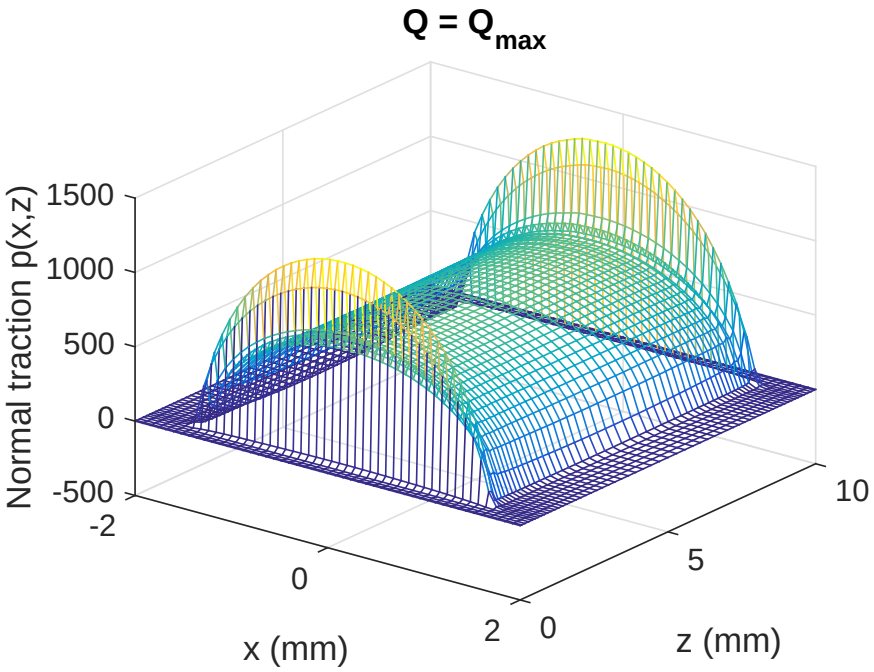

Figure 4.18: Normal contact pressure for the reference crystal orientation of the single-crystal pad ($\phi_1 = \phi_2 = \phi_3 = 0$).

fatigue cycle, the shear loads in the direction of loading x, $q_1(x,z)$, are given in Figure 4.19, again for the case of the reference orientation of the single-crystal. Although the values of the contact tractions may change at different orientations, the general trend of the distributions is displayed in Figures 4.18 & 4.19.

In the case of the shear stress along the z direction, $q_3(x,z)$, the behaviour at different crystal orientations may be significantly different. The out-of-plane shear traction in the centre of the contact, $q_3(x,0)$, is displayed in Figure 4.20 at the time instant of $Q = Q_{max}$. At directions of elastic symmetry, i.e. directions with no coupling between direct and shear stresses and strains, the shear traction in the out-of plane direction given that the loading is close to zero. In fact, the shear stress is exactly zero when both the specimen and the pads are made of similar isotropic materials, but some noise is seen for single-crystal pads with orientations of symmetry. This noise is probably due to the elastic mismatch of both materials and some imprecisions in the boundary conditions of the model. At the orientation of $\phi_1 = 30^\circ$ the shear traction is significantly higher at the load instant $Q = Q_{max}$, which is also the instant of highest applied bulk stress. It is true that the magnitude of the shear tractions are still very small (approximately one-tenth) when compared with the in-plane shear traction, $q_1(x,z)$. However, it is a reasonable

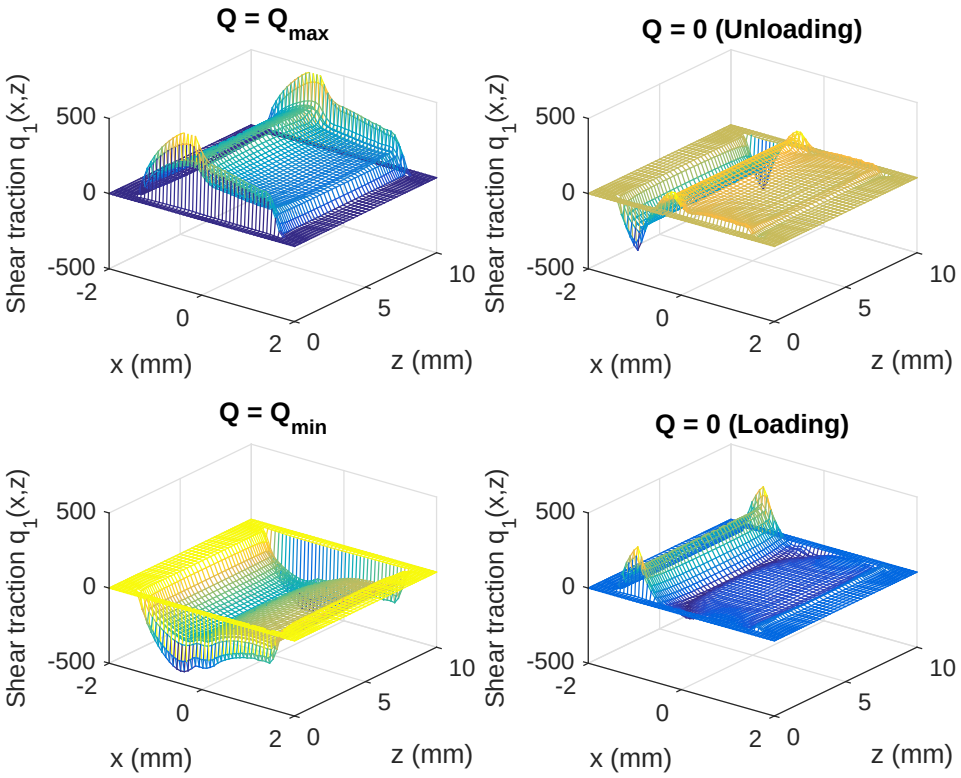

Figure 4.19: Shear contact tractions for the reference crystal orientation of the single-crystal pad ($\phi_1 = \phi_2 = \phi_3 = 0$) at different fretting cycle instants.

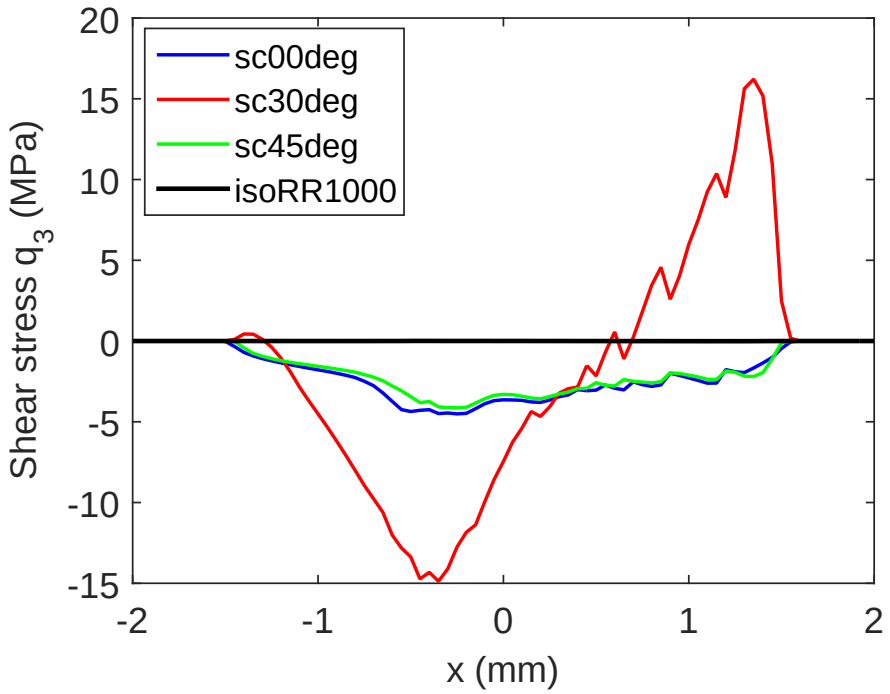

Figure 4.20: Out-of-plane shear traction at the centre of the contact for different crystal orientations at load instant $Q = Q_{max}$.

conjecture that the presence of other stress components near the contact edge very locally at the surface, is sufficient to accelerate the crack initiation. This may explain why the tests in §4.1.2 with single-crystal pads at orientation $\phi_1 = 30^\circ$ have shown shorter lives than the tests at orientations $\phi_1 = 0^\circ$ and $\phi_1 = 45^\circ$.

4.5 Discussion

The changes in contact stresses due to crystallographic orientation did not significantly improve the correlation of results. The orientation with higher contact stress in § 4.2.3 presented a longer life for similar applied stress range in the tests. However, the real value of the coefficient of friction still needs to be taken into account and, here, it was assumed to be constant for all crystallographic orientations. Furthermore, contact shear tractions in the out-of-plane direction (z axis) occur in tests with crystal orientation $0^\circ < \phi_1 < 45^\circ$ and they were not present in the two-dimensional finite element analysis. The shear in the out-of-plane direction occurs when non-zero components of the elastic stiffness causes coupling between direct stresses and shear strains and vice versa, which is true at those directions. These components of the elastic stiffness matrix are zero for orthotropic materials at the symmetry orientations $\phi_1 = 0^\circ$ and $\phi_1 = 45^\circ$, as well as for isotropic materials. The presence of out-of-plane shear tractions are possibly one of the reasons why tests with orientations $\phi_1 \approx 60^\circ$ presented shorter lives when compared to other orientations. Bear in mind that all measurements of the single-crystal pads were restricted to the plane of the contact and the misalignment in the principal direction $\langle 010 \rangle$ with respect to the normal contact direction was not taken into account. The influence of the 20° deviation on the stress may also have a greater influence than it was thought at first. The highest variations in stress occur for vertically misaligned orientations and this would be needed to be taken into account for a more complete analysis of the problem.

A difference in the results of tests conducted with the RR1000 alloy pads at 0.25 Hz and 3.0 Hz was noted. This difference is believed to be due to the time that the oxide glaze takes to form in the contact zone. The presence of oxide in the contact would reduce the coefficient of friction and change the stresses near the contact. The tests conducted at 0.25 Hz would therefore have a lower value of coefficient of friction when compared to the ones carried out at

a load frequency of 3.0 Hz. Moreover, friction tests conducted with RR1000 pads on RR1000 specimens and with CMSX-4 pads on RR1000 specimens have shown that the coefficient of friction for the CMSX-4/RR1000 pair is higher than the RR1000/RR1000 pair. The coefficient of friction was assumed to be constant for all tests conditions. However, the idea that the coefficient is changed due to the "glaze" formation and that it is higher for the tests with single-crystal pads seems to be valid. An investigation on the orientation dependency on the coefficient of friction is also advised. If friction is direction dependent, the variation of stress as a function of orientation would be higher than the 4.5% obtained in §4.2.3. Further studies on the frictional behaviour of those alloys are suggested for more accurate results of the contact stresses.

Tests with controlled crystal orientation have shown significant less scatter than previous uncontrolled ones. In these tests, conducted at high temperature, the scatter due to different secondary principal direction orientation, however present, has been significantly smaller. These results are in agreement with the analytical analysis and the stress analysis in §4.2.3, where the variation of stresses due to different crystallographic orientation has not been greater than 4.5%. So the question then becomes why were the scatter in the tests at room temperature so large?

By analogy with linear elastic fracture mechanics, the region around the edge of contact may be subdivided in zones of different *scales*. Very close to the contact a plastic zone may develop. The assumptions of linear elasticity are only valid beyond this plastic zone and no longer valid inside it. Surrounding the plastic zone there is a K-field zone, where the stresses may accurately be represented by asymptotes characterised by stress intensity factors, K. As the point of observation moves further away from the corner, the stresses are governed by the contact tractions. Finally, far from the edge of contact, the effect of the contact tractions on the stress field fades away and the far field loading defines the state of stress on the specimen. The size of the zone of influence of the contact tractions is approximately given by the contact half-width, a, i.e. when $y > a$ the stresses are governed by the far field loading (here y is the depth into the body away from the contact interface). In the problems investigated in this chapter the size of the contact half-width was approximately between $a = 1.49$ mm ($\phi_1 = 0^\circ$) and $a = 1.45$ mm ($\phi_1 = 45^\circ$). The definition of these zones may shed light on why the correlation between linear elastic stresses and fatigue life works well in some cases but not in others. For example, if the

plastic zone is large when compared with other relevant dimensions of the problem, such as the contact width and the size of the process zone used to average the stresses in §4.2.2, then 'small scale yielding' does not apply and a purely elastic analysis is no longer appropriate.

In this chapter it was assumed that the plastic zone near the edge of contact was sufficiently small for the average stress in the process zone to be reasonably obtained with linear elasticity. If the plastic zone is sufficiently small and the stress concentration sufficiently high, the size of the plastic zone near the contact edge can be approximately described by a singular asymptote, which is itself characterised by a stress intensity factor, K. In linear elastic fracture mechanics, the stress intensity factor is obtained by neglecting the higher order terms and assuming that the stresses near the crack tip are governed by the square-root singular term. Here, the problem is different from that of a crack and the stress component σ_{xx} is finite and does not go to infinity at the edge of the contact. Nevertheless, a singular asymptote may be used to describe the stresses in a zone close to edge of the contact, but which is no longer square-root singular and which is not valid *very* close to the interface ($y = 0$). Despite the inaccuracy at the surface due to its singular behaviour, this singular asymptote does describe reasonably well the stress profile in a small zone surrounding the plastic zone, i.e. the K-field. The stress σ_{xx} may then be written as $\sigma_{xx} = Ky^m$, where K and m may be calibrated from the finite element obtained stress distribution at the edge of the contact. The profile of the stress component σ_{xx} and its asymptote under the edge of contact are given in Figure 4.21 for a fretting problem case at room temperature and 680°C. Note that the size of the K-field zone may also be estimated from Figure 4.21, where the error of the asymptotes with respect to the σ_{xx} stress profiles is greater than 10% at a distance of approximately $y = 0.2$ mm from the notch root.

The most severe case analysed in this chapter is for the single-crystal punch with the crystal oriented at $\phi_1 = 45°$. The estimated coefficient of friction for the CMSX-4/RR1000 pair at 680°C is $\mu = 0.35$. From Figure 4.21, it is found that $m = -0.096$ and $K = 833$ MPa.mm^{-m} with the high temperature material properties. The plastic zone size, r_p, may be obtained from the calibrated K and m by equating the singular representation of the stress in the K-field with the yield stress of the material, i.e. $\sigma_y = K{r_p}^m$, where σ_y is the yield stress of the RR1000 at 680°C. The yield stress for this nickel alloy increases slightly at 680°C from its room tempera-

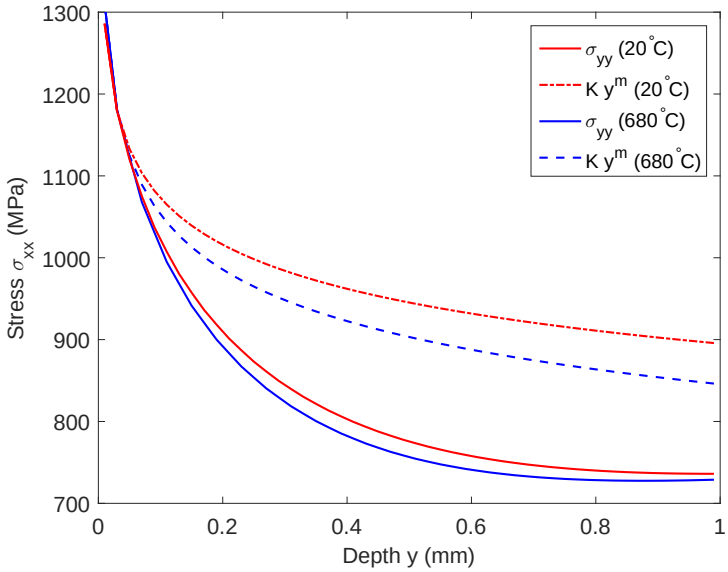

Figure 4.21: Stress component σ_{xx} under the edge of the contact and K-field asymptote for room temperature and 680°C ($\phi_1 = 45°$ and $\mu = 0.35$).

ture value of about 1100 MPa before a sharp drop at temperatures above 800°C. The estimated size of the plastic zone near the edge of the contact, assuming that only the component σ_{xx} is non-zero, is about $r_p = 0.0223$ mm for the high temperature tests, which is less than $1/3$ of the size of the process zone used to average the stresses in the analyses.

At room temperature, the Young's modulus of the RR1000 superalloy increases by about 17% and the stresses at the edge of the contact are slightly higher (see Figure 4.21). The changes in material properties, i.e. higher Young's modulus and lower yield stress, result in a larger plastic zone when compared with the tests carried out at 680°C. The asymptote terms K and m for the room temperature case may also be obtained from Figure 4.21) and the estimated size of the plastic zone is approximately $r_p = 0.0544$ mm. This is more than twice the size of the plastic zone at the high temperature case. This larger plastic zone means that the assumption of linear elasticity when calculating the direct stress σ_{xx} and correlating it with the experimental results might not work as well for room temperature tests. Analysis of the plastic deformation near the edge of contact is outside the scope of this thesis but future work may include plasticity in both polycrystalline and single-crystal alloys.

The approach outlined helps with understanding why for some cases the experimental results may not correlate well with the stresses obtained with a purely linear elastic analysis. However, it is only an approximate estimation of the plastic zone size. The state of stress in

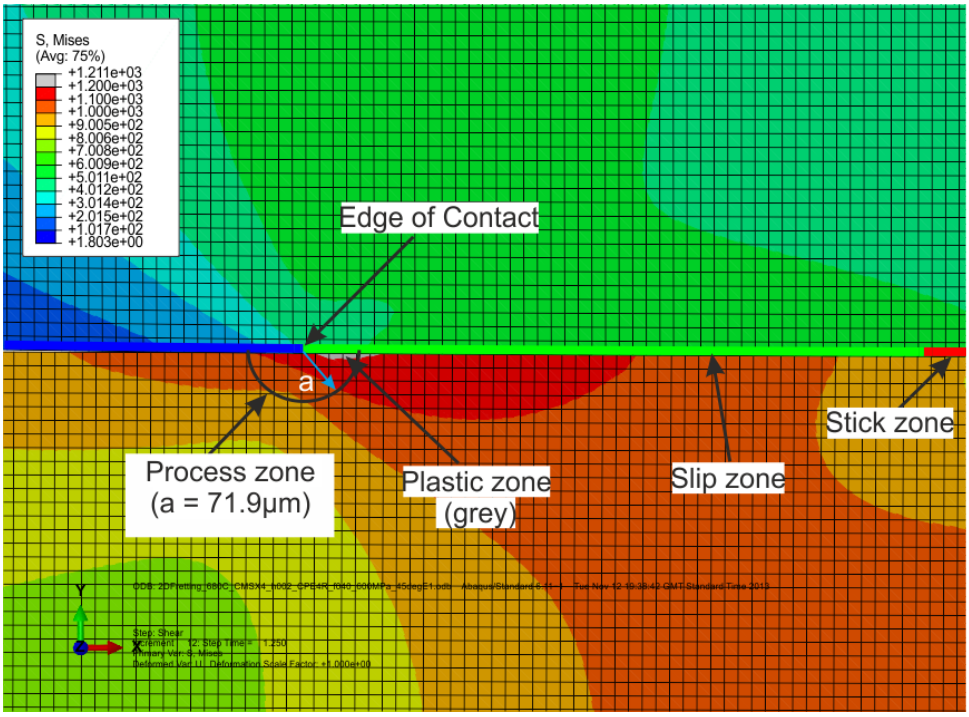

Figure 4.22: Von Mises equivalent stress, plastic zone and process zone at the contact edge at instant $Q = Q_{max}$ at the temperature of 680°C

the surroundings of the contact edge is in fact multiaxial and a better prediction of the plastic zone may be obtained by a multiaxial criterion, such as the von Mises yield criterion. If the von Mises equivalent stress is used, for example, the plastic zone for the fretting problem analysed at 680°C and single-crystal orientation of the punch $\phi_1 = 45°$ is given in Figure 4.22. The radius of the plastic zone is approximately 10 μm, which is also the nominal grain size of this alloy. Note that the element size in Figure 4.22 is $h_e = 20$ μm. The size of the plastic zone here is approximately half that by asymptotic approach above, which assumed that only the component σ_{xx} is non-zero. These results show that the linear elastic analysis carried out in this chapter is valid for the high temperature fretting tests and if a plastic zone exists near the edge of the contact it is unlikely to significantly change the averaged stress in the process zone used in the fatigue life correlation.

Chapter 5

Measuring the coefficient of friction in partial slip contacts

One of the main issues in the partial slip problem is the fact that the coefficient of friction is unknown inside the contact zone. It has been suggested that the coefficient of friction in a partial slip contact is different from that under gross sliding [Hills and Nowell, 1994]. One of the reasons for that is the fact that the surfaces are significantly less damaged under partial slip when compared to gross slip cases. Moreover, the contact has a central stick zone, where slip does not occur, and the surface damage is negligible. The traditional method of measuring friction is by measuring the shear load necessary for sliding to occur. However, this method not suitable for determining the coefficient of friction in a partial slip contacts, since a significant part of the contact is in fact stuck. In order to try measuring the coefficient of friction in partial slip, two approaches are investigated. The first approach is a non-sliding technique to measure the coefficient of friction. Tests were carried out in an attempt to measure the coefficient of friction in single-crystal contacts using this technique. The second one is an energy based approach to measure the friction in the interface. A study of the energy dissipated in Hertzian contacts of elastically similar isotropic cylinders is conducted and some procedures to measure the coefficient of friction are suggested. However, the implementation of the energy approach has shown to be experimentally difficult due to the low sensitivity of the method.

5.1 The "walking pad" friction test

In an attempt to measure the coefficient of friction between CMSX-4 single-crystal pads and a RR1000 superalloys under partial slip conditions, a non-sliding experimental test was carried out. This technique was first suggested by Reina et al. [2010]. These experimental approach are referred to as the "walking pad" friction test, in an allusion to the fact that the pad has a net displacement at the end of a load cycle without ever fully sliding.

5.1.1 Experimental procedure

The "walking pad" tests were conducted using the fretting fatigue experimental rig with two in-line actuators, as illustrated in Figure 5.1a. Note that the experiments were conducted at room temperature. In the experimental procedure, the pads are pressed onto the specimen with a constant normal force $P = 2.5$ kN throughout test. Then, a cyclic bulk tension, σ, is applied to the specimen. The range of the bulk tension cyclic load is raised to a specified amplitude and kept constant thought the test as well. Using the second (small) actuator, the shear force between the pads and the specimen is incrementally increased in a "staircase" fashion. Schematic representations of the loading history and of the applied loads are displayed in Figures 5.1b & Figure 5.1c. In each shear force step, the test ran for about one minute, equivalent to 15 cycles of the bulk tension. The pads remain in partial slip regime at all times and, as the shear load increases, reverse slip starts to occur at the edges of the contact. After a certain limit, the stick zone moves from one side to the other in the contact, such that the pads start "walking" along the specimen without ever fully sliding. The higher the coefficient of friction the slower the rate of displacement. During the experiments, the shear loads and displacements data were recorded. With this information, it is possible to calculate an average displacement per load cycle for each shear force increment and, hence, the coefficient of friction.

The solution of the rate of displacement for the "walking" problem can be obtained by quadratic programming [Reina et al., 2010]. By comparing the quadratic programming solution for different values of coefficient of friction with the experimental data, it is possible to infer the value of the coefficient of friction by interpolation of the experimental results. The coefficient of friction can also be obtained by the shear load limit at which the pads start to walk. However, it

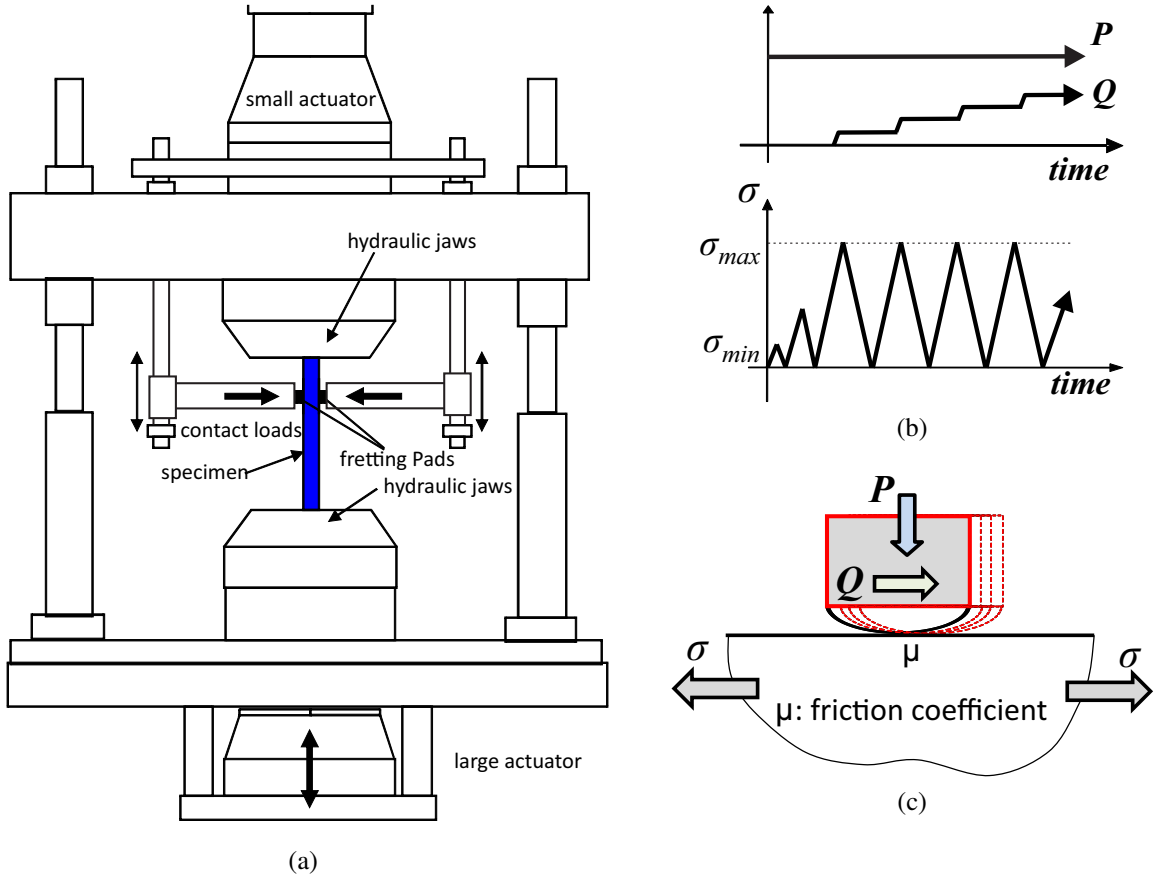

Figure 5.1: (a) Schematic representation of the in-line fretting rig; (b) Load history used in the walking pad tests; (c) Schematic representation of the loading in the "walking pad" test [Reina et al., 2010].

is impossible to define experimentally the precise moment in which the pads start accumulating a net displacement at the end of each cycle. Examples of the graph that were used to interpolate the coefficient of friction are presented in Figures 5.2 & 5.3. The straight lines represent the displacement per cycle obtained from the quadratic programming solution for each coefficient of friction μ as the ratio Q/P increases from 0 to 1. The blue cross points are the displacement per cycle obtained experimentally, with an appropriate normalization. This normalization takes into account the peak pressure, p_0, the contact semi-width, a, and the elastic compliance between the materials, A. Note that for the CMSX-4 pads, these variables were obtained by solving the anisotropic contact solution presented in §2.2.2. In the case of the elastic compliance, it can be shown that the constant A used in isotropic solutions is equivalent to $\mathrm{Re}(\gamma)$ in equation (2.49). Finally, the green circular points represent the values of the coefficient of friction obtained by interpolating the experimental data and the quadratic programming solution

for the rate of displacement.

As second measurement of the coefficient of friction was carried out using the standard gross sliding test. At the end of each "walking" test, the cyclic bulk loading was interrupted and the shear load reduced to zero. Then, the control of the actuators of the pad carriage was changed to displacement control. A displacement was applied with constant velocity, inducing the pad to slide along the interface of the specimen. As the pad was sliding, the shear force, Q, was measured, from which the sliding coefficient of friction can be calculated. Problems associated with this method include the fact that the pads' surfaces are significantly damaged during the test. Furthermore, at the beginning of the gross sliding tests, the surfaces of the pad were already slightly damaged, since the tests were carried after the "walking test". Note that, although the partial slip test always had a central stick zone, in the "walking test", the stick zone alternates sides during the load cycle and all points on the surface slip, but not all at the same time. This means that the entire contact zone will have some surface damage caused by the micro slip in the slip zones, even before the gross sliding tests begin.

5.1.2 Results of the coefficient of friction tests

Two typical tests with CMSX-4 pads are displayed in Figure 5.2, one with pads of orientation $\phi_1 = 6.45°$, Figure 5.2a, and one with pads at $\phi_1 = 42.7°$. In partial slip regime, the coefficient of friction for CMSX-4 pads varied significantly as the test was being conducted (Figure 5.2a), often with clear steps of constant coefficient of friction (see Figure 5.2b). This variation may be associated with the response of the material as the shear load increases. The same behaviour was not seen in the tests with RR1000 pads (Figure 5.3). The coefficient of friction for tests with RR1000 pads were also lower than the ones with CMSX-4. Both tests carried out with RR1000 pads have shown a coefficient of about 0.20-0.35.

Two methods were adopted to compare the coefficients of friction for the CMSX-4 pads in partial slip. The first, takes into account the coefficient of friction in the last cycles before full slip occurs. The second, compares the coefficient of friction for an arbitrary value of $Q/P = 0.3$. The coefficient of friction obtained experimentally as a function of the crystallographic orientation of the CMSX-4 pads are shown in Figure 5.4. The results are also listed in table 5.1. Other

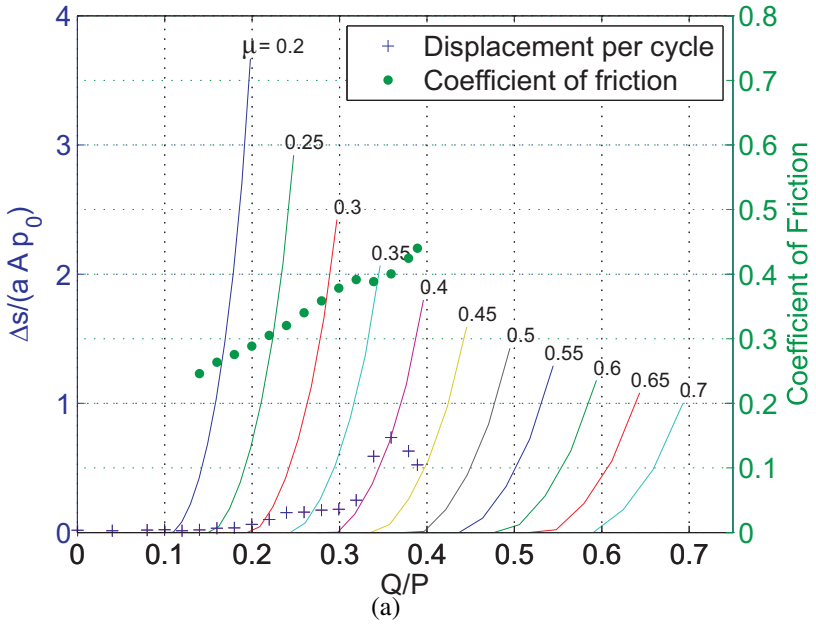

(a)

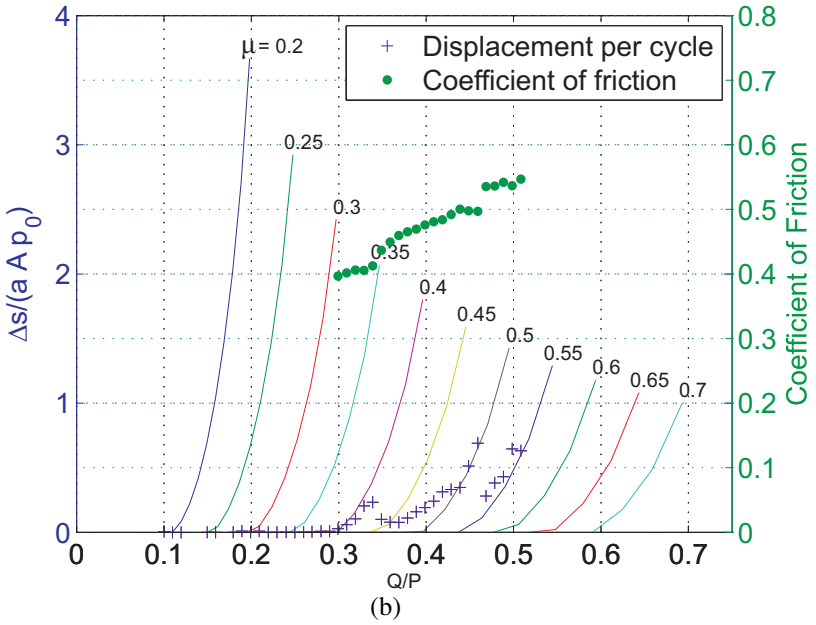

(b)

Figure 5.2: Coefficient of friction in partial slip for CMSX-4 pads on RR1000 specimen. (a) Test CMSX00d2 ($\phi_1 = 6.4°$); and (b) Test CMSX45d1 ($\phi_1 = 42.7°$).

plots of the evolution of coefficient of friction and the measured shear force obtained during gross sliding tests are shown in appendix B.

Tests with the same name and different terminations (a, b and c) indicates the same pair of pads. Due to the limited number of pads, the surface of the pads were reground and the tests repeated to give an indication of variability. A large variation in repeated tests was observed for the gross slip and final cycles in partial slip cases. It is believed that this large scatter is

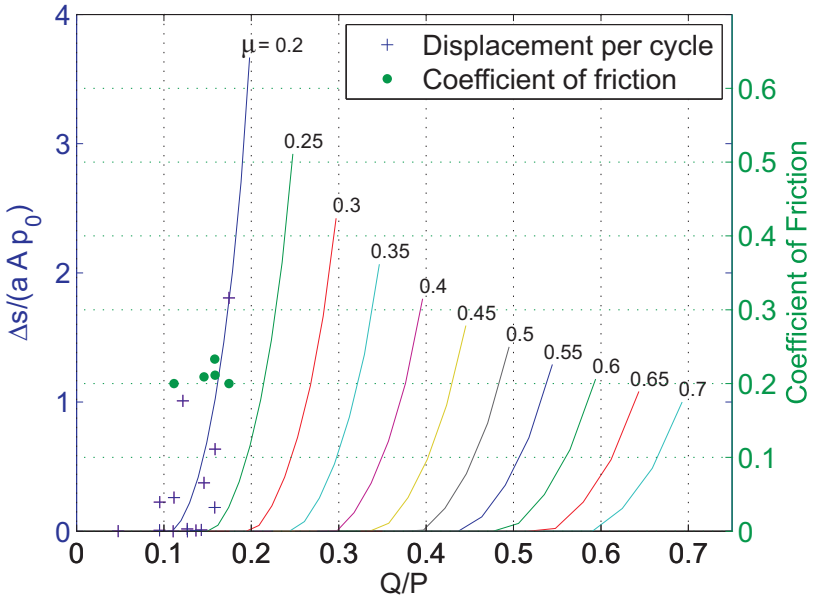

(a)

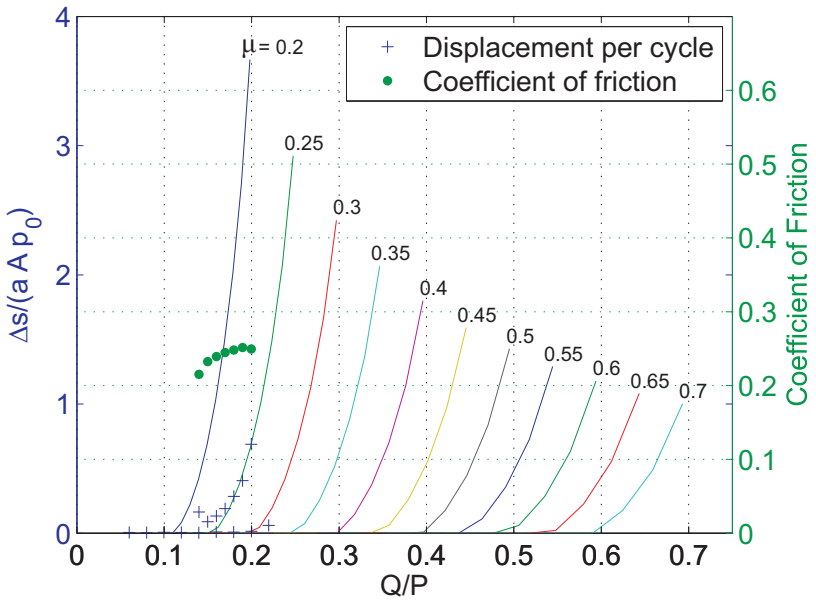

(b)

Figure 5.3: Coefficient of friction in partial slip for RR1000 pads on RR1000 specimen. (a) Test RR1000-1; (b) Test RR1000-2.

due to variations in the roughness of the specimen and pads as they were reground. The two methods listed above resulted in similar coefficients for each test. However, a higher coefficient was measured in gross slip, which could be explained by the increasing wear at the interface of the contact as the test was carried out. Due to the large scatter in the results, it is not possible to correlate coefficient of friction with crystal orientation. At a fixed value of $Q/P = 0.3$ the results

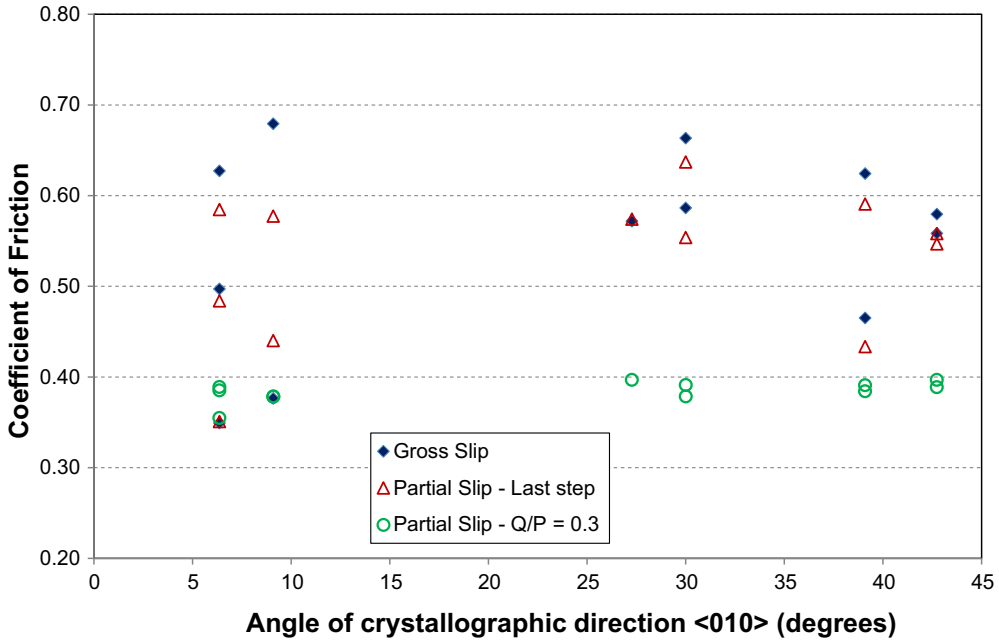

Figure 5.4: Coefficient of friction between CMSX-4/RR1000 alloys as a function of the crystal orientation.

are much more consistent, with all results presenting a coefficient of about 0.38. Nevertheless, very small difference in the coefficient of friction was observed as the crystal orientation of the pads changed. Averaging the repeated tests, a small increase between the minimum ($\phi_1 = 6.36°$) and maximum ($\phi_1 = 30°$) values of the coefficient was found, but no conclusions can be drawn. It is also important to highlight that the tests carried out with similar RR1000 pads presented a much more stable coefficient of friction until the test entered the gross sliding regime.

Test Number	Angle (degrees)	CoF Gross Slip	CoF - Partial Slip Last Cycle	CoF - Partial Slip Q/P = 0.3
CMSX00d1a	6.36	0.349	0.3477	0.3549
CMSX00d1b	6.36	0.497	0.472	0.3891
CMSX30d2a	9.09	0.376	0.4216	0.3782
CMSX00d2b	9.09	0.679	0.5661	0.3786
CMSX30d1a	30.0	0.586	0.5441	0.3786
CMSX30d1b	30.0	0.663	0.6186	0.3913
CMSX30d2a	27.7	0.572	0.5692	0.397
CMSX45d1a	42.73	0.558	0.5417	0.3969
CMSX45d1b	42.73	0.580	0.5458	0.3888
CMSX45d2a	39.09	0.465	0.4207	0.3844
CMSX45d2b	39.09	0.624	0.578	0.391

Table 5.1: Coefficient of friction between CMSX-4 pads and RR1000 specimens.

5.2 Energy dissipation in partial slip contact problems

Many authors have correlated the energy dissipation concept with damage. Fouvry et al. [1995] have associated the energy dissipation in gross slip contact problems with the wear rate. Mindlin and Deresiewicz [1953] have shown that axis-symmetric contact problems, e.g. two spheres in contact, have a finite constant displacement at any point sufficiently far from the contact region. Following the work of Mindlin, Fouvry et al. [1997] have obtained an analytical solution for the ratio between the energy dissipated and the total energy available $E_T = 4Q\delta$, where Q is the applied shear load and δ is the remote displacement. Using the analytical solution for the energy dissipated in a spherical contact problem, Pasanen et al. [2009] have presented an energy approach for calculating the energy dissipated that works for the three slip regimes; partial, mixed and gross slip.

The approach used in [Pasanen et al., 2009; Fouvry et al., 1997] depend largely on the fact that for a contact between two spheres, or a sphere on a plane, the displacement at any point far enough from the contact region is finite and converges to a value which can be obtained analytically. In a two-dimensional half-plane problem this is not the case. The solution of the displacement has a logarithmic form and tends to infinity as the distance from the contact centre increases. However, the work done by each point at the interface due to the slip and shear tractions ought to match the total energy dissipated and hence a study of the shear tractions and slip on the contact interface should be sufficient to provide information on the energy dissipation.

In a complete load cycle under fretting the displacement is not recovered. That is, if no initial displacement exists between the bodies and an incremental shear load is applied at one of the bodies up to a maximum value Q_{max} and then decreased back to zero, a residual relative displacement δ_0 between the two bodies exists. The occurrence of the residual displacement δ_0 happens because of the non-linearity introduced to the problem by the presence of friction. According to Amontons's law of friction [Amontons, 1699], the frictional force between two bodies is dependent on the direction of the velocity of movement, being always opposite in sign. In a complete reverse cycle, a hysteresis loop is formed when plotting the relative displacement δ versus the shear load Q, and the area inside the loop is the energy dissipated per cycle. The objective of this section is to derive equations for the energy dissipation of two isotropic

elastically similar cylinders. These equations can then be used to suggest experiments based on the measurement of the energy dissipation by the hysteresis loop of fretting tests.

5.2.1 Contact tractions

Consider the shear traction between two isotropic cylinders. Following the theory of Hertz with spherical contacts, Cattaneo [1938] and Mindlin [1949] have shown that the presence of a stick zone can be represented by superimposed sliding solutions. The solution was later extended to plane contacts and presented by Johnson [1985]. Coulomb friction is assumed at the interface with a coefficient of friction μ. Using the superposition of the solution of the sliding problem and the contribution of the stick zone on the contact traction, the shear traction distribution over a contact region along the x axis comprised by the interval $|x| \leq a$, can be written as

$$q(x) = \mu p_0 \sqrt{1 - \left(\frac{x}{a}\right)^2} - q'(x) \qquad -1 \leq \frac{x}{a} \leq 1 \tag{5.1}$$

where the peak stress, p_0, depends on the applied load, P, and the contact semi-width, a, ($p_0 = 2P/\pi a$) and $q'(x)$ is the perturbation due to the stick zone. The contact area is a function of the applied normal load, the curvature of the cylinders' surfaces, k, and the elastic compliance, A, of the contact pair. The contribution of the central stick zone has the same form as the normal pressure solution and is written as

$$q'(x) = \mu p_0 \frac{c}{a} \sqrt{1 - \left(\frac{x}{c}\right)^2} \qquad -1 \leq \frac{x}{c} \leq 1 \tag{5.2}$$

This term, however, is valid only within the stick zone $-c \leq x \leq c$ and the size of the stick zone can be written as

$$\frac{c}{a} = \sqrt{1 - \frac{Q}{\mu P}} \tag{5.3}$$

In the presence of a bulk tension on one of the bodies, the central stick zone is displaced by an offset, e, and the perturbation of the shear traction becomes

$$q'(x) = \mu p_0 \frac{c}{a} \sqrt{1 - \left(\frac{x-e}{c}\right)^2} \qquad -1 \leq \frac{x-e}{c} \leq 1 \tag{5.4}$$

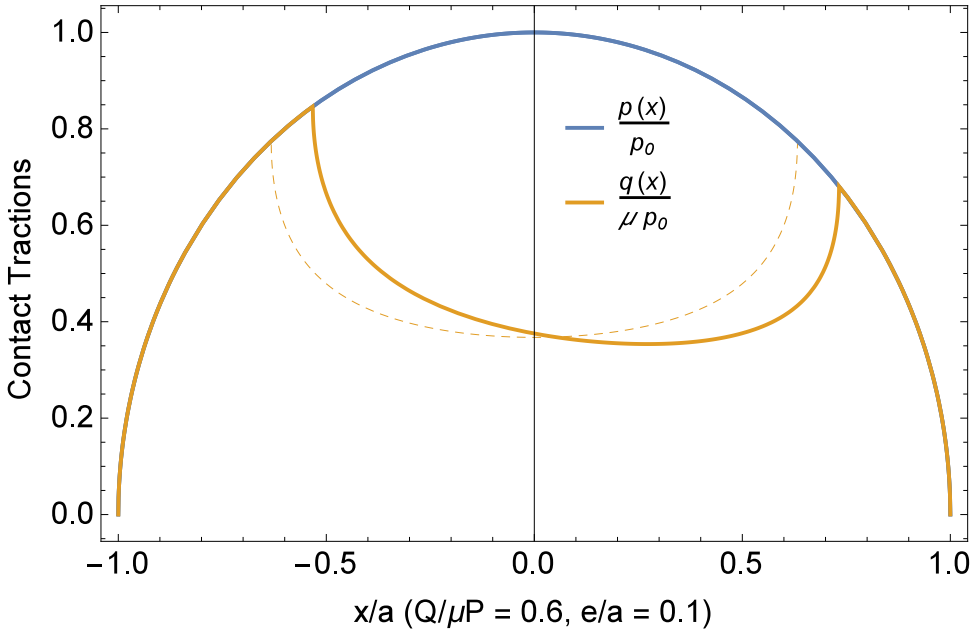

Figure 5.5: Contact tractions for a contact between two elastically similar isotropic cylinders. Effect of bulk tension on the contact shear traction.

with the offset e given by the maximum bulk stress, σ_0, the peak stress, p_0 and the coefficient of friction μ as [Nowell and Hills, 1987]

$$\frac{e}{a} = \frac{\sigma_0}{4\mu p_0} \tag{5.5}$$

The normal and shear traction distributions for the contact between two isotropic elastically similar cylinders is presented in Figure 5.5 for an arbitrary case of $\mu = 1$, $Q/P = 0.6$ and $e/a = 0.1$. The shear traction is also shown, and a slip region exists near the edges of the contact. In order to calculate the energy dissipated at the contact interface, a study of the displacements is presented next.

5.2.2 Contact displacements

The equations for the normal, $h(x)$, and tangential, $g(x)$, relative displacements between two isotropic elastically similar contacting cylindrical bodies, and with one body submitted to a

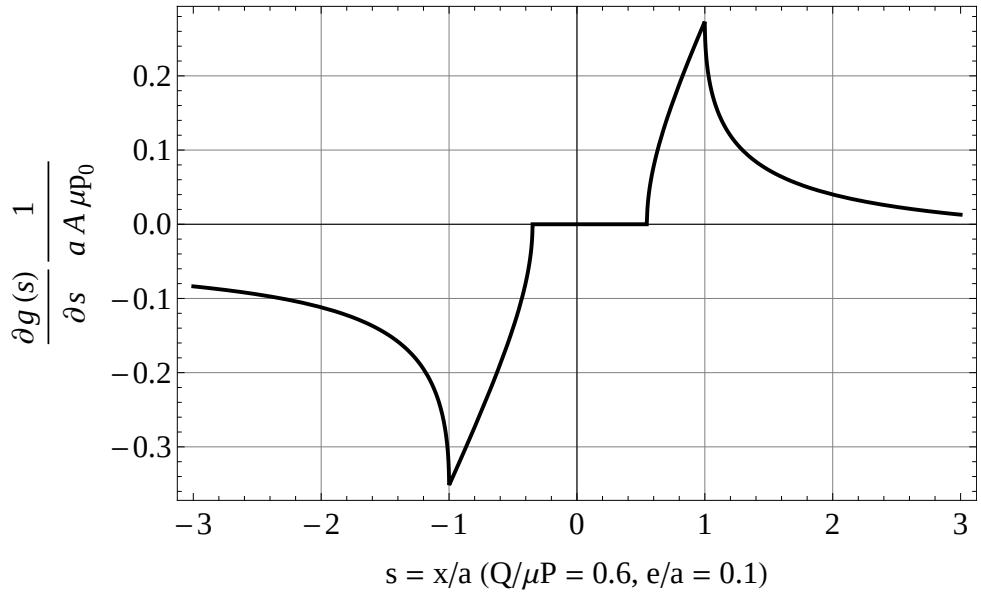

Figure 5.6: Slip gradient for a contact between isotopic elastically similar cylinders with the presence of bulk Stress.

bulk stress tension, are given by [Nowell and Hills, 1987]

$$\frac{\partial h(x)}{\partial x} = \frac{A}{\pi}\int_{-a}^{a}\frac{p(\xi)}{x-\xi}d\xi \tag{5.6a}$$

$$\frac{\partial g(x)}{\partial x} = \frac{A}{\pi}\int_{-a}^{a}\frac{q(\xi)}{x-\xi}d\xi - \frac{\sigma_0}{E}(1-\nu^2) \tag{5.6b}$$

In order to obtain the slip function at the interface, equation (5.6b) needs to be solved. Note that if the bodies are isotropic and elastically similar, the constant β in equation (2.7b) is zero and the problem is uncoupled. Furthermore, if the bodies are elastically similar, the elastic compliance parameter is $A = 4\frac{(1-\nu^2)}{E}$ and the last term of the left hand side of (5.6b) can be rewritten using (5.5). The equation for the shear traction is given in equations (5.1) and (5.4), and the integral equation for the tangential relative displacement can be written as

$$\begin{aligned}\frac{\partial g(x)}{\partial x} = A\mu p_0 \Bigg[&\frac{1}{\pi}\int_{-a}^{a}\frac{\sqrt{1-(\xi/a)^2}}{x-\xi}d\xi \\ &-\frac{c}{a}\frac{1}{\pi}\int_{-c+e}^{c+e}\frac{\sqrt{1-((\xi-e)/c)^2}}{x-\xi}d\xi\Bigg] - A\mu p_0\frac{e}{a}\end{aligned} \tag{5.7}$$

The solution of the first integral of the right hand side of equation (5.7) can be split into two

regions, one inside the contact zone, $|x| \leq a$, and one outside, $|x| > a$. Similarly, the second term of (5.7) can be split into a linear function inside the interval $|x-e| \leq c$ and another term outside the stick zone $|x-e| > c$. Defining $\frac{\partial g^{(1)}(x)}{\partial x}$ as the piecewise solution of the first integral in (5.7) and $\frac{\partial g^{(2)}(x)}{\partial x}$ the solution of the second integral, equation (5.7) is rewritten as

$$\frac{\partial g(x)}{\partial x} = A\mu p_0 \left[\frac{\partial g^{(1)}(x)}{\partial x} + \frac{\partial g^{(2)}(x)}{\partial x} - \frac{e}{a} \right]. \tag{5.8}$$

If no bulk tension is applied to one of the bodies, the two partial derivatives of (5.8) result in zero gradient inside the stick zone. If a component of strain is introduced to the problem by the presence of a bulk stress in the interior of one of the bodies, an offset e of the stick zone results in a non-zero difference between the two components of slip inside the stick zone. This difference is exactly Afp_0e/a, which is the last term of equation (5.8). The resultant slip gradient in a contact between two isotropic elastically similar cylinders is shown in Figure 5.6.

The only region of interest for the calculation of energy dissipation is the slip region, which is the only region where energy is dissipated. The slip is zero in the stick zone and the shear traction is zero outside the contact zone. Therefore, both these regions have zero work done. The gradient inside the slip zone is given by

$$\frac{\partial g(x)}{\partial x} = A\mu p_0 \frac{x-e}{a} \sqrt{1 - \left(\frac{c}{x-e} \right)^2}, \qquad c \leq |x-e| \leq a \tag{5.9}$$

In order to calculate the displacements, equation (5.9) needs to be integrated over the slip zone. A variable substitution is made, such that, $t = (x-e)/c$ and $\chi = (\xi - e)/c$, and the integration is done from $x = c+e$ ($t = 1$), up to the contact edge, $x = a$ ($t = (1-e/a)/(c/a)$). In order to obtain the slip equation, the following integral needs to be solved

$$\frac{1}{c}\frac{\partial g(t)}{\partial t} = A\mu p_0 \frac{c}{a} \int_1^t \chi \sqrt{1 - \left(\frac{1}{\chi} \right)^2} d\chi, \qquad 1 \leq |t| \leq \frac{1-e/a}{c/a} \tag{5.10}$$

Then, by making the substitution back to x ($x = ct + e$) and multiplying the solution of (5.10) by c/a, the function describing the slip at the interface with the presence of a bulk tension in

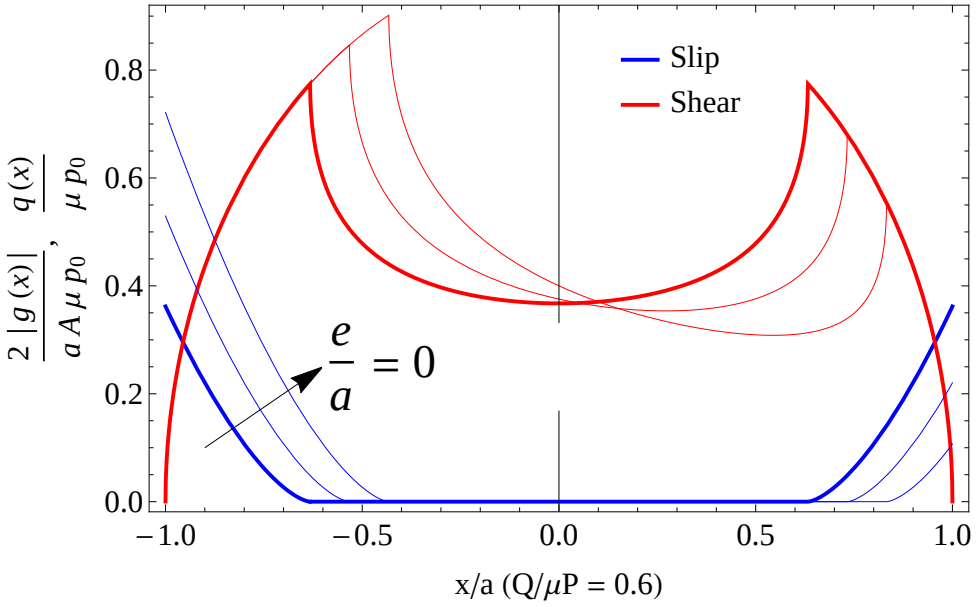

Figure 5.7: Shear traction and slip distribution for different values of the stick zone offset.

one of the bodies is given by

$$\frac{g(x)}{aA\mu p_0} = \frac{1}{2}\left[\frac{x-e}{a}\sqrt{\left(\frac{x-e}{a}\right)^2 - \left(\frac{c}{a}\right)^2} - \left(\frac{c}{a}\right)^2 \log\left(\frac{x-e}{c} + \sqrt{\left(\frac{x-e}{c}\right)^2 - 1}\right)\right]. \tag{5.11}$$

The solution in equation (5.11) is valid for the both regions of slip and also presents the correct answer for the stick zone, which is $g(x) = 0$ for $|x-e| \leq c$. The absolute slip, $|g(x)|$, and corresponding shear tractions are shown in Figure 5.7. The equations describing the shear traction and slip in the contact between two isotropic elastically similar cylinders will be compared with a numerical solution obtained via finite element analysis in §5.2.4.

5.2.3 Frictional energy dissipation

The frictional energy dissipated needs to equal the sum of work done by the frictional force at each point in contact. If the shear traction and slip are known throughout the contact interface, the work done at each point of the surface during a complete loading and unloading can be obtained. As it is shown by the Cattaneo-Mindlin solution, as the load is decreased from its maximum value, the stick zone changes in size, but the shear traction at each point in the

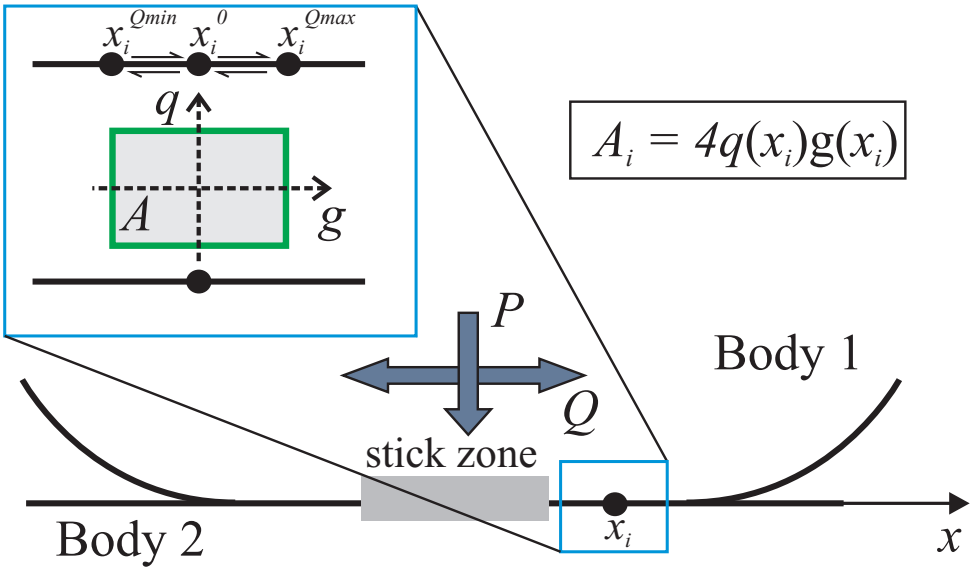

Figure 5.8: Energy dissipated at each point of the slip zone.

sliding region remains constant up to the moment when the point stops sliding. Once stuck, no work is done at that point and it will remain at rest until a reverse shear load is sufficient to cause sliding in the opposite direction. The complete load-displacement cycle of an arbitrary point in the sliding zone is illustrated in Figure 5.8. The area inside the square in the $q-g$ plot represents the work done by the frictional force at an arbitrary point. The distribution of work done along the contact interface *per unit of area*, $w(x)$, is given by

$$w(x) = 4q(x)g(x) \tag{5.12}$$

$$= 2aA\mu^2 p_0^2 \sqrt{1-\left(\frac{x}{a}\right)^2}\left[\left(\frac{x-e}{a}\right)\sqrt{\left(\frac{x-e}{a}\right)^2-\left(\frac{c}{a}\right)^2} - \left(\frac{c}{a}\right)^2 \log\left(\frac{x-e}{c}+\sqrt{\left(\frac{x-e}{c}\right)^2-1}\right)\right] \tag{5.13}$$

The distribution of work done per unit of area is given in Figure 5.9. Note that the maximum energy dissipated in the contact zone is not at the contact edge, where the peak stress occurs, but at about a distance $0.1a$ away from the edge. This location is likely to be where the most severe wear might occur and not necessarily at the point of maximum stress, the contact edge. The total energy dissipated in the system is given by the integral of equation (5.13) over the contact region. In a plane problem of length z_0 in the z direction, the total work done is given

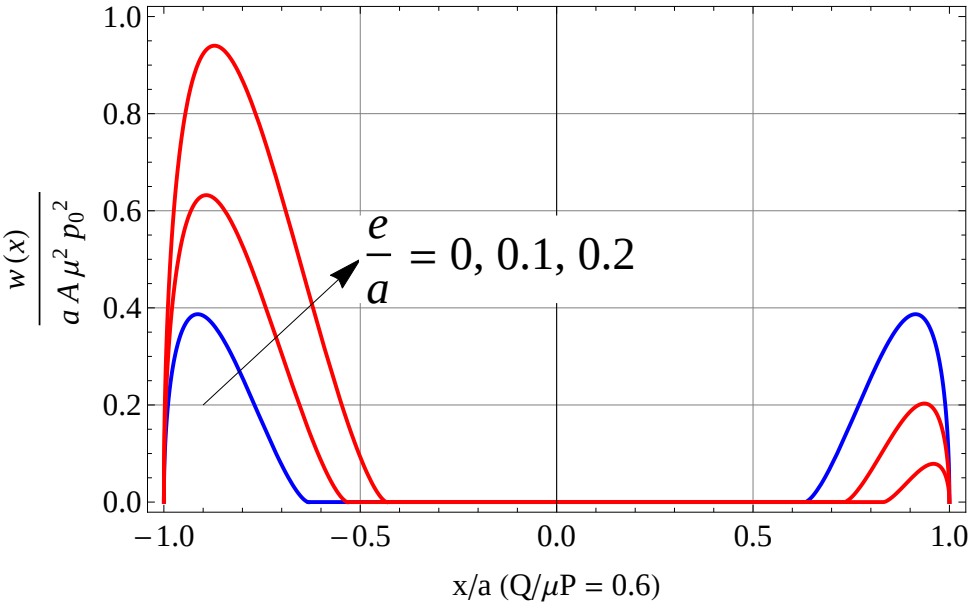

Figure 5.9: Energy dissipated per unit of area for different values of the stick zone offset ($Q/\mu P = 0.6$).

by the following equation,

$$\mathscr{W} = \int_A w(x)\,dA = \int_0^{z_0}\int_{-a}^{a} w(x)\,dx\,dz = z_0 \int_{-a}^{a} w(x)\,dx \tag{5.14}$$

5.2.4 Analysis of the energy dissipation

Comparison with finite element analysis

The equations above are compared with a finite element model in ABAQUS of a cylinder pressed onto a half-plane. The geometries of both the cylinder and plane was very large when compared with the contact zone so that the solution can be comparable to that of two half-planes. The loads applied to the model are similar to the one used in §4.2.1, but the resultant moment on each of the bodies was assured to be zero. The comparison of the analytical solutions for the shear tractions derived above with the ones obtained via finite element analysis is shown in Figure 5.10 for different values of $Q/\mu P$. The same is done for the energy dissipated, equation (5.13), but without the presence of a bulk tension (Figure 5.11). A good agreement is observed between the numerical and analytical solutions. The analytical solution for the energy dissipated and the finite element model is used next to investigate the effect of the applied shear traction and bulk tension on the total energy dissipated in the contact.

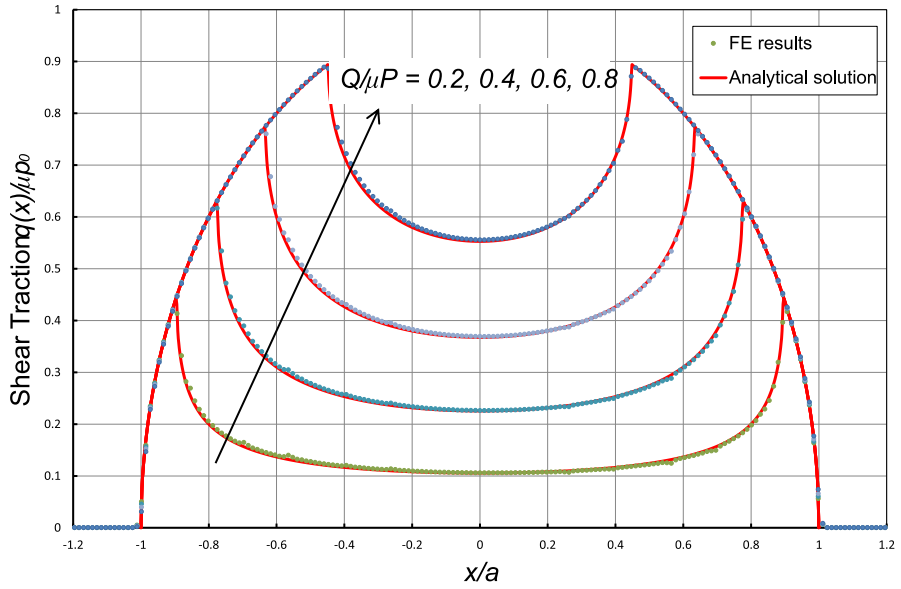

Figure 5.10: Comparison of shear traction between the analytical and numerical solutions.

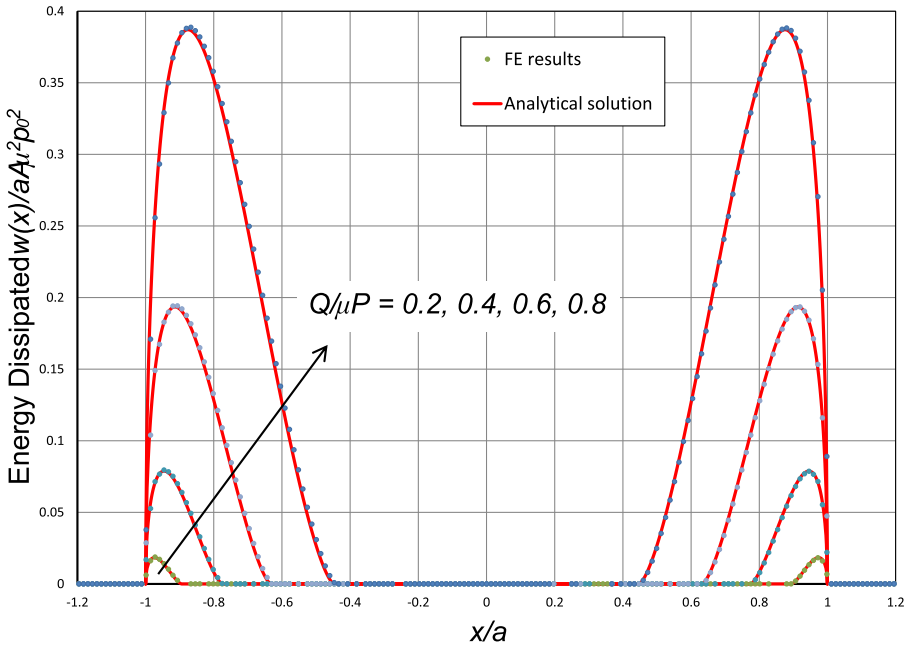

Figure 5.11: Comparison of energy dissipation per unit of area between the analytical and numerical solutions.

The effect of bulk stress on the energy dissipation

As it has been pointed out earlier in this section, the presence of a bulk load on one of the bodies in contact introduces an offset, e, to the stick zone. Because of the non-linearity of the energy dissipated in equation (5.13), the shift of the stick zone changes the total energy dissipated. The

increase in work done in one slip zone is greater than the decrease in work done on the other slip zone when an offset is added to the stick zone. The benefit of changing the position of the slip zone as a mean of varying the total energy dissipated is that it would be possible to vary the total energy dissipated while keeping the ratio Q/P constant. This approach would reduce the number of variables in the contact problem, since the varying variable, i.e. the bulk force inside one of the bodies, is of little relevance at the interface apart from the offset of the stick zone.

It is shown in Figure 5.7 the change in shear traction and slip distributions along the surface for an arbitrary load ratio $Q/\mu P = 0.6$ and with the presence of different values of bulk stress, resulting in an offset, $e = 0.0, 0.1, 0.2$. Due to the change in the shear traction and slip distributions, the energy dissipation also varies with the offset of the tick zone. By using equation (5.13), the energy dissipated per unit of area along the interface can be obtained and it is shown in Figure 5.9. The total energy dissipated, or work done by frictional force, can be obtained by using a numerical integration technique to integrate equation (5.14).

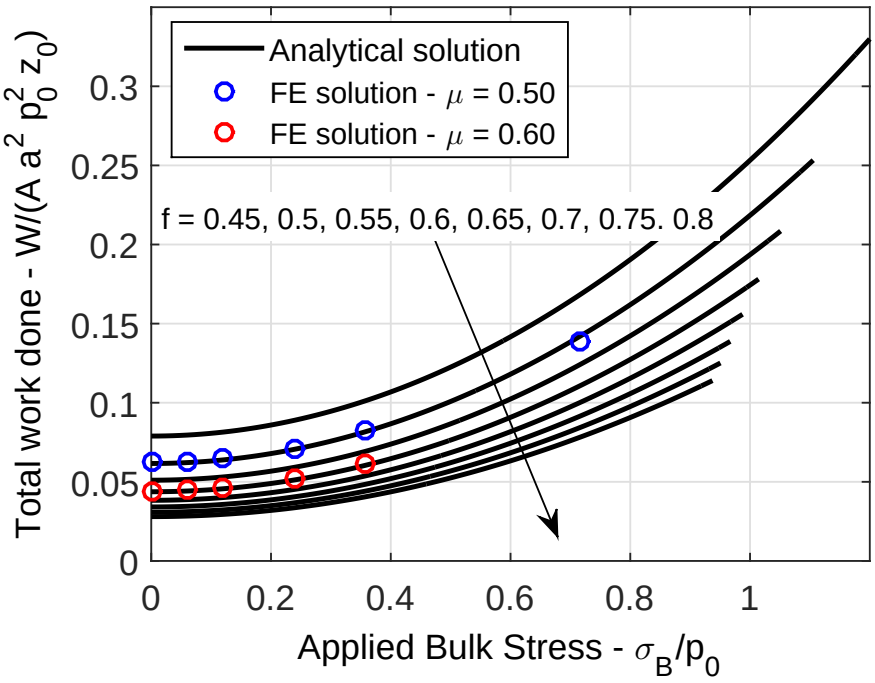

Figure 5.12: Total work done as a function of the applied bulk stress ($Q/\mu P = 0.6$).

It is also important to correlate the offset e with the correspondent bulk stress applied in an example problem. Consider a two-dimensional Hertzian contact between a cylinder and a flat plane of unitary thickness, $z_0 = 1$. The total work done at the interface as a function of the

bulk stress is given in Figure 5.12, where the applied bulk stress σ_0 is normalized by the normal contact peak stress p_0. The solution was compared with numerical results obtained via finite element analysis and a good match agreement the solutions is observed.

The effect of shear stress on the energy dissipated

Similarly to the variation of the stick zone offset, the variation of the load ratio Q/P varies the work done at the interface. However, this approach still depends on the assumption that the coefficient does not change with the Q/P load ratio. The work done per unit of area can again be obtained by making use of equation (5.13), which here can be simplified due to the absence of bulk stress, and resulting in the following expression

$$w(x) = 2aA\mu^2 p_0^2 \sqrt{1-\left(\frac{x}{a}\right)^2}\left[\left(\frac{x}{a}\right)\sqrt{\left(\frac{x}{a}\right)^2-\left(\frac{c}{a}\right)^2} - \left(\frac{c}{a}\right)^2 \log\left(\frac{x}{c}+\sqrt{\left(\frac{x}{c}\right)^2-1}\right)\right] \tag{5.15}$$

The distribution of work done at the contact interface for different values of load ratio Q/P is shown in Figure 5.13. The variation of the shear load ratio Q/P results in a symmetric dissipation of the energy on both slip zones. Similarly to the previous case, the total energy dissipation can be obtained by solving the integral in (5.14) and the variation of the energy dissipated with the applied shear load ratio is presented in Figure 5.14. However, large changes in friction do not make much difference to the energy expended, so that, experimentally, this is unlikely to be a good method of determining the coefficient of friction with good accuracy.

5.3 Discussion

The measurement of the coefficient of friction under partial slip contact is not an easy task. Some techniques for measuring the coefficient of friction have been suggested, but none has yet been very well established. The non-sliding "walking pad" test is conceptually very interesting, but the results are still inconsistent. Experimentally, there are many challenges in this test. Particularly, the identification of the shear load in the transition from stationary to rigid body

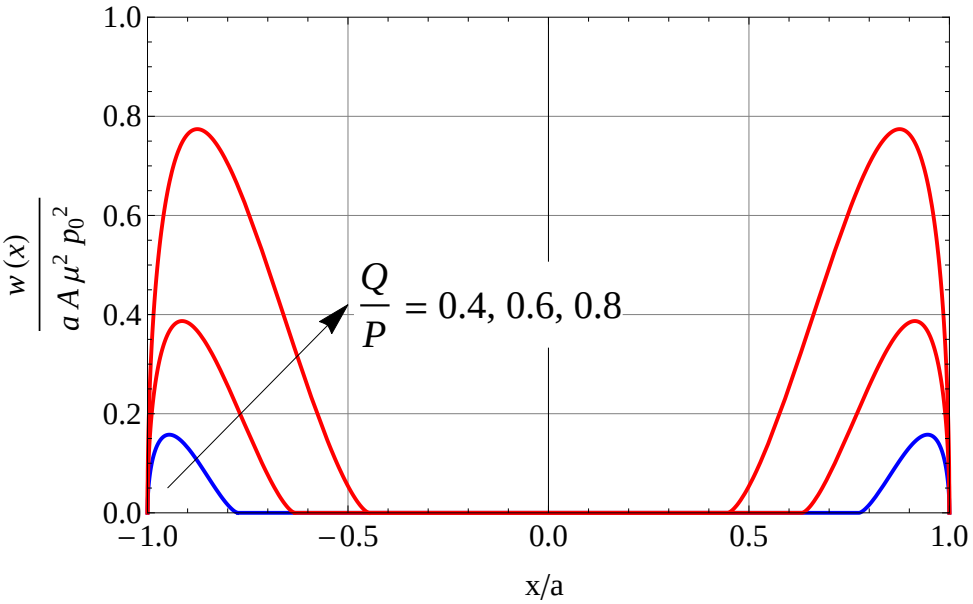

Figure 5.13: Energy dissipated per unit of area for various Q/P ratio.

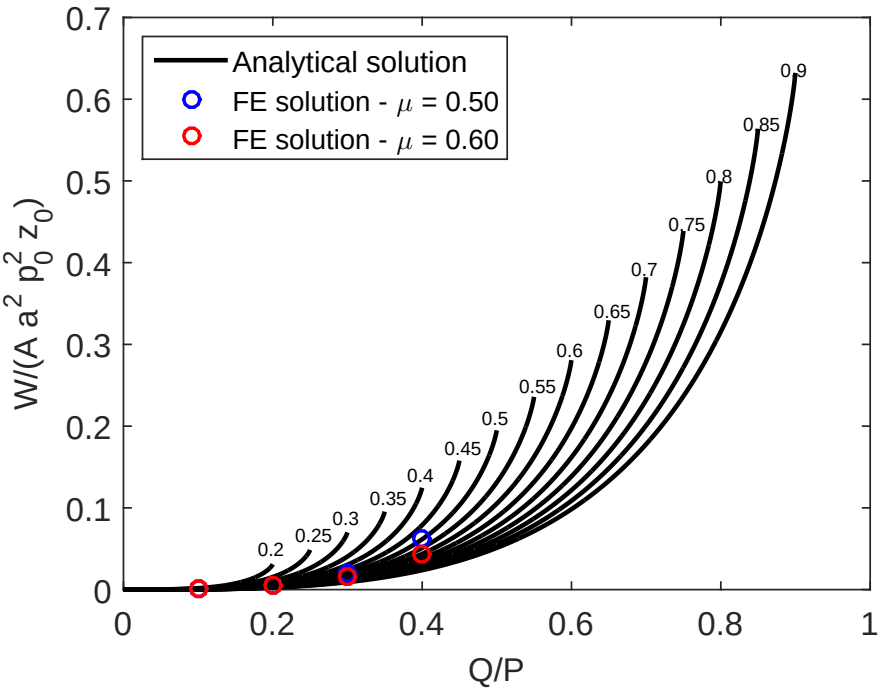

Figure 5.14: Total work done as a function of Q/P.

net displacement of the pad is difficult to precise. However, the approach of using the rate of displacement and interpolate the experimental results with the semi-analytical solution is a good alternative to measuring the coefficient of friction. This test would also benefit greatly from a dedicated rig for measuring the coefficient of friction, with force and displacement sensors located closer to the contact. The work presented in this chapter demonstrates that there are

methods available to measure the coefficient of friction in partial slip, and those are preferable for estimating the coefficient of friction in the fretting problem due to reduced surface damage in partial slip contacts when compared with gross sliding tests.

The results for the coefficient of friction between the single-crystal CMSX-4 pads and RR1000 specimen were higher than the coefficient of friction obtained with similar RR1000 pads. This results were useful in the implementation of the "corrected" coefficient of friction for the correlation of near edge stresses with fretting fatigue life in §4.3. However, due to the large scatter, particularly after each time the pad and specimen were reground, it is not possible to precisely estimate the coefficient of friction for this pair of material. It is also not apparent that there is a correlation between single-crystal orientation and friction at the interface. Further analysis are required with a larger number of samples and controlled surface finishing to draw any conclusions.

Energy based approaches for measuring the coefficient of friction has been used for the contact between spheres. However, cylindrical contacts do not have a finite displacement remote from the contact region and the challenge of using energy based methods is greater. As it was shown in this chapter, several factors may influence the energy dissipated in the contact, such as, the applied shear load and the bulk remote tension. It is possible to design an experimental procedure where one of these loads is varied and, by measuring the area of the curve for the remote displacement of a point and the applied tangential loads (i.e. the hysteresis loop of $Q-\delta$), the coefficient of friction may be calculated. Although the displacements in a two-dimensional contact do not converge to a finite value in the remote region, the total energy dissipated measured from the hysteresis loop of tangential force and remote displacements do converge. This is because the energy is dissipated only in the slip zones and, hence, provided that no other source of dissipation occur near the contact zone, the area inside the curve $Q-\delta$ must match the energy dissipated in the contact.

It is true that it is not easy to get an accurate measurement of the displacement near the contact zone and most rigs have a LVDT sensor very far from the contact. Note that, in an experimental rig, the further the measurement point moves away from the contact, the more likely it is that other sources of energy dissipation interfere with the measurements of the dis-

placements. One solution for this problem could be using digital image correlation (DIC) to calibrate the LVDT sensors placed far from the contact. If a reliable measurement of the energy dissipation can be obtained, through the measurement of the area in the hysteresis loop, then the calculation of the coefficient of friction may be obtained from the total energy dissipated.

Issues with the use of DIC may also be anticipated and perhaps the most obvious in these experiments is that one may only be able to get a measurement on the free face of the pad and/or specimen. Therefore, the alignment of the pad and specimens need to be carefully carried out, so that the edges of the pads and specimen match perfectly, i.e. their free faces are coplanar. The use of DIC in the friction, or fretting fatigue, tests could provide a more accurate hysteresis loop output, which could then be used to obtain the energy dissipated per cycle. If the energy dissipated per cycle is known, it could then be used to calculate the evolution of the coefficient of friction over the cycles as given in §5.2. In the case of fretting fatigue, the measured energy dissipation may also be used to calculate the initiation and fatigue lives. Energy dissipation criterion generally provide good accuracy and greater sensibility when compared with other criteria. A microscopic energy dissipation criterion have also shown good accuracy when compared with experimental results [Korsunsky et al., 2007].

Part II

The effect of edge-rounding on complete contact between elastically similar bodies

Chapter 6

Basic contact characteristics in terms of Williams' notch stress intensity factors

A new solution for solving the contact problem of an elastic flat punch with edge rounding pressed against an elastically similar half-plane is presented in the next two chapters. In chapter 6, the concept of using a three-quarter plane as an asymptote to the edge of the flat and rounded punch contact is introduced. Basic characteristics of the contact are also investigated, such as the contact law and the maximum contact peak pressure. The partial slip problem is solved in chapter 7. Edge asymptotes to describe the contact tractions very close to the edge of contact are introduced. They can be thought of as asymptotes to the asymptote problem. The work presented in the next two chapters is described in detail in [Fleury et al., 2015a,b].

6.1 Introduction

The partial slip problem of a flat punch with rounding at the edges has been the target of researchers in the past fifteen years, particularly because of its relevance to the dovetail blade to disc assembly in aero-engines. The normal pressure distribution for the frictionless contact between a flat and rounded punch and a half-plane under normal loading was first presented by Steuerman [1949]. Ciavarella et al. [1998] solved the singular integral equations based on uncoupled half-plane theory to provide a solution for the contact tractions and interior stress field incorporating a rounded edge on a flat punch pressed onto an elastic half-plane. Friction

and shear tractions were included in the analysis and a detailed study of the strength of the contact as a function of the radius of the rounded edge and the finite punch width was presented. The partial slip solution for the inclined finite elastic punch problem was later presented in a closed form by Goryacheva et al. [2002]. Both Ciavarella's and Goryacheva's solutions have been used in the analysis of crack nucleation in fretting problems to calculate the state of stress near the contact edge of an elastic finite flat punch with the presence of rounding at the corners. However, they are only truly applicable when the coefficient of friction at the interface is very low, when the punch can be thought of as rigid and the plane incompressible, or when both bodies can be approximated by elastically similar half-planes. Although the contact tractions and interior stresses can be fully obtained from these solutions, finite element analysis solutions of the elastic flat and rounded punch problem have shown that shear traction develops at the edge of the contact when only the normal load is applied, suggesting that the geometrical coupling often cannot be neglected and the approximation by half-planes is not valid. Furthermore, designing a geometry for carrying out laboratory experiments that are representative in terms of stresses and slip local to the contact edge of blade roots in the engine remains a difficult task.

An alternative and compelling approach to the contact problem based on asymptotic solutions has been first introduced by Sackfield et al. [2003]. The approach of using asymptotes is capable of fully characterizing the state of stress local to the edge and to reproduce in laboratory problems with local conditions matched to more complex geometries found in the engine, for example. Note that the edge of the contact is generally where cracks are likely to nucleate due to the high stress concentration and, in many cases, the existence of a slip zone where irreversible deformation is likely to occur. Several authors have looked at the semi-infinite rigid punch partial slip problem pressed onto an elastic half-plane by using an asymptotic approach [Mugadu et al., 2004; Dini and Hills, 2004; Dini et al., 2005]. A solution for an inclined finite and semi-infinite punch was also presented by Sackfield et al. [2005]. In these solutions, a semi-infinite punch was used by taking Ciavarella's finite punch solution and letting the dimensions of the punch go to infinity whilst keeping the radius finite (Figure 6.1). In doing so, a restriction is added to the problem since the half-plane approximation is no longer possible when the observation point moves away from the radiused edge. In that case, and in the presence of friction,

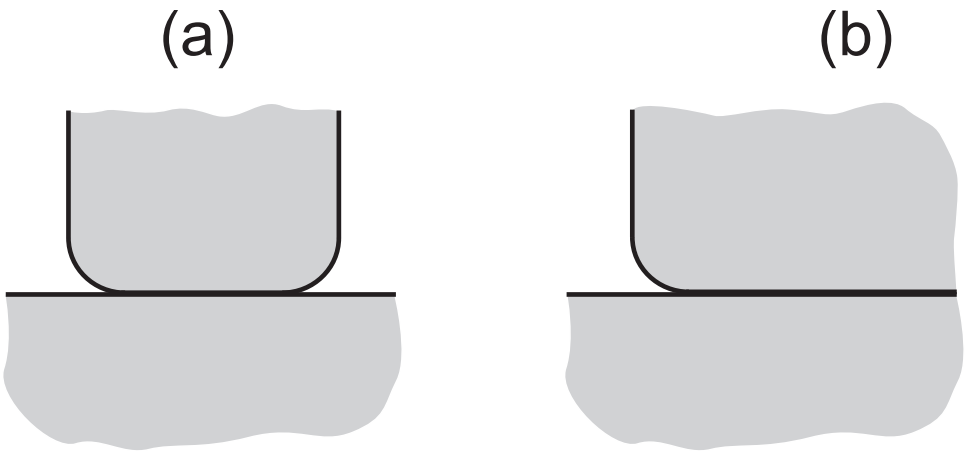

Figure 6.1: Example of (a) a finite flat punch with rounded edges and (b) a semi-infinite punch with rounded edge.

the problem is uncoupled only if the punch is rigid and the half-plane incompressible.

The problem of an elastically similar flat semi-infinite punch with rounded edges was studied by Banerjee et al. [2009]. Banerjee's work presented a formulation for the normal traction using a finite element calibration, which was able to reproduce with some accuracy the shape of the normal pressure distribution near the rounded edge. The solution was written in terms of dimensional contact parameters corresponding to the bounded and singular asymptotes of the contact pressure. The work, however, assumed a frictionless interface between the punch and the half-plane, so that shear tractions were not taken into account.

In this work, the problem of a semi-infinite elastic flat punch with rounded edges is re-examined by taking the outer solution as that of a three quarter plane notch problem. If the coefficient of friction is sufficient to maintain adhesion at the corner in the absence of the rounding, it will also be high enough to maintain stick at all interior points [Churchman and Hills, 2006]. Furthermore, provided that the radius of the rounded edge is sufficiently small for its influence to be felt wholly within the region in which the Williams' asymptote applies, the interfacial boundary will also be stuck at the interior of contact for the punch with edge rounding. Then, the far region of the problem is, indeed, that of the three quarter plane notch problem and Williams' solution can be used. It is proposed, here, that the contact parameters, i.e. the size of the contact, the peak pressure, and the size of the slip zone, be obtained as a function of the Williams' stress intensity factors, K_I and K_{II}. The mode I and mode II stress intensity factors will be used as the input of the problem and later correlated with local dimensional scaling

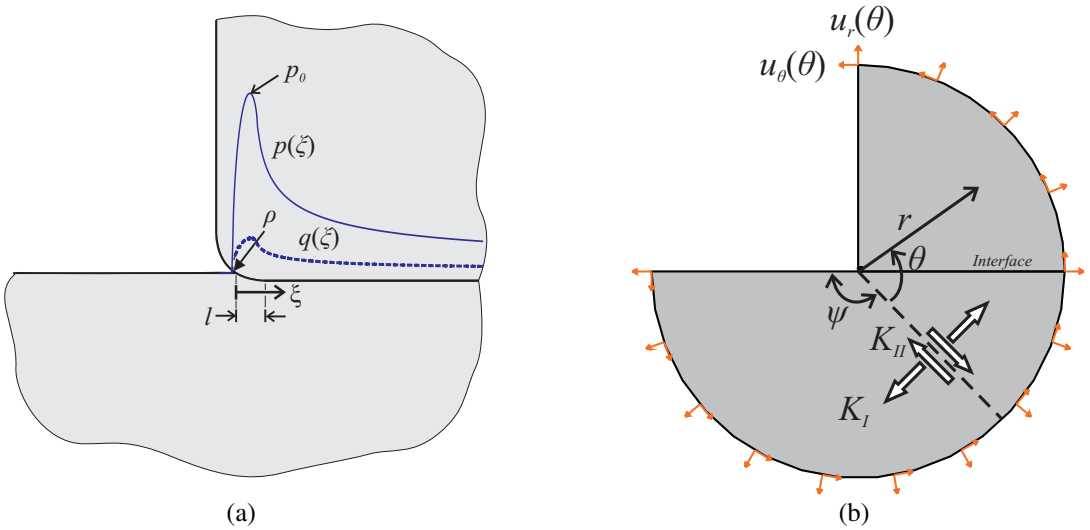

Figure 6.2: (a) Flat and rounded elastic contact between two elastically similar bodies; (b) Finite element model of a three quarter plane with a rounded edge.

factors for the shear and normal tractions.

Let some of the contact parameters be defined; the contact size is hereafter defined as the length of the rounded edge, l, which is in contact with the half-plane, and ρ is the radius of the rounded edge (Figure 6.2a). The size of l is the only part of the contact that is 'incomplete'; i.e. the length l varies with the applied load. Both the plane and the punch have Young's modulus, E, and Poisson's ratio, ν, and plane strain is assumed. Although the problem is treated as a monolith, the elastic stiffness of the material will be represented here by the quantity E^*, where $E^* = 4E/(1-\nu^2)$ and which is a composite equivalent stiffness when both bodies are elastically similar in a contact problem.

From Williams' solution, the state of stress can be written down in the form

$$\sigma_{ij}(r,\theta) = K_I r^{\lambda_I - 1} f_{ij}^{I}(\theta) + K_{II} r^{\lambda_{II} - 1} f_{ij}^{II}(\theta), \tag{6.1}$$

where the quantities $\lambda_I, \lambda_{II}, f_{ij}^{I}(\theta), f_{ij}^{II}(\theta)$ depend on the notch angle. In the case of a quarter plane bonded to an elastically similar half-plane, the symmetric and antisymmetric eigenvalues are given by $\lambda_I = 0.5445$ and $\lambda_{II} = 0.9082$, respectively. Note that the eigensolutions uncouple along the bisector line, i.e. $f_{r\theta}^{I}(0) = f_{\theta\theta}^{II}(0) = 0$, and the stress intensity factors can be found from the stress components along the notch's bisector line (Figure 6.2b),

$$K_I = \lim_{r\to 0} \frac{\tilde{\sigma}_{\theta\theta}(r,0)}{r^{\lambda_I - 1}}, \tag{6.2a}$$

$$K_{II} = \lim_{r\to 0} \frac{\tilde{\sigma}_{r\theta}(r,0)}{r^{\lambda_{II} - 1}}, \tag{6.2b}$$

where $\tilde{\sigma}_{ij}$ are the components of stress in the far field and are not perturbed by the presence of the rounded edge.

The formulation for the contact parameters in terms of the remote loading is given next in this chapter but, first, the numerical procedure used in the calibration of the derived solutions is presented. The stress intensity factors K_I and K_{II} will be used as the input to the problem through prescribed displacements (see §6.2). Pure mode *I* and pure mode *II* loading will be analysed separately first and, later, a combination of both modes will be studied. The analysis of each loading mode separately is used to obtain an initial insight into the solution of the problem, although it is known that pure modes of loading are extremely unlikely to happen in a real contact problem; when either a normal load, P, or a shear load, Q, is applied at the interface, a mapping from the $P \times Q$ space to the $K_I \times K_{II}$ space results in a combination of both modes *I* and *II*. This chapter is restricted to basic characteristics of the contact field in terms of the remote loading, where the study of the slip zone, for example, is not yet covered. This is an introductory, and yet relevant, step to a more complete contact formulation using asymptotes centred at the edge of contact presented in chapter 7.

6.2 Numerical procedure

Finite element analysis was used to obtain the contact parameters and to calibrate a general semi-analytical solution to the problem of a semi-infinite punch pressed onto a half-plane. The problem is treated as a three quarter plane notch, with the contact interface placed at an angle of $\pi/4$ from the bisector line. Displacement boundary conditions are prescribed, such that, modes *I* and *II* loading are applied to the problem independently. Along the bisector line, $\sigma_{r\theta}(0)$ is zero when a pure mode *I* loading is applied, and is the only non-zero component of stress along that line for a pure mode *II* loading. This property of the solution was used to verify that appropriate boundary conditions were indeed being applied and that an independent control of

modes I and II was achieved. The displacements applied were derived by Karuppanan [2007] and are written for plane strain as follows

$$\left\{ \begin{array}{c} u_r(\theta) \\ u_\theta(\theta) \end{array} \right\} = \frac{1+\nu}{E} R^{\lambda_I} K_I \left\{ \begin{array}{c} u_r^I(\theta) \\ u_\theta^I(\theta) \end{array} \right\} + \frac{1+\nu}{E} R^{\lambda_{II}} K_{II} \left\{ \begin{array}{c} u_r^{II}(\theta) \\ u_\theta^{II}(\theta) \end{array} \right\}, \tag{6.3}$$

where

$$u_r^I(\theta) = -\frac{-(\lambda_I - 1)\cos(\lambda_I + 1)\theta \frac{\sin(\lambda_I - 1)\psi}{\sin(\lambda_I + 1)\psi} - (\kappa - \lambda_I)\cos(\lambda_I - 1)\theta}{\lambda_I(\lambda_I + 1)\left(1 - \frac{\cos(\lambda_I - 1)\psi}{\cos(\lambda_I + 1)\psi}\right)}, \tag{6.4a}$$

$$u_r^{II}(\theta) = -\frac{(\lambda_{II} - 1)\sin(\lambda_{II} + 1)\theta \frac{\cos(\lambda_{II} - 1)\psi}{\cos(\lambda_{II} + 1)\psi} + (\kappa - \lambda_{II})\sin(\lambda_{II} - 1)\theta}{\lambda_{II}(\lambda_{II} - 1)\left(1 - \frac{\cos(\lambda_{II} - 1)\psi}{\cos(\lambda_{II} + 1)\psi}\right)}, \tag{6.4b}$$

$$u_\theta^I(\theta) = -\frac{(\lambda_I - 1)\sin(\lambda_I + 1)\theta \frac{\sin(\lambda_I - 1)\psi}{\sin(\lambda_I + 1)\psi} - (\kappa + \lambda_I)\sin(\lambda_I - 1)\theta}{\lambda_I(\lambda_I + 1)\left(1 - \frac{\cos(\lambda_I - 1)\psi}{\cos(\lambda_I + 1)\psi}\right)}, \tag{6.4c}$$

$$u_\theta^{II}(\theta) = -\frac{(\lambda_{II} - 1)\cos(\lambda_{II} + 1)\theta \frac{\cos(\lambda_{II} - 1)\psi}{\cos(\lambda_{II} + 1)\psi} - (\kappa + \lambda_{II})\cos(\lambda_{II} - 1)\theta}{\lambda_{II}(\lambda_{II} - 1)\left(1 - \frac{\cos(\lambda_{II} - 1)\psi}{\cos(\lambda_{II} + 1)\psi}\right)}. \tag{6.4d}$$

The quantity θ is the angular coordinate from the notch bisector and ψ is the angle from the bisector to the free surface (Figure 6.2b). For a punch with internal angle $\pi/2$, $\psi = 3\pi/4$ and the eigenvalues are $\lambda_I = 0.5445$ and $\lambda_{II} = 0.9082$. The prescribed displacements are applied at a distance $R = 100$ mm away from the centre and the rounded edge has a radius $\rho = 1$ mm. The ratio ρ/R was chosen to be large enough, such that the effects of the rounded edge are very localized and there is no interference from the boundary conditions on the traction near the contact edge. The ABAQUS "DISP" user subroutine was used to define the displacements as a function of the cylindrical coordinate θ as given in equation (6.3). The subroutine is presented in appendix C.3. Plane strain was assumed and an arbitrary material with $E = 100$ GPa and $\nu = 0.3$ was used in the analysis.

The mesh used is shown in Figure 6.3 and two dimensional elements with reduced integration, CPE4R, were used. A convergence analysis was used to determine the element size near the transition from the rounding to the flat and an element size of $h_e = 0.0005\rho$ was chosen in that zone. Note that, although the loading multipliers are arbitrarily chosen as the input of the

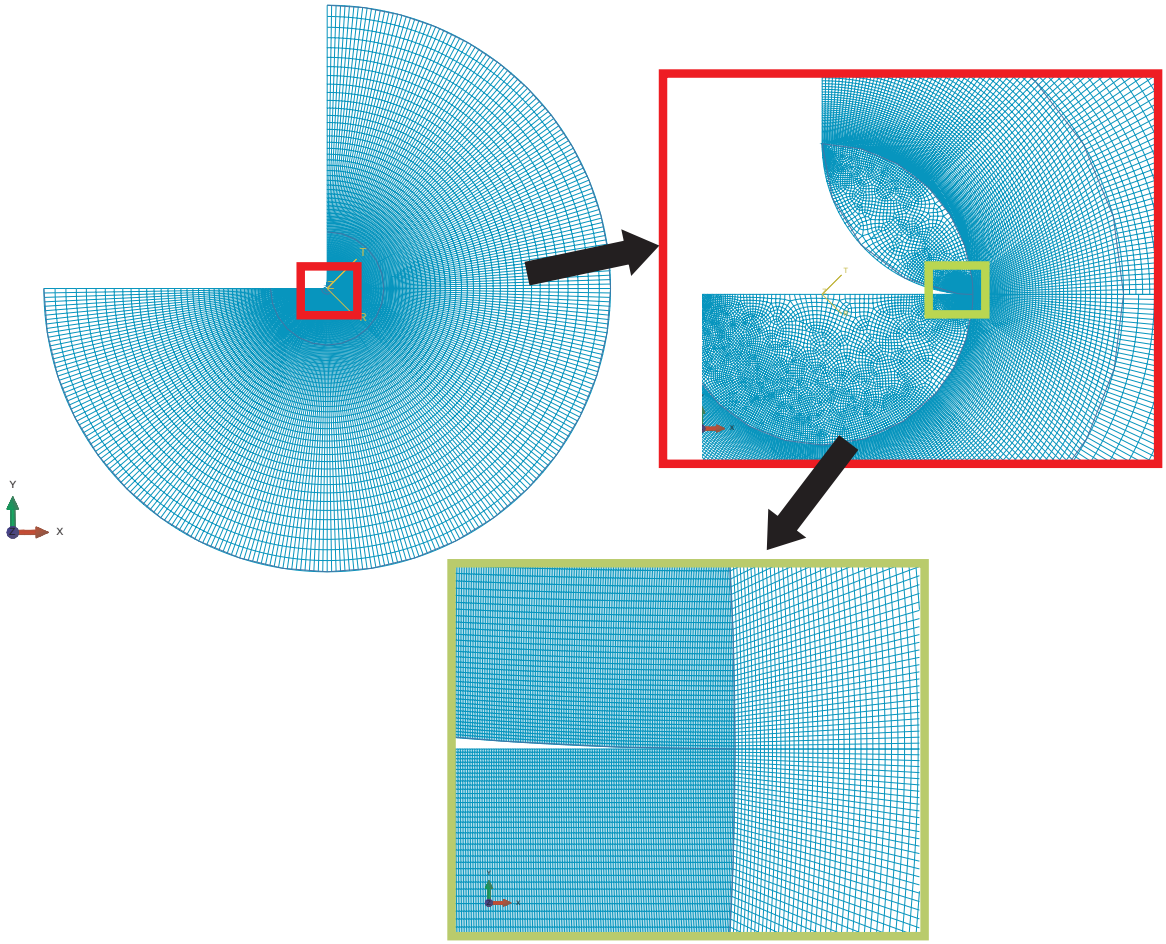

Figure 6.3: Finite element mesh used in the quarter plane punch on a half-plane problem.

problem, it is essential that the length of the contact be much smaller than the radius, $l \ll \rho$, in order for the half-plane assumption to be valid near the contact edge. Furthermore, the signs of the load multipliers were chosen to assure compression at the contact interface for both modes *I* and *II* loading; negative K_I and positive K_{II}.

Both mode *I* and *II* loading induce simultaneous normal and shear tractions on the interface. For a pure mode *I* loading, for example, the ratio of the shear to normal traction $|q(\xi)|/p(\xi)$ along the interface, in the absence of the edge rounding, is 0.543. A perturbation, due to the rounding, will exist near the edge of the punch, but in the interior of the contact, far from the edge, this ratio will hold. Because both normal and shear forces are introduced simultaneously, the problem is therefore one of proportional loading and, as long as the coefficient of friction is higher than the $|q(\xi)|/p(\xi)$ ratio, a fully stuck shear traction distribution, proportional to the normal pressure, is expected. Due to an inappropriate numerical strategy, a Mindlin-Cataneo

type partial slip solution was initially obtained when solving the problem in one single load step, as if the normal and shear parts of the matrix were being solved sequentially in the scheme adopted by the solver, rather than simultaneously. However, a correct formulation of the continuum problem demands that an incremental formulation is used. Hence, 100 time steps were subsequently used to ramp up the load to an arbitrarily chosen value. The incremental loading solution reduces the impact of the partial slip solution obtained in each individual time step; the higher the number of load steps, the smoother the numerical solution of the tangential traction. The solutions obtained numerically via finite element analysis with a Coulomb friction model are used to calibrate the semi-analytical formulation of the contact law and peak pressure, in terms of K_I and K_{II}.

6.3 Contact formulation under pure mode *I* loading

6.3.1 Stress analysis of pure mode *I*

In a pure mode I loading, for a true three quarter plane with sharp internal corner the components of stress $\sigma_{rr}(r,\theta)$ and $\sigma_{\theta\theta}(r,\theta)$ are symmetric about the bisector line, whilst $\sigma_{r\theta}(r,\theta)$ is anti-symmetric (Figure 6.4). The components of stress along the bisector line are shown in Figure 6.5. Furthermore, the ratio between the two non-zero components when $r/\rho \gg l$, i.e. when the observation point is far from the rounded corner and the problem behaves as a true tree-quarter plane, can be deduced from the quantities $f^I_{rr}(\theta)$ and $f^I_{\theta\theta}(\theta)$ of equation (6.1). These quantities are fully defined by the notch's internal angle, 2ψ, and the expressions for calculating $f^I_{ij}(\theta)$ can be found in the work of Karuppanan [Karuppanan, 2007]. For the quarter plane punch problem on an elastic half-plane, the internal angle is $2\psi = 3\pi/2$ and one finds that along the bisector line, $f^I_{\theta\theta}(0)/f^I_{rr}(0) = 1.47$. The ratio between the stress components $\sigma_{\theta\theta}(r,0)/\sigma_{rr}(r,0)$ obtained by finite element method converges to this analytical value with excellent accuracy; the relative error with respect to the analytical solution is less than 0.1% for points at r greater than ten times the radius ρ.

The contact tractions for different values of K_I were also obtained via finite element analysis. The convention adopted is that a positive normal traction is compressive between the

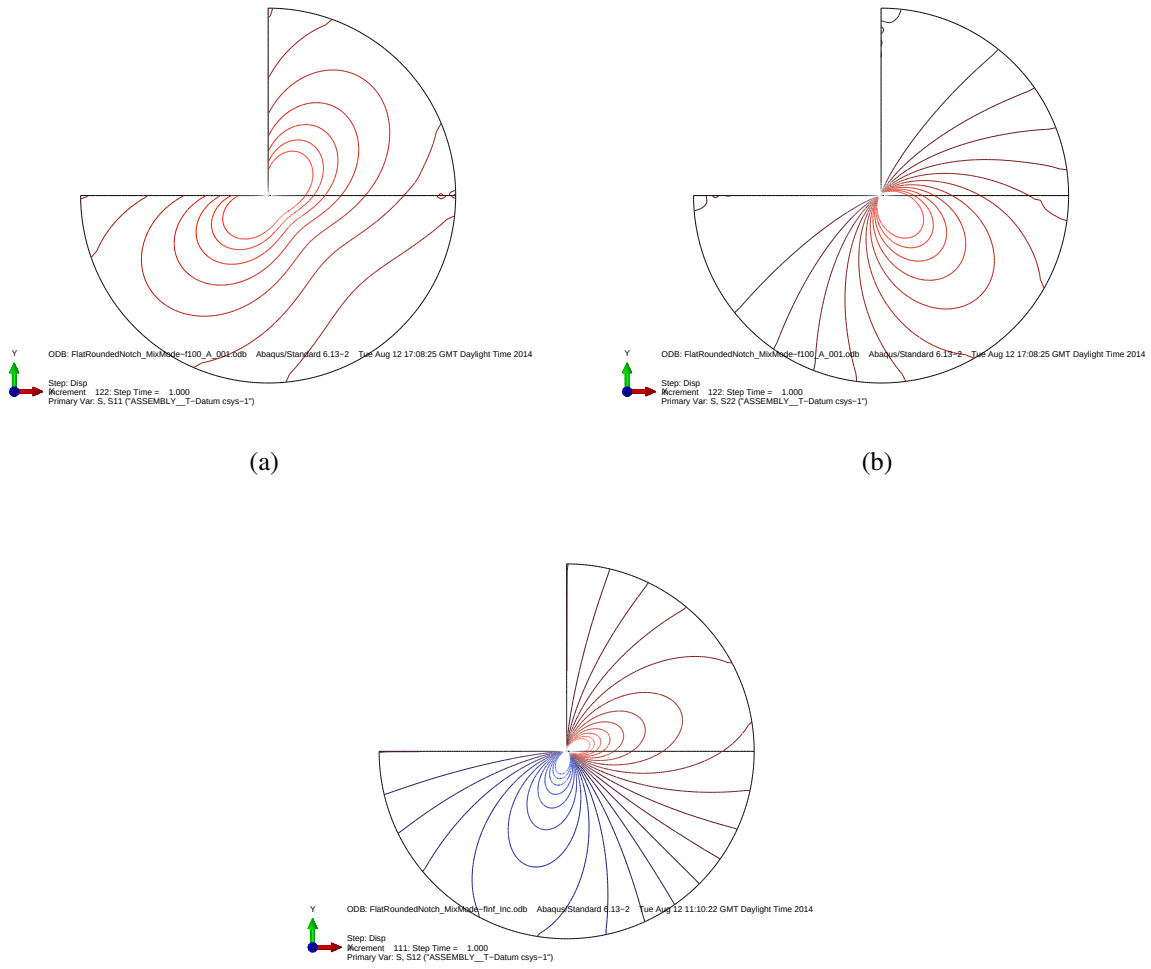

Figure 6.4: Finite element solution of the stress field for pure mode I loading; symmetric (a) $\sigma_{rr}(r,\theta)$ and (b) $\sigma_{\theta\theta}(r,\theta)$; and anti-symmetric (c) $\sigma_{r\theta}(r,\theta)$. The scale blue and red represent positive and negative stresses, respectively.

two bodies; and a positive shear traction is that, in which, a shear force acts in the direction of positive r on the punch. As mentioned previously, the contact opens when K_I is positive, i.e. the surfaces are not in contact, and a positive contact pressure exists when a negative K_I is applied. The tangential traction for a negative K_I acts on the punch in the direction of negative r along the interface, being, therefore, negative in sign with the convention adopted. Both normal and tangential tractions for different values of K_I are shown in Figure 6.6. An appropriate normalization in terms of the contact size, the material properties and length dimensions of the problem was used to compare the solutions with different values of K_I. The coordinate ξ is normalised by the contact length, l, and a dimensional analysis was done for the normalisation

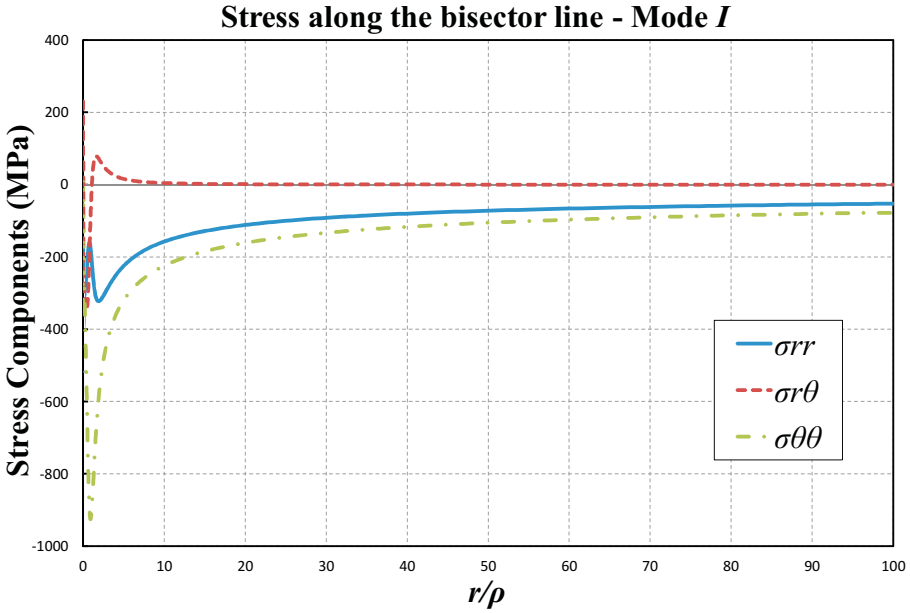

Figure 6.5: State of stress in polar coordinates along the bisector line a pure mode I loading case with $K_I = 62.67$ N.mm$^{-1-\lambda_1}$.

of the contact tractions (see §6.3.3). The finite element analysis results are used in the next section to calibrate a semi-analytical formulation for the contact size and peak stress.

6.3.2 Contact law under pure mode *I*

An expression for the contact law under pure mode I loading is derived. The length of the contact is written in terms of the stress intensity factor, K_I, and the remaining independent variables of the problem. The independent variables are: the stress intensity factor, K_I, the composite elastic stiffness, E^*, and the radius of the rounded edge, ρ. Note that the radius of the rounded edge is the only physical length dimension of the problem, since the punch is semi-infinite and the half-plane, by definition, has no length dimension. A generic expression for the contact size, l, can be written as a power law in terms of the independent variables, such that,

$$l^3 = \Lambda_I K_I{}^m E^{*n} \rho^p, \tag{6.5}$$

where m, n and p are unknown exponents, and Λ_I is a dimensionless multiplier. The exponents m, n and p are used here only as unknowns in the intermediate step of the dimensional analysis and should not be mistaken with the unknowns in the other dimensional analyses of this chapter,

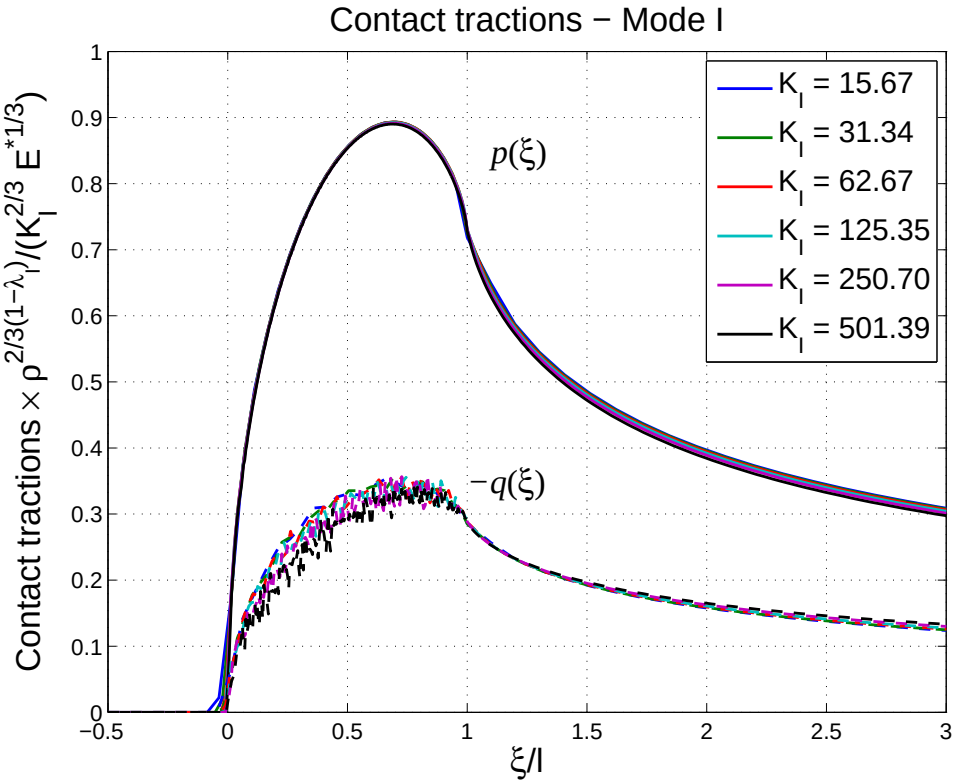

Figure 6.6: Normalized normal traction, $p(\xi)$, and negative shear traction, $-q(\xi)$, for different values of applied K_I.

where similar symbology is used for the exponents.

A dimensional analysis may be conducted to determine the exponents m, n and p. Substituting the quantities in equation (6.5) by their dimensions and equating both sides of the equation in terms of the dimensions of force, $[F]$, and of length, $[L]$, separately, two equations are obtained for the exponents m, n and p. It is then possible to rewrite the contact law in terms of one of the exponents only and use the finite element calibration to obtain the value of the exponent. The algebra and calibration of the contact law is presented in appendix C.1.1. It was found that the exponent of the K_I term, m, tends to 2 as K_I decreases. An alternative way to write down the dimensionless equation is by a power series representation, where the first term has a power 2. This work will be restricted to situations where the contact length is much smaller than the radius ρ, such that the half-plane assumption can be used in the surroundings of the rounded edge in contact and higher order terms neglected. The value of the multiplier can also be obtained from the calibration and it was found that $\Lambda_I = 13.08$. Note that, the values of the exponent, m, and multiplier, Λ_I, obtained in the calibration are valid not only for the specific

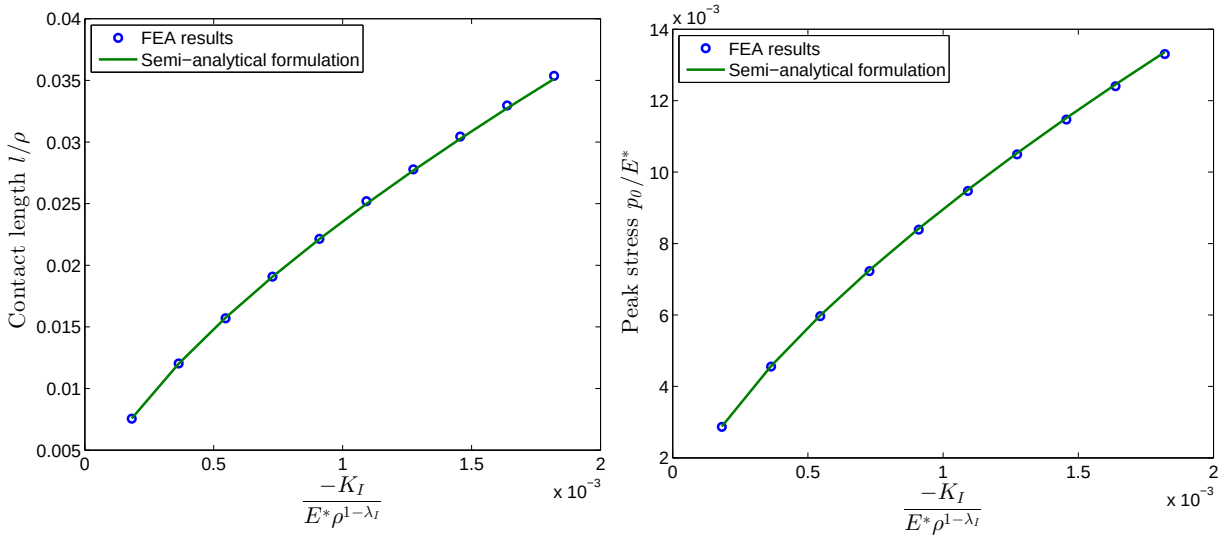

(a) (b)

Figure 6.7: Comparison between finite element analysis results and analytical formulation under pure mode I of (a) contact length and (b) peak stress.

problem analysed, but the dimensional analysis of the problem means that these results are true for any material and rounded edge radius combination.

The final expression for the contact law under pure mode I is given by

$$\left(\frac{l}{\rho}\right)^3 = 13.08\left(\frac{-K_I}{E^*\rho^{(1-\lambda_I)}}\right)^2, \tag{6.6}$$

and a comparison with finite element analysis results is shown in Figure 6.7a. Note that the error of the analytical solution increases at higher loads. This occurs because the contribution of higher order terms that describe the contact law becomes more and more relevant at higher load levels. For higher loads, one may write the contact law as a power series where the expression given in (6.6) is the first term in the series.

6.3.3 Peak stress as a function of K_I

The peak contact stress, p_0, can also be written down as a function of the independent variables of the problem for the pure mode I loading case,

$$p_0{}^3 = \Pi_I K_I{}^m E^{*n} \rho^p, \tag{6.7}$$

where the multiplier Π_I and the exponents m, n and p, are to be found [1]. In a similar manner to the approach used in the contact law formulation, a dimensional analysis of equation (6.7) can be used to reduce the number of unknown variables. If the dimensions of force, $[F]$, and of length, $[L]$, are analysed separately, two equations are obtained for the exponents m, n and p and equation (6.7) can be written in terms of the exponent coefficient m only. The algebra and results from the finite element calibration are shown in appendix C.1.2. The value of the exponent was found to be $m \simeq 2$. The only missing parameter to correlate completely the peak stress p_0 with the independent variables is the multiplier Π_I.

The contact tractions in Figure 6.6 were normalised by $\rho^{2(1-\lambda_I)/3}/{K_I}^{2/3}{E^*}^{1/3}$ and the maximum normalised peak stress can be used to obtain the value of the multiplier Π_I, which yields $\Pi_I \simeq 0.72$. Hence, the expression for the peak stress in a pure mode I loading case is given by

$$\left(\frac{p_0}{E^*}\right)^3 \simeq 0.72 \left(\frac{-K_I}{E^* \rho^{(1-\lambda_I)}}\right)^2. \tag{6.8}$$

The quality of equation (6.8) compared with the finite element solution output is shown in Figure 6.7b.

Both the expressions obtained for the contact length and peak stress as a function of the applied mode I stress intensity factor are valid for any material property and rounded edge radius. Note that the solution assumes that both the punch and the half-space have elastically similar isotropic materials and that the expressions obtained are only valid if no mode II loading exists; $K_{II} = 0$. Next a similar approach will be used for the pure mode II loading. Once the formulations for both pure modes are obtained, one may proceed with an analysis of a problem in which both modes exist simultaneously.

[1] The exponents m, n and p are simply unknowns to be found in the dimensional analysis and should not be mistaken with the unknown exponents in equation (6.5).

6.4 Pure mode *II* loading

6.4.1 Stress analysis of pure mode *II*

In contrast to the mode *I* case, the state of stress under pure mode *II* loading is anti-symmetric for the components of stress $\sigma_{rr}(r,\theta)$ and $\sigma_{\theta\theta}(r,\theta)$ with respect to the bisector line, and symmetric for $\sigma_{r\theta}(r,\theta)$ (Figure 6.8). Therefore, there is only one non-zero component of stress, $\sigma_{r\theta}(r,0)$, along the bisector. The remaining components non-zero only in the zone close to the edge rounding. The state of stress along the notch's bisector is shown in Figure 6.9. It can be seen that the edge rounding causes a perturbation in the stresses within the region $r < 10\rho$, but for r greater than 10ρ the stress field is in a pure mode *II* state. Hence, as long as there is no slip on the interface in the interior of the contact, one finds that the state of stress in the semi-infinite punch on a half-plane in the far field is similar to that of the three quarter plane notch.

The contact tractions for the pure mode *II* loading are shown in Figure 6.10 with an appropriate normalization with respect to the independent variables and the mode *II* stress intensity factor, K_{II}. The normalization is detailed in §6.4.3. In order for the contact to experience positive normal tractions, the sign of K_{II} needs to be positive. In that case, the shear force acting on the punch is in the direction of positive r and, therefore, is positive in sign. Furthermore, by loading the problem in a pure mode *II* state, and with advancing contact size, the interface sees both normal and shear tractions increasing simultaneously as K_{II} is ramped up to its defined value. Hence, as for the pure mode *I* case, as long as the coefficient of friction is higher than the ratio between the resultant normal and shear tractions on the interface, $|q(\xi)|/p(\xi) = 0.2189$, no slip occurs. Although both pure mode *I* and *II* have shown no slip as the problem is loaded incrementally, it is perfectly reasonable to assume that for some combination of K_I and K_{II} a partial slip situation near the edge may occur. Slip will be dependent not only on the combination of both applied K_I and K_{II}, but also on the load history of the problem, i.e. the path taken in the $K_I \times K_{II}$ space to reach the final point. The contact parameters obtained for different values of K_{II} are used next in the calibration of the contact length and peak stress formulations.

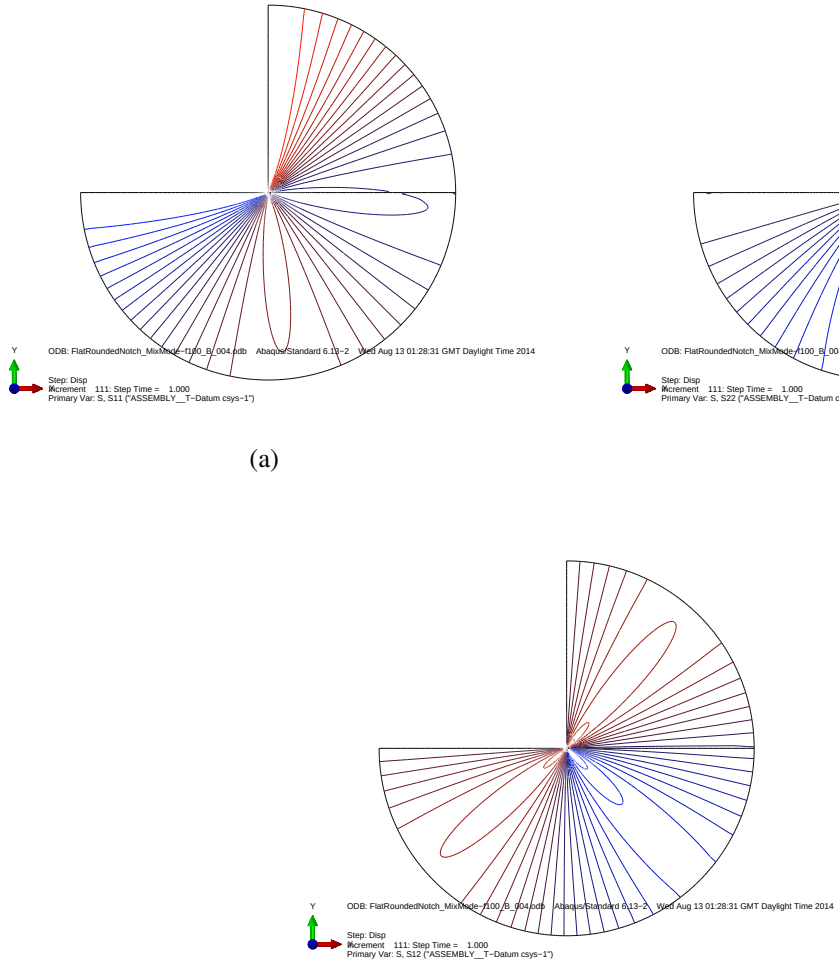

(a) (b)

(c)

Figure 6.8: Finite element solution of the stress field for pure mode *II*; anti-symmetric (a) $\sigma_{rr}(r,\theta)$ and (b) $\sigma_{\theta\theta}(r,\theta)$; and symmetric (c) $\sigma_{r\theta}(r,\theta)$. The scale blue and red represent positive and negative stresses, respectively.

6.4.2 Contact law under pure mode *II*

A similar approach to the one used in §6.3.2 is used for obtaining the contact law formulation under pure mode *II* loading. A dimensional analysis is carried out with the independent variables of the problem and the algebra used in the dimensional analysis is presented in appendix C. The contact length obtained via finite element analysis is then used in the calibration. For the pure mode *II* loading case, and for values of K_{II} sufficiently small, it was found that the exponent of the K_{II} term is approximately 2 and the multiplier $\Lambda_{II} = 15.66$. The final expression

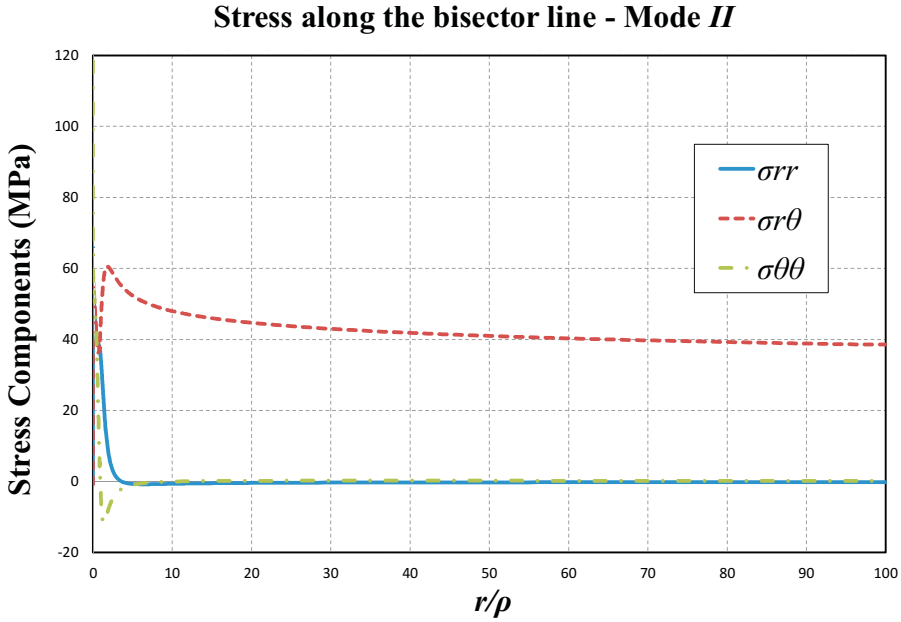

Figure 6.9: State of stress in polar coordinates along the bisector line in a pure mode II loading case with $K_{II} = 46.89$ N.mm$^{-1-\lambda_{II}}$.

for the contact law under pure mode II loading is given by

$$\left(\frac{l}{\rho}\right)^3 = 15.66 \left(\frac{K_{II}}{E^* \rho^{(1-\lambda_{II})}}\right)^2. \tag{6.9}$$

Again, it is worth noting that as K_{II} increases the error of the analytical solution increases and that the solution is valid for small loads, such that the higher order terms that describe the contact law can be neglected.

6.4.3 Peak stress as a function of K_{II}

The derivation of the formulation for the peak stress under pure mode II was also carried out as described in §6.3.3. The algebra of the dimensional analysis is shown in appendix C.1.2. The calibration via finite element analysis of the problem with different values of K_{II} was used to determine the unknown exponent correlating the peak stress and the applied stress intensity factor. As for the problem under pure mode I, it was found that the exponent of the stress intensity factor is approximately 2 for sufficiently small loads. The term "sufficiently" here refers to the assumption that if the contact length is much smaller than the radius of the rounded edge the small region near the rounded edge can be approximated to a half-plane. Deep inside

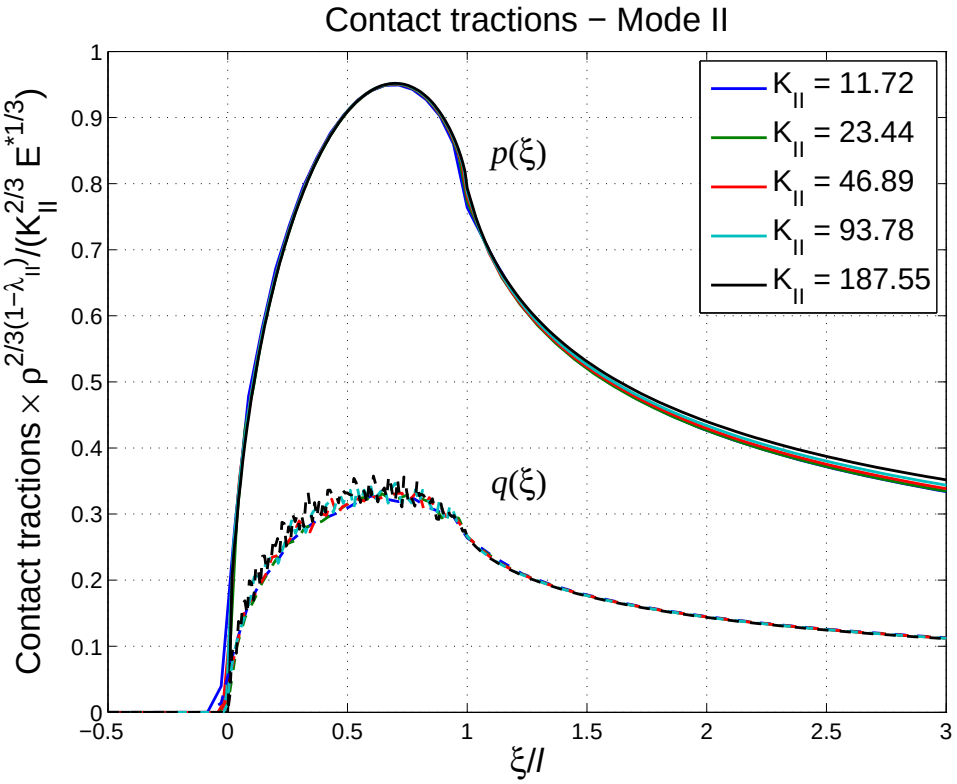

Figure 6.10: Normalized normal traction, $p(\xi)$, and shear traction, $q(\xi)$, for different values of K_{II}.

the contact, where the interface is stuck everywhere, the half-plane assumption is not valid and the problem behaves as a three-quarter plane.

The normalization of the contact tractions used in Figure 6.10 was obtained by isolating the multiplier from the equation for the peak stress. This can be done by multiplying the contact tractions by $\rho^{2/3(1-\lambda_{II})}/E^{*1/3}{K_{II}}^{2/3}$. It then becomes evident that the multiplier can be obtained from the normalized maximum contact normal pressure, and it was found to be $\Pi_{II} \simeq 0.85$. The calibrated formulation for the peak stress under pure mode *II* loading is given as

$$\left(\frac{p_0}{E^*}\right)^3 \simeq 0.85 \left(\frac{K_{II}}{E^* \rho^{(1-\lambda_{II})}}\right)^2. \tag{6.10}$$

The contact law and peak stress formulation are now completely defined for the pure mode *I* or mode *II* problems. However, the main interest lies when a combination of both modes exists and a study of the mixed mode problem is explored in §6.5.

6.5 Mixed mode

Consider now a situation where both mode *I* and *II* exist simultaneously. That is, in fact, what one will find for most problems where normal and shear external forces are applied to a punch pressed onto an elastic flat body. Furthermore, in order to characterize the 'mode mixity', i.e. the combination of mode *I* and mode *II* loads in a particular problem, let the quantity d_0 be introduced [Hills and Dini, 2011], which is defined by

$$d_0 = \left(\frac{K_I}{K_{II}}\right)^{\frac{1}{\lambda_{II}-\lambda_I}}. \tag{6.11}$$

It is noteworthy that, since $\lambda_{II} > \lambda_I$, the problem approximates to a pure mode *II* loading as d_0 tends to zero; and to a pure mode *I* case as d_0 tends to infinity. The quantity d_0 can be thought of as an inherent length dimension abstracted from the stress intensity ratio, which defines the size of the zone that is predominantly dominated by the mode *I* loading, and which is measured from the edge of the notch. The far field, at distances greater than d_0, will experience a state of stress characteristic of mode *II* because of its weaker singularity. If the radius of the rounded edge, ρ, has approximately the same magnitude as the quantity d_0, the region near the edge will 'see' the contribution from both modes *I* and *II*, and the contact tractions at the rounded edge will be different from the solutions obtained under either of the pure modes of loading. In most practical applications there will be no single predominant mode near the edge, and both modes *I* and *II* contribute to the tractions under the rounding. The quantity d_0 has dimensions of length, $[L]$, and a dimensionless quantity d_0/ρ will hereafter be used as a measure of the mode mixity of the problem.

6.5.1 Contact law under mixed mode loading

Recall that the pure mode analysis produced the following equations for the contact law,

$$\left(\frac{l}{\rho}\right)^3 = \Lambda_I \left(\frac{-K_I}{E^* \rho^{(1-\lambda_I)}}\right)^2 \qquad \text{for pure mode } I, \tag{6.12}$$

$$\left(\frac{l}{\rho}\right)^3 = \Lambda_{II} \left(\frac{K_{II}}{E^* \rho^{(1-\lambda_{II})}}\right)^2 \qquad \text{for pure mode } II. \tag{6.13}$$

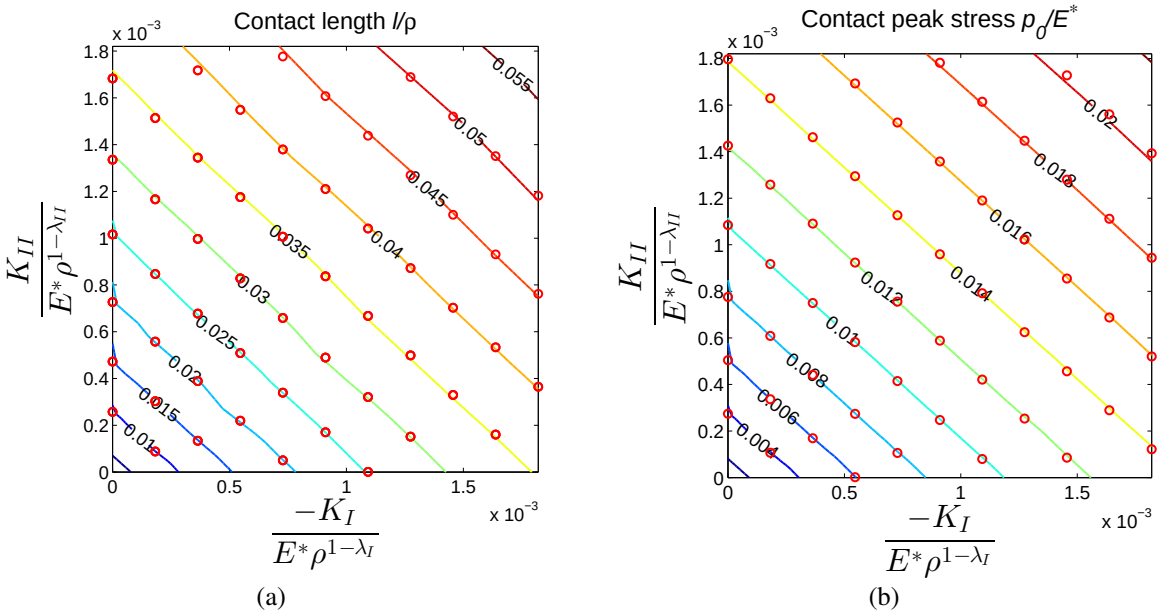

Figure 6.11: Level lines obtained analytically (red circles) and via finite element analysis for constant (a) contact size, l/ρ; and (b) peak stress, p_0/E^*.

where $\Lambda_I = 13.08$ and $\Lambda_{II} = 15.66$. The analytical solution has a good match with the finite element results at small values of K_I and K_{II}, when the slope of the curves in a logarithmic plot is approximately 2. At higher stress intensity factors a second higher order term would have to be included for better accuracy. This work is restricted to small values of contact size, such that the higher order terms of the power law describing the contact length can be neglected.

The contour plot obtained via finite element analysis for constant contact size and constant peak pressure in the normalised $K_I \times K_{II}$ space are presented in Figure 6.11 (straight lines). The level lines for constant contact size are fairly straight and, therefore, it is reasonable to assume that the contact law is a linear combination of the pure mode *I* and pure mode *II* solutions.

Assuming that the contact law is a linear combination of both pure mode loading formulations, the final contact length in a mixed mode problem can be rewritten as

$$\left(\frac{l}{\rho}\right)^3 = \Lambda_I \left(\frac{-K_I}{E^*\rho^{(1-\lambda_I)}} + \Lambda \frac{K_{II}}{E^*\rho^{(1-\lambda_{II})}}\right)^2, \tag{6.14}$$

where Λ_I is the multiplier obtained in the pure mode *I* analysis and $\Lambda^2 = \Lambda_{II}/\Lambda_I$, with the finite element calibration giving $\Lambda \simeq 1.09$. The derivation of equation (6.14) is presented in appendix C.1.3. Level lines for constant contact length are plotted using the contact law in

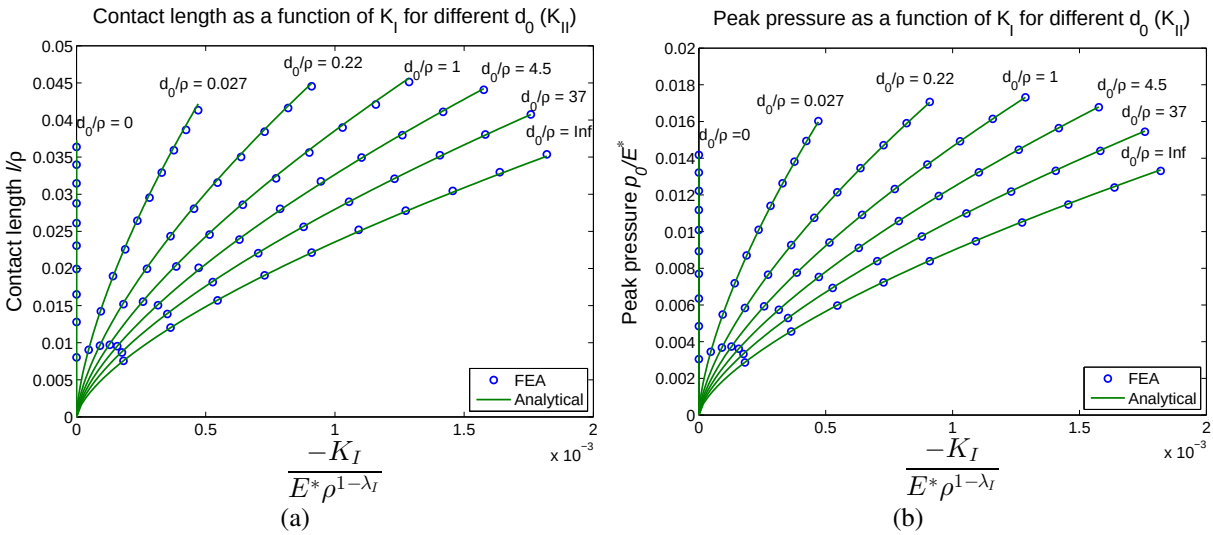

Figure 6.12: (a) Contact size, l/ρ, and (b) peak stress, p_0/E^*, as a function of normalized K_I for different values of d_0/ρ (K_{II}).

equation (6.14) and the quality of the solution is compared with the finite element analysis solution output in Figure 6.11a. Note that the red circles representing the solution of equation (6.14) match extremely well the finite element analysis solution. An alternative way of representing the comparison between the numerical and analytical solutions is shown in Figure 6.12a, where d_0/ρ is used as a dimensionless measure of the mode mixity and d_0 is given in equation (6.11). The lines of $d_0/\rho = \infty$ and $d_0/\rho = 0$ represent the pure mode I and pure mode II cases.

6.5.2 Peak pressure under mixed mode loading

The equations for the peak stress obtained under pure mode loading are

$$\left(\frac{p_0}{E^*}\right)^3 = \Pi_I \left(\frac{-K_I}{E^*\rho^{(1-\lambda_I)}}\right)^2 \qquad \text{for pure mode } I, \tag{6.15a}$$

$$\left(\frac{p_0}{E^*}\right)^3 = \Pi_{II} \left(\frac{K_{II}}{E^*\rho^{(1-\lambda_{II})}}\right)^2 \qquad \text{for pure mode } II. \tag{6.15b}$$

where $\Pi_I = 0.72$ and $\Pi_{II} = 0.85$. Following the contact length formulation, a similar procedure can be used here to derive the peak pressure formulation in a mixed load case, and the final peak stress formulation is given as

$$\left(\frac{p_0}{E^*}\right)^3 = \Pi_I \left(\frac{-K_I}{E^*\rho^{(1-\lambda_I)}} + \Pi \frac{K_{II}}{E^*\rho^{(1-\lambda_{II})}}\right)^2 \tag{6.16}$$

where Π_I is the multiplier obtained in the pure mode I analysis and $\Pi^2 = \Pi_{II}/\Pi_I$, with the calibration giving $\Pi \simeq 1.09$. The comparison between the analytical formulation of the peak stress in equation (6.16) and the numerical results obtained via finite element analysis are shown in Figure 6.11b. The analytical lines for constant peak stress also match with excellent accuracy the numerical results. An alternative comparison between the numerical and analytical solution is presented in Figure 6.12b.

6.6 Discussion

Basic contact characteristics were defined in this chapter by using an analogy with a three-quarter plane notch. This new approach provides numerically calibrated formulations for fundamental contact parameters in terms of Williams' notch stress intensity factors. One of the advantages of this approach is that the stress field of a squared ended punch without edge rounding can be used to deduce the contact solution in the presence of edge rounding by matching the outer stress field using Williams' stress intensity factors K_I and K_{II}. By treating the problem as a three quarter plane notch instead of a contact problem, one can apply prescribed displacement boundary conditions in the finite element model (§6.2), making the stress field truly that of a three quarter plane. This introduces an advantage in comparison with the previous solution by Banerjee et al. [2009], where the finite length of the finite element model had to be treated carefully to introduce dimensional scaling factors in terms of the applied load P in the finite element model. Note that the applied normal load, P, has no meaning in the semi-infinite punch problem, while the Williams' intensity factors K_I and K_{II} do. This approach is, therefore, a more elegant form of representing the loading in the far field.

One important aspect of the solutions derived for the contact length and the peak pressure in a mixed mode problem, is that a load path in the $K_I \times K_{II}$ space that has constant contact length, l, is also a path of constant peak pressure, p_0. The formulation for the peak stress and contact length follows the same pattern, since the ratio of the multipliers in a mixed mode problem are approximately the same $\Lambda \simeq \Pi \simeq 1.09$. The formulations differ only by the scaling multipliers Λ_I and Π_I. This result is extremely relevant and it will be used in the next chapter in the calibration of the bounded normal pressure asymptote. It was also found that the normal

contact pressure is very weakly coupled and path independent. Hence, the results derived in this chapter are unique for any combination of mode *I* and mode *II* loading, respecting the assumptions of the solution, i.e. that the contact length is small with respect to the radius of curvature.

Another assumption used in the solution presented here is that along the interior of the contact interface, i.e. away from the contact edge, there is adhesion. The ratio of shear to direct tractions is given by $f^{I}_{r\theta}/f^{I}_{\theta\theta}$ in the mode *I* dominated region and $f^{II}_{r\theta}/f^{II}_{\theta\theta}$ in the mode *II* dominated region. For the 90° punch, these ratios are 0.543 and 0.219, respectively, and, therefore, the solution developed applies independently of the loading *only* if the actual coefficient of friction exceeds the larger of these two values. Note that for metallic bodies in contact this is not unusual and some of the coefficients of friction presented in §5.1 satisfy this requirement. For lower coefficients of friction, the condition for no slip in the flat region of the punch will depend on the mode "mixity" parameter, d_0, and the radius of the rounding, ρ. Otherwise slip would extend significantly along the flat interface, and this would destroy the validity of the model.

In the next chapter, the contact solution will be characterized by using an asymptotic approach. The solutions centred on the far field loading derived in this chapter will be used to derive the contact law in terms of a normal pressure scaling factor that describes the bounded asymptote near the edge. The use of asymptotes to describe the contact tractions near the edge of contact also simplifies the partial slip solutions. The shear traction distribution and the size of the slip zone will be obtained by representing the contact shear tractions in terms of bounded and singular asymptotes near the edge of contact.

Chapter 7

Elastic flat and rounded contact formulation using edge asymptotes

Formulations for the contact law and peak stress were obtained for the semi-infinite elastic punch with rounded edge in terms of the remote loading in chapter 6, by using a three-quarter plane notch analogy. Although the solution centred on the far field is a step-forward in obtaining the contact characteristics in an elastic flat and rounded punch problem, an approach centred on the edge of the contact is suggested in order to solve the partial slip problem. The solution presented in this chapter builds on the principles established in the previous chapter and uses the far field loading parameters to derive edge asymptotes for the normal and shear tractions. One of the advantages of this method is that the use of edge asymptotes enables one to correlate better the state of stress at the edge of contact in complex geometries, such as blade to disk assemblies, with simpler specimens geometries tested in laboratory, providing more representative results.

New dimensional scaling parameters, analogous to generalized stress intensity factors, for the normal and shear tractions will be introduced and correlated with Williams' stress intensity factors, K_I and K_{II}. Then, the contact parameters are completely characterized in the vicinity of the edge of contact in terms of these new edge scaling factors for the elastic punch with edge rounding problem. These parameters are introduced in the following sections and a study of the slip zone under the edge rounding is presented subsequently. In the last section of the chapter, an example problem of a finite punch pressed onto an elastic half-plane will be presented using

the formulations derived.

7.1 Asymptotic contact formulation

7.1.1 Edge tractions dimensional scaling factors

Characteristic scalar dimensional factors are introduced for the normal contact traction and two situations of shear tractions: i) bounded and ii) singular,

$$\begin{aligned} p(\xi) &= K_N\sqrt{\xi} \\ q(\xi) &= K_Q\sqrt{\xi} \qquad \text{when shear bounded} \\ q(\xi) &= K_T/\sqrt{\xi} \qquad \text{when shear singular,} \end{aligned}$$

where K_N, K_Q and K_T are the scaling factors which will later be correlated with the applied remote stress intensity factors K_I and K_{II}. The scaling factors K_N and K_Q have dimensions of $[FL^{-5/2}]$ and K_T, dimensions of $[FL^{-3/2}]$. The coordinate ξ is measured inwards from the contact edge. The contact tractions scaling factors can be found from finite element analysis by selecting the 'rough' contact condition in ABAQUS, i.e. no slip is allowed on the contact interface, and the scaling factor K_N, for example, can be obtained by plotting $p(\xi)\sqrt{\xi}$ as $\xi \to 0$. Since the contact normal traction is very weakly coupled, it does not depend on the load history and the normal traction scaling factor, K_N, is unique for any point in the dimensionless $K_I^* \times K_{II}^*$ space. A procedure similar to the one used for the contact length and peak pressure can be used to obtain K_N for any combination of applied remote K_I and K_{II}. However, the bounded shear scaling factor, K_Q, and certainly the singular scaling factor, K_T, will both depend on the load history of the problem.

Note that one may envision three distinct situations of shear tractions; one when no slip occurs at the edges, one when a slip zone develops at the edge of the punch, and a third one for the case of full sliding of the punch. The first is observed, for example, when remote loading was pure mode *I* or pure mode *II* in character. In those cases, no slip occurs in the interface and the shear tractions are bounded near the edge. These load scenarios are analogous to a problem

of proportional loading in which the ratio of the load increment is less than the sliding limit, $dQ/dP < \mu$. Of course, this analogy with the proportional loading problem cannot be carried through since in the current problem the punch is semi-infinite and there are no such equivalent total applied loads P and Q. Nevertheless, the analogy helps visualising some of the conditions that drive stick and slip in the interface. The singular shear traction asymptote describes the limiting case of an infinitely high coefficient of friction that inhibit any slip at the edge of a load case which otherwise be in partial slip. Keep in mind that the development of a slip zone in a proportional loading problem for a finite contact occurs when the increment ratio is greater than or equal to the coefficient of friction, $dQ/dP \geq \mu$.

Next, the calculations of the edge tractions dimensional scaling factors will be obtained. The normal scaling factor, K_N, is the only one that is unique for any combination of the applied remote stress intensity factors. The shear tractions scaling factors K_Q and K_T are dependent on the load history and, therefore, one should work in terms of their increments and as a function of the increment of the applied remote loading. Note that in the analyses of the edge scaling factors presented next, slip is inhibited.

7.1.2 The normal edge traction scaling factor

As mentioned in the previous section, the normal contact traction scaling factor is unique for any combination of dimensionless K_I^* and K_{II}^* and any load path. Furthermore, the formulations derived in §6.5 have shown that a trajectory of constant contact length in the dimensionless $K_I^* \times K_{II}^*$ space is also a trajectory of constant peak pressure. Therefore, since the scaling factor K_N describes the normal contact traction near the edge, it is reasonable to assume that K_N will also remain constant along a load path that exhibits constant contact length and peak pressure. This implies that if a formulation for the normal scaling factor can be obtained for the pure mode I and mode II cases, the normal edge scaling factor in a mixed mode problem is also a linear combination of the two pure mode formulations. However, nothing can be said *a priori* about how the normal scaling factor varies with respect to each stress intensity factor, K_I and K_{II}, independently.

The procedure to find the formulation of K_N for each pure mode case is therefore similar

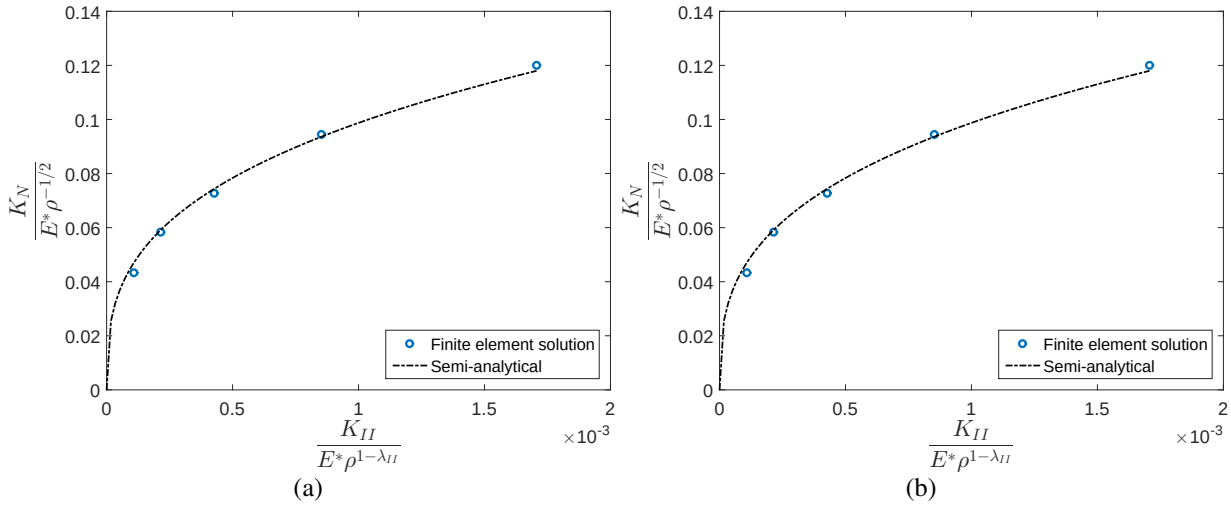

Figure 7.1: Semi-analytical and finite element analysis results of K_N as a function of (a) mode I stress intensity factor; (b) mode II stress intensity factor.

to the one used in the derivation of the expressions of the contact length and peak pressure as a function of the pure mode loadings in previous sections. Through a dimensional analysis, one may write an expression equating K_N and the independent variables of the problem. The algebraic procedure is given in appendix C.2.1. The resulting dimensionless equation can be written as

$$\frac{K_N}{E^*\rho^{-1/2}} = H_k \left(\frac{|K_k|}{E^*\rho^{1-\lambda_k}} \right)^m \equiv H_k \left(|K_k^*| \right)^m, \quad k = I, II, \tag{7.1}$$

where m and H_k are to be found from FEA calibration and k is the index of each loading mode. The numerical calibration with applied pure mode I loading resulted in $m \simeq 1/3$ for small values of K_I. At higher loads, one may represent the formulation as a power series, such as

$$\frac{K_N}{E^*\rho^{-1/2}} = H_k^{(1)} (K_k^*)^{1/3} + H_k^{(2)} (K_k^*)^{2/3} + \dots, \quad k = 1, 2, \tag{7.2}$$

where $H_k^{(1)}, H_k^{(2)}$ are the multipliers which can be obtained by an finite element calibration and K_k^* is the dimensionless stress intensity factor of modes I and II. Equation (7.1) is valid only for small loads in which the contact length is sufficiently small when compared with the radius of the rounded edge. Here, it will be assumed that the 1-term series approximation is sufficient to characterize the state of stress near the edge of the contact. It will be shown in a example problem later in the chapter that this assumption is reasonable for many practical problems.

A similar formulation for the normal scaling factor in a pure mode *II* case can also be obtained. The equations for both pure mode loadings may be rewritten and the multiplier redefined, such that, the formulation of K_N can now be written as

$$\left(\frac{K_N\sqrt{\rho}}{E^*}\right)^3 = H_k\left(\frac{|K_k|}{E^*\rho^{1-\lambda_k}}\right), \qquad k = I, II, \tag{7.3}$$

where the index, k, represents the loading mode and the multipliers H_k are found from the finite element analysis as $H_I \simeq 0.9$ and $H_{II} \simeq 0.98$.

Recall that the scaling factor K_N will be constant along a load path that exhibits constant contact length and peak pressure. Hence, the formulation of K_N in a mixed mode case is also a linear combination of both pure mode equations. The algebra of the mixed mode formulation is presented in appendix C.2.2 and the final dimensionless formulation of K_N in terms of K_I and K_{II} is given by

$$\left(\frac{K_N\sqrt{\rho}}{E^*}\right)^3 = H_I\left(\frac{-K_I}{E^*\rho^{1-\lambda_I}} + H\frac{K_{II}}{E^*\rho^{1-\lambda_{II}}}\right), \tag{7.4}$$

where $H = H_{II}/H_I$. From the argument above and the results obtained in chapter 6, K_N is constant if l and p_0 remain constant throughout a load trajectory, and $H = H_{II}/H_I = 1.09$. The comparison between the calibrated equation (7.3) with finite element analysis output under pure mode *II* loading is presented in Figure 7.1b. The calibrated formulation for the mixed mode case is compared with FEA results for different mode mixity, given by d_0/ρ, in Figure 7.2.

Now that the formulation of the normal scaling factor in a mixed mode problem has been obtained, one may seek an equation of the contact length in terms of K_N. Equations (6.14) and (7.4) may be rewritten as follows

$$\sqrt{\left(\frac{l}{\rho}\right)^3\frac{1}{\Lambda_I}} = \left(\frac{-K_I}{E^*\rho^{1-\lambda_I}} + \Lambda\frac{K_{II}}{E^*\rho^{1-\lambda_{II}}}\right), \tag{7.5a}$$

$$\left(\frac{K_N}{E^*\rho^{-1/2}}\right)^3\frac{1}{H_I} = \left(\frac{-K_I}{E^*\rho^{1-\lambda_I}} + H\frac{K_{II}}{E^*\rho^{1-\lambda_{II}}}\right). \tag{7.5b}$$

Since $H = \Lambda$, the right-hand side of both equations (7.5a) and (7.5b) are equal. Combining the left-hand side of both equations, an expression relating the contact edge pressure scaling factor

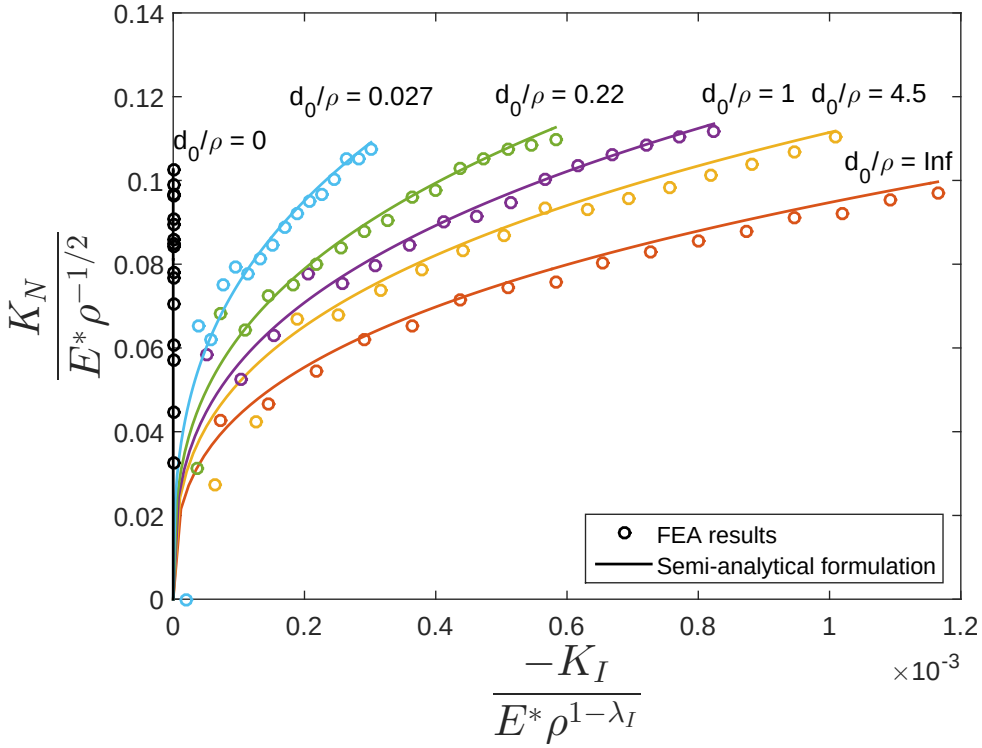

Figure 7.2: Comparison between the semi-analytical and finite element analysis results in a mixed mode case, where $d_0/\rho = \infty$ is pure mode I in character and $d_0/\rho = 0$ pure mode II.

with the contact length can be obtained. Finally, one arrives at

$$K_N = \left(\frac{H_I}{\Lambda_I{}^{1/2}}\right)^{1/3} \frac{E^*}{\sqrt{\rho}} \left(\frac{l}{\rho}\right)^{1/2} \simeq 0.629 \frac{E^*}{\sqrt{\rho}} \left(\frac{l}{\rho}\right)^{0.5}, \tag{7.6}$$

For comparison, if K_N is written as a function of the contact semi-width, a, in a two-dimensional Hertzian problem, and where ρ_c represents the radius of curvature of the cylindrical surface, the following expression is obtained,

$$K_N = \frac{\sqrt{2}}{2} \frac{E^*}{\rho_c^{1/2}} \left(\frac{a}{\rho_c}\right)^{1/2} \simeq 0.7071 \frac{E^*}{\sqrt{\rho_c}} \left(\frac{a}{\rho_c}\right)^{0.5}. \tag{7.7}$$

The normal contact traction asymptote characterised by the scaling factor K_N can now be used to define the contact law of the problem of a flat punch with rounded edges. It may be noted that equation (7.6) derived here is similar to the two-dimensional hertzian equation (7.7), with the normal pressure scaling factor being dependent on the contact length term to the same power. Furthermore, it will be shown later in the chapter that the contact pressure can be obtained from K_N when the approximation by a half-plane is valid in the region surrounding the

rounded edge in contact.

7.1.3 The bounded shear traction scaling factor

In most practical problems, the simple application of a normal force pressing a punch with rounded edge against a half-plane will induce a bounded shear traction at the edge of contact. Even if the materials of both bodies are elastically similar, the geometrical coupling on this type of geometry cannot be neglected. In a typical fretting problem, a normal load is applied first to ensure that the contact does not fully slide when the oscillating tangential load is applied subsequently. Although the main focus of this work is to obtain the shear tractions in a partial slip problem, i.e. when a small slip zone develops at the edge of the contact, the calculation of the bounded shear traction in a first load step is necessary to determine the final state of the tangential traction. Furthermore, one may think of a more complex load cycle in which both normal and tangential loads vary in time and as shown by Barber et al. [2011], there are combinations of normal and tangential loading that will result in a bounded shear traction and no slip.

The calculation of the bounded tangential scaling factor, K_Q, will first be obtained for each pure mode stress intensity factor variation, ΔK_I and ΔK_{II}. K_Q is not unique for any combination of K_I and K_{II}, and the analysis presented here is valid only for the initial loading step, i.e. when no contact traction exists previously and $\Delta K_k = K_k$, with $k = I, II$. It will also be assumed that the bounded shear traction will vary by the same power as the normal tangential traction. Hence, the formulation of the bounded shear scaling factor in a each of the pure mode loading cases may be written as

$$\left(\frac{K_Q}{E^*\rho^{-1/2}}\right)^3 = \Theta_k \left(\frac{K_k}{E^*\rho^{1-\lambda_k}}\right), \quad k = I, II \tag{7.8}$$

where $\Theta_I = -\Theta_{II} \simeq -0.04$. A comparison between the calibrated solution of equation (7.8) with finite element analysis results is presented in Figure 7.3. It is worth noting that the numerical computation of K_Q is not trivial due to oscillations in the finite element analysis results as the contact is advancing, as explained in §6.2, specially at lower loads when fewer nodes are in contact.

In order to obtain a formulation for the mixed mode case, several problems with different

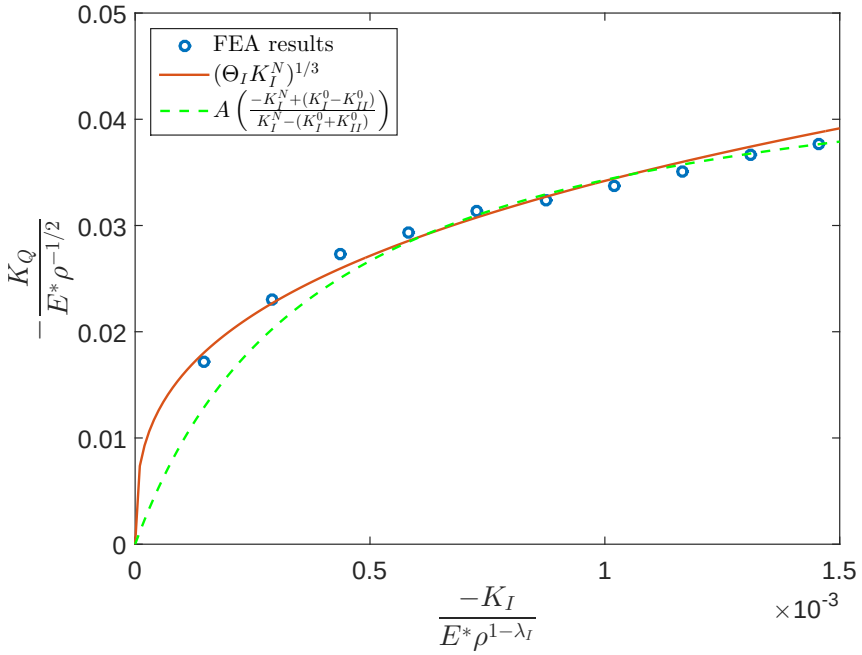

(a)

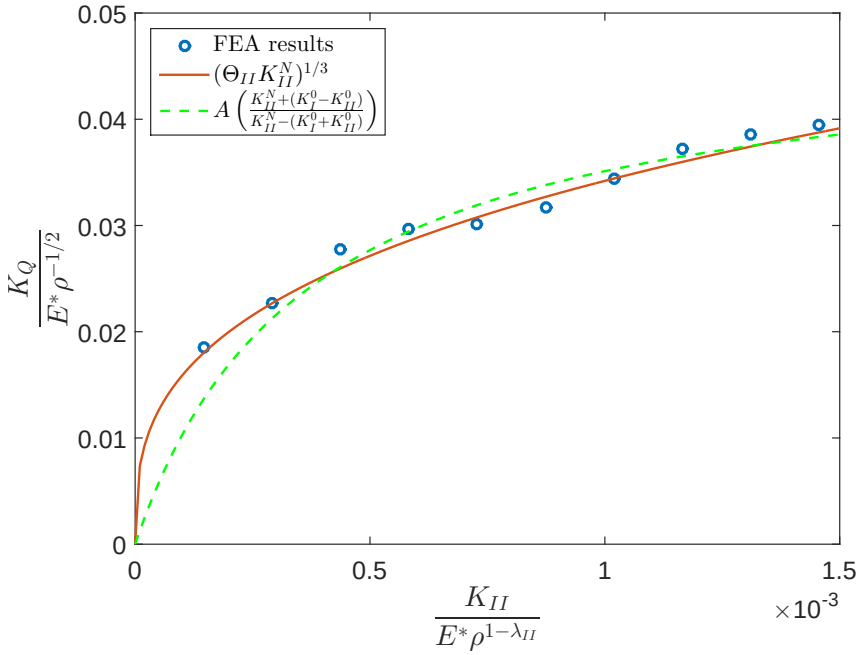

(b)

Figure 7.3: Semi-analytical and finite element analysis results of K_Q as a function of (a) mode I stress intensity factor; (b) mode II stress intensity factor.

mode mixities were conducted. The value of K_Q was obtained for ten increments in each mode mixity case. The lines of constant K_Q in the normalised $K_I^* \times K_{II}^*$ space are plotted in Figure 7.4. It can be observed that the lines of constant K_Q are approximately radial with respect to K_I^* and K_{II}^* and they are antisymmetric with respect to an angle $\theta \simeq 45°$. Under conditions of proportional, combined modes loading, the relationship between the local multiplier and the far

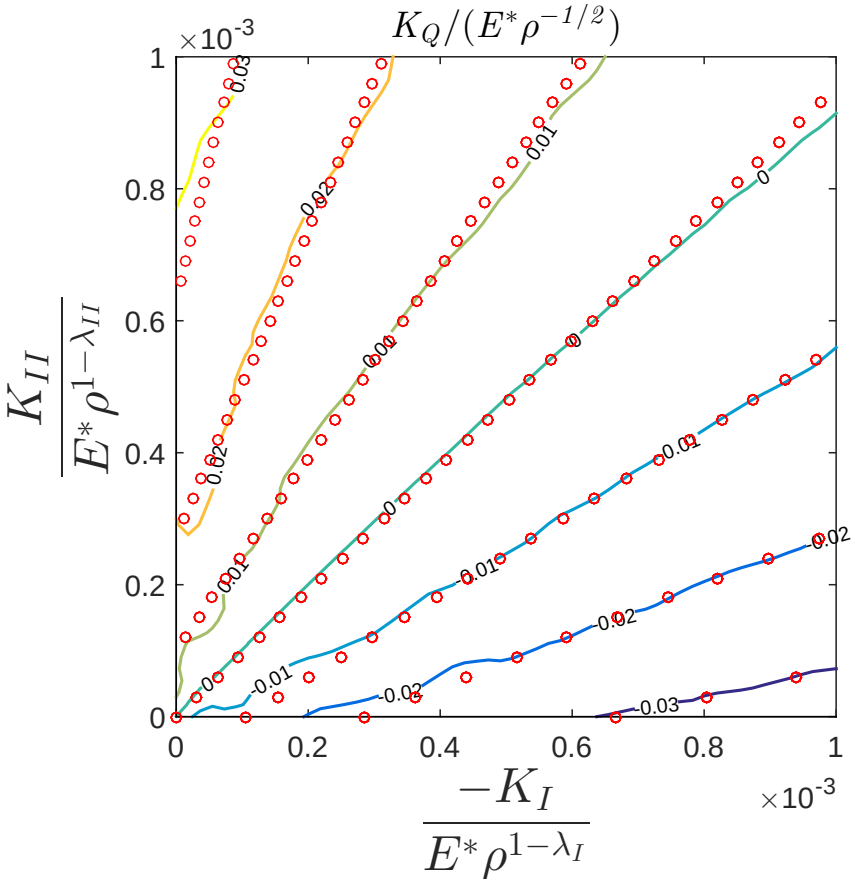

Figure 7.4: Level lines of constant K_Q in the dimensionless $K_I^* \times K_{II}^*$ space obtained numerically via finite element analysis (solid lines) and analytically (red circles).

field loading is found to be as shown in Figure 7.4. Note that the trajectory

$$\frac{K_{II}}{K_I}\rho^{\lambda_I-\lambda_{II}} \simeq -1 \qquad \text{or} \qquad \frac{\rho}{d_o} \simeq 1$$

induces no shear tractions along the interface. The radial lines of constant value of the bounded shear load multiplier, K_Q, may be represented, approximately, by

$$\frac{K_Q}{E^*\rho^{-1/2}} = A\frac{(bK_{II}^* + K_I^*) + (K_I^0 - K_{II}^0)}{(bK_{II}^* - K_I^*) - (K_I^0 + K_{II}^0)}, \tag{7.9}$$

where K_I^* and K_{II}^* are the normalised terms of mode I and II intensity factors. The constants are found from finite element results and $A = 0.048$, $b = 1.09$ and $K_I^0 = K_{II}^0 = -0.0002$. The latter pair are the coordinates of the intersection of radial lines in the $K_I^* \times K_{II}^*$ space (Figure 7.4). In pure modes of loading equation (7.9) produces the green dashed lines in Figure 7.3, and which fit approximately the numerical results. However it is worth noting that whilst equation (7.9)

may be used for moderate values of K_I and K_{II}, it implies a finite value of K_Q as K_I or K_{II} tend to infinity, when in fact we know that the K_Q should tend to infinity as well. Nevertheless, given that our solution requires that the load be small enough for the rounded region in contact to be much smaller than the radius of the rounded edge, the approximate value of K_Q given by equation (7.9) is appropriate and consistent with the limitations of the idealisation.

7.1.4 The singular shear traction scaling factor

This work is restricted to the second quadrant of the $K_I \times K_{II}$ space where K_I is negative and K_{II} is positive. Both modes produce positive normal traction at the rounded edge in this quadrant. Furthermore, in order to get a situation where slip will occur it is first required that an initial load step is taken to a point $({K_I}^0, {K_{II}}^0)$ such that the contact remains closed near the rounded edge. The final shear traction will be dependent on the path taken during the first loading phase, since the shear traction is path dependent. However, if the contact length is small such that the problem near the edge is governed by half-plane mathematics, the incremental problem should be independent of the state before the increment if (i) the contact zone is advancing or constant in size and (ii) full stick is assumed at the edge. Hence, the variation of the shear traction in a second loading phase will be independent of the initial point and will depend only on the variation of the applied remote stress intensity factors ΔK_I and ΔK_{II}.

If the argument above is valid, two problems that take different initial paths in the first loading phase, but which have similar change ΔK_I and ΔK_{II} in the second step, should present the same change in shear traction and, therefore, same K_T. As an example, two problems with different initial loading are illustrated in Figure 7.5. The first case (blue) was loaded to a point (K_I^0, K_{II}^0), where $-K_{II}^o/K_I^o \simeq \rho^{\lambda_I - \lambda_{II}}$ or $\rho/d_o \simeq 1$. The second case (red) was loaded with a pure mode I loading in the first step. Both problems followed a load trajectory of constant contact length in the second loading phase and the same change of load. The contact tractions at the end of second loading phase and the change in shear traction are shown in Figure 7.6, where a normalization based on equation (6.16) was used. The singular scaling factor, K_T, corresponding to the second phase of loading of both loading paths was obtained from the change in shear traction in the second step, $\Delta q(\xi) = q^{(2)}(\xi) - q^{(1)}(\xi)$. Both load histories

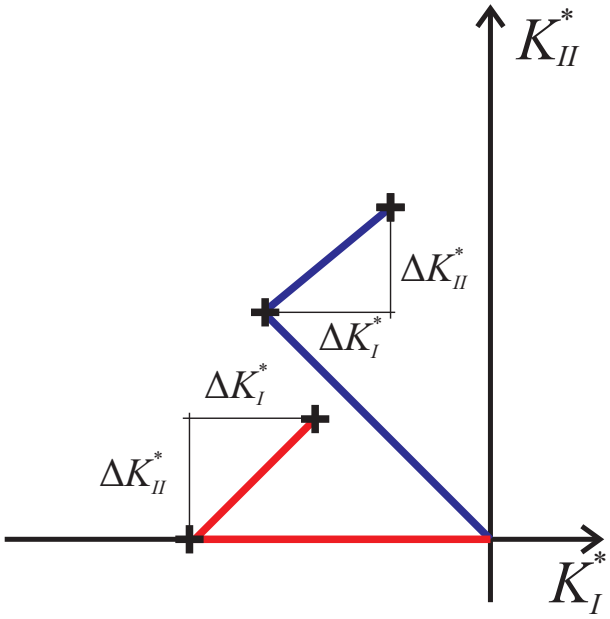

Figure 7.5: Example problem of two different initial paths taken followed by similar variation ΔK_I and ΔK_{II} in the second step.

gave a singular shear scaling factor of $K_T \simeq 12.3$, with dimensions of $[FL^{-3/2}]$. The singular asymptote scaled by K_T is also shown in Figure 7.6 together with the contact tractions. Note that in the first loading case (blue path) the accumulated shear traction at the end of the first step is very small and the shear traction at the end of the second step match reasonably well the singular asymptote (Figure 7.6a). However, if the shear traction is not negligible in the first loading phase, as in the pure mode I case, the region where the asymptote matches the shear traction near the edge is very small (Figure 7.6b). If only the variation of shear traction in the second phase of loading is plotted (Figures 7.6c & 7.6d), a very good match with the singular asymptote is found for both cases, confirming the assumption made that the variation of shear traction is independent of the previous load history.

The asymptotes and their scaling factors are presented in Figure 7.8. The numerical values presented were obtained for a problem with the following material and geometrical properties: $E = 100$ GPa; $\nu = 0.3$; and $\rho = 1$ mm. The applied loads are such that $K_I = -31.33$ N.mm$^{-1-\lambda_I}$ and $d_0/\rho = -1$ on the first phase of the blue path. The red path had pure mode loading in the first phase of loading with $K_I = -62.67$ N.mm$^{-1-\lambda_I}$. On the second phase of loading, both load paths had a change of $\Delta K_I = 21.97$N.mm$^{-1-\lambda_I}$ and $\Delta K_{II} = 20.42$N.mm$^{-1-\lambda_{II}}$ to maintain the contact length constant.

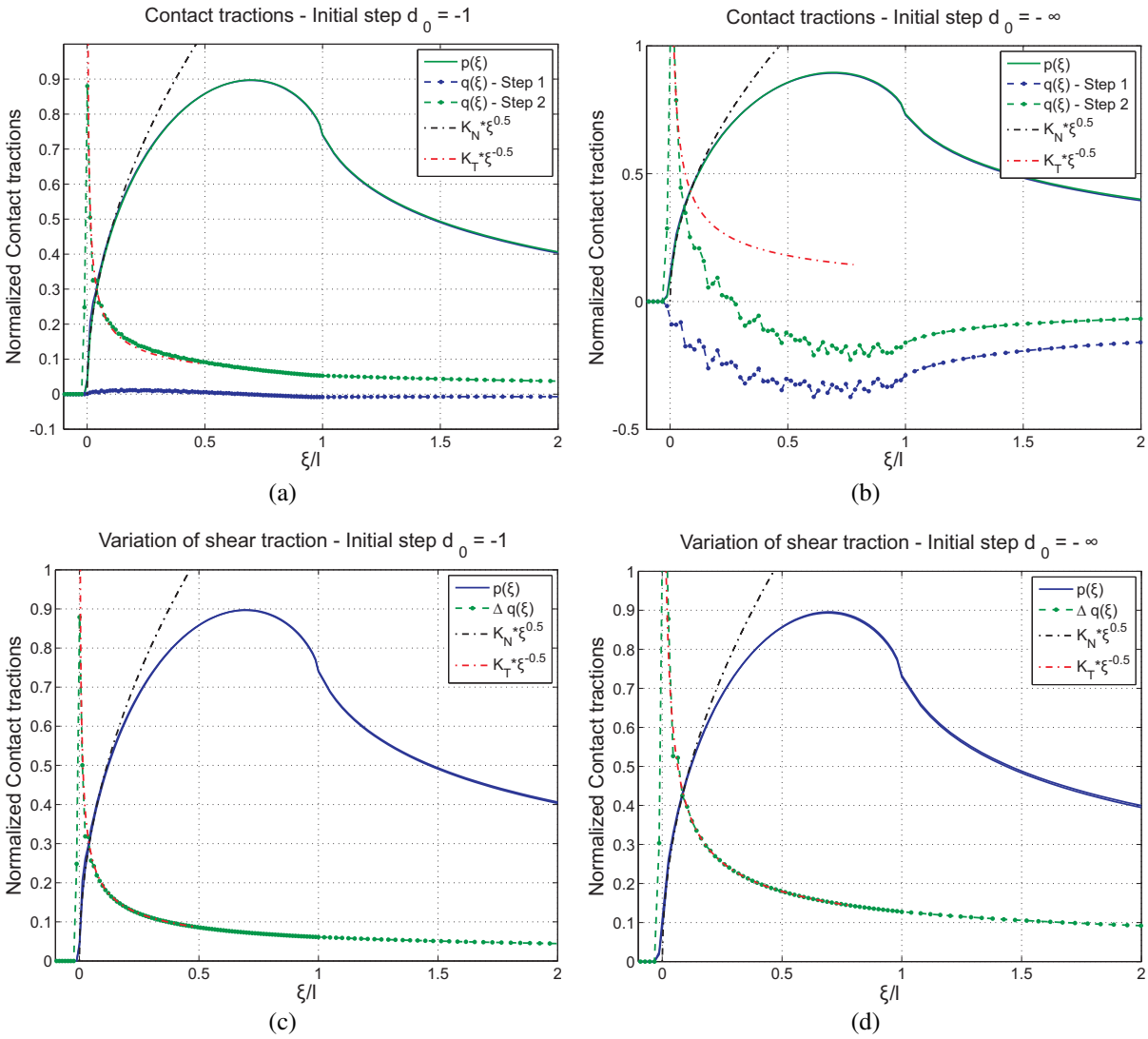

Figure 7.6: Contact tractions without slip and singular asymptotes for initial loading (a) $d_0/\rho = -1$ and (b) pure mode I; Variation of contact traction for initial loading (a) $d_0/\rho = -1$ and (d) pure mode I.

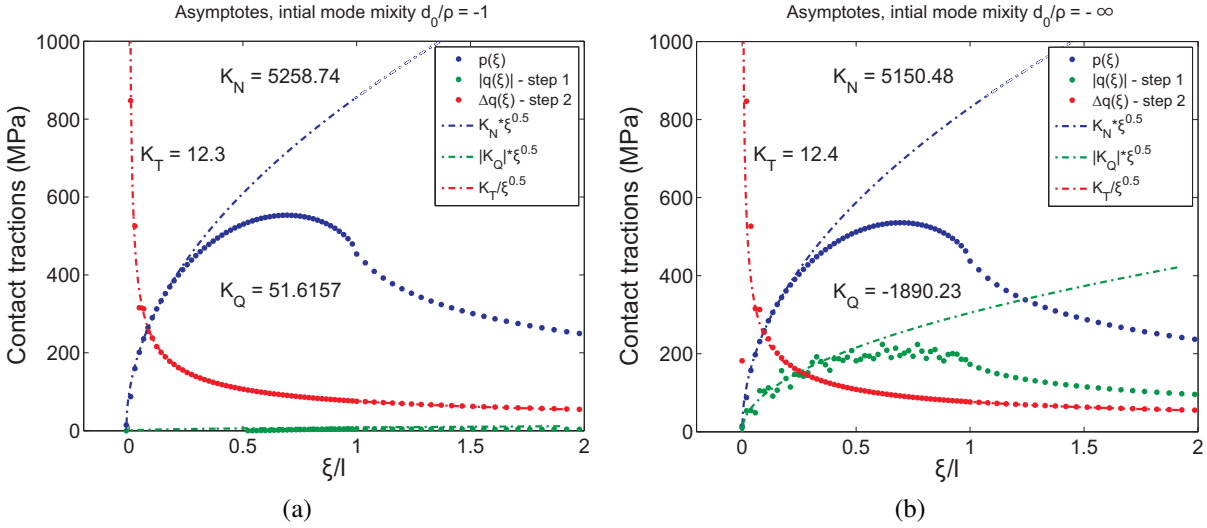

Figure 7.7: Contact tractions without slip obtained via finite element analysis and asymptotes for initial loading (a) $d_0/\rho = -1$ and (b) pure mode I, $d_0/\rho = -\infty$.

The analysis above is valid only when the contact size remains constant throughout the second load phase. If the contact size changes than are two possibilities; i) the contact is advancing and ii) the contact is receding. If the contact is advancing, the newly created contact zone has no pre-existing shear traction from the previous step. However, numerical results suggest that the contact traction in the new zone of an advancing contact is bounded even when slip is inhibited. On the other hand, if the contact is receding, the shear traction developed in the previous step will 'interfere' with the singularity and K_T will then depend on the load path taken in the first step.

Formulation of K_T for constant contact length

If the contact length does not change during a second phase of loading, and if slip is inhibited, a singular shear traction is developed. In the constant contact length load trajectory, the dimensionless load increments of loading ΔK_I^* and ΔK_{II}^* are correlated by

$$\left(\frac{l}{\rho}\right)^3 = \Lambda_I \left(-K_I^{*(1)} + \Lambda K_{II}^{*(1)}\right)^2 = \Lambda_I \left(-K_I^{*(2)} + \Lambda K_{II}^{*(1)}\right)^2 = C, \tag{7.10}$$

$$-K_I^{*(1)} + \Lambda K_{II}^{*(1)} = -K_I^{*(2)} + \Lambda K_{II}^{*(2)}, \tag{7.11}$$

$$\Delta K_I^* = \Lambda \Delta K_{II}^*. \tag{7.12}$$

Now, a dimensionless variable of load increment, ΔK_l^*, along the trajectory of constant contact length is introduced in terms of dimensionless K_I^* and K_{II}^*, such that,

$$\Delta K_l^* = \sqrt{\Delta K_I^{*2} + \Delta K_{II}^{*2}} = \Delta K_{II}^* \sqrt{\Lambda^2 + 1} = \Delta K_I^* \sqrt{\frac{\Lambda^2 + 1}{\Lambda^2}}. \tag{7.13}$$

The numerical results used in Figure 7.5 can now be used to derive a semi-analytical equation for K_T as a function of ΔK_l^*. By taking 10 equally spaced points along the trajectory of the second phase of loading for any of the two load histories of Figure 7.5, the value of K_T can be obtained and plotted against ΔK_l^* (Figure 7.8a). A linear correlation between K_T and the load increment ΔK_l^* was obtained. A semi-analytical formulation of K_T for constant contact length trajectories can be written as

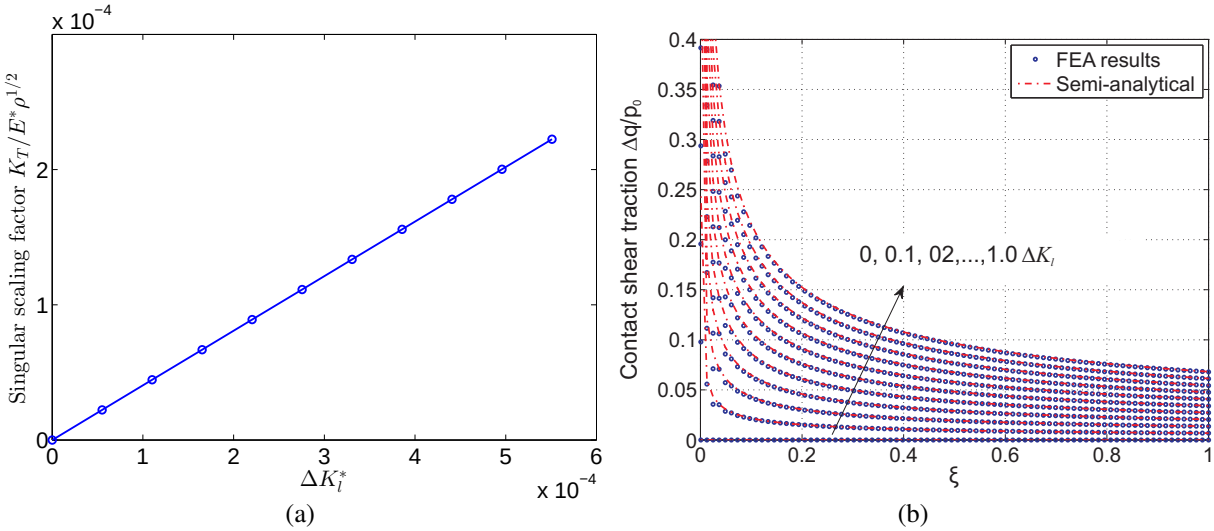

Figure 7.8: (a) Singular scaling factor K_T as a function of the load variable along the constant contact length trajectory, ΔK_I^*; (b) Numerical and analytical singular shear tractions for the second load phase with constant contact size and inhibited slip.

$$\frac{K_T}{E^*\rho^{\frac{1}{2}}} \simeq 0.403\Delta K_I^* = 0.597\frac{\Delta K_{II}}{E^*\rho^{1-\lambda_{II}}} = 0.546\frac{\Delta K_I}{E^*\rho^{1-\lambda_I}} \tag{7.14}$$

where equation (7.13) gives the correlation between ΔK_I^*, K_I and K_{II}, and $\Lambda = 1.09$.

The equation above can be used to determine the scaling factor of the singular asymptote as long as the contact size remains constant during the second load phase. The comparison between the calibrated formulation (7.14) and finite element analysis results are presented in Figure 7.8b for different values of load variation ΔK_I^*. In most real applications the contact size will not remain constant when a shear load is applied to a finite punch. However, if the change in contact size is small during the second load phase, equation (7.14) can be used as an approximation to the singular scaling factor. The cases of advancing and receding contact are significantly more complex and will not be covered in this work.

7.2 Slip in the semi-infinite elastic punch problem

7.2.1 Mixed mode slip

Of the problems studied so far, only when a second phase of loading was applied while keeping the contact size constant, was the contact traction singular, indicating the existence of a slip

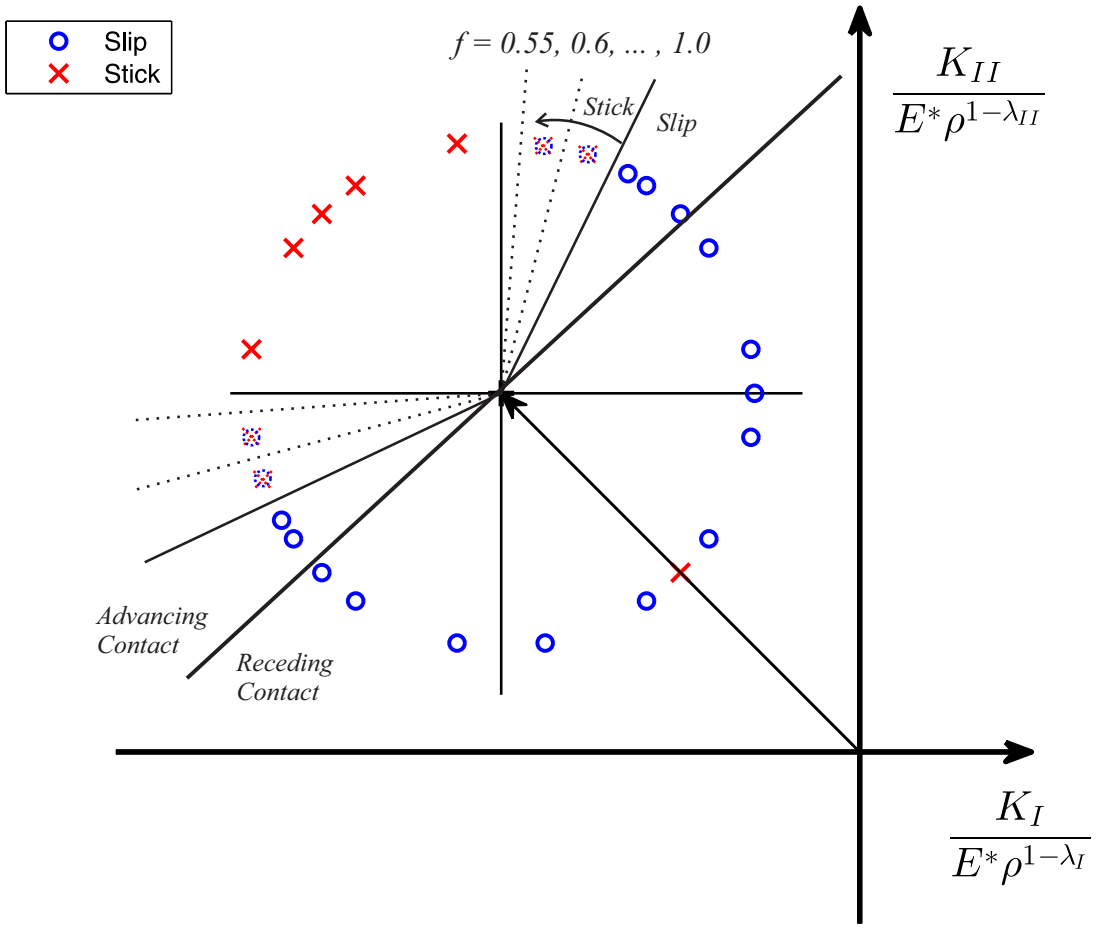

Figure 7.9: Slip and stick in the $K_I \times K_{II}$ space after a initial loading to a point where $({K_I}^0, {K_{II}}^0)$ for advancing contact.

zone near the edge if slip in the interface is allowed. Hence, there exists a combination of incremental load dK_{II}/dK_I which will produce a contact traction ratio sufficient to cause slip at the edge of contact. The analogy with the proportional load problem has also been mentioned previously. In the traditional proportional loading problem between two elastic half-planes with finite contact length, the occurrence of slip depends on the increment of the applied load ratio and the coefficient of friction, such that, if $dQ/dP \geq \mu$ slip will occur at the edge of contact. However, although this analogy is useful to have in mind, it is not evident how it can be translated to the $K_I \times K_{II}$ space in the semi-infinite punch problem.

In order to get a picture of the trajectories in the $K_I \times K_{II}$ space that will give rise to a slip zone at the edge of contact, several finite element simulations were conducted. First, the problem was loaded to a general point in the third quadrant in order to ensure that the contact would remain closed at all times. Then, different loading directions were taken and the presence,

or absence, of slip at the edge was recorded for a coefficient of friction of $\mu = 1.0$ (Figure 7.9). Note that there seems to be a clear boundary between stick and slip depending on the ratio dK_{II}/dK_I. This boundary, however, does not coincide with the line of constant contact length, so that the conditions for slip and stick are not directly correlated to the condition for advancing or receding contact. Above this line the interface is stuck everywhere and below the line a slip zone exists near the edge of contact. The only exception is when the path taken in the second step retraces exactly the load path taken in the initial step. The boundary between stick and slip was also obtained for $\mu = 0.6$ and $\mu = 0.55$ and the transition between stick and slip is also displayed in Figure 7.9. It is also evident that the stick/slip condition depends on the coefficient of friction as well as on the mode I and mode II load ratio. An analysis of the size of the slip zone is presented next.

7.2.2 Defining the size of the slip zone

Previous work by Dini and Hills [2004] describes an expression for obtaining the size of the slip zone if K_N and K_T are known. The work was done for incomplete elastic contact problems, and it was shown that the slip zone size, s, is related to the scaling factors K_N and K_T by the following expression,

$$s = \frac{2K_T}{\mu K_N}. \tag{7.15}$$

The same general idea should be valid for the flat punch with rounded edge, if no shear traction exists when K_T is applied to the problem. Of course, it can be argued that such a situation might not exist due to the coupling between normal and shear tractions, but if the initial shear traction given by K_Q is sufficiently small compared to contribution of K_T, the equation above should hold, at least approximately.

A correction of equation (7.15) for problems with a pre-existing shear traction can be derived. If the contact remains constant and the shear traction is increased enough as to cause slip near the edge, the shear traction in the slip zone, $0 < \xi < s$, is given by

$$q(\xi) = \mu p(\xi) = \mu K_N \sqrt{\xi}. \tag{7.16}$$

Hence, the change in $q(\xi)$ in the slip zone during this new phase is

$$\Delta q(\xi) = \mu K_N \sqrt{\xi} - K_Q \sqrt{\xi}. \tag{7.17}$$

Now, if the zone near the rounded edge behaves approximately as a half-plane, one may apply the Ciavarella-Jäger theorem (see §7.2.3) [Ciavarella, 1998; Jäger, 1998], and the shear traction correction may be written as

$$\Delta q(\xi) = (\mu K_N - K_Q)\sqrt{\xi} - (\mu K_N - K_Q)\sqrt{\xi - s} = (\mu K_N - K_Q)(\sqrt{\xi} - \sqrt{\xi - s}). \tag{7.18}$$

The change in K_N due to fictitious normal load needed for stick correction was neglected in equation (7.18). Furthermore, if $\xi >> s$, it can be shown that in this limit equation (7.18) becomes,

$$q(\xi) \simeq (\mu K_N - K_Q)\frac{s}{2\sqrt{\xi}}, \tag{7.19}$$

so that equating (7.19) to $K_T/\sqrt{\xi}$, one obtain the following expression for the corrected slip zone size,

$$s = \frac{2K_T}{\mu K_N - K_Q}. \tag{7.20}$$

In order to validate the slip zone size prediction, the two loading paths of Figure 7.5 are now used with Coulomb friction instead of the 'rough' contact condition. The shear traction in both situations will cause slip near the edge in the second load step and the size of the slip zone is compared with the predicted size of equation (7.20). The results for the predicted slip zone size are used in the next section in the calculation of the contact tractions and are shown in Figure 7.10. A good prediction of the slip zone was obtained for both loading cases with the corrected formulation (7.20).

The problem studied in the prediction of the slip zone size is a special case in which the contact size remained constant during the second step of the load history. If the contact is either advancing or receding the problem becomes significantly more complex. The receding contact case will not be covered in this work. In the case of advancing contact with the presence of edge slip, the shear traction developed in the "new" contact zone is dominated entirely by the

increment of load in the second load step, with little influence of the previous K_Q. It can be conjectured, therefore, that if the change in contact length is small and advancing, the equations of the slip zone size derived above will also be valid.

7.2.3 Contact tractions in the presence of slip

The normal contact traction was derived by Ciavarella et al. [1998] for a finite punch and later rewritten in terms of the asymptotes by Sackfield et al. [2003]. This solution assumes half-plane theory, which implies that the contact tractions are uncoupled and that the decay of the singular asymptote is square root singular as the observation point moves from the edge inwards into the flat surface of the punch. The formulation derived by Sackfield et al. [2003] can be written as

$$p(\xi) = \frac{K_N}{4\sqrt{l}} \left[2\sqrt{\xi l} + (\xi - l) \ln \left| \frac{\sqrt{l} - \sqrt{\xi}}{\sqrt{l} + \sqrt{\xi}} \right| \right], \quad \xi > 0. \tag{7.21}$$

In the current elastic punch problem, it has been shown that an approximation to a half-plane can often be made near the rounded edge portion of the contact, as long as the contact length of the rounded edge is much smaller than the radius of the rounding. If half-plane theory was valid everywhere, the decay of the contact pressure would be square-root singular away from the rounded edge of the contact. However, as the observation point move inwards away from the corner, the problem behaves as a three-quarter plane notch and the tractions are singular to a power λ, where $\lambda = \lambda_I = 0.5445$ and $\lambda = \lambda_{II} = 0.9082$ for pure mode I and pure mode II loadings, respectively. Therefore, equation (7.21) is only approximately valid in the region near the rounded edge in contact.

The equation for the normal contact traction is also sufficient to describe the shear traction [Jäger, 2003]. From the Ciavarella-Jäger theorem, derived independently by Ciavarella [1998] and Jäger [1998], the shear traction may be obtained from the normal contact traction formulation by

$$q(\xi) = \mu(p(\xi) - p^*(\xi - s)) \tag{7.22}$$

where $p^*(\xi - s)$ is the scaled contact pressure that correspond to a smaller contact zone of the same size as the stick zone, and which is used for the correction of the shear traction. If the

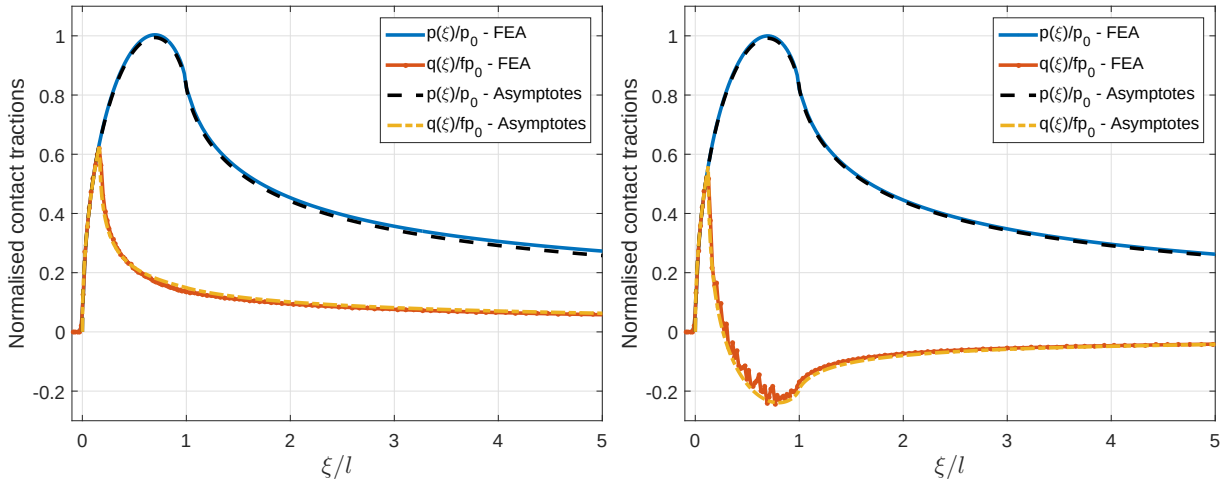

Figure 7.10: Contact tractions obtained via finite element analysis and the asymptotes solution of a problem with constant contact length in the second step and initial loading with mode mixity (a) $d_0/\rho = -1$; and (b) pure mode I, $d_0/\rho = \infty$.

slip zone is small compared with the length of the contact under the rounded edge, one may neglect the change in the contact pressure, so that the corrected pressure can be approximately written as $p^*(\xi - s) \simeq p(\xi - s)$. However, since the equation for K_N was obtained as a function of the contact length, equation (7.6), the correction in K_N due to the stick zone can be obtained, provided the contact length and slip zone size are known.

It is also important to remember that in many situations a bounded shear traction is developed during the first load step. The occurrence of slip near the edge of contact will erase any information regarding the accumulated shear during the initial load step. But the initial shear traction will be 'trapped' in the stick zone and the final shear traction needs to take it into account. The bounded shear traction can be obtained from equation (7.21) by substituting K_N for K_Q. The final shear traction may be obtained from equations (7.21) and (7.22) as

$$q(\xi) = \mu(p(\xi) - p^*(\xi - s)) + q_B(\xi)|_{stick}, \quad \xi > s > 0, \tag{7.23}$$

where $q_B(\xi)$ is the contribution of the bounded shear traction in the first load step.

The formulation in (7.23) was used for the two load histories of Figure 7.5 and the comparison between the finite element analysis results and the formulation using the asymptotes is presented in Figure 7.10. The size of the slip zone was obtained from equation (7.20) and

a good match with the finite element analysis results is observed, even in the presence of an initial shear traction. The contact traction obtained from the asymptotic approach matches reasonably well the finite element analysis results near the edge of the contact. However, the half-plane assumption is no longer true as the observation point moves away from the rounded edge, meaning that the contact normal pressure decay is not square-root singular. This is more evident in the first load case of initial mode mixity $d_0/\rho = -1$ (Figure 7.10a), which is almost pure mode *II* in character at the end of the second load step. Therefore, the contact pressure decays approximately by $\xi^{\lambda_{II}-1} \simeq \xi^{-0.09}$. The contact normal pressure for the second load path is shown in Figure 7.10b and, although it has a stronger singularity near the transition from the flat interface to the rounded edge, it also has a mode *II* decay when $\xi >> d_0$ because of the weaker singularity of the mode *II* eigenvalue.

It has been shown that the asymptotic formulation using the half-plane assumption can be used to describe the contact tractions near the edge of the contact. One limitation of this analysis is that the contact length needs to be small compared to the radius of the rounding. Furthermore, an approximation of the Ciavarella-Jäger theorem was used by neglecting the change in the correction of the normal pressure due to the stick zone in the calculation of the slip zone, which limits the analysis to problems in which the size of the slip zone is small when compared to the length of the rounded edge in contact. However, a corrected slip zone size could be worked out for cases with large slip zone size, as long as the slip does not occur in the flat region of the contact. As it will be shown in the next section, the approximations made here are possible for some applications.

7.3 Finite elastic flat and rounded punch

An example problem will be presented in this section in order to illustrate the analysis presented in this chapter. The problem analysed is one of a finite elastic punch pressed onto an elastically similar half-plane. First, the calibration of the finite elastic sharp-edged punch will be presented, providing a mapping from the normal and tangential applied loads to the corresponding stress intensity factors K_I and K_{II}. Next, the contact tractions, contact size and slip zone size of a finite flat punch with rounded edges will be compared with the asymptotic semi-analytical

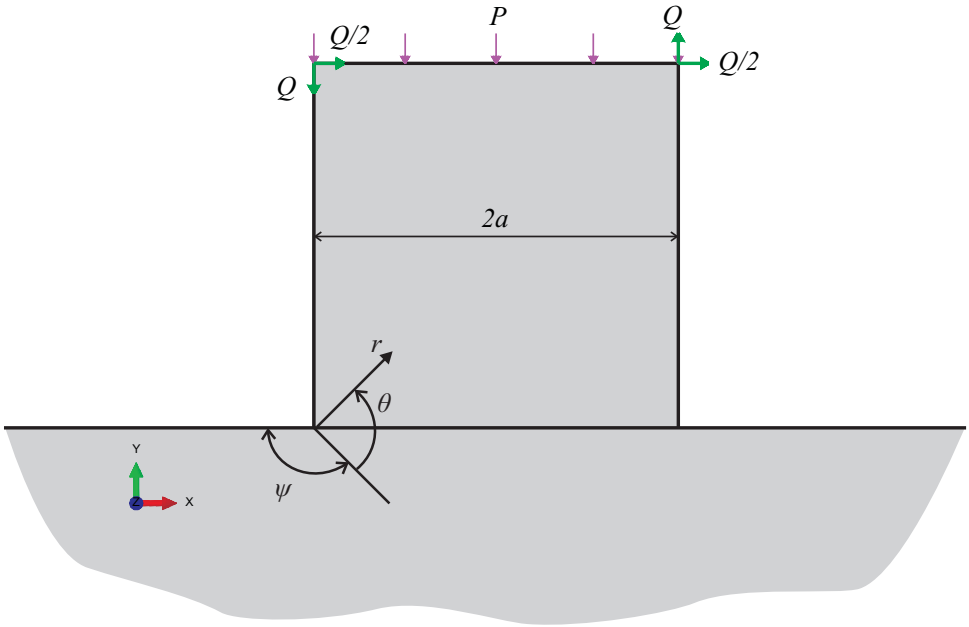

Figure 7.11: Geometry and loads used in the finite element model to obtain the mapping from $P \times Q$ to $K_I \times K_{II}$ along the notch's bisector.

formulation presented in this chapter.

7.3.1 Calibration of the finite sharp punch

One of the main advantages of the approach presented in this work is that *any* contact problem in which a flat a rounded punch is pressed onto a plane elastic surface of elastically similar material can be approximated to a three-quarter plane. Hence, the problem may be dealt in terms of the outer Williams' stress intensity factors. It is first necessary to obtain the mapping of the applied normal and tangential loads in $P \times Q$ space to the outer $K_I \times K_{II}$ space. If the radiused edge has little influence in the far field, it is convenient to obtain the mapping for a square-edged punch submitted to a combination of normal and tangential loads.

The square-edged punch problem was solved numerically in ABAQUS. A schematic representation of the geometry and loads used in the numerical analysis are presented in Figure 7.11. First, a normal load P was applied and, then, a load Q was applied subsequently whilst keeping P constant, such that $Q/P = \pm 0.5$ in the second loading phase. Note that the moment caused by the shear load is counter balanced so that rigid body rotation is avoided, without compromising the applied normal load. A transformation of the stresses to polar coordinates (r, θ) was made and the stress intensity factors were obtained from equations (6.2a) and (6.2b). In the first

loading phase, when only P is applied, it is possible to obtain the coefficients that correlate K_I and K_{II} with P. And in the second phase, the coefficients correlating K_I and K_{II} with Q may be found. The following mapping between spaces $P \times Q$ and $K_I \times K_{II}$ was obtained for the left corner,

$$\begin{Bmatrix} K_I a^{\lambda_I - 1} \\ K_{II} a^{\lambda_{II} - 1} \end{Bmatrix} = \begin{bmatrix} -0.4245 & 0.5057 \\ 0.2480 & 0.5032 \end{bmatrix} \begin{Bmatrix} P/2a \\ Q/2a \end{Bmatrix}, \tag{7.24}$$

where a is the semi-width of the punch and the normalisation used is necessary to let the matrix of coefficients be dimensionless. Note that P and Q are regarded as line loads in a two-dimensional problem and have dimensions of $[FL^{-1}]$. Therefore, equation (7.24) has dimensions of $[FL^{-2}]$ throughout and if divided on both sides by E^*, for example, it becomes dimensionless.

The path of an applied normal load P followed by a shear load Q in the $K_I \times K_{II}$ space is presented in Figure 7.12. From the analysis presented earlier in this chapter, it is expected that a negative shear traction will occur on the left rounded corner when a normal load P is applied. On the right corner, however, the shear due to a normal load P will be positive in sign. Along the line of the applied shear load, $\pm Q$, the contact size may vary. It is important to note that Figure 7.12 cannot be directly correlated with Figure 7.9, and the condition for advancing, or receding, contact as $\pm Q$ is applied depends on the semi-width "a" of the punch.

7.3.2 Example problem: the finite flat punch with rounded edges

A punch of semi-width $a = 10$ mm with rounded edges of radius $\rho = 1$ mm is pressed onto an elastic half-plane. Both the punch and the half-plane have Young's modulus $E = 200$ GPa and Poisson's ratio $\nu = 0.3$. The load is applied in two steps; a normal load $P = 2000$N/mm distributed along the top of the punch is applied first, and a shear load is applied next, such that, $Q/P = \pm 0.5$. The coefficient of friction at the contact interface is $\mu = 1.0$. A moment was also applied to counter balance the one induced by the shear load and stop an rigid body rotation. The resultant stress intensity factors on the left corner due to the normal and tangential loads for this problem are $K_I = -121.2$ Nm$^{-1-\lambda_I}$ and $K_{II} = 30.6$ Nm$^{-1-\lambda_{II}}$ in the first step and a change $\Delta K_I = 72.2$ Nm$^{-1-\lambda_I}$ and $\Delta K_{II} = 31.1$ Nm$^{-1-\lambda_{II}}$ for a positive applied shear Q in the second

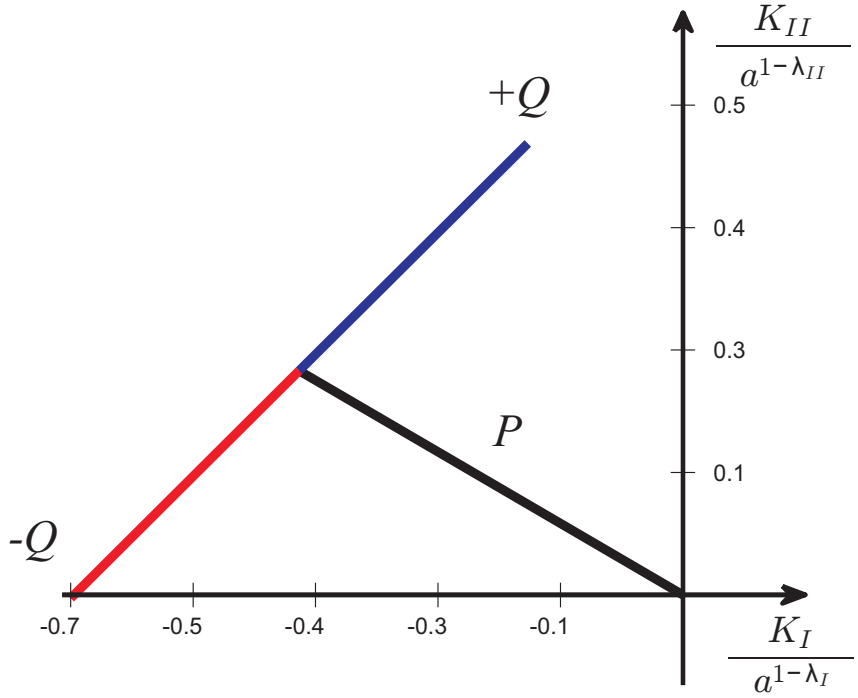

Figure 7.12: Map of an applied load P and subsequent applied load Q, with $Q/\mu P = 0.5$, on the $K_I \times K_{II}$ space.

step. A schematic drawing of the model used in ABAQUS is presented in Figure 7.13. The mesh refinement used near the contact edge is similar to the one used in §6.2.

The contact tractions obtained via finite element analysis for both positive and negative Q are presented in Figures 7.14a & 7.14b, respectively. The blue lines on both Figures 7.14a & 7.14b are the contact tractions due to the normal load P only, and the green lines are the contact tractions after a shear load is applied. As the shear load is introduced, the contact recedes when a positive Q is applied and advances when Q is negative, for the given ratio of the semi-width and radius of the punch a/ρ. The change in contact length is not negligible when the shear load is introduced in the second loading phase. The calculation of the slip zone from equation (7.20), which assumes constant contact size, would need to take into account the change in contact length, l, and the change in K_N for a better prediction of the region where slip occurs. However, equation (7.20) is used here to determine, approximately, the slip zone size.

The normalised tractions due to the applied normal load P during the first loading phase are presented in figure 7.15. Equation (7.21) was used to obtain $p(\xi)$ and the bounded $q_B(\xi)$ in the first step. The contact length, l, was obtained from equation (6.14) and K_N from (7.6). The normal pressure edge scaling factor, K_N, and the contact size, l, obtained with the semi-

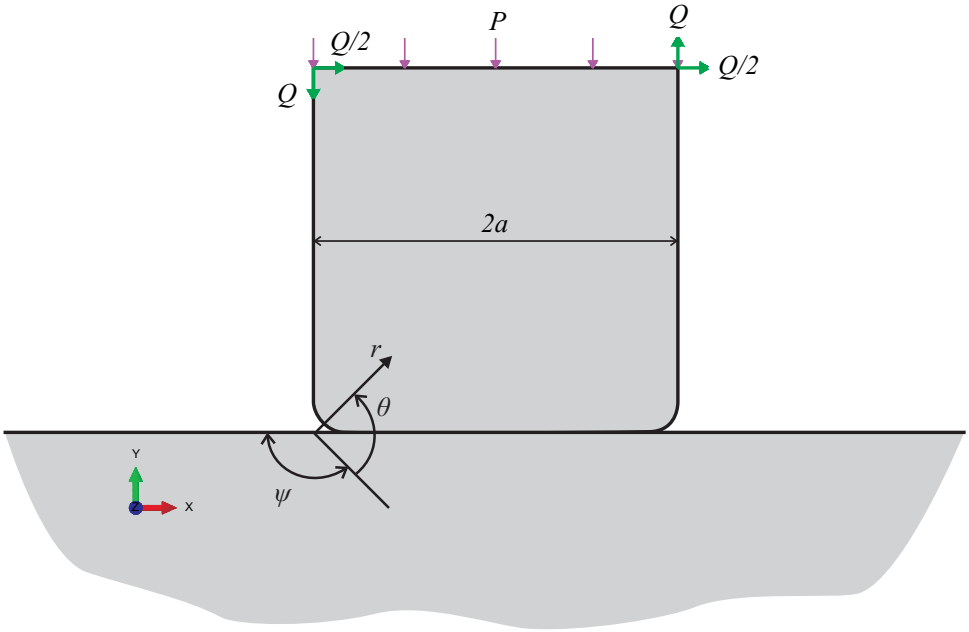

Figure 7.13: Geometry and loads used in the finite element analysis for the flat and rounded punch example problem.

analytical formulations match with good accuracy the finite element results. The singular shear traction scaling factor, K_T, during the second phase of loading was obtained from equation (7.14), by approximating the load trajectory $(\Delta K_I^*, \Delta K_{II}^*)$ to one of constant contact length. The bounded shear scaling factor, K_Q, in the first loading phase was obtained from the approximate solution for mixed mode loading in §7.1.3.

The contact tractions obtained when a positive and negative Q are applied subsequently are shown in Figures 7.16 & 7.17. The normal traction obtained from the semi-analytical formulation is slightly lower than the finite element results for the positive Q and higher for the negative Q load. This implies that the K_N obtained from equations (7.4) and (7.6) does not match exactly the normal scaling factor of the finite punch during the shear load step, although it matched well during the first phase of loading, when only a normal load was applied. One possible reason for this is that, although a moment was applied to counter balance the rigid body rotation induced when a shear load is applied, locally, rotation of the punch is still happening near the edge of contact in the finite element model. The slip zone obtained with equation (7.20) was overestimated with respect to the numerical slip zone size when the applied shear force was positive and underestimated when a negative shear force was applied. In order to get better prediction for the slip zone size, further analysis are needed for advancing and receding contact problems.

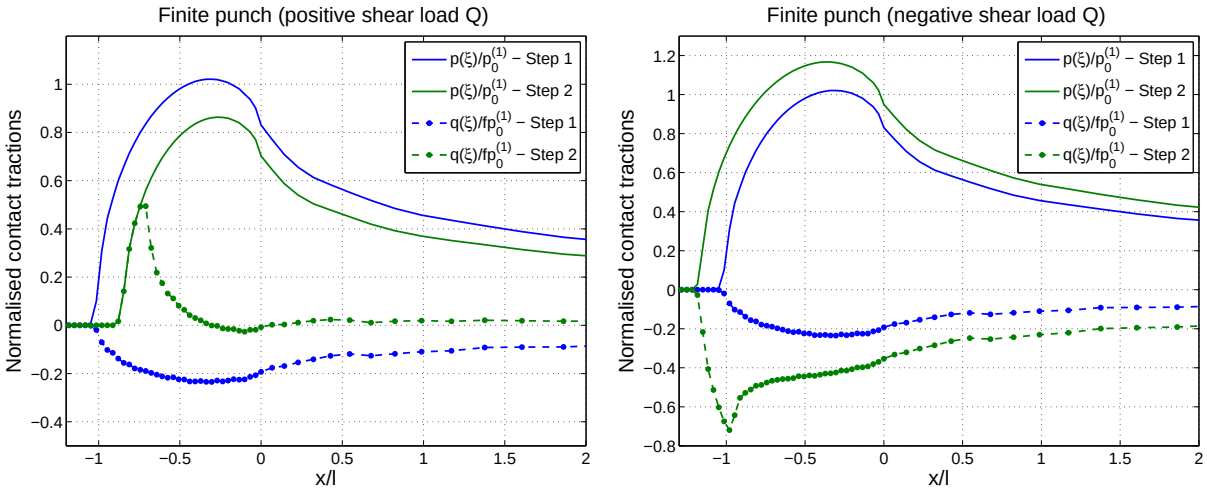

(a) (b)

Figure 7.14: Contact tractions of the finite punch with rounded edges problem obtained via finite element analysis for a (a) positive shear load Q; and (b) negative shear load Q.

7.4 Discussion

A formulation in terms of edge asymptotes for the problem of an elastic punch pressed onto an elastic half-plane was presented in this chapter. The contact edge scaling factors were derived from the far field Williams' stress intensity factors using the analogy with the three-quarter plane problem presented in chapter 6. The normal contact pressure scaling factor, K_N, has been defined for any combination of mode I and mode II loading, since it is very weakly coupled and, hence, unique for any combination of dimensionless K_I^* and K_{II}^*. The shear tractions edge scaling factors K_Q and K_T, on the other hand, depend on the load history because of the non-linearity introduced by friction. Formulations for the bounded scaling factor K_Q have been developed for both pure modes of loading. And an alternative approximate solution for the bounded shear traction asymptote was introduced to solve mixed mode problems. The singular scaling factor K_T has only been obtained for the special case of constant contact length during the second phase of loading. However, for many problems the approximation of constant contact length during the second phase of loading is reasonable, particularly Cattaneo-Mindling type problems with constant normal load and oscillating shear load. Hence, this solution is a good start in solving cyclic shear loading problems.

The edge scaling factors were used to determine the size of the slip zone in a partial slip problem, which was shown to predict reasonably well in the semi-infinite problem of §7.2.3.

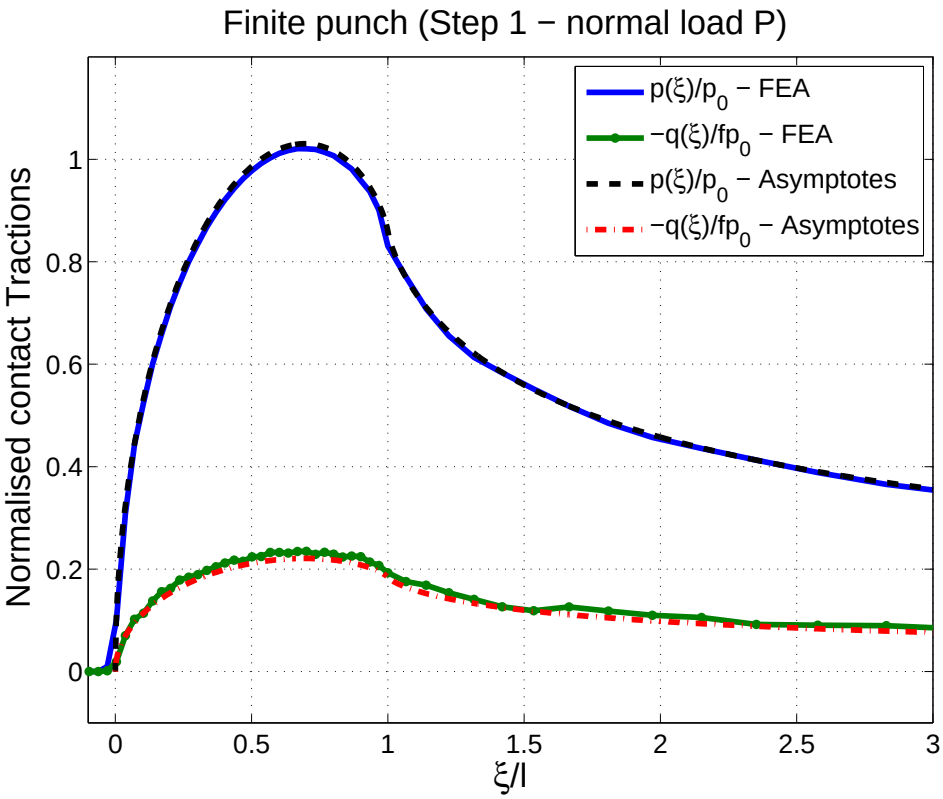

Figure 7.15: Numerical and semi-analytical contact tractions due to the applied normal load P (negative $q(\xi)$).

However, the formulation of the slip zone size assumes that the contact remains constant during the second phase of loading and that the region surrounding the rounded part of the contact interface can be approximated to a half-plane for the Ciavarella-Jäger theorem to be valid. Although the assumption of constant contact length in the second phase of loading has shown to limit the range of application of the formulation derived, the half-plane assumption was proven to be valid when the size of the contact is small when compared to the radius of the rounding, as observed in §7.3.2. Using the half-plane approximation in the surrounding of the rounded edge in contact, the contact normal and shear traction distributions were obtained from the equation derived by Sackfield et al. [2003] and the Ciavarella-Jäger theorem. However, the formulation is only valid in the region near the rounded edge, since the problem behaves as a three-quarter plane problem as the observation point moves inwards into the contact interface and the singular decay of the contact pressure is not square-root singular for the elastic problem.

The work presented in the last two chapters has described a new approach to solving the partial slip problem of elastic flat punches with rounded edges. The formulations derived are

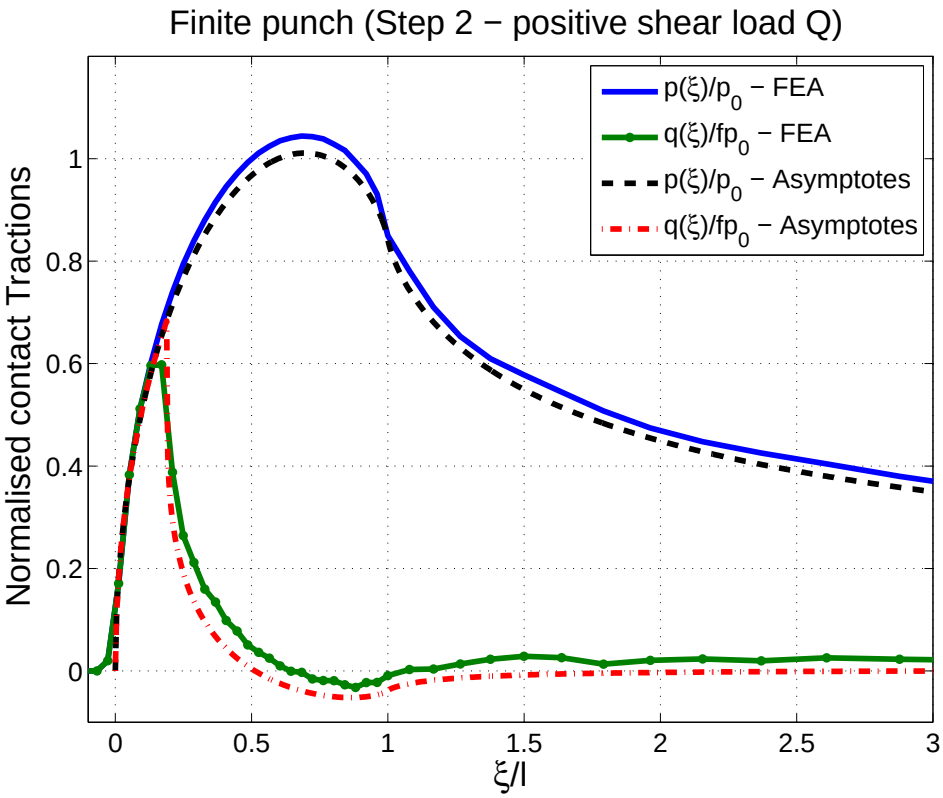

Figure 7.16: Numerical and semi-analytical contact tractions due to the positive shear load Q (positive $q(\xi)$).

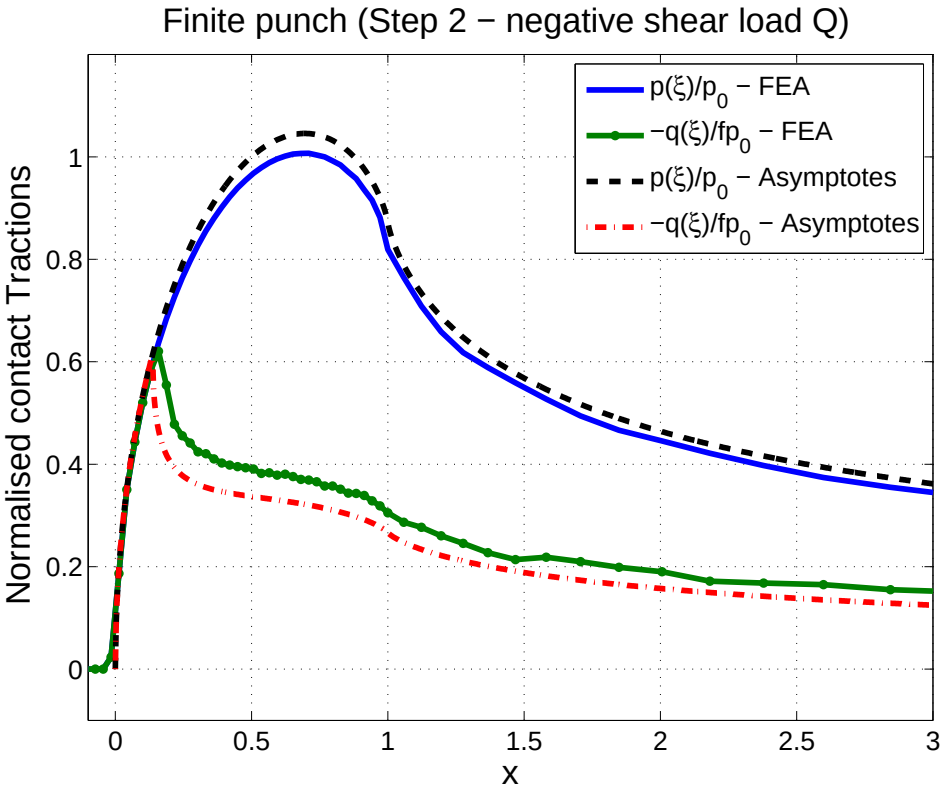

Figure 7.17: Numerical and semi-analytical contact tractions due to the negative shear load Q (negative $q(\xi)$).

sufficiently to solve, approximately, problems of simple load histories and is an initial step for solving the partial slip fretting problem. One of the main problems that need yet to be solved in order to make this solution more generally applicable is to understand how the contact tractions and slip zone size will behave if the contact advances or recedes. Then, one will be able to solve not only the problem of fretting with oscillating shear and constant normal force, but any load history in the $P \times Q$ space.

Chapter 8

Conclusions

The main conclusions obtained in this work are highlighted in this chapter. First, a summary of the work undertaken in this thesis is presented. Then, the main achievements and conclusions obtained are highlighted. Finally, recommendations are made in the end of the chapter for the continuation of some of the work presented.

8.1 Overview

The work carried out in this thesis aimed to investigate some aspects of contact and fretting in fir-tree blade to disc assemblies. From the solid mechanics point of view, the contact between blades and disc in turbine engines is an extremely complex and challenging problem. This is mainly due to the fact that the parts in the turbine operate at extreme temperatures, sometimes above the materials' melting point, and high loading conditions. Furthermore, there are multiple contact points between the blade and the disc in the fir-tree assembly (see chapter 1) and every time the engine is started/stopped, slip occurs at the contact interface. The presence of slip accelerates the initiation of cracks at the edge of the contact and, hence, may lead to fretting fatigue. The severe environment in which turbines blades and discs operate has led to a search for materials that can sustain their mechanical properties at elevated temperatures, and nickel superalloys are currently the preferred materials in the hottest stages of the engine. Other failure mechanisms are also relevant in turbines and resistance to creep is one of the main requirements for the choice of material. With that in mind, the use of single-crystal alloys in the hot stages of

the turbine has become widespread in turbines of aero-engines.

Single-crystal parts introduce other variables to the contact problem. In a polycrystalline body, the random distribution of crystal orientations result in bulk elastic properties of the material, which are different in each individual crystal, but which are macroscopically isotropic, i.e. the material response is the same in any direction of loading. If the whole component is made of one single crystal, then the elastic properties will depend on the crystal structure. In the case of nickel crystals, its face centred structure (FCC) results in orthotropic elastic properties with crystal symmetry. This means that elastic properties in three principal crystallographic directions are the same but in any other direction the material response varies. The crystal orientation then becomes one more variable to be taken into account in the contact problem. Note that only one principal crystal direction is controlled in the manufacturing of blades, with a 20° tolerance. The other two principal direction are completely uncontrolled and questions have been raised concerning their impact in fretting fatigue lives.

In blade to disc assemblies, failure may occur on both sides of the contact. Both the blades and the discs are subjected to cyclic bulk tensions and if crack are initiated at the contact interface, they are likely to propagate on both parts. This was observed, for example, on the 'H-specimen' tests carried out by Rolls-Royce plc and briefly introduced in §1.1. However, a special focus is given in this thesis to the discs, which are not easily replaced and are considered a more critical part of the engine. Blades, on the other hand, are relatively easily replaced and although a good knowledge of their fretting fatigue lives is also required, this is outside the scope of the current work. Therefore, fretting fatigue tests were carried out at the University of Oxford to investigate the fretting fatigue life of isotropic nickel alloys (disc) when pressed against single-crystal pads (blade) at high temperature. The results were presented in chapter 4.

Another relevant aspect of the contact problem found in blade to disc assemblies is the presence of a second stress concentrator, in the form of a notch, near the edge of contact. However, before one can investigate the impact of two proximate stress concentrators, the partial slip contact problem for an elastic flat punch with rounded edge pressed onto an elastic plane needs to be solved. The presence of edge rounding at the edge of the contact makes the contact incomplete and, hence, the tractions fall to zero at the edge of contact. However, in contrast

to the Hertzian contact problem, where the peak contact pressure occurs at the centre of the contact, the highest peak pressure in the flat and rounded punch problem occurs near the edge of contact where the cracks are more likely to initiate. Hence, the interest in investigating the tractions for this type of contact, which occurs in both 'dovetail' and 'fir tree' blade to root assemblies, has increased in the past decade. Most solutions developed for this type of contact assume the contact to be uncoupled, which is not true when the contact is frictional and both bodies are elastic. An understanding of the partial slip contact in elastic flat and rounded contact problems is essential to study the problem of a notch near the edge of contact in blade to root assemblies.

8.2 Summary

This thesis aimed at answering some aspects of fretting fatigue in high pressure turbines of aero-engines that require improved understanding. An investigation of the effect of the crystal orientation in single-crystal bodies on the contact tractions has been carried out. The predicted effects have been compared with experimental results at room and high temperatures. The focus of this investigation has been on the contact between a cylindrical body and a flat specimen. This is an idealisation of the geometry in the blade to disc assembly in aero-engines. However, the geometry of 'fir-tree' blade to disc assemblies in turbines is similar to that of a flat punch with rounded edges. The reason cylindrical pads are often preferred in laboratory fretting fatigue experiments is that the solution of the contact tractions can be more easily calculated. In fact, the problem of a frictional contact between an elastic flat punch with rounded edges and an elastic half-plane does not have a general closed form solution. In chapters 6 & 7, a semi-analytical solution of the flat and rounded punch is presented. So far, this was developed only for elastically similar isotropic materials. However this is a first step towards solving more complex contact problems with this geometry, for example, when one of the bodies is made of a single-crystal alloy.

A summary of the main sections of this thesis is presented next. The first section concerns the effect of single-crystal alloys on the contact tractions for Hertzian contacts. The second section presents a summary of the findings of the fretting fatigue tests, including the investigation

of friction between nickel superalloys. Finally, the main findings of an investigation of elastic contacts with flat and rounded pads are also summarised.

8.2.1 Single-crystal orientation and contact pressure

General aspects of single-crystal materials were presented in chapter 3. A brief discussion of the elastic stiffness of the CMSX-4 alloys at room and high temperatures were presented. The objective was to investigate how the change of the elastic properties with the crystal orientation might change the contact tractions. When the single-crystal's principal directions are parallel to the Cartesian coordinate system axes of the loads and boundary conditions, the only difference between an ortothropic material with cubic symmetry and an isotropic material is the fact that $D \neq 1$, where D is a measure of the anisotropy of the material. In fact, for any orientation of symmetry of the elastic stiffness with respect to the loading direction, the response of nickel single-crystals is similar to that of isotropic materials, i.e. direct stresses will cause only direct strains and shear stresses will cause only shear strains. However, if the crystal's principal directions are arbitrarily oriented in any direction, the elasticity matrix will have other non-zero terms and coupling between direct and shear stresses and strains may exist. Using a transformation of basis of the elasticity tensor by Euler rotations (§3.1.2), the stiffness of each crystal directions was calculated and the variation in stiffness between the different directions of the CMSX-4 alloy may be as great as 2.3 times the stiffness in the principal direction.

An understanding of the elastic stiffness in different directions of the crystal was also needed in the indentation technique for determining the crystal's principal directions presented in §3.2.1. By indenting an axisymmetric indenter (e.g. conical or ball indenter) in the face normal to one of the crystal's principal directions, the other two principal directions were measured using the squared shaped residual deformation mark. This technique was used in previous fretting fatigue tests presented in [Sarsfield, 2008]. The results are discussed in §3.2.2. The plot of crystal orientation of single-crystal pads and fretting fatigue cycles to failure suggests a correlation between the contact tractions and the crystal orientation. However, there was insufficient data and not enough spread in crystal orientation in the tests observed. Therefore, it is difficult to assess the general trend.

The variation in contact pressure for different orientations of the CMSX-4 alloy was investigated using the analytical solutions presented in chapter 2. The change in contact stress when the orientation of the crystal is rotated about each of the crystal's principal directions has been investigated. It has been shown that the most severe change in contact traction occurs when the crystal rotates about the x axis, i.e. out-of-plane rotation. When the crystal is rotated 45° about the z axis, and the stiffer directions $\langle 110 \rangle$ are aligned with the normal and tangential directions of the crystal, no change in contact pressure occurs. This result may be counter intuitive, but may be explained by looking at the anisotropic analytical solution of the contact problem. In a two-dimensional contact problem, the contact tractions depend on the integral of the elastic stiffness of the bodies in contact on the plane of contact, and when a rotation about the z axis is made, the sum of elastic stiffness in all directions of the plane of contact remains constant. The maximum possible increase in contact traction of 6.3% occurs at crystal orientations similar to the crystal rotation of 45° about the x axis (e.g. $\phi_1 = 0^\circ$, $\phi_2 = 45^\circ$ and $\phi_3 = 0^\circ$). When taking into account the manufacturing tolerance of 20° deviation between the $\langle 010 \rangle$ direction and y axis in the fretting fatigue pads, the maximum increase in peak contact stress of 3.5% is found at crystal orientations similar to $\phi_1 = 0$, $\phi_2 = 20^\circ$ and $\phi_3 = 45^\circ$.

Although the variation of contact pressure due to the elastic stiffness of single-crystals is very small for the CMSX-4 single-crystal alloy, other aspects of the contact problem still need to be investigated. The analysis in chapter 3 focused only on the contact normal pressure. However, the shear tractions are also of extremely importance in the variation of fretting fatigue lives, since they cause surface damage and crack initiation at the interface of the contact. A numerical analysis was carried out in chapter 4 for a more complete investigation of the fretting stresses and correlation with experimental results.

8.2.2 Fretting fatigue of nickel alloys at high temperatures

A new test programme was carried out at the University of Oxford to investigate fretting fatigue of nickel superalloys at high temperature. The specimen subjected to fatigue loads was made of the polycrystalline nickel superalloy RR1000. Tests with both single-crystal and similar RR1000 pads were used. The tests were carried out at 680°C. Different frequencies of loading

were tested with RR1000 pads, resulting in distinct fatigue curves. It is believed that tests with lower frequency allowed more time for the formation of oxides in the interface of the contact. Oxides are known to have lower coefficient of friction and, hence, the contact shear tractions are reduced for low frequency tests, resulting in an increase in the fretting fatigue life. Note that one cycle in the laboratory tests represents an event that happens once per flight. Therefore, none of the frequencies are truly representative of the real conditions, but lower frequencies are desirable. Hence, all tests with single-crystal pads were carried out at the frequency of 0.25 Hz only. The results obtained when analysing the previously conducted MACE tests were very important in the design of the new test programme, particularly, regarding the measurement of crystal orientations of single-crystal pads before each test. Tests with pads at different crystal orientations were carried out at the same applied load range. A scatter in the results was observed for tests with single-crystal pads, but it has to be highlighted that the scatter was significantly smaller than what was observed in previous tests.

Shear tractions and the stresses under the contact edge were investigated in chapter 4 by the finite element method. A model of the fretting fatigue tests was designed in ABAQUS/CAE to investigate the contact tractions in a complete fretting cycle. The results showed a small variation, of the same order of magnitude found in the analytical analysis, in the stresses near edge of contact as a function of the orientation of the crystal. If assumed that the coefficient of friction does not change with the crystal orientation, the maximum variation in the stresses near the edge of contact is about 4.5% with respect to the reference orientation, taking into account the 20° tolerance in the pad manufacturing. The work carried out in this thesis has demonstrated that the variation of the elastic stiffness alone in single-crystals is not responsible for the large scatter often observer in fretting fatigue tests. Other factors, such as the change in coefficient of friction with respect to the crystal orientation may play a bigger role in the crack initiation time than was previously expected. The results obtained may be useful in the design of new fretting tests, where, provided that the loading is insufficient to cause plastic deformation and that one of the principal directions is positioned normal to the contact, control of the orientation of the secondary principal directions may be unnecessary.

An area averaging approach for the correlation between fretting fatigue and plain fatigue

experiments was suggested in §4.3. The direct stress component in the direction of the cyclic loading was average over a region of radius defined by the El Haddad's parameter [El Haddad et al., 1978]. By averaging the stresses in a 'process zone' near the contact edge, the correlation between fretting fatigue and plain fatigue curves improved significantly. A 'correction' of the coefficient of friction was suggested based on the initial observations of higher coefficient of friction for the CMSX-4/RR1000 pair in comparison with the RR1000/RR1000 pair, and based on the argument of oxide formation on the contact interface for lower frequency tests.

Attempts to measure the coefficient of friction were made and are discussed in chapter 5. A non-sliding technique for measuring the coefficient of friction, also known as the "walking pad" test, was carried out with CMSX-4 pads and RR1000 specimens at room temperature. The theory behind this technique is conceptually very elegant and interesting. It consists of changing the central stick zone location in the contact by a certain combination of loading to achieve a net displacement at the end of one load cycle. The rate of displacement can be correlated with the coefficient of friction in the contact zone. However, the repeatability of the tests was shown to be a problem, particularly when single-crystal pads were used. The results were therefore inconclusive, although it was evident that the pair CMSX-4/RR1000 has higher coefficient of friction than the RR1000/RR1000 pair. An energy based technique has also been investigated. By calculating the total energy dissipated inside the slip zones of the contact, and measuring the displacement of points along the specimen to obtain the 'hysteresis loop', it could be possible to correlate the energy dissipated with the coefficient of friction. Although the sensitivity of the energy dissipated for different coefficient of friction appears to be small, the equations of the energy dissipated derived here may be used together with digital image correlation methods to obtain accurate measurements of the energy dissipated in one complete load cycle.

8.2.3 Elastic flat punch with rounded edges

A new approach for solving the problem of an elastic flat punch with rounded edges pressed onto an elastic half-plane was presented here. Previous attempts to solve this problem have assumed that the problem is uncoupled, which is only true if the problem is frictionless or the punch is rigid and the elastic plane incompressible. The solution proposed here uses a three-

quarter plane model as an asymptote to the zone *very* close to the edge of the contact. In doing so, Williams' solution for notches and wedges may be used and the problem is written in terms of the mode *I* and mode *II* stress intensity factors, K_I and K_{II}, respectively. The contact basic characteristics in terms of K_I and K_{II} were obtained in chapter 6. Using a dimensionless analysis and a calibration via the finite element method, the equations for the contact law, i.e. the variable length of contact under the rounded edge, and the maximum contact peak pressure were obtained. First, pure modes of loading were assumed and then the solution for mixed mode loading was derived. Note that most practical examples of loading of a punch pressed onto a half-plane are in fact mixed mode when written in terms of William's stress intensity factors.

In order to solve the partial slip problem, edge asymptotes to the contact tractions were introduced in chapter 7. The concept of contact traction asymptotes has been used by several researchers in the past decade, since it provides a means of correlating laboratory fretting fatigue experiments with complex prototypes tests by matching the state of stress in the vicinity of the contact, where cracks are likely to initiate. Three edge asymptotes were introduced: i) a square-root bounded asymptote for the contact normal pressure; ii) a square-root bounded asymptote for the shear traction conditions of proportional loading; and iii) a square-root singular asymptote for the singular shear traction if slip is inhibited and under conditions of non-proportional loading. The multipliers, or edge scaling factors, of the asymptotes are given by K_N, K_Q, and K_T, respectively. The calibrations for the edge three edge asymptotes were obtained in terms of William's stress intensity factors and the contact law and peak pressure were rewritten. By using the Ciavarella-Jäger theorem, the size of the slip zone was derived and the shear traction distribution for different loading paths were derived.

An example problem of a finite punch with rounded edges was solved by using the three-quarter plane asymptote approach. First the calibration for a sharp-edged punch under normal and tangential loading was obtained via ABAQUS/CAE to correlate the normal force, P, and the shear force, Q, with the William's stress intensity factors K_I and K_{II} (see §7.3.1). Once the calibration was completed, the equations derived in chapters 6 & 7 were used to obtain the contact tractions. Note that the equation derived for the edge scaling factor K_T assumes that the

contact size does not change during the second phase of loading. This is, of course, a limitation to the current solution, but this approximation may be used for several problems and, in fact, a good agreement with the numerical solution was obtained in the example problem of §7.3.

8.3 Concluding remarks

Some of the main findings of this work are highlighted next:

- The variations in contact pressure and fretting stresses due to the orientation of single crystal pads, under purely elastic analysis, is small and on their own do not seem sufficient to cause the variation in fretting lives as observed experimentally. The results may be useful in the design of new fretting tests with single-crystal pads, where the control of the secondary principal directions may not be necessary, provided the loads are insufficient to cause significant plastic deformation.

- The area averaging approach of the variation of direct stress in the direction of loading provided a good correlation between fretting fatigue results and plain fatigue data, despite the fact that the state of stress under the contact is in fact multiaxial and the other components of stress were neglected.

- The three distinct curves obtained in the fretting fatigue tests at high temperature for the three different test groups highlights the importance of investigating the coefficient of friction for each contact pair and test condition. Tests carried out at lower frequencies are likely to have a lower coefficient of friction, and tests with the CMSX-4/RR1000 pads are also likely to have higher coefficient of friction than tests with the RR1000/RR1000 pair. Taking into account the variation in coefficient of friction between the different contact pairs and test frequencies improves the correlation between fretting fatigue lives and averaged direct stress in the direction of loading.

- Measuring the coefficient of friction in partial slip contact remains a difficult task, particularly, for cylindrical contact, when the remote displacements do not converge to a finite

value. The "walking pad" tests remains the best approach, but further tests need to be carried out and, preferably, at a more appropriate rig designed specifically for this test.

- The three-quarter plane asymptotic approach for the flat and rounded elastic punch as a means of obtaining expressions for the contact edge asymptotes has been successfully implemented. The partial slip contact problem for simple load trajectories has been solved. The approach is a first step in solving the partial slip contact under periodic load histories.

8.4 Future work

Although the anisotropic contact formulation in §2.2.2 was general and included the shear tractions, only the contact normal pressure was solved analytically in §2.2.3, and only for the frictionless case of contacting cylinders. The solution of the shear tractions, particularly under partial slip conditions, could be very useful in solving fretting problems with anisotropic bodies. However, it is unlikely that an analytical solution can be derived, since the problem is coupled when friction is taken into account. Nevertheless, a numerical solution of the contact singular integral equations could be more advantageous than finite element analysis. The calculation of the out-of-plane shear tractions, for example, can be obtained from the solution of equation (2.41), avoiding the use of finite element three-dimensional models, which can be computationally expensive and generally with poor discretisation of the stresses near the edge of contact.

Regarding the fretting fatigue stress with single-crystal pads, the numerical and analytical two-dimensional solutions have presented consistent results. One aspect that can be improved is a better understanding of the out-of-plane tractions for certain orientations, as well as a more thorough investigation of variation in the coefficient of friction as a function of the crystal orientation. Other fatigue methods may also be used in the correlation with fretting fatigue results. The approach used in chapter 4 only took into account the direct stress in the direction of loading. Multiaxial fatigue criteria, such as Dang Van's model [Dang Van, 1972], have been implemented in fretting fatigue experiments [see Araújo et al., 2008; Nowell and Dini, 2003; Murthy et al., 2006]. An investigation into different criteria could provide better correlation

between the stresses near the edge of contact and the number of cycles to failure in fretting fatigue experiments.

Further investigation of the coefficient of friction in contacts with single-crystal bodies in partial slip is suggested. An investigation of the consistency of the "walking pad" test needs to be carried out. Furthermore, more samples under different crystallographic directions are needed for any conclusions to be drawn regarding the variation in coefficient of friction due to crystal orientation. It is important that any test be carried out with unused pads, to avoid the problems faced in the analysis of chapter 5, where every time the pad was reground, a higher coefficient of friction was measured. Further study in developing an energy approach for measuring friction for the contact of cylinders is also required. Another important limitation in the fretting fatigue experiments at high temperature is that most pads had similar orientation. A wider spread of crystal ornamentations is necessary to identify whether distinct curves are obtained for different crystal orientations.

The semi-analytical equations presented in chapters 6 & 7 are the first step in solving fretting fatigue problems with such geometry of contact. The problem is, so far, restricted to a load history where an initial proportional load is applied, followed by one load step, in which the size of the contact remains constant and slip zone appears at the edge of contact. The challenge is now to extend this solution to a general periodic loading problems. Barber et al. [2011] have presented a detailed formulation for determining the contact tractions in partial slip Hertzian contacts for any load history of the normal and tangential applied forces. It is suggested that the formulation be now rewritten in terms of the edge asymptotes, first for the same Hertzian problem and then for any incomplete problem. If this is achieved, as long as the contact is incomplete, regardless of the geometry of the contact, the partial slip shear tractions at any instant in a cyclic load history can be obtained, provided the calibrated equations for the edge asymptotes multipliers are known.

Bibliography

Amontons, G. (1699). De la resistance cause dans les machines. *Memoires de L'Academie Royale*, A:275–282.

Arakere, N. K. and Swanson, G. (2001). Fretting stresses in single crystal superalloy turbine blade attachments. *Journal of Tribology*, 123(2):413–423.

Arakere, N. K. and Swanson, G. (2002). Effect of crystal orientation on fatigue failure of single crystal nickel base turbine blade superalloys. *Journal of Engineering for Gas Turbines and Power*, 124(1):161–176.

Araújo, J. A. (1998). *On the initiation and arrest of fretting cracks*. PhD thesis, University of Oxford.

Araújo, J. A. and Nowell, D. (2002). The effect of rapidly varying contact stress fields on fretting fatigue. *International Journal of Fatigue*, 24(7):763–775.

Araújo, J. A., Susmel, L., Taylor, D., Ferro, J. C. T., and Ferreira, J. L. A. (2008). On the prediction of high-cycle fretting fatigue strength: Theory of critical distances vs. hot-spot approach. *Engineering Fracture Mechanics*, 75(7):1763–1778.

Bagault, C., Nélias, D., and Baietto, M. C. (2012a). Contact analyses for anisotropic half space: Effect of the anisotropy on the pressure distribution and contact area. *Journal of Tribology*, 134(3).

Bagault, C., Nélias, D., Baietto, M. C., and Ovaert, T. C. (2012b). Contact analyses for anisotropic half-space coated with an anisotropic layer: Effect of the anisotropy on the pressure distribution and contact area. *International Journal of Solids and Structures*.

Banerjee, N., Hills, D. A., and Dini, D. (2009). The derivation and application of a semi-infinite flat and rounded asymptotic frictionless contact. *International Journal of Mechanical Sciences*, 51(9):662–666.

Barber, J. R., Davies, M., and Hills, D. A. (2011). Frictional elastic contact with periodic loading. *International Journal of Solids and Structures*, 48(13):2041–2047.

Barnett, D. M. and Lothe, J. (1973). Synthesis of the sextic and the integral formalism for dislocations, green's function and surface waves in anisotropic elastic solids. *Phys Norv*, 7:13–19.

Boussinesq, J. (1885). *Application des potentiels à l'étude de l'équilibre et du mouvement des solides élastiques*. Gauthier-Villars.

Bower, A. F. (2012). *Applied Mechanics of Solids*. http://solidmechanics.org/.

Carter, F. W. (1922). *Railway Electric Traction*. Edward Arnold, London.

Cattaneo, C. (1938). Sul contatto di due corpi elsatici: distribuzion local degli sfozi. *Reconditi dell accademia nazionale dei lincei*, 27:342–348,434–436,474–478.

Churchman, C. M. and Hills, D. A. (2006). General results for complete contacts subject to oscillatory shear. *Journal of the Mechanics and Physics of Solids*, 54(6):1186–1205.

Ciavarella, M. (1998). The generalized cattaneo partial slip plane contact problem. i: Theory. *International Journal of solids and structures*, 35(18):2349–2362.

Ciavarella, M., Hills, D. A., and Monno, G. (1998). The influence of rounded edges on indentation by a flat punch. *Proceedings of the Institution of Mechanical Engineers, Part C: Journal of Mechanical Engineering Science*, 212(4):319–327.

Coulomb, C. A. (1785). Théorie des machines simples. *Mémoires de Mthématique et de Ohysique de l'Académie Royale*, pages 161–342.

Dang Van, K. (1972). Sur la resistance à la fatigue des matériaux. *Sciences Techniques de lArmement*, 47.

Dini, D. and Hills, D. A. (2004). Bounded asymptotic solutions for incomplete contacts in partial slip. *International journal of solids and structures*, 41(24):7049–7062.

Dini, D., Sackfield, A., and Hills, D. A. (2005). Comprehensive bounded asymptotic solutions for incomplete contacts in partial slip. *Journal of the Mechanics and Physics of Solids*, 53(2):437–454.

Dongye, C. and Ting, T. C. T. (1989). Explicit expressions of barnett-lothe tensors and their associated tensors for orthotropic materials. *Quarterly Journal of Mechanics and Applied Mathematics*, 47:723–734.

Dowson, D. (1998). *History of Tribology*. Wiley, 2nd edition.

El Haddad, M., Smith, K., and Topper, T. (1978). Fatigue crack propagation of short cracks. *American Society of Mechanical Engineers (Paper)*, (78 -Mat-7).

Fan, H. and Keer, L. M. (1994). Two-dimensional contact on an anisotropic elastic half-space. *Journal of applied mechanics*, 61(2):250–255.

Ferré, R., Fouvry, S., Berthel, B., and Ruiz-sabariego, J. A. (2013). Stress gradient effect on the crack nucleation process of a ti-6al-4v titanium alloy under fretting loading: comparison between non-local fatigue approaches. *International Journal of Fatigue*.

Flamant, A. (1892). Sur la répartition des pressions dans un solide rectangulaire chargé transversalement. *Compte. Rendu. Acad. Sci. Paris*, 114:1465.

Fleury, R. M. N., Hills, D. A., and Barber, J. R. (2015a). Flat punch with rounded edges-part i: basic contact characteristics in terms of williams notch intensity factors. *International Journal of Solids and structures*, in print.

Fleury, R. M. N., Hills, D. A., and Barber, J. R. (2015b). Flat punch with rounded edges-part ii: near edge asymptotes and the effect of shear. *International Journal of Solids and structures*, in print.

Fleury, R. M. N., Paynter, R. J. H., and Nowell, D. (2014). The influence of contacting ni-based single-crystal superalloys on fretting fatigue of ni-based polycrystalline superalloys at high temperature. *Tribology International*, 76:63–72.

Fouvry, S., Kapsa, P., and Vincent, L. (1995). Analysis of sliding behaviour for fretting loadings: determination of transition criteria. *Wear*, 185(1):35–46.

Fouvry, S., Kapsa, P., and Vincent, L. (1996). Quantification of fretting damage. *Wear*, 200(1):186–205.

Fouvry, S., Kapsa, P., and Vincent, L. (2000). Multiaxial fatigue analysis of fretting contact taking into account the size effect. Number 1367, pages 167–182.

Fouvry, S., Kapsa, P., Zahouani, H., and Vincent, L. (1997). Wear analysis in fretting of hard coatings through a dissipated energy concept. *Wear*, 203:393–403.

Galin, L. A. (1953). *Contact problems of the theory of elasticity*. Gostekhizdat, Moscow.

Gladwell, G. M. L. (1980). *Contact Problems in the Classical Theory of Elasticity*. Sijthoff and Noordhoff.

Goodman, L. E. (1962). Contact stress analysis of normally loaded rough spheres. *Journal of Applied Mechanics*, 29(3):515–522.

Goryacheva, I. G., Murthy, H., and Farris, T. N. (2002). Contact problem with partial slip for the inclined punch with rounded edges. *International journal of fatigue*, 24(11):1191–1201.

Green, A. E. and Zerna, W. (1954). *Theoretical Elasticy*. Oxford University Press.

Hertz, H. (1881). Über die Berührung fester, elastischer Körper. *Journal für die reine und angewandte Mathematik*, 92:156–171.

Hertz, H. (1885). Über die Berührung fester, elastischer Körper und über die Härte. *Heinrich Hertz, Gesammelte Werke, Band 1*, pages 156–171.

Hills, D. A. and Dini, D. (2011). Characteristics of the process zone at sharp notch roots. *International Journal of Solids and structures*, 48(14):2177–2183.

Hills, D. A. and Nowell, D. (1994). *Mechanics of Fretting Fatigue*. Kluwer Academic Publishers, United Kingdom.

Hills, D. A., Nowell, D., and O'Connor, J. J. (1988). On the mechanics of fretting fatigue. *Wear*, 125(1):129–146.

Hills, D. A., Nowell, D., and Sackfield, A. (1993). *Mechanics of Elastic Contacts*. Butterworth-Heinemann Ltd.

Hills, D. A., Paynter, R. J. H., and Dini, D. (2012). An overview of the quantification of fretting fatigue lives of complete contacts. *Engineering Fracture Mechanics*, 80:3–12.

Huang, X., Gibson, T. E., Zhang, M., and Neu, R. W. (2009). Fretting on the cubic face of a single-crystal ni-base superalloy at room temperature. *Tribology International*, 42(6):875–885.

Hwu, C. (1993). Fracture parameters for the orthotropic bimaterial interface cracks. *Engineering Fracture Mechanics*, 45(1):89–97.

Hwu, C. (2010). *Anisotropic elastic plates*. Springer Science & Business Media.

Hwu, C. and Fan, C. W. (1998a). Contact problems of two dissimilar anisotropic elastic bodies. *Journal of applied mechanics*, 65(3):580–587.

Hwu, C. and Fan, C. W. (1998b). Sliding punches with or without friction along the surface of an anisotropic elastic half-plane. *The Quarterly Journal of Mechanics and Applied Mathematics*, 51(1):159–177.

Jäger, J. (1997). Half-planes without coupling under contact loading. *Archive of applied mechanics*, 67(4):247–259.

Jäger, J. (1998). A new principle in contact mechanics. *Journal of tribology*, 120(4):677–684.

Jäger, J. (2003). Properties of equal bodies in contact with friction. *International journal of solids and structures*, 40(19):5051–5061.

Johnson, K. L. (1958). The effect of spin upon the rolling motion of an elastic sphere on a plane. *Journal of Applied Mechanics*, 25:332–338.

Johnson, K. L. (1985). *Contact Mechanics*. Cambridge University Press.

Karadge, M., Preuss, M., Withers, P. J., and Bray, S. (2008). Importance of crystal orientation in linear friction joining of single crystal to polycrystalline nickel-based superalloys. *Materials Science and Engineering: A*, 491(1):446–453.

Karuppanan, S. (2007). *Analysis of incomplete and complete contacts in sliding and partial slip*. PhD thesis, University of Oxford.

Knothe, K. (2008). History of wheel/rail contact mechanics: from redtenbacher to kalker. *Vehicle System Dynamics*, 46(1-2):9–26.

Korsunsky, A. M., Dini, D., Dunne, F. P., and Walsh, M. J. (2007). Comparative assessment of dissipated energy and other fatigue criteria. *International Journal of Fatigue*, 29(911):1990 – 1995. Fatigue Damage of Structural Materials {VIThe} Sixth International Conference on Fatigue Damage of Structural Materials.

Lekhnitskii, S. G. (1963). *Theory of Elasticity of an Anisotropic Elastic Body*. Holden-Day, San Francisco.

Liou, J. Y. and Sung, J. C. (2008). On the barnett-lothe tensors for anisotropic elastic materials. *European Journal of Mechanics, A/Solids*, 27(6):1140–1160.

Lykins, C. D. (1999). *An investigation of fretting fatigue crack initiation behavior of the titanium alloy Ti-6Al-4V*. PhD thesis, University of Dayton.

Matlik, J. F., Farris, T. N., Haynes, J., Swanson, G. R., and Ham-Battista, G. (2009). Prediction of fretting crack location and orientation in a single crystal nickel alloy. *Mechanics of Materials*, 41(10):1133–1151.

Mindlin, R. D. (1949). Compliance of elastic bodies in contact. *Journal of Applied Mechanics*, 16:259–268.

Mindlin, R. D. and Deresiewicz, H. (1953). Elastic spheres in contact under varying oblique forces. *Trans. ASME Ser. E. J. Appl. Mech.*, 20:372–344.

Mugadu, A., Hills, D. A., Barber, J. R., and Sackfield, A. (2004). The application of asymptotic solutions to characterising the process zone in almost complete frictional contacts. *International Journal of Solids and Structures*, 41(2):385–397.

Mulvihill, D. M., Kartal, M. E., Nowell, D., and Hills, D. A. (2011). An elastic–plastic asperity interaction model for sliding friction. *Tribology international*, 44(12):1679–1694.

Murthy, H., Gao, G., and Farris, T. N. (2006). Fretting fatigue of single crystal nickel at 600 c. *Tribology International*, 39(10):1227–1240.

Nakamura, G. and Tanuma, K. (1997). Formula for the fundamental solution of anisotropic elasticity. *Quarterly Journal of Mechanics and Applied Mathematics*, 50(pt 2):179–194.

Nowell, D. (1988). *An analysis of fretting fatigue*. PhD thesis, University of Oxford.

Nowell, D. and Dini, D. (2003). Stress gradient effects in fretting fatigue. *Tribology international*, 36(2):71–78.

Nowell, D. and Hills, D. A. (1987). Mechanics of fretting fatigue tests. *International Journal of Mechanical Sciences*, 29(5):355–365.

Nowell, D., Hills, D. A., and Sackfield, A. (1988). Contact of dissimilar elastic cylinders under normal and tangential loading. *Journal of the Mechanics and Physics of Solids*, 36(1):59–75.

Nye, J. F. (1985). *Physical property of Crystals: Their representation by tensors and matrices*. Oxford University Press.

Pagano, N. J. (1970). Exact solutions for rectangular bidirectional composites and sandwich plates. *Journal of composite materials*, 4(1):20–34.

Pasanen, A., Lehtovaara, A., Rabb, R., and Riihimäki, P. (2009). Friction behavior of quenched and tempered steel in partial and gross slip conditions in fretting point contact. *Wear*, 267(12):2200–2207.

Paynter, R. J. H. and Fleury, R. M. N. (2013). Fretting fatigue correlation work for turbine disc to blade joints. Technical report, UTC University of Oxford.

Rajeev, P. T. and Farris, T. N. (2002). Numerical analysis of fretting contacts of dissimilar isotropic and anisotropic materials. *The Journal of Strain Analysis for Engineering Design*, 37(6):503–517.

Ramesh, R. and Hills, D. A. (2015). The condition for first slip in a common edge contact subject to in-plane and anti-plane loading. *The Journal of Strain Analysis for Engineering Design*, 50(6):386–390.

Redtenbacher, F. J. (1855). *Die Gesetze des Lokomotiv-Baues*. Verlag von F. Bassermann, Mannheim.

Reed, R. C. (2006). *The Superalloys Fundamentals and Applications*. Cambridge University Press, Cambridge, UK.

Reina, S., Paynter, R. J. H., Hills, D. A., and Dini, D. (2010). Determining the coefficient of friction between solids without sliding. *Wear*, 269(5):339–343.

Ritchie, R., Knott, J., and Rice, J. (1973). On the relationship between critical tensile stress and fracture toughness in mild steel. *Journal of the Mechanics and Physics of Solids*, 21(6):395 – 410.

Sackfield, A., Dini, D., and Hills, D. A. (2005). The finite and semi-infinite tilted, flat but rounded punch. *International journal of solids and structures*, 42(18):4988–5009.

Sackfield, A., Mugadu, A., Barber, J. R., and Hills, D. A. (2003). The application of asymptotic solutions to characterising the process zone in almost complete frictionless contacts. *Journal of the Mechanics and Physics of Solids*, 51(7):1333–1346.

Sarsfield, H. (2008). Fretting fatigue tests on udimet 720li with single crystal cmsx-4 pads. Technical Report 250, UTC University of Oxford.

Savage, M. W. R. (2012). The influence of crystal orientation on the elastic stresses of a single crystal nickel-based turbine blade. *Journal of Engineering for Gas Turbines and Power*, 134:012501.

Seemann, R. (2010). *Modeling the Life Cycle Costof Jet Engine Maintenance*. PhD thesis, TU Hamburg-Harburg.

Sims, C. T. (1987). *Superalloys: Genesis and Character, Superalloys II*. Wiley, New York.

Steuerman, I. (1949). *Contact Problem of the Theory of Elasticity*. Available from the British Library in an English Translation by Foreign Technology Division, FTD-MT-24-61-70, 1970.

Stroh, A. N. (1962). Steady-state problems in anisotropic elasticity. *Journal of Mathematics and Physics*, 41:77–103.

Sveklo, V. A. (1964). Boussinesq type problems for the anisotropic half-space(superposition principle applied to equilibrium equation for anisotropic medium in absence of mass forces). *Journal of Applied Mathematics and Mechanics*, 28(5):1099–1105.

Swanson, S. R. (2004). Hertzian contact of orthotropic materials. *International Journal of Solids and Structures*, 41(7):1945–1959.

Szolwinski, M. P. and Farris, T. N. (1996). Mechanics of fretting fatigue crack formation. *Wear*, 198(1):93–107.

Taylor, D. (1999). Geometrical effects in fatigue: a unifying theoretical model. *International Journal of Fatigue*, 21(5):413–420.

Timoshenko, S. P. and Goodier, J. N. (1963). *Theory of Elasticity*. McGraw Hill, New York.

Ting, T. C. T. (1996). *Anisotropic Elasticity - Theory and Applications*. Oxford Science Publications, New York.

Ting, T. C. T. (1997). New explicit expression of barnett-lothe tensors for anisotropic linear elastic materials. *Journal of Elasticity*, 47(1):23–50.

Ting, T. C. T. (2000). Recent developments in anisotropic elasticity. *International Journal of Solids and Structures*, 37(1):401–409.

Ting, T. C. T. and Hwu, C. (1988). Sextic formalism in anisotropic elasticity for almost non-semisimple matrix n. *International Journal of Solids and Structures*, 24(1):65–76.

Tinga, T. (2006). Stress intensity factors and crack propagation in a single crystal nickel-based superalloy. *Engineering fracture mechanics*, 73(12):1679–1692.

Van Peteghem, B., Fouvry, S., and Petit, J. (2011). Effect of variable normal force and frequency on fretting wear response of ti–6al–4v contact. *Wear*, 271(9):1535–1542.

Vingsbo, O. and Söderberg, S. (1988). On fretting maps. *Wear*, 126(2):131–147.

Waterhouse, R. B. (1981). *Fretting fatigue*. Applied Science Publishers, London.

Willis, J. R. (1966). Hertzian contact of anisotropic bodies. *Journal of the Mechanics and Physics of Solids*, 14(3):163–176.

Willis, J. R. (1967). Boussinesq problems for an anisotropic half-space. *Journal of the Mechanics and Physics of Solids*, 15(5):331–339.

Appendix A

The Barnett-Lothe Integral Formalism

A.1 Elasticity matrices in a rotated coordinate system

The first step to derive the integral formalism is to obtain the elasticity matrices in a rotated coordinate system. Making use of the orthogonal transformation $\mathbf{\Omega}$ defined as

$$\mathbf{\Omega} = \begin{bmatrix} \cos\theta & \sin\theta & 0 \\ -\sin\theta & \cos\theta & 0 \\ 0 & 0 & 1 \end{bmatrix}, \tag{A.1}$$

with θ being the angle of rotation. Knowing that the elastic stiffness tensor $\mathbf{C}$ is a tensor of rank four, the rotated tensor with respect to x_3 can be written as

$$C^*_{ijks} = \Omega_{ip}\Omega_{jq}\Omega_{kr}\Omega_{st}C_{pqrt}. \tag{A.2}$$

The rotated elasticity matrices $\mathbf{Q}^*, \mathbf{R}^*$ and $\mathbf{T}^*$ with respect to the rotated coordinate system $x^*_i = \Omega_{ij}x_j$ are given by

$$\mathbf{Q}^* = \mathbf{\Omega}\mathbf{Q}(\theta)\mathbf{\Omega}, \quad \mathbf{R}^* = \mathbf{\Omega}\mathbf{R}(\theta)\mathbf{\Omega}, \quad \mathbf{T}^* = \mathbf{\Omega}\mathbf{T}(\theta)\mathbf{\Omega}. \tag{A.3}$$

It can be used a dual coordinate system in which the fundamental equations (2.24a-2.24c) are written in terms of x_i and the independent variables referred to x^*_i [Ting, 1996]. The matrices

written in terms of the rotation angle θ in (A.3) are defined as,

$$\begin{aligned}
\mathbf{Q}(\theta) &= \mathbf{Q}\cos^2\theta + (\mathbf{R}+\mathbf{R}^T)\sin\theta\cos\theta + \mathbf{T}\sin^2\theta, \\
\mathbf{R}(\theta) &= \mathbf{R}\cos^2\theta + (\mathbf{T}-\mathbf{Q})\sin\theta\cos\theta - \mathbf{R}^T\sin^2\theta, \\
\mathbf{T}(\theta) &= \mathbf{T}\cos^2\theta - (\mathbf{R}+\mathbf{R}^T)\sin\theta\cos\theta + \mathbf{Q}\sin^2\theta.
\end{aligned} \tag{A.4}$$

The components of the fundamental elasticity matrix (A.6) can also be written as a function of θ as

$$\begin{aligned}
\mathbf{N}_1(\theta) = -\mathbf{T}^{-1}(\theta)\mathbf{R}^T(\theta), \quad \mathbf{N}_2(\theta) = \mathbf{T}^{-1}(\theta), \\
\mathbf{N}_3(\theta) = \mathbf{R}(\theta)\mathbf{T}^{-1}(\theta)\mathbf{R}^T(\theta) - \mathbf{Q}(\theta).
\end{aligned} \tag{A.5}$$

A.2 Integral formulation

It was shown in [Barnett and Lothe, 1973] and [Ting, 1996] that the integral of the fundamental elasticity matrix results in the following expression

$$\frac{1}{\pi}\int_0^\pi \mathbf{N}(\theta)\,d\theta = \begin{bmatrix} \mathbf{S} & \mathbf{H} \\ -\mathbf{L} & \mathbf{S}^T \end{bmatrix} \tag{A.6}$$

or

$$\mathbf{S} = \frac{1}{\pi}\int_0^\pi \mathbf{N}_1(\theta)\,d\theta, \quad \mathbf{H} = \frac{1}{\pi}\int_0^\pi \mathbf{N}_2(\theta)\,d\theta, \quad \mathbf{L} = -\frac{1}{\pi}\int_0^\pi \mathbf{N}_3(\theta)\,d\theta \tag{A.7}$$

Equation (A.7) is sufficient to obtain the elasticity tensors **S**, **H** and **L** directly from the elastic stiffness C_{ijks}. By using this approach there is no need to obtain the eigenvalue and eigenvectors p, **a** and **b**, and the problems associated with degenerate materials are circumvented. However, the integrals (A.7) can be extremely lengthy to be obtained analytically and numerical integration is often necessary to solve them.

A.3 Numerical integration of the Barnett-Lothe tensors

One can obtain, with good accuracy, approximate values for the tensors **S**, **H** and **L** by applying simple numerical integration methods (i.e. Trapezoidal rule or Simpson's rule). The numerical

scheme of the integrals (2.37) by using the Trapezoidal rule may be written as

$$\begin{aligned}
\mathbf{S} &\simeq \frac{1}{\pi}\sum_{n=2}^{N}\frac{h_\theta}{2}\left[N_1(\theta_n)+N_1(\theta_{n-1})\right] \\
\mathbf{H} &\simeq \frac{1}{\pi}\sum_{n=2}^{N}\frac{h_\theta}{2}\left[N_2(\theta_n)+N_2(\theta_{n-1})\right] \\
\mathbf{L} &\simeq -\frac{1}{\pi}\sum_{n=2}^{N}\frac{h_\theta}{2}\left[N_3(\theta_n)+N_3(\theta_{n-1})\right]
\end{aligned} \tag{A.8}$$

with N being the total number of integration points and h_θ the increment $(h_\theta = \theta_n - \theta_{n-1})$ of the discrete space of θ.

The solution of $\mathbf{S}$ and $\mathbf{L}$ obtained numerically were compared with the explicit solution given in [Hwu and Fan, 1998a] for a normalised orthotropic and isotropic materials. Considering an orthotropic material with properties $E = 1$, $\nu = 0.3$ and $G = 1.1$, the explicit solution gives the non-zero components $S_{21} = -S_{12} = 0.3905$, $L_{11} = L_{22} = 0.7509$ and $L_{33} = 1.1$. The isotropic material analysed had the same elastic properties E and ν, and shear modulus given by $G = E/(2(1+\nu))$. The non-zero values of the explicit solution of the isotropic material are $S_{21} = -S_{12} = 0.2857$, $L_{11} = L_{22} = 0.5495$ and $L_{33} = 0.3846$. The numerical solution of the tensors $\mathbf{S}$ and $\mathbf{L}$, by using the Barnett-Lothe integral formalism and trapezoidal rule are presented next as follows

$$\mathbf{S}_{ortho} = \begin{bmatrix} 0 & -0.3905 & 0 \\ 0.3905 & 0 & 0 \\ 0 & 0 & 0 \end{bmatrix} \quad \mathbf{L}_{ortho} = \begin{bmatrix} 0.7509 & 0 & 0 \\ 0 & 0.7509 & 0 \\ 0 & 0 & 1.1 \end{bmatrix}$$

$$\mathbf{S}_{iso} = \begin{bmatrix} 0 & -0.2857 & 0 \\ 0.2857 & 0 & 0 \\ 0 & 0 & 0 \end{bmatrix} \quad \mathbf{L}_{iso} = \begin{bmatrix} 0.5495 & 0 & 0 \\ 0 & 0.5495 & 0 \\ 0 & 0 & 0.3846 \end{bmatrix}.$$

A very good precision of the integrals (2.37) was obtained with 100 integration points, $N = 100$, when compared with the explicit solution given in [Hwu, 1993]. This methodology will be used henceforth to obtain the elasticity tensors $\mathbf{S}$ and $\mathbf{L}$ in the contact problem between two anisotropic elastic bodies.

Appendix B

Additional experimental data for the "walking pad" experiments

B.1 Experimental set-up

An LVDT sensor was used to measure the relative net displacement of the pad. The armature was attached to the centre of the contact and the body was attached to the pad holder (Figure B.1). The relative displacement between the centre of the contact and the pads was measured.

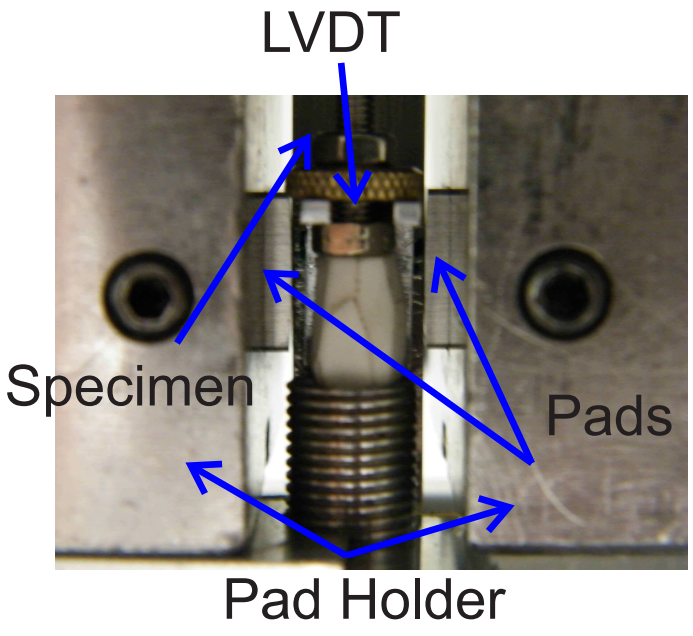

Figure B.1: Experimental set-up. LVDT and pads in the 'in-line' rig.

B.2 Partial slip results

The results under partial slip contact for the CMSX-4 pads are presented next for all tests with CMSX-4 pads. Figures (a) represent the first test carried out with each pad and figure (b) the second test after the pads and specimen were reground.

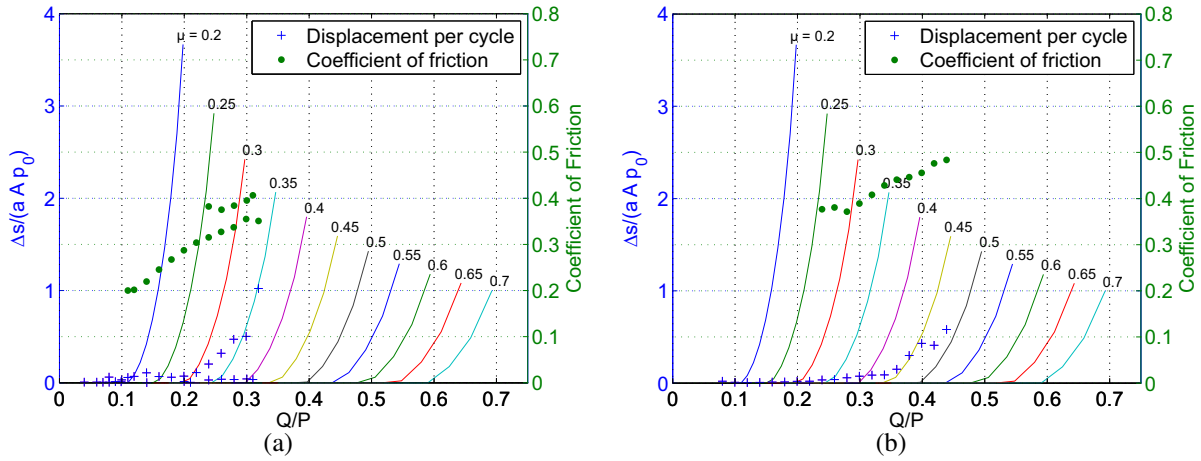

Figure B.2: Coefficient of friction in partial slip for CMSX-4 pads on RR1000 specimen. (a) Test CMSX00d1 ($\phi_1 = 6.4°$); and (b) Test CMSX00d1b ($\phi_1 = 6.4°$).

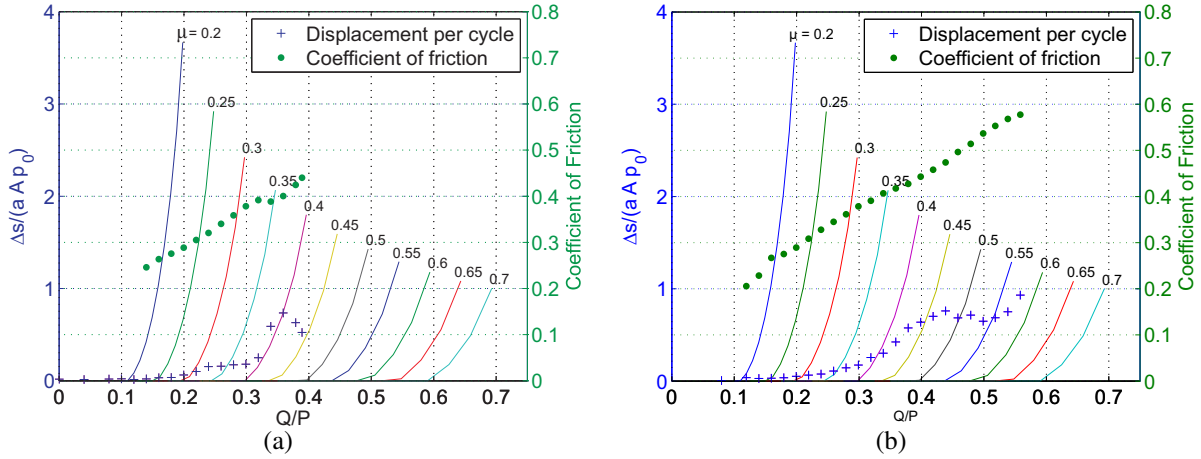

Figure B.3: Coefficient of friction in partial slip for CMSX-4 pads on RR1000 specimen. (a) Test CMSX00d2 ($\phi_1 = 9.09°$); and (b) Test CMSX00d2b ($\phi_1 = 9.09°$).

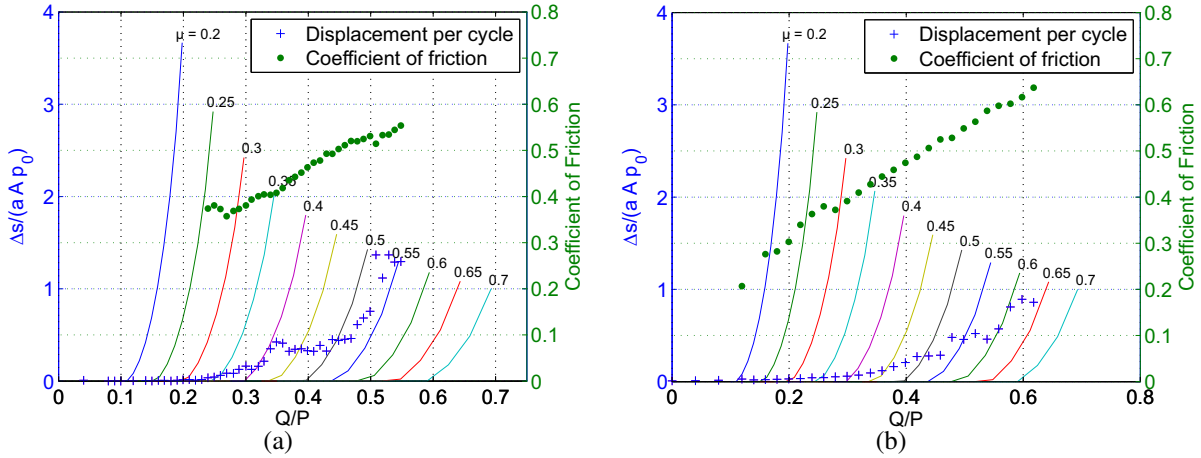

Figure B.4: Coefficient of friction in partial slip for CMSX-4 pads on RR1000 specimen. (a) Test CMSX30d1 ($\phi_1 = 30°$); and (b) Test CMSX30d1b ($\phi_1 = 30°$).

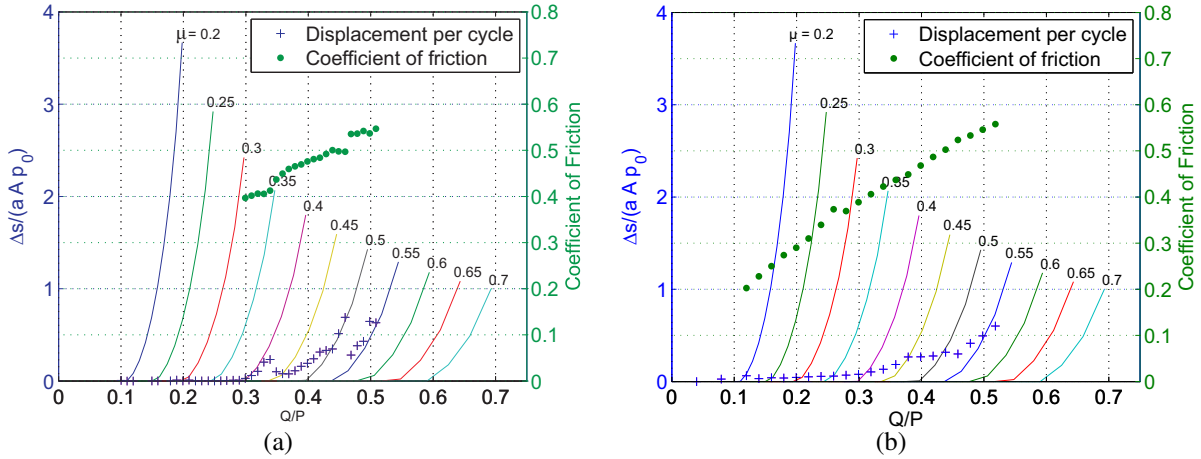

Figure B.5: Coefficient of friction in partial slip for CMSX-4 pads on RR1000 specimen. (a) Test CMSX45d1 ($\phi_1 = 42°$); and (b) Test CMSX45d1b ($\phi_1 = 42°$).

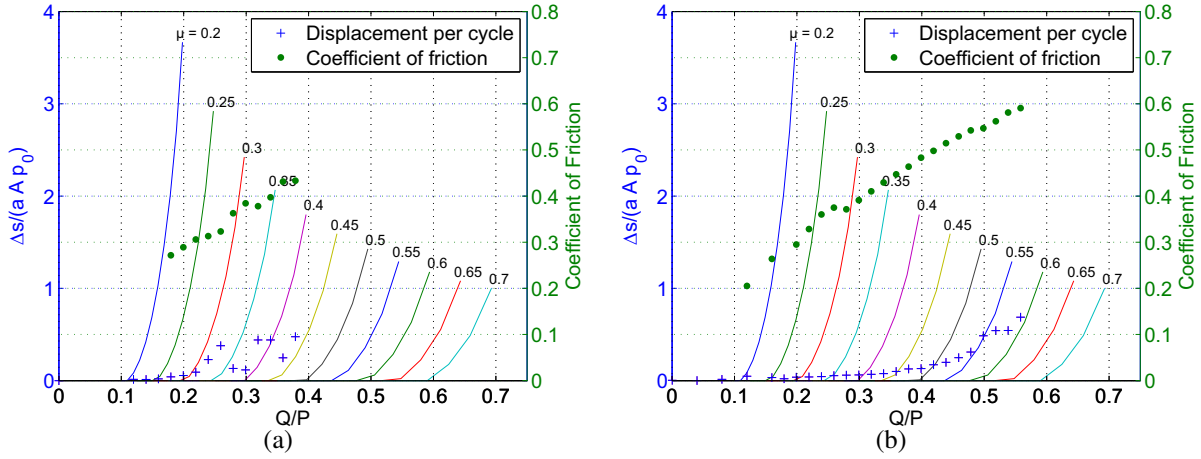

Figure B.6: Coefficient of friction in partial slip for CMSX-4 pads on RR1000 specimen. (a) Test CMSX45d2 ($\phi_1 = 39°$); and (b) Test CMSX45d2b ($\phi_1 = 39°$).

B.3 Gross sliding

An example of the measurement of the coefficient of friction are presented next for the test number CMSX45d2. The shear load in which sliding occurs at the end of the partial slip tests was recorded as in Figure B.7. Then, the test was changed to displacement control and the shear force measured with the load cell was recorded and the average taken (Figure B.8)

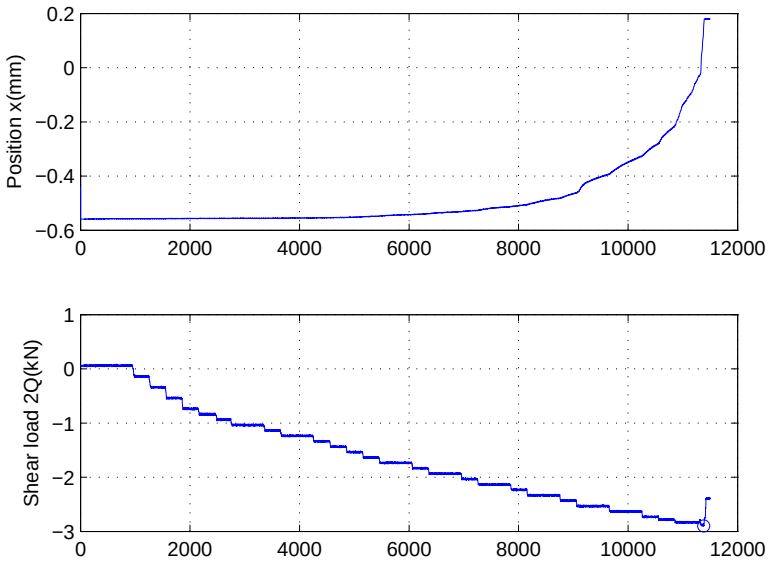

Figure B.7: Partial slip test and limit load where gross slip occur.

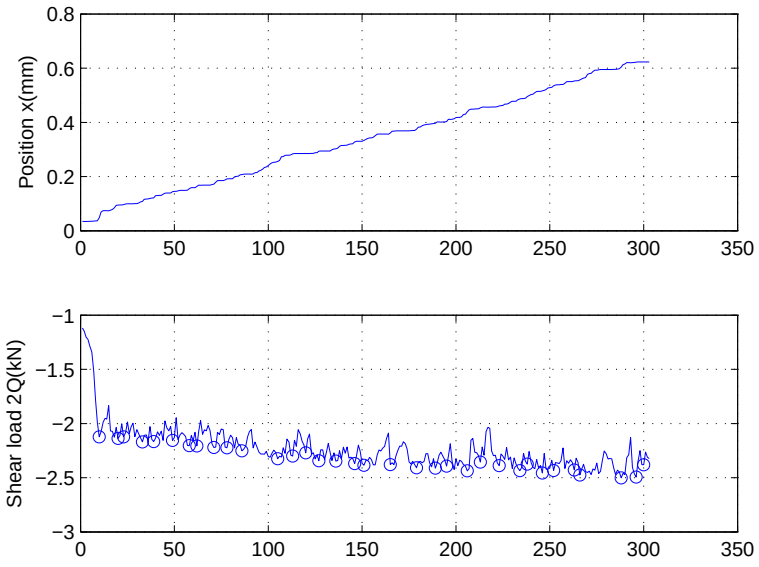

Figure B.8: Gross sliding test and shear load during sliding.

Appendix C

Dimensional analysis and calibrations of the three quarter plane solution

C.1 Pure modes of loading

C.1.1 Contact law

A generic expression for the contact size, l, can be written as a power law in terms of the independent variables, such that,

$$l^3 = \Lambda_k {K_k}^m {E^*}^n \rho^p, \tag{C.1}$$

where m, n and p are unknown exponents, Λ_k is a dimensionless multiplier, and K_K is the applied stress intensity factor, where the index k represent the load modes, $k = I, II$. A dimensional analysis may be conducted to determine the exponents m, n and p. Substituting the quantities in equation (C.1) by their dimensions and equating both sides of the equation in terms of the dimensions of force, $[F]$, and of length, $[L]$, separately, two equations are obtained for the exponents m, n and p,

$$\begin{aligned} [L]^3 &= [FL^{-1-\lambda_k}]^m [FL^{-2}]^n [L]^p \\ [F] \quad &\rightarrow \quad n = -m \\ [L] \quad &\rightarrow \quad p = 3 - m(1-\lambda_k). \end{aligned} \tag{C.2}$$

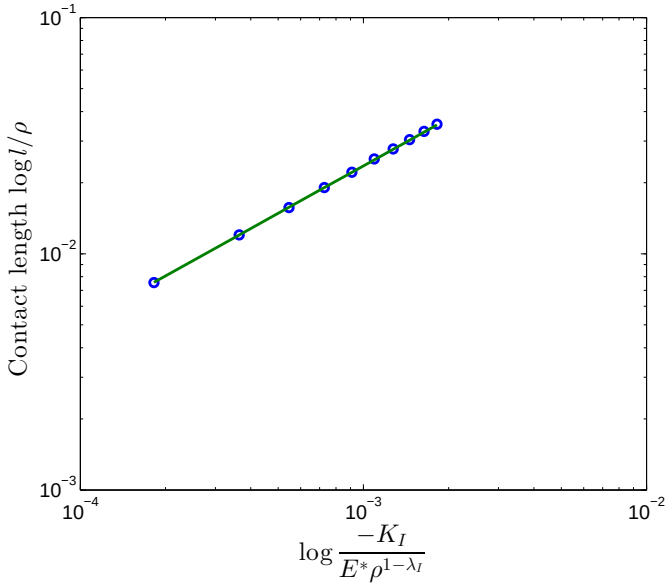

Figure C.1: Contact length l as a function of the stress intensity factor K_I for determining the exponent m in a pure mode I loading problem.

The system of equations cannot be solved completely with these two equations, since there are three unknowns, and a numerical calibration is necessary. The expression for the contact size in a pure mode loading problem can be rewritten in terms of one exponent only, m_k, as

$$\left(\frac{l}{\rho}\right)^3 = \Lambda_k \left(\frac{K_k}{E^* \rho^{(1-\lambda_k)}}\right)^m, \tag{C.3}$$

where m and the multiplier Λ_k are to be obtained by finite element analysis calibration. The logarithm of equation (C.3) can be written down as

$$3\log l = \log \Lambda_k + m_k \log K_k - m_k \log E^* + [3 - m_k(1-\lambda_k)]\log \rho. \tag{C.4}$$

Therefore, the slope of the curve of the variation of the contact length as function of K_k in a logarithmic scale gives the value of m. An example of the variation of the contact length as a function of the pure mode I load intensity factor is presented in Figure C.1.

C.1.2 Peak Stress

The peak contact stress, p_0, can also be written down as a function of the independent variables of the problem for the pure mode loading case can be written as

$$p_0{}^3 = \Pi_k K_k{}^m E^{*n} \rho^p, \tag{C.5}$$

where the multiplier Π_k and the exponents m, n and p, are to be found. The index k represent the load mode, $k = I, II$. Similarly to the approach used in the contact law formulation, a dimensional analysis of equation (C.5) can be used to reduce the number of unknown variables. If the dimensions of force, $[F]$, and of length, $[L]$, are analysed separately, two equations are obtained for the exponents m, n and p,

$$\begin{aligned} [FL^{-2}]^3 &= [FL^{-1-\lambda_k}]^m [FL^{-2}]^n [L]^p \\ [F] \quad &\rightarrow \quad n = 3 - m \\ [L] \quad &\rightarrow \quad p = -m(1-\lambda_k). \end{aligned} \tag{C.6}$$

Then, equation (C.5) may be simplified and written in terms of the unknown exponent m only,

$$\left(\frac{p_0}{E^*}\right)^3 = \Pi_k \left(\frac{K_k}{E^* \rho^{(1-\lambda_k)}}\right)^m. \tag{C.7}$$

The exponent for the pure mode I case can be obtained by taking the logarithm of equation (6.7), which can be written down as

$$3 \log p_0 = \log \Pi_k + m \log K_k + (3-m) \log E^* - m(1-\lambda_k) \log \rho, \tag{C.8}$$

and by using the results of peak stress obtained via finite element analysis for different values of K_k to get the slope of the plot $\log K_k \times \log p_0$ (Figure C.2). The value of the exponent was found to be $m \simeq 2$.

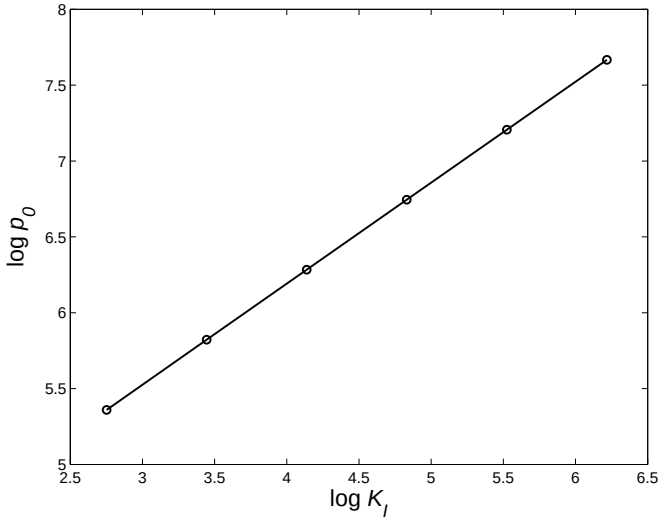

Figure C.2: Peak stress as a function of mode I stress intensity factor for determining m.

C.1.3 Contact law in mixed mode loading

From the finite element analysis it was found that the contact law in a mixed mode loading is a linear combination of modes I and II. Hence, the contact law may be written as

$$\left(\frac{l}{\rho}\right)^3 = f(K_I^* + \Lambda K_{II}^*) \tag{C.9}$$

where K_I^* and K_{II}^* are the dimensionless terms containing the stress intensity factors in equations (6.12) and (6.13). When $K_{II}^* = 0$, one obtains that

$$\left(\frac{l}{\rho}\right)^3 = \Lambda_I(K_I^*) \tag{C.10}$$

and hence the contact length can be written as

$$\left(\frac{l}{\rho}\right)^3 = \Lambda_I(K_I^* + \Lambda K_{II}^*)^2 \tag{C.11}$$

Furthermore, if $K_I^* = 0$, then

$$\left(\frac{l}{\rho}\right)^3 = \Lambda_I \Lambda^2 (K_{II}^*)^2 = \Lambda_{II}(K_{II}^*)^2 \qquad \text{and} \qquad \Lambda^2 = \frac{\Lambda_{II}}{\Lambda_I} \tag{C.12}$$

Therefore, the final contact length in a mixed mode problem can be rewritten as

$$\left(\frac{l}{\rho}\right)^3 = \Lambda_I \left(\frac{K_I}{E^*\rho^{(1-\lambda_I)}} + \Lambda \frac{K_{II}}{E^*\rho^{(1-\lambda_{II})}}\right)^2, \tag{C.13}$$

C.2 Algebra for the edge dimensional scaling factor

C.2.1 Dimensional analysis of K_N in a pure mode case

A generic formulation of K_N in terms of the independent variables may be written as

$$K_N = H_k {K_k}^m {E^*}^n \rho^p. \tag{C.14}$$

A dimensional analysis of the equation above gives two equations of the coefficients m, n and p,

$$\begin{aligned}
[FL^{-5/2}] &= [FL^{-1-\lambda_k}]^m [FL^{-2}]^n [L]^p \\
[F] \quad \rightarrow \quad & n = 1-m \\
[L] \quad \rightarrow & -5/2 = (-1-\lambda_k)m - 2n + p \\
& p = 2(1-m) - (-1-\lambda_k)m - 5/2 \\
& p = -m(1-\lambda_k) - 1/2.
\end{aligned} \tag{C.15}$$

Rewriting equation (C.14) in terms of the exponent m only, one gets the following expression

$$\frac{K_N}{E^*\rho^{-1/2}} = H_k \left(\frac{K_k}{E^*\rho^{1-\lambda_k}}\right)^m \tag{C.16}$$

where H_k and m are the multiplier and exponent to be obtained from the finite element calibration.

C.2.2 Normal dimensional scaling factor in mixed loading

The pure mode loading formulations of K_N in terms of the applied stress intensity factors are given as

$$\left(\frac{K_N}{E^*\rho^{-1/2}}\right)^3 = H_I\left(\frac{K_I}{E^*\rho^{2-\lambda_I}}\right), \tag{C.17}$$

$$\left(\frac{K_N}{E^*\rho^{-1/2}}\right)^3 = H_{II}\left(\frac{K_{II}}{E^*\rho^{2-\lambda_{II}}}\right), \tag{C.18}$$

If we assume that the variation of K_N is linear in the $K_I \times K_{II}$ space, the following can be written,

$$(K_N^*)^3 = f(K_I^* + HK_{II}^*), \tag{C.19}$$

where K_N^*, K_I^* and K_{II}^* are the dimensionless variables in equations (C.17) and (C.18), respectively. If $K_{II}^* = 0$, equation (C.19) simplifies to

$$(K_N^*)^3 = H_I(K_I^*), \tag{C.20}$$

so that (C.19) can be rewritten as

$$(K_N^*)^3 = H_I(K_I^* + HK_{II}^*). \tag{C.21}$$

Now, if $K_{II}^* = 0$, the following equation can be written,

$$(K_N^*)^3 = H_I H(K_{II}^*) = H_{II}(K_{II}^*), \qquad H = \frac{H_{II}}{H_I} \tag{C.22}$$

So the final dimensionless formulation of K_N in terms of K_I and K_{II} is given by the following expression,

$$\left(\frac{K_N}{E^*\rho^{-1/2}}\right)^3 = H_I\left(\frac{K_I}{E^*\rho^{1-\lambda_I}} + H\frac{K_{II}}{E^*\rho^{1-\lambda_{II}}}\right), \qquad \text{with } H = \frac{H_{II}}{H_I}. \tag{C.23}$$

C.3 DISP user subroutine

The subroutine presented here was used to implement the equations for the displacements in (6.3) and (6.4). First the node coordinates need to be transformed to polar coordinates (R, θ). Then a load magnitude M is chose and the angle loading direction in the $K_I^* \times K_{II}^*$ space, α.

```
      SUBROUTINE   DISP(U,KSTEP,KINC,TIME,NODE,NOEL,JDOF,COORDS)
C
      INCLUDE 'ABA_PARAM.INC'
C
      DIMENSION U(3),TIME(2),COORDS(3)
      REAL  A, E, nu, mu, K1, K2, B, d0, lambda1, lambda2
C


      ! defining Pi = 3.14....
      PI=4.D0*DATAN(1.D0)

          ! Cartesian Coordinates (Abaqus)
      X = COORDS(1)
      Y = COORDS(2)

          ! Transformation to polar coordinates
      R = SQRT(X**2 + y**2)   ! Radius
      ! Angle Theta
      IF (X.GE.0 .AND. Y.GE.0) THEN
        Th= ATAN(abs(Y/X))
      ELSE IF (X.LT.0 .AND. Y.GT.0) THEN
        Th= PI-ATAN(abs(Y/X))
      ELSE IF (X.LT.0 .AND. Y.LE.0) THEN
        Th= ATAN(abs(Y/X))-PI
      ELSE IF (X.GE.0.AND.Y.LT.0) THEN
        Th= -ATAN(abs(Y/X))
      END iF

      Th = Th + PI/4
```

```
      ! William's eigenvalues for a 3/4 pi
 lambda1 = 0.544483736782464;
 lambda2 = 0.9085291898460973;

      ! Modulus of the applied load
M = 100;
 alpha = 0*PI/180; ! Angle of direction in the KI x KII space

      ! Material properties
 E  = 100000.
 nu = 0.3
 mu = E/(2*(1+nu))
      ! Initial step loading coordinates
 K1 = M*COS(alpha);
 K2 = M*SIN(alpha);
 ! Displacements multipliers for the applied load K1 K2
 A = -abs(K1)*R**lambda1/(2*mu)
 B = abs(K2)*R**lambda2/(2*mu)
 ! Increments of displacements multipliers
 A = A*TIME(1)
 B = B*TIME(1)

 ! Applying displacement boundary conditions
 IF (JDOF.EQ.1) THEN
    urI = -0.770627583754802*(-1.255516263217536*Cos(0.455516263217536*Th)
- + 0.8387713993570622*Cos(1.544483736782464*Th))
    urII = 2.1607846785247813*(-0.8918*Sin(0.09179999999999999*Th) +
-      0.41777370645003803*Sin(1.9082*Th))

    U(1) = A*urI + B*urII

 ELSE IF (JDOF.EQ.2) THEN
    uThI = -0.770627583754802*(2.344483736782464*Sin(0.455516263217536*Th)
- - 0.8387713993570622*Sin(1.544483736782464*Th))
    uThII = 2.1607846785247813*(-2.7082*Cos(0.09179999999999999*Th) +
```

```
–       0.41777370645003803*Cos(1.9082*Th))
  U(1) = A*uThI + B*uThII
  END IF
  RETURN
  END
```